Mechanistic Modeling of Degrading Perovskite Solar Cells – Investigating Device-Level Degradation Phenomena and Informing Predictive Machine Learning Models for Operational Lifetimes

William Vincent Heins

A thesis

submitted in partial fulfillment of the

requirements for the degree of

Master of Science in Chemical Engineering

University of Washington

2025

Committee:

Hugh W. Hillhouse

David S. Bergsman

Program Authorized to Offer Degree:

Chemical Engineering

University of Washington

Abstract

Mechanistic Modeling of Degrading Perovskite Solar Cells – Investigating Device-Level Degradation Phenomena and Informing Predictive Machine Learning Models for Operational Lifetimes

William Vincent Heins

Chair of the Supervisory Committee:

Hugh W. Hillhouse

Department of Chemical Engineering

Halide perovskite (HP) photovoltaics (PV) are a high-performance, low-cost alternative to traditional crystalline silicon (c-Si) PV, but their short operational lifetimes prevent them from reaching commercial scale. Alongside other processes, HPs chemically degrade under elevated temperature, oxygen, moisture, illumination, and electrical bias, and this chemical decomposition is the primary driver of HP PV performance decline. In previous studies, we proposed mechanisms and developed kinetic rate law models for the chemical decomposition of three relevant HP materials, and we developed predictive machine learning (ML) models for the optoelectronic properties of these HP films and for device operational lifetimes. Although, no mechanistic models of device performance decline exist. Additionally, our initial predictive

models of operational lifetimes require our kinetic rate law models to be accurate, and these models are both composition-specific and time-intensive to develop. In this work, we fill these essential gaps by mechanistically modeling degrading perovskite solar cells (PSCs) and improving our predictive ML models for their operational lifetimes. Specifically, we globally fit the non-ideal diode model and a custom, one-dimensional (1D) drift-diffusion model to light and dark current-voltage (J-V) scans over time for devices degrading under varying temperatures, oxygen concentrations, humidities, and illumination intensities. Moreover, we quantify effective fractional active areas and thicknesses of HP films over degradation from in situ dark-field (DF) microscopy measurements, constituting an effective model of degradation profile over degradation. The extracted diode and drift-diffusion fitting parameters and their corresponding derived parameters are mechanistic properties of the device, and coupled with these effective degradation profile parameters, the evolutions of and correlations among these parameters over degradation illuminate the mechanisms of device performance decline. Furthermore, in a unique cumulative sensitivity analysis (CSA), we calculate the exact influence of each fitting parameter on each solar cell parameter over time, quantifying the exact influence of each degradation mechanism on device performance decline. Last, we analyze the relationships between parameter evolutions and degradation conditions including Arrhenius modeling to inform the development of both accelerated aging models and long-lived device design in future work. Overall, these analyses constitute the most advanced mechanistic model of PSC performance decline to date. Then, beyond mechanistic modeling, we utilize these various parameter sets as features in predictive machine learning (ML) models of operational lifetimes (T_{80}), achieving a champion model applicable to all three of our PSC architectures with a mean-normalized root-mean-squared (RMS) error (NRMSE) of 26.5% using features derived only from temperature and the

first 20 J-V measurements, without requiring the other degradation conditions or the composition-specific kinetic rate law models necessary for our previous predictive ML model. The predictive ML models developed in this study are the strongest we have produced in both accuracy and applicability, and we thus demonstrate the ability to use empirical and modeling parameters as features to construct predictive ML models for the operational lifetimes of multiple PSC architectures from small device degradation datasets using common, low-cost electronic measurements (e.g., J-V scans). This establishes a strong foundation for and represents a powerful step toward high-throughput device testing and thus long-lived device development.

Table of Contents

List of Tables

List of Figures

Acknowledgements

"If I have seen further, it is by standing on the shoulders of giants." – Isaac Newton in a Letter to Robert Hooke (1675)

I am immensely grateful to the many incredible individuals who have supported me both personally and professionally in life and in this work. First, I would like to thank my graduate mentor, Dr. Spencer Cira, for his incredible support and guidance as a mentor and friend. He has supported and guided me in every way throughout this entire endeavor, and this would not have been possible without him. I would also like to thank my advisor, Professor Hugh Hillhouse, for his technical and professional mentorship, along with his inspiring intellect, work ethic, and love for science. Thank you also to Professor David Bergsman for being a fantastic instructor and serving on this thesis committee, to Professor Alex Prybutok for her infectious energy and guidance in developing code in this study, and to Professor John Berg for being a truly inspiring figure in scientific knowledge and love for the sciences. These professors have all been inspiring in their unwavering dedication to their students and have been an integral part of my education in this program. I cannot thank these individuals enough. Thank you.

I would also like to thank Professor Vincent Le Corre from the University of Southern Denmark and Professor Jan Anton Koster from the University of Groningen in the Netherlands for sharing their drift-diffusion models and optimization routines without which the mechanistic modeling in this study would not have been possible. Moreover, I would like to specially thank Professor Vincent Le Corre for his support and guidance which have been integral in both this work and my learning throughout this entire endeavor. These professors' willingness to share their models and educate researchers on their use has made this and many other projects possible.

I would also like to thank my incredible colleagues in the Hillhouse research group including Dr. Yuhuan Meng, Dr. Preetham Sunkari, and Daniel Kuo for their continuous support and guidance throughout this work, alongside their inspiring intellect and work ethic in scientific discovery. Moreover, I would like to specially thank Dr. Preetham Sunkari for both his encouragement and kindness throughout this work and both Dr. Wiley Dunlap-Shohl and Dr. Preetham Sunkari for sharing their machine learning (ML) models, without which the ML modeling in this study would not have been possible. I cite the above quote to illustrate the mountain of work individuals in our group and Professors Le Corre and Koster have contributed in perovskite solar cell degradation and modeling, all of which has made this research possible. Indeed, this work rests on this mountain of incredible work performed before it.

Thank you also to my collaborators from my time as an undergraduate in Professor John Devin Mackenzie's group for a fantastic undergraduate research experience. I would like to specially thank Dr. Michael Crump and Dr. Greg Guymon for their guidance and mentorship in my undergraduate research, Dr. Oliver Nakano-Baker for his initial guidance in developing data pipelines, and Professor Devin Mackenzie for his support and mentorship. Thank you also to Ethan Schwartz, Dr. Tanka Rana, and Dr. Mazhar Abbas for being fantastic coworkers during my time as an undergraduate researcher.

For my personal friends and family, I would like to thank my dearest friends Kristin Bennett, Carly Williams, Ethan Wu, Joel Bailin, Graydon Gamache, and Avi Mittal for your continued friendship and support in life and in this endeavor. Thank you also to all of my fellow students in both my undergraduate and graduate chemical engineering (ChemE) cohorts for their friendship and creating a fantastic ChemE community. Finally, I would like to thank my brother, Bradley Heins, my mother, Tracy Heins, and my father, Bill Heins for your unbounded and unwavering love and support, without which I would not be who I am today.

Last, I would like to acknowledge the U.S. Department of Energy (DOE) Solar Energy Technologies Office (SETO) for their financial support of our group's work, and the Clean Energy Institute (CEI), University of Washington (UW), UW Molecular Analysis Facility (MAF), and the UW Hyak supercomputer cluster for making this work possible.

Dedication

For my brother, Bradley Heins, my mother, Tracy Heins, and my father, Bill Heins, without whom this work would not have been possible. Your love and support have been unbounded and unwavering, and you have been and will always be dearest to my heart.

1 INTRODUCTION

1.1 Motivation for Halide Perovskite (HP) PV Research

1.1.1 Motivation for Thin Film PV Research

Traditional crystalline silicon (c-Si) PV possesses the lowest levelized cost of energy (LCOE) of all energy conversion technologies except wind,[1] but it demands significant capital expenditure. Constructing a c-Si PV module factory with 2 GW/year capacity requires on the order of $2 billion,[2] and this economic barrier hinders c-Si PV from achieving the commercial scale necessary to meet growing energy demands. This has incentivized research for novel alternatives, and thin film PV has become one such option.[3] Manufactured by monolithic deposition over large areas, thin film PVs eliminate the capital expenditure (CapEx) of c-Si wafer processing and interconnection. Additionally, their micron-scale thicknesses enable flexibility for installation on curved surfaces and reduced material cost,[4,5] incentivizing research to discover and optimize thin film PV materials.

1.1.2 Motivation for Halide Perovskite (HP) PV Research

Among other materials, this research revealed halide perovskites (HPs) as a promising light-absorbing material.[6] In the decade following their discovery, halide perovskite photovoltaics (HP PV) have seen unprecedented growth in certified power conversion efficiency (PCE) from 3.8% to 25.5%,[5,7] and they possess many favorable properties including high carrier mobilities, minority carrier lifetimes, minority carrier diffusion lengths, high absorption coefficients, and direct bandgap absorption.[6] HPs thus enable high-efficiency, low-cost, flexible solar cells[5,8,9] which may be installed on curved surfaces and can improve crystalline silicon (c-Si) PCEs with tandem architectures.[10,11] Additionally, HPs are the first solution-processable material applied to PV technology to achieve > 25% PCE,[5,7,12] enabling high-throughput, low-cost roll-to-roll (R2R) and sheet-to-sheet (S2S) production lines.[5] For these reasons, HP PVs could enable a 94% decrease in capital expenditure (CapEx) relative to c-Si PV,[2] incentivizing research to unlock their commercial potential.

1.2 Short Operational Lifetimes – The Primary Barrier to HP PV Scalability

1.2.1 HP Film Degradation – The Primary Driver of Short Operational Lifetimes in HP PV Devices

Alongside difficulties in transitioning from small-area cells to large-area modules, short operational lifetimes present the greatest barrier to HP PVs reaching commercial scale and thus meeting growing energy demands.[5] In 2018, the longest PSC lifetimes did not exceed one year,[13] yet a U.S. Department of Energy (DOE) analysis estimated devices with 20% total area efficiency and a standard $0.19/Wp module cost[14] would require > 30 year operational lifetimes and <0.5% year-over-year PCE degradation rate to achieve the target $0.03/kWh LCOE.[15] As multidecade device performance testing is infeasible, operational lifetimes must be estimated to enable manufacturers to identify relevant markets and provide warranties to customers. Although, alongside other processes, HP films chemically degrade under elevated temperature, oxygen, moisture, illumination, and electrical bias (see Figure 1).[16] As the HP film is responsible for light absorption and thus current generation, this decomposition is the primary driver of HP PV performance decline and must therefore be studied to enable development of long-lived devices.[17,18]

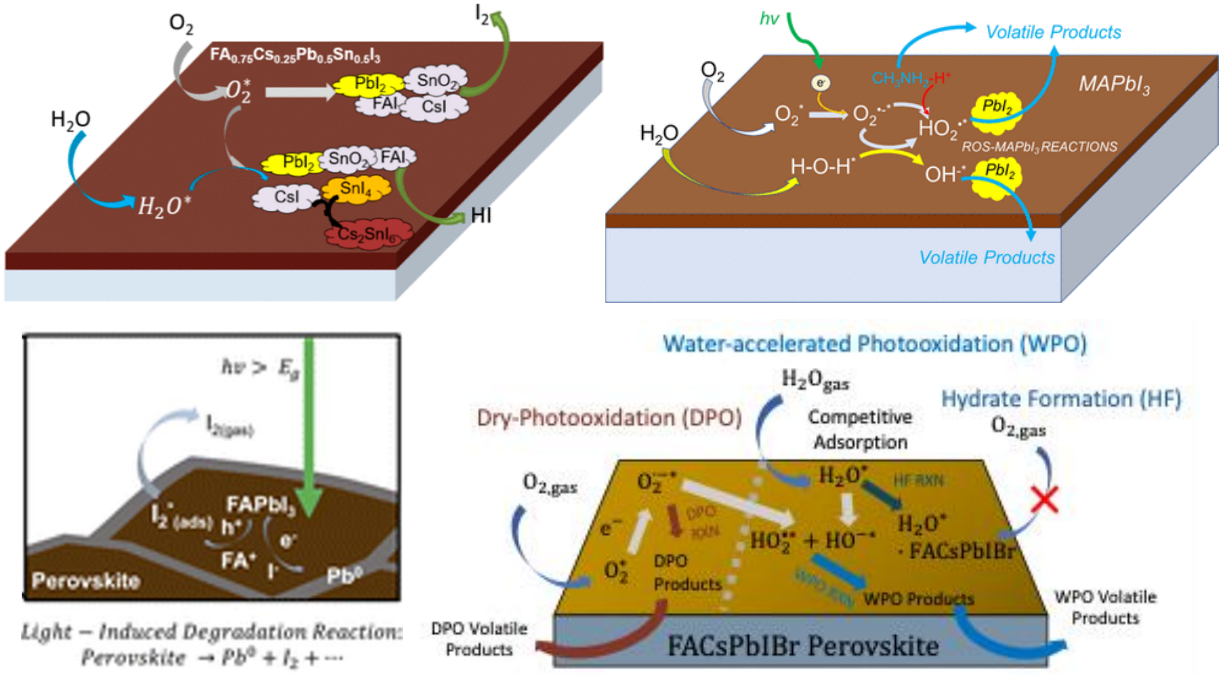

Figure 1. Schematics of the Chemical Decomposition Pathways for Each of Our HP Compositions. These pathways include the (top left) photooxidation pathways for our low-bandgap HP composition ($FA_{0.75}Cs_{0.25}Pb_{0.5}Sn_{0.5}I_3$),[19] (top right) photooxidation pathways for our medium-bandgap HP (archetypal $MAPbI_3$),[16] and both the (bottom left) light-induced degradation (LID) pathway[20] and (bottom right) photooxidation pathways of our high-bandgap HP compositions ($FA_xCs_{1-x}Pb(I_yBr_{1-y})_3$).[21]

1.2.2 The Inefficacy of Accelerated Aging Tests as Motivation for the Development of Advanced Predictive Models of Operational Lifetime

Although, this degradation of the absorber layer (which is not appreciable for other PV technologies) complicates the relationships between the evolutions of device properties and environmental conditions and thus the estimation of operational lifetimes with traditional accelerated aging tests (e.g., the IEC 61215 standard solar cell durability tests).[22] These tests expose devices to intensified degradation conditions and relate the devices' degradation dynamics to those in standard conditions using predictive operational lifetime models which depend on degradation conditions. Such tests include damp heat (e.g., Module Quality Test 13 for tracking PCE decline at 85 °C and 85% relative humidity (RH) for 1000 h),[22–25] thermal cycling (200 cycles of between −40°C and 85°C in the dark),[23,24] outdoor testing,[26] ultraviolet (UV) light,[26] and unique tests developed by individual research groups.[27] Although, such models are based on degradation mechanisms of traditional inorganic devices, not the more complex degradation phenomena in HP PVs. Moreover, recent models attempting to account for HP PV's dominant degradation mechanisms still suffer from an incomplete knowledge of these phenomena,[28] many of which are unique to specific architectures.[29] These models thus do not accurately predict operational lifetimes in reasonable measurement times, or conversely, require excessive measurement times to yield accurate predictions. These models must therefore improve in overall accuracy or model a wider range of operational lifetimes to increase the accelerated aging factor (AAF). We therefore improve our predictive model by incorporating new transformations of J-V features and new device degradation datasets for all three HP compositions studied in our previous work,[16,18–21,30,31]

along with variation of the considered measurement time and the number of measurement points utilized in J-V feature transformations. Additionally, we discuss the potential for our small-dataset predictive machine learning (ML) models to construct accelerated aging models of operational lifetimes based on degradation conditions. Furthermore, these models (including our previous predictive machine learning (ML) models)[17,32] require fabrication and degradation testing of dozens of devices to develop a model for each architecture. This is acceptable, but it is optimal to develop a model which applies to all architectures, and we thus also develop an overall predictive machine learning (ML) model over all architectures alongside models for each individual architecture, eliminating this requirement.

1.2.3 Overview of Our Previous Studies on HP Film and Device Degradation

These shortcomings are essential gaps in the development of such predictive models and motivate our group's mission of developing effective predictive models of operational lifetime for HP PV devices. In this and previous work, we have approached this goal in three stages: modeling the mechanisms and kinetics of HP film degradation, studying the evolution of film optoelectronic properties and device properties over film and device degradation, and developing predictive machine learning (ML) models of operational lifetime. Specifically, for the first stage, we developed the first kinetic rate law models for three relevant and distinct HP compositions (low-bandgap ($FA_{0.75}Cs_{0.25}Pb_{0.5}Sn_{0.5}I_3$), medium-bandgap ($MAPbI_3$), and high-bandgap ($FA_{0.8}Cs_{0.2}Pb(I_{0.83}Br_{0.17})$, very similar to those in this study) and proposed various chemical mechanisms, constituting the first mechanistic models for HP film degradation.[16,19–21] Furthermore, in the second stage, we characterized HP films in situ while degrading in varying conditions with dark-field (DF) microscopy, steady-state photoluminescence (SSPL), and steady-state photoconductivity (PC) measurements to visualize the distribution of degraded products (i.e., degradation profile), measure the quasi-Fermi level splitting (QFLS, ΔE_F), and measure the ambipolar carrier diffusion length (L_d), respectively. We used the evolutions of such properties over time to speculate information about the degradation profile and its influence on film optoelectronic properties, and we then trained machine learning (ML) models of ambipolar carrier diffusion length (L_d) on these in situ SSPL and PC measurements as an initial step in predictive modeling of HP film optoelectronic properties and as a precursor to predictive modeling of device performance.[18,30,31] Finally, we developed the first predictive machine learning (ML) model for operational lifetimes of $MAPbI_3$ devices, informed with the degradation conditions, solar cell parameters over time, and kinetic rate law model.[17]

1.2.4 Motivation for Current Work

However, no mechanistic models exist for device performance decline, despite being crucial to understanding the mechanisms of device performance decline and thus to its prevention. Furthermore, such models may also enable stronger predictive models of device performance decline and operational lifetimes, crucial for the high-throughput testing of device durability required for the development of long-lived devices. We therefore fill this essential gap by mechanistically modeling degrading perovskite solar cells (PSCs), globally fitting mechanistic models to light and dark current-voltage (J-V) scans over time for our three HP PV architectures degrading under varying environmental stresses. Additionally, regarding our previous predictive models of $MAPbI_3$ device operational lifetimes,[17,32] these models required our kinetic rate law model for $MAPbI_3$ decomposition[16] to be accurate, and this kinetic model is both composition-specific and time-intensive to develop. We therefore improve our predictive model by incorporating new transformations of J-V features and new device degradation datasets for all three

HP compositions studied in our previous work,[16,18–21,30,31] along with variation of the considered measurement time and the number of measurement points utilized in J-V feature transformations.

1.3 Mechanistic Modeling of Degrading HP PV Devices

1.3.1 Overview of Existing Mechanistic Models and Simulators

The utility of quantifying properties of PV devices by fitting models to characterization data has driven the development of many models. The diode models are widely used for their simplicity, analytical form, and moderate accuracy, but they suffer from many inaccurate, idealizing assumptions (see Section 4.3.3.2 and 4.3.3.3).[33] Additionally, various open-source software programs (e.g., SCAPS,[34–36] PC 1D,[37,38] and AFORS HET[39]) and custom programs[40–42] have been developed to numerically simulate PV devices with drift-diffusion models accounting for greater complexity. These simulations numerically solve discretized versions of the set of coupled partial differential equations governing semiconductor devices – the drift-diffusion equation, continuity equation, and Poisson equation – to rigorously model free carrier and ion drift and diffusion and the corresponding electrostatic potential profile, often by Gummel iteration or its variants.[43,44] Moreover, models for carrier generation, trapping, de-trapping, recombination, and extraction, along with boundary conditions for carrier concentrations and electrostatic potential, are included as inputs to the governing equations. Although, these drift-diffusion models and simulators make various assumptions in their modeling of device phenomena, compromising their ability to provide insights into such phenomena.[45] We therefore list all phenomena considered by existing drift-diffusion models and simulators below and specify if and how these phenomena are considered.

- Device Geometry (e.g., the number of layers, grain boundaries, and interfaces, and the number of dimensions)
- Electron-Hole Pair Generation
    - Optical Absorption
    - Exciton Formation, Dissociation, Decay into Electrons and Holes
- Trapping and De-Trapping of Electrons and Holes
- Recombination
    - Trap-assisted, nonradiative, monomolecular Shockley-Read-Hall (SRH) Recombination (occurs in crystal bulk, both sides of grain boundaries, and/or both sides of layer interfaces)
    - Bimolecular Recombination
        - Direct, band-to-band, radiative bimolecular recombination
        - Trap-assisted, nonradiative, Auger bimolecular recombination
    - Trimolecular Auger Recombination
- Boundary Conditions at Interfaces
    - Carrier Concentrations (effectively modeling carrier extraction)
        - Electron and Hole Concentrations
        - Ion Concentrations
    - Electrostatic Potential or Electric Field Strength

Indeed, despite the complexity of these models, some important elements remained unmodeled (e.g., multiple dimensions, nonuniform distributions of degradation products along grain boundaries),[45,46] especially by traditional software programs (e.g., SCAPS,[34–36] PC 1D,[37,38] and AFORS HET[39]) which are also difficult to improve compared with custom models. We therefore

employ a custom, open-source drift-diffusion model and simulator in addition to the standard non-ideal diode model.

1.3.2 Existing Applications of Mechanistic Models to PSCs

This importance of mechanistically understanding device phenomena in optimizing device performance and lifetime (as for any technology) has driven widespread developments in drift-diffusion modeling of PSCs.[45] These models were originally used to develop a mechanistic model of current-voltage (J-V) scan hysteresis caused by the migration of mobile ions (especially iodide anions (I^-) and vacancies (V_I^+)). This phenomenon was first observed by Henry Snaith and coworkers (widely known as key contributors in demonstrating the potential of HP PVs)[47] in 2014 and is now a widely accepted barrier to the scalability of HP PVs (alongside instability). Indeed, drift-diffusion modeling provided the means to mechanistically and directly model this and other phenomena. Moreover, since models present the opportunity for optimization, drift-diffusion models have been utilized to optimize PSCs,[48] and these studies have further illuminated the potential of HP PVs.

1.3.3 Introduction to the Employed Drift-Diffusion Model and Simulator (SIMsalabim)

In a series of studies, Koster *et al.* developed a custom, one-dimensional (1D) drift-diffusion model with steady state and transient simulations to model—in addition to standard models included in drift-diffusion simulators—ion migration, Shockley-Read-Hall (SRH) recombination, and bimolecular recombination in all device layers, at grain boundaries, and at both sides of all interfaces.[40,46,49–52] Moreover, Koster *et al.*'s model and simulations are fully custom, open-source, and written in common programming languages (i.e., Pascal, Python), enabling easy integration of the model and simulators into high-throughput, custom, large-dataset data pipelines as in this study (e.g., the 143 experiments and 20499 current-voltage (J-V) hysteresis loops considered in this study). This has led to their dozens of publications and thousands of citations across semiconductor research applications and has inspired their ongoing work. For these reasons, we employ Koster *et al.*'s model and simulators to fit the drift-diffusion model to all current-voltage (J-V) scans (143 runs, 20499 measurements, 32847 scans) in this study, enabling state-of-the-art accuracy in modeling device performance decline. Additionally, our data pipeline is also custom, open-source, and written in Python, establishing it as the strongest open-source data pipeline for high-throughput, large-dataset mechanistic and predictive modeling, analysis, and visualization for degrading PSCs.

1.3.4 Existing Applications of Mechanistic Models to Degrading PSCs

Although, until recently, drift-diffusion models had not been applied to studying the degradation of PSCs, despite extensive experimental studies. In his 2024 PhD thesis and publication, Clarke modified the open-source drift-diffusion program IonMonger[41,42] to simulate the influence of device degradation on simulated current-voltage (J-V) scans and impedance spectroscopy experiments of PSCs through a linearly increasing bulk SRH recombination rate.[53,54] This represents an initial step toward drift-diffusion modeling of degrading PSCs while accounting for transient ion migration and multiple electronic measurement techniques.

Although, this does not distinguish among the deep defect (trap) densities in the crystal bulk, at grain boundaries, or at interfaces with the TLs, meaning the effects of changes to the SRH recombination profile are not captured. Moreover, both experimental and computational studies suggest deep defect (trapping) states are concentrated at grain boundaries and interfaces with TLs,[46,52] implying SRH recombination dominates in these locations and not in the bulk

crystal. Additionally, since the primary mechanism for degradation of the HP film is photooxidation of exposed sides, its interface with the back transport layer (which is the ETL in our devices), and grain boundaries, deep defect (trap) densities at these locations would be expected to change much more than the bulk deep defect (trap) density, as seen in this work. Beyond recombination, IonMonger accounts for the HTL, absorber layer, and ETL, but it does not allow for additional layers such as additional TLs (present in many devices) or degradation products (a logical next step in drift-diffusion modeling of PSCs with a distribution of degraded products, see Section 4.2.2.1.2). Furthermore, despite accounting for the migration of a single mobile ion species (shown to be an accurate representation of ion migration in PSCs),[53,54] the model does not account for both cations and anions, nor does it account for the migration of ions into TLs (which has been observed for iodide anions (I^-) with fullerene ETLs).[55–57]

Although, beyond modeled phenomena, the study is computational (not experimental) since the model is not fitted to experimental measurements of degrading PSCs, meaning the study does not have a direct foundation in experiment. As such, the study does not provide evolutions of device properties over degradation or their relative contributions to empirical performance metrics (e.g., the solar cell parameters). Moreover, as a result, the reduction in electron-hole pair generation rate due to the loss in HP film absorptivity through its chemical decomposition and changes in electron, hole, and ion mobilities, series and shunt resistances, and ion concentrations (i.e., all other device properties) are also not considered in this initial model. Therefore, in this study, we fit all device properties which may vary during degradation to ascertain accurate evolutions of such device properties over degradation. Additionally, Clarke *et al.* does not consider the effects of varying degradation conditions on device characteristics, and since such effects are important in both understanding degradation processes and their relationships with degradation conditions, we consider a wide space of degradation conditions in this study and analyze their influence on device property evolutions (e.g., Arrhenius modeling).

Thus, despite Clarke *et al.*'s initial computational study, drift-diffusion models still have not been used to model experimental measurements of degrading PSCs, and resultantly, there is still no mechanistic model for device performance decline. Additionally, despite the complexities considered by IonMonger, the important elements listed above still remain unmodeled. This represents a significant gap in the community's understanding of the mechanisms of device performance decline, ultimately important for both predictive modeling of operational lifetimes and design of long-lived devices robust to the discovered degradation pathways.

1.3.5 Fitting Mechanistic Models to Current-Voltage (J-V) Scans, Analyzing Evolutions and Correlations of Parameters over Degradation, and the Cumulative Sensitivity Analysis (CSA)

We fill this essential gap by globally fitting the non-ideal diode model and Koster *et al.*'s drift-diffusion model (SIMsalabim) with steady-state simulations to light and dark current-voltage (J-V) scans over time for three HP PV architectures (see Figure 3) degrading under varying temperatures (25°C to 85°C), oxygen partial pressures (0% to 21%), relative humidities (0% to 70%), and illumination intensities (0 sun to 1 sun) (see Table 6). This variation produces a wide range of degradation behaviors and operational lifetimes (≈0.5 hr to ≈100 hr), maximizing the information extracted from these mechanistic models, the information fed into our predictive models of operational lifetime, and accelerated aging factor. The extracted fitting parameters and the corresponding derived parameters are mechanistic properties of the device, and their evolutions and correlations over degradation therefore provide insights into mechanisms of device performance decline. This constitutes the most advanced mechanistic model of PSC

performance decline to date. Although, evolutions of parameters and their correlations over time do not quantify device performance decline. Thus, in a novel approach we term a cumulative sensitivity analysis (CSA) (not to be confused with time-dependent sensitivity analysis (TDSA) or global sensitivity analysis (GSA)),[58–62] we calculate the exact influence of each fitting parameter on each solar cell parameter over time, quantifying the exact influence of each degradation mechanism on device performance decline. Last, we also perform an Arrhenius analysis of parameter evolutions to both identify thermally activated degradation processes and how they are shared among parameter evolutions (see Section 6), providing additional insights into the mechanisms of device performance decline.

1.4 Degradation Profile Modeling with Dark-Field (DF) Microscopy, Steady-State Photoluminescence (SSPL), and Current-Voltage (J-V) Scanning

Beyond quantifying fitting parameters' influences on device performance, a complete drift-diffusion model of device performance decline would simulate device performance from degradation profiles (i.e., the distribution of degraded products among interfaces, grain boundaries, and crystal bulk) by feeding a measured or simulated degradation profile to a drift-diffusion model which accommodates degradation products accumulated at these locations. Koster *et al.*'s model is capable of this (accommodating any number of device layers and grain boundaries) in one dimension,[40] but since we do not measure or simulate such a degradation profile, we cannot investigate such results. Instead, we rely on in situ dark-field (DF) microscopy and steady-state photoluminescence (SSPL) imaging as in previous studies.[18,30,31]

1.4.1 Overview of Previous Work

Specifically, in our studies of HP films on glass,[16,18–21,30,31] we calculated HP films' active and degraded thicknesses by measuring their absorbance decline during degradation. We then measured optoelectronic properties including the quasi-Fermi level splitting (QFLS, ΔE_F) and ambipolar carrier diffusion length (L_d) using in situ steady-state photoluminescence (SSPL) imaging and steady-state photoconductivity (PC) measurements,[18,30,31] respectively, followed by correlating these quantities with the fractional thickness of degraded HP.[30] Moreover, in many of these studies and our $MAPbI_3$ device degradation study,[17] we collected dark-field (DF) microscopy images over degradation to visualize and semi-quantitatively measure the HP film degradation process and corresponding distribution of degraded products (i.e., the degradation profile). Specifically, the measured dark-field (DF) intensity is sensitive to surface reflectivity changes caused by degradation-induced surface roughening, and various parameters may be thus calculated from the intensity profile to describe the degradation process and profile. Similarly, the quasi-Fermi level splitting (QFLS) is sensitive to SRH recombination changes due to degradation-induced changes in deep defect (trap) densities or carrier mobilities, meaning SSPL provides another visualization and semi-quantitative measure of the HP film degradation process and profile. Finally, we used the DF parameters as features in a predictive machine learning (ML) model of the time for the ambipolar diffusion length (measured by steady-state photoconductivity) to reach 85% of its initial value.[30] These analyses represented initial steps toward correlating device properties with degradation profile.

Although, unlike HP films on glass, devices contain opaque back-side transport and electrode layers which prevent absorbance measurements. Nevertheless, the HP film degradation process and profile may still be visualized with in situ dark-field (DF) microscopy and steady-state photoluminescence (SSPL) imaging over the device area. Although, in our $MAPbI_3$ device degradation study, we did not calculate parameters quantifying properties of the degradation

profile or extent (i.e., degradation profile parameters) with these measurements, and we thus did not quantitatively correlate device properties with degradation profile parameters.

1.4.2 Summary of Methodology

To address this, we calculate effective active and degraded HP film areas and thicknesses in a novel approach combining in situ dark-field (DF) microscopy and current-voltage (J-V) scanning results over degradation. Specifically, we define the effective active area as the device area with insignificant changes in dark-field (DF) intensity, and we calculate the effective active HP film thickness from the electron-hole pair generation rate (G_{ehp}) assuming an exponential (Beer-Lambert) absorption profile. We then calculate the corresponding fractional quantities relative to their time-zero values and plot all considered parameters against them on filled contour plots to ascertain general, dimensionless relationships between device properties and the effective extents of area and thickness degradation.

These "effective degradation profile parameters" constitute an initial model of degradation profile from experimental data, and their relationships with other parameters over degradation further illuminate mechanisms of device performance decline. They also serve as features in our predictive models of operational lifetime and, furthermore, would enable development of a fully computational model which simulates the evolution of device properties and thus performance during degradation using only undegraded device properties and degradation conditions as inputs. This fully computational model would accurately predict operational lifetimes and could thus be used to optimize device design to maximize operational lifetimes without experiments (see Section 4.4.2.1.2).

1.5 Predictive Machine Learning (ML) Modeling of Operational Lifetime

Following these analyses, we utilize both untransformed and transformed versions of these parameters as features in predictive machine learning (ML) models of operational lifetime (T_{80}), as in our previous study.[17] Transformations included first-order and second-order time differentiation of parameters normalized to their time-zero values ($\frac{d(X/X_{t=0})}{dt}$ and $\frac{d^2(X/X_{t=0})}{dt^2}$, respectively), and we only considered solar cell parameters at time-zero, not the various new architectures, parameter sets, combinations of degradation conditions, parameter specifications, and predictive model specifications considered in this study, and not over the course of degradation. Additionally, since even slight volatility can cause very large changes in derivatives calculated by finite difference methods, we fitted polynomials over the first seven time points to calculate derivatives (see Section 2.2.10.3). However, unlike our previous study, we now include normalization to time-zero values (i.e., $X_t/X_{t=0}$) and moving averaging ($\bar{X}_{t\in[t-\Delta t,t+\Delta t]}$) as additional transformations, and we now also vary the numbers of points used in calculating moving averages and derivatives. Additionally, instead of only considering time-zero parameter values as in our previous study,[17] we now construct models with features evaluated at or up to many percentages of T_{80}, enabling us to determine how predictive model accuracy and parameters vary with the T_{80}-normalized measurement time considered. Regarding the parameters considered, we now incorporate the new parameter sets – the non-ideal diode fitting parameters, drift-diffusion fitting parameters, derived drift-diffusion parameters, and degradation profile parameters – providing additional features with which to improve model accuracy and ascertain correlations among parameters. Last, with an ML model for each parameter set, we draw correlations among the features selected in each model, and the selected features and their

weighting coefficients match the results of our cumulative sensitivity analysis (CSA). These additions are all areas upon which this study improves upon our previous predictive models.[17,32]

2 METHODS

2.1 Experimental

2.1.1 Device Architectures

Traditional c-Si PV cells consist of a standard c-Si wafer which is n-doped for a thin region on one side and p-doped in the thicker adjacent region. This forms the classic p-n junction which provides the built-in electric field necessary to drive current flow. This wafer is sandwiched by a back contact (e.g., aluminum) for p-type carrier collection and metal grid electrodes deposited on the c-Si wafer's front side for n-type carrier collection. This cell is then placed on a supporting substrate (often glass) and interconnected with other cells to form modules.

In contrast, thin film PVs utilize charge transport layers (TLs) to selectively extract carriers from the absorber layer (i.e., extract carriers of the desired charge type while blocking the opposite charge type) which are then extracted from the transport layers by electrodes. In general, the absorber layer is sandwiched by electron transport layers (ETLs) and hole transport layer (HTLs) which selectively extract electrons and holes, respectively, often with multiple TLs (sometimes including thin layers with thicknesses less than 10 nm) to maximize selective extraction while preventing mobility losses. This stack is sandwiched by the anode and cathode which conduct the extracted electrons and holes from the device to the external circuit. As for c-Si, these devices are deposited on a supporting substrate including glass or many flexible substrates (e.g., polyethylene terephthalate (PET)) for installation on curved surfaces.

For HP PV devices, the absorber layer is a HP of the general structure shown in Figure 2.[64] Although, it is often favorable to utilize multiple species for each site, leading to a class of mixed-composition HPs with properties (e.g., bandgap) tunable with composition.[65] This tunability enables optimization for various applications and namely for perovskite-perovskite or perovskite-Si tandem PVs.

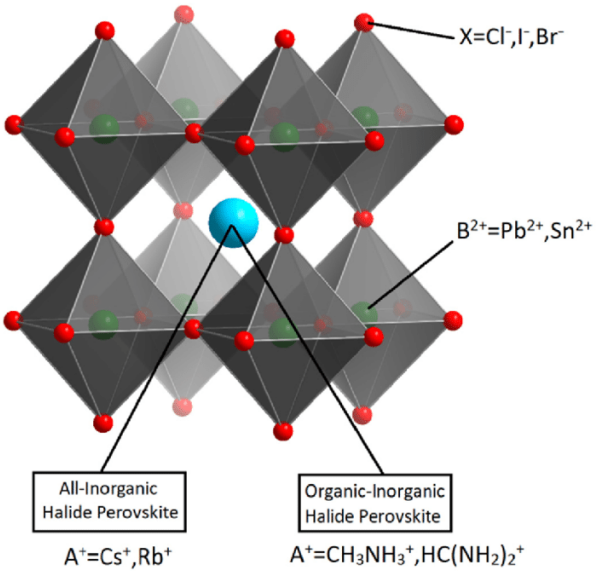

Figure 2. General ABX_3 crystal structure for halide perovskites (HPs). HP crystal structures are of the general form ABX_3 where A is the organic (either the methylammonium ion (MA^+) or formamidinium ion (FA^+)) or inorganic (either cesium (Cs^+) or rubidium (Rb^+)) A-site cation, B is the metal ion (either lead (Pb^{+2}) or tin (Sn^{+2})), and X is the halide ion (either chloride (Cl^-), bromide (Br^-), or iodide (I^-)).[64]

In this work, as for many lab-scale (<0.01 cm^2 area) devices, we utilize a glass substrate for easy handling with three well-known compositions of low bandgap, medium bandgap, and high bandgap studied in our previous work.[16,18–21,30,31] Regarding device architectures, we select inverted (i.e., p-i-n) architectures optimized in this and our previous studies (see Figure 3).

- Low-bandgap
  - Substrate – Glass
  - Cathode – Indium tin oxide (ITO) (≈100 nm)
  - HTL – Poly(2,3-dihydrothieno-1,4-dioxin)-poly(styrenesulfonate) (PEDOT:PSS) (≈10-20 nm)
  - Absorber Layer – Cesium-doped formamidinium lead-tin triiodide ($FA_{0.75}Cs_{0.25}Pb_{0.5}Sn_{0.5}I_3$) (≈300 nm)
  - ETL – Fullerene-C_{60} (≈50 nm)
  - ETL – Bathocuproine (BCP) (≈7 nm)
  - Anode – Silver (Ag) (≈100 nm)
- Medium-bandgap
  - Substrate – Glass
  - Cathode – Indium tin oxide (ITO) (≈100 nm)
  - Nickel oxide (NiO_x) (≈30 nm)
  - Methylammonium lead iodide ($MAPbI_3$) (≈300 nm)
  - ETL – Fullerene-C_{60} (≈40 nm)
  - ETL – Bathocuproine (BCP) (≈7 nm)
  - Anode – Silver (Ag) (≈100 nm)
- High-bandgap
  - Substrate – Glass
  - Cathode – Indium tin oxide (ITO) (≈100 nm)
  - HTL – Poly(N,N'-bis-4-butylphenyl-N,N'-bisphenyl)benzidine (PolyTPD) (≈40 nm)
  - HTL – Poly(9,9-bis(3'-(N,N-dimethyl)-N-ethylammoinium-propyl-2,7-fluorene)-alt-2,7-(9,9-dioctylfluorene))dibromide (PFN-P2) (≈300 nm)
  - Absorber Layer – Cesium-doped formamidinium lead iodobromide ($FA_{0.8}Cs_{0.2}Pb(I_{0.83}Br_{0.17})_3$) (≈300 nm)
  - ETL – Fullerene-C_{60} (≈50 nm)
  - ETL – Bathocuproine (BCP) (≈7 nm)
  - Anode – Silver (Ag) (≈100 nm)

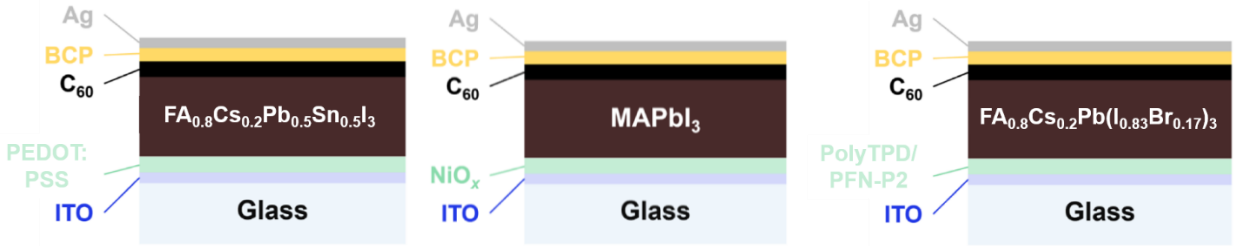

Figure 3. Schematics of the Device Architectures (i.e., Device Stacks) Utilized in This Study. These architectures include our (left) low-bandgap, (middle) medium-bandgap ($MAPbI_3$), and (right) high-bandgap architectures.

In our previous study developing our initial predictive ML model, we utilized the medium-bandgap (archetypal $MAPbI_3$) architecture. Although, $MAPbI_3$ is relatively unstable compared to FA-containing, higher-bandgap perovskites such as our high-bandgap ($FA_{0.8}Cs_{0.2}Pb(I_{0.83}Br_{0.17})_3$) architecture, and as shown in this work, PCE decline in $MAPbI_3$ devices is dominated by the decline in electron-hole pair (EHP) generation rate due to loss of film absorptivity during HP decomposition. Thus, we include our high-bandgap ($FA_{0.8}Cs_{0.2}Pb(I_{0.83}Br_{0.17})_3$) architecture for its unique decomposition mechanisms and kinetics, greater stability, and thus commercial relevance, especially for perovskite/c-Si tandems. We also include our low-bandgap ($FA_{0.75}Cs_{0.25}Pb_{0.5}Sn_{0.5}I_3$) architecture (dataset collected by Daniel Kuo and Yuhuan Meng) for its unique decomposition mechanisms and kinetics and commercial relevance in perovskite-perovskite tandems. Overall, the modeling of multiple architectures enables identification of common and unique degradation mechanisms and their influences on device performance, demonstrates the applicability of these mechanistic and predictive models to multiple architectures, and assists in generalizing the overall predictive model over many architectures.

2.1.2 Device Fabrication

2.1.2.1 Nomenclature, Vendors, and Grades for Raw Materials

Table 1. Nomenclature, Vendors, and Grades for Raw Solid Materials*

Name	Chemical Formula	Vendor	Specifications
Electrode Materials			
Patterned, indium tin oxide (ITO)-coated glass slides	$In_{2-x}Sn_xO_3$	Yingkou Shangneng Photoelectric Material Co.	1.5 × 1.5 cm, 15 Ω sq^{-1}, ≈100 nm ITO thickness
Silver	Ag	Kurt Lesker	99.99% purity
Hole Transport Layers (HTLs)			
Poly(2,3-dihydrothieno-1,4-dioxin)-poly(styrenesulfonate) (PEDOT:PSS)	---	---	---
Nickel acetate tetrahydrate	$Ni(OAc)_2 \cdot 4H_2O$	Sigma Aldrich	99.998% trace metals basis purity (not anhydrous)
Poly(N,N'-bis-4-butylphenyl-N,N'-bisphenyl)benzidine (PolyTPD)	---	---	---
Poly(9,9-bis(3'-(N,N-dimethyl)-N-ethylammoinium-propyl-2,7-fluorene)-alt-2,7-(9,9-dioctylfluorene))dibromide (PFN-P2)	---	---	---

Name	Chemical Formula	Vendor	Specifications
Perovskite Precursors			
Methylammonium iodide	MAI	GreatCell Solar	---
Formamidinium Iodide	FAI	GreatCell, Sigma	Anhydrous grade
Cesium Iodide	CsI	Alfa Aesar	Ultra dry grade
Lead iodide	PbI_2	TCI, Alfa Aesar (do not use Sigma Aldrich PbI_2)	99.999% purity, ultra dry grade only
Lead bromide	$PbBr_2$	---	---
Tin iodide	SnI_2	Sigma Aldrich	---
Tin fluoride	SnF_2	Sigma Aldrich	---
Electron Transport Layers (ETLs)			
Fullerene-C_{60}	C_{60}	Lumtec	---
Bathocuproine	BCP	Sigma Aldrich	Sublimed grade

* Information corresponding to empty entries (denoted by "---") in the above table may be provided upon request.

Table 2. Nomenclature, Vendors, and Grades for Solvents*

Name	Chemical Formula	Vendor	Specifications
Solvents for Precursor Solutions for Hole Transport Layers (HTLs)			
Ethanol	Ethanol	Sigma Aldrich	Anhydrous grade
Ethanolamine	Ethanolamine	Sigma Aldrich	≥ 99.5% purity
Chlorobenzene (CB)	C_6H_5Cl	---	---
Methanol	CH_3OH	---	---
Solvents for Precursor Solutions for Perovskite Absorber Layers			
Dimethylformamide (DMF)	$HCON(CH_3)_2$	---	---
Dimethylsulfoxide (DMSO)	$(CH_3)_2SO$	---	---

Name	Chemical Formula	Vendor	Specifications
γ-butyrolactone (GBL)	$C_4H_6O_2$	---	---
N-methyl-2-pyrrolidone (NMP)	C_5H_9NO	---	---
Antisolvents for Perovskite Absorber Layers			
Toluene	$C_6H_5CH_3$	Sigma Aldrich	Anhydrous grade
Chlorobenzene (CB)	C_6H_5Cl	---	---

* Information corresponding to empty entries (denoted by "---") in the above table may be provided upon request.

2.1.2.2 Preparation of Precursor Ink for Spin Coating

All precursor solutions were prepared in 2-mL or 20-mL vials, where 20-mL vials were often used for long-lasting solutions (e.g., $Ni(OAc)_2 \cdot 4H_2O$ maintains high quality for ≈3 weeks) and/or to enable magnetic stirring. For the addition of solids, we employed a balance and tared it before the addition of each material. Each solid was slowly added one at a time with a small, clean spoon to reach the mass required for the desired solution concentration, and given the importance of mass ratios to film composition and performance, we recommend and ensured a maximum precision error of ≈1%. Additionally, since solids with relatively high particle masses (e.g., 3-12 mg PbI_2 beads or 1-3 mg CsI beads) present risk for precision error in the masses and thus their ratios, special care was taken in adding these solids. One recommended technique is adding solids of larger particle size first to enable easy recalculation of the required masses for the remaining solids. Next, the designated volumes of each solvent were added (in order of appearance below) and the contents mixed (by magnetic stirring or shaking) to form the desired solution. Solution vials were then placed on a ceramic plate on a standard hot plate overnight at the desired temperatures and sometimes magnetically stirred (e.g., $Ni(OAc)_2 \cdot 4H_2O$) to ensure homogeneity. This ceramic plate possesses a very high thermal conductivity which ensures all vials and samples placed on the plate are maintained at the specified temperature. Vial volumes, solvent volume ratios, concentrations in solution, mixing methods, and overnight temperature and stirring conditions are specified for the HTLs and perovskite absorber layers in Table 3 and * Information corresponding to empty entries (denoted by "---") in the above table may be provided upon request.
Table *4* below, respectively.

Table 3. Precursor Solution Preparation Parameters for Spin-Coated Hole Transport Layers (HTLs)*

	PEDOT:PSS	NiO_x	PolyTPD	PFN-P2
Atmospheric Conditions	---	Air or inert glove box	Inert glove box	Inert glove box

	PEDOT:PSS	NiO_x	PolyTPD	PFN-P2
Vial Volume	---	20 mL	2 mL	2 mL
Solution Volume	---	10.060 mL	1 mL	1 mL
Solid Component Masses	---	248.8 mg $Ni(OAc)_2 \cdot 4H_2O$	1 mg PolyTPD	0.5 mg PFN-P2
Solid Component Molar Ratios	---	N/A	N/A	N/A
Solvent Volumes and Ratios	---	10 mL of ethanol	1 mL chlorobenzene (CB)	1 mL methanol
Solute Concentrations	---	0.1 M $Ni(OAc)_2 \cdot 4H_2O$ 0.1 M ethanolamine (as a stabilizer)	1 mg/mL	0.5 mg/mL
Mixing Method	---	Magnetic stirring at 500 rpm	Shaken for a few minutes	Shaken for a few minutes
Overnight Temperature and Stirring Conditions	---	65°C, magnetic stirring at 500 rpm (begun after ethanol addition)	N/A	N/A
Solution Color	---	Green for ethanol only, blue after ethanolamine addition, and reaches deep turquoise overnight	---	---
Recommended Solution Lifetime	---	3 weeks	< 1 hr	< 1 hr

* Information corresponding to empty entries (denoted by "---") in the above table may be provided upon request.

Table 4. Precursor Solution Preparation Parameters for Spin-Coated Perovskite Absorber Layers*

	$FA_{0.75}Cs_{0.25}Pb_{0.5}Sn_{0.5}I_3$	$MAPbI_3$	$FA_{0.8}Cs_{0.2}Pb(I_{0.83}Br_{0.17})_3$
Atmospheric Conditions	Inert glove box	Inert glove box	Inert glove box
Vial Volume	2 mL	2 mL	2 mL
Solution Volume	1 mL	1 mL	1 mL

	$FA_{0.75}Cs_{0.25}Pb_{0.5}Sn_{0.5}I_3$	$MAPbI_3$	$FA_{0.8}Cs_{0.2}Pb(I_{0.83}Br_{0.17})_3$
Solid Component Masses	FAI: 257.9 mg (1.5 mol); 193.47 mg (1.125 mol); 154.773 mg (0.9 mol) CsI: 129.9 mg (0.5 mol); 97.43 mg (0.375 mol); 77.9 mg (0.3 mol) PbI_2: 461.01 mg (1 mol); 345.76 mg (0.75 mol); 276.6 mg (0.6 mol) SnI_2: 372.52 mg (1 mol); 279.39 mg (0.75 mol); 223.5 mg (0.6 mol) SnF_2: 15.67 mg (0.1 mol); 11.75 mg (0.075 mol); 9.4 mg (0.06 mol)	MAI: 159 mg (1 mol) PbI_2: 461 mg (1 mol)	PbI2: 343.5 mg (0.83 mol) PbBr2: 93.6 mg (0.17 mol) FAI: 137.6 mg (0.8 mol) CsI: 52.0 mg (0.2 mol)
Solid Component Molar Ratios	0.75 FAI : 0.25 CsI : 0.5 PbI_2 : 0.5 SnI_2 (mol/mol)	1:1 (mol/mol) MAI/PbI_2 (stoichiometric)	0.8 FAI : 0.2 CsI : 0.83 PbI_2 : 0.17 $PbBr_2$ (mol/mol)
Solvent Volumes	0.75 mL DMF, 0.25 mL DMSO or 0.85 mL DMF, 0.15 mL DMSO	700 μL GBL, 300 μL DMSO	0.5 mL DMF, 0.5 mL NMP
Solvent Ratio	3:1 (v/v) DMF/DMSO or 7:3 (v/v) DMF/DMSO	7:3 (v/v) GBL/DMSO	1:1 (v/v) DMF/NMP
Solute Concentrations	2.0 M; 1.5 M; 1.2 M	1 M	1 M
Mixing Method	Shaken vigorously for 5 min, shaken intermittently over	Shaken vigorously for 5 min, shaken intermittently over 2-3 hours until dissolved	Shaken vigorously for 5 min, shaken intermittently over 2-3 hours until dissolved

	$FA_{0.75}Cs_{0.25}Pb_{0.5}Sn_{0.5}I_3$	$MAPbI_3$	$FA_{0.8}Cs_{0.2}Pb(I_{0.83}Br_{0.17})_3$
	2-3 hours until dissolved		
Overnight Temperature and Stirring Conditions	Room temp., no overnight stirring	Room temp., no overnight stirring	Room temp., no overnight stirring
Solution Color	---	Light yellow	---
Recommended Solution Lifetime	1 day	1 day	1 day

* Information corresponding to empty entries (denoted by "---") in the above table may be provided upon request.

2.1.2.3 Substrate Preparation/Cleaning

Patterned, ITO-coated glass slides (1.5 × 1.5 cm, 15 Ω sq^{-1}, ≈100 nm ITO thickness, Yingkou Shangneng Photoelectric Material Co.) were cleaned by sonication in Alconox detergent solution, deionized (DI) water, acetone, and isopropanol (IPA) for 10 min in each solvent and rinsed multiple times in fresh DI water after each step (especially after alconox treatment) except the last sonication in IPA. The slides were then blow-dried with pressurized nitrogen gas (N_2) and cleaned for 10 min in an Ar plasma. Last, sample ID codes were scribed (2-3 mm) with a Dremel on the bottom edge (not in active device areas) and on the glass side (i.e., not the ITO side) to enable identification of samples throughout fabrication and characterization. 2-3 mm of Kapton tape was then applied on the ITO side of this edge to prevent deposition of the remaining layers in this region and thus enable electrical probes to contact the ITO during J-V scanning. Substrates were then immediately transferred to a nitrogen-filled glovebox for spin coating.

2.1.2.4 Spin Coating

In their respective atmospheric conditions, solutions were extracted from their original vials, filtered through a 0.2-μm PTFE filter (0.45-μm was used for the low-bandgap composition), and deposited into new vials for immediate use in spin coating. The samples were then placed onto the spin coater's vacuum chuck (i.e., sample surface), secured with the coater's vacuum mechanism, and the designated volume of solution deposited onto the center of the sample with a 100-μL pipette. The spin coating program with designated parameters (i.e., spin acceleration, speed, and time) is initiated, and for the perovskite absorber layers, the specified volume of antisolvent is extracted from its 20-mL vial and slowly dripped onto the sample's center at the designated time and for the specified duration with a 1-mL pipette. In this method, the antisolvent promotes uniform nucleation and thus growth of large, compact perovskite grains. Last, the Kapton tape strips used to prevent deposition of HTL onto ITO at the bottom edge of each sample were removed to prevent melting during annealing, and the samples were then annealed on a ceramic plate placed on a standard hot plate at the designated temperature and for the specified duration. Due to the time sensitivity of these process steps, we recommend preparation of all materials prior to initiating this procedure. See Table 5 below for the spin coating parameters corresponding to each layer and architecture.

Table 5. Spin Coating Parameters for Each Layer and Architecture*

Degradation Condition	Low-Bandgap		Medium-Bandgap		High-Bandgap		
	PEDOT:PSS	$FA_{0.75}Cs_{0.25}Pb_{0.5}Sn_{0.5}I_3$	NiO_x	$MAPbI_3$	PolyTPD	PFN-P2	$FA_{0.8}Cs_{0.2}Pb(I_{0.83}Br_{0.17})_3$
Deposition Atmosphere	---	Inert glove box with continuous purge	Air or inert glove box	Inert glove box with continuous purge	Inert glove box with continuous purge	Inert glove box with continuous purge	Inert glove box with continuous purge
Volume of Precursor Solution Deposited per Film	---	50 μL	50 μL	50-100 μL	60 μL	50 μL deposited over first 3 sec.	100 μL
Spin Acceleration	---	---	5000 rpm/s (max)	---	2000 rpm/s	5000 rpm/s (max)	2000 rpm/s
Spin Speed	---	Step 1: 1000 rpm Step 2: 4000 rpm	3000 rpm	4000 rpm	4000 rpm	5000 rpm	4000 rpm
Spin Time	---	Step 1: 10 sec. Step 2: 40 sec.	1 min.	45 sec.	30 sec.	20 sec.	45 sec.
Antisolvent – Type, Application Time, and Volume	None	700 mL toluene or 200 mL chlorobenzene (CB) for ≈5 seconds starting ≈10-12 sec. before the end of coating (i.e., after 32-30 sec.)	None	580 μL of toluene for ≈5 seconds starting ≈15 sec. before the end of coating (i.e., after 30 sec.)	None	None	700 μL for 5-6 sec. starting ≈15 sec. before the end of coating (i.e., after ≈30 sec.)
Post-Deposition Treatment (e.g., Annealing) Parameters	---	100°C, 10 min.	300°C in air, 60 min.	100°C, 10 min.	60°C, 10 min.	Dried at room temp. for 28-32 min.	120°C for 15 min.

* Information corresponding to empty entries in the above table (denoted by "---") provided upon request.

2.1.2.5 Thermal Evaporation

Following deposition of the HTL(s) and perovskite absorber layers, the samples were transferred to a separate glovebox with a thermal evaporator (Angstrom Engineering Nexdep). This separate glove box did not contain solvent processing equipment, meaning only trace solvent concentrations may exist, and solvent coordination with the perovskite layers was much less compared to the glove box in which spin coating was performed. Samples were then loaded into

the evaporator's sample holder without an evaporation mask to enable uniform deposition of the ETLs over the samples.

After sample loading, the material evaporation process was performed as follows. For each material and one material at a time, a tungsten boat was loaded with a small amount of the material (e.g., 2-3 pellets for Ag), the evaporator sealed and ultra-high vacuum (i.e., $< 5 \times 10^{-6}$ Torr) drawn with a turbo vacuum pump, and the evaporation performed at the specified temperature to achieve the desired deposition rate. The deposition rate was controlled at all stages by the evaporator computer based on readings from its deposition rate sensor.

This process was performed for both fullerene-C_{60} (Lumtec) and BCP (Sigma Aldrich, sublimed grade) at respective maximum deposition rates of 0.5 and 0.3 Angstroms per second (Å/s). The samples were then removed from the sample holder for insertion of the shadow evaporation mask, enabling deposition of patterned Ag electrode contacts to create eight device pixels with areas of approximately 0.068 cm^2 for each substrate. Additionally, the HP and ETLs at the bottom 2-3 mm of the samples (i.e., where the Kapton tape was applied) were scratched off with a razor blade to enable direct deposition of the Ag contact onto the ITO. See Figure 5 for a depiction of a completed set of devices on a single substrate. Specifically, the samples were removed and placed in their original petri dish, the evaporation mask placed inside the sample holder, and the samples placed in the masked sample holder for deposition of patterned silver (Ag) (Kurt Lesker, 99.99%). For Ag depositions, 2-3 Ag pellets were placed in the tungsten boat and evaporated at a maximum deposition rate of 2 Angstroms per second (Å/s).

2.1.2.6 General Procedures

All samples are handled with clean, common metal tweezers to minimize introduction of macroscopic defects through solid contaminants or handling damage. Furthermore, samples are always stored in fresh petri dishes wrapped in aluminum foil to block illumination of samples and thus prevent unintended photooxidation. When samples are not in use, these petri dishes are evacuated and filled with nitrogen gas while entering the nitrogen-filled glove box, and they are again sealed and wrapped in aluminum foil to minimize degradation and contamination (e.g., causing coordination or solvation) by residual solvent vapors in the glove box.

2.1.2.7 Final Remarks

As for all HP PV devices, the details of these fabrication procedures significantly influence device performance.[66] Specifically, different materials across architectures exhibit different electronic properties, meaning different layer thicknesses may be chosen for the same material across different architectures to optimize performance.[67] Furthermore, these materials have differing solution properties and crystallization behaviors, meaning unique spin coating procedures are often designed for each spin-coated layer across architectures[66] (e.g., the differing procedures for each of our perovskite absorber layers). This is especially important for HPs due to the strong dependence of their optoelectronic performance on deposition quality[67–69] (see Table 5 for the spin coating parameters for each layer and architecture). Indeed, human error in achieving the chosen spin-coating parameters is the primary source of variation in the performance of our HP films and devices. For our antisolvent-based process, such parameters include solution composition, spin speed and acceleration, antisolvent drop volume, frequency, and flow rate, and annealing temperature and time (with a special dependence on antisolvent parameters). Although, many solution deposition methods exist (e.g., spin coating, slot-die coating, doctor blade coating, inkjet printing), and each have their own fabrication parameters which may be optimized to maximize performance.

2.1.3 In Situ Characterization of Devices Degrading in Controlled Environment

2.1.3.1 Ranges of Degradation Conditions

As in our previous study,[17] devices are characterized in situ while degrading in an environmental control chamber (see Figure 5) under varying sets of temperatures (25°C to 85°C), oxygen concentrations (0% to 21%), relative humidities (0% to 70%), and illumination intensities (0 sun to 1 sun). These ranges of environmental conditions were selected to maximize the range of T_{80} values (e.g., ≈0.5-100 hr for these datasets) and degradation condition parameter space (see Figure 4 and Table 6), thus maximizing the accuracy and applicability of both our mechanistic models and predictive ML models, and enabling an accelerated aging component for these models (see Section 2.2.12.3.2). Although, some of these bounds were selected to constrain our models to realistic conditions (despite the devices being unencapsulated) or due to limitations of our experimental apparatus. Specifically, controlling temperatures below room temperature (i.e., 25°C) would require refrigeration (not enabled by our current hot plate setup), and temperatures above 85°C (around 100°C) have been shown to cause rapid thermal decomposition of $MAPbI_3$ which significantly modify the degradation behavior and thus convolute the presented models (alongside being unrealistic). Furthermore, despite being achievable, O_2 concentrations and relative humidities were limited to realistic values. Nonetheless, we recommend inclusion of higher temperatures (especially for high-bandgap compositions which thermally decompose at much higher temperatures such as, e.g., 150°C), oxygen concentrations (e.g., 100% (pure) oxygen), relative humidities (e.g., 100% RH), and illumination intensities (e.g., 10 sun, 100 sun) to further extend the range of T_{80} values and the degradation condition parameter space, again for maximizing the accuracy and applicability of our mechanistic models, predictive ML models, and their accelerated aging components. For the full list of experiments and their conditions, see the feature tables for our predictive models on our "DegradePV" GitHub repository (see Section 6).[63]

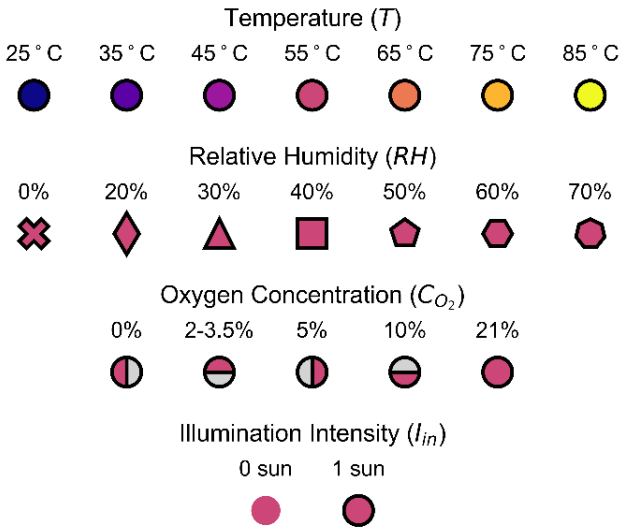

Figure 4. Legend of Marker Encodings for Degradation Conditions in Plots Referencing Multiple Experiments. Temperature, relative humidity (RH), oxygen concentration (C_{O_2}), and illumination intensity (I_{in}) are encoded by fill color, marker shape, fill style, and edge color, respectively. The use of the fill color for 55°C in the rows describing degradation conditions other than temperature is simply an illustration (i.e., fill colors may be any of those indicated).

Table 6. Sets of Degradation Conditions and Corresponding Ranges of Operational Lifetimes (T_{80}) and Total Number of Measurement Cycles by Architecture

	Low-Bandgap	Medium-Bandgap	High-Bandgap	Overall
Temperature (T) [°C]	25, 40, 55	25, 35, 45, 55, 65, 75, 85	25, 30, 40, 55, 70	25-85
Relative Humidity (RH) [%]	0, 30, 50	5, 10, 30, 40, 50, 60, 70	2, 15, 50	0-70
Oxygen Concentration (C_{O_2}) [%]	0, 3.5, 5, 10.5, 21	21	0, 2, 5, 10, 21	0-21
Illumination Intensity (I_{in}) [suns]	0, 1	1	1	0, 1
Range of Operational Lifetimes (T_{80}) [hr]	≈0.9-70	≈0.5-100	≈1-70	≈0.5-100
Total Number of Runs and Measurements	61 runs, 3462 measurements	45 runs, 10125 measurements	37 runs, 6912 measurements	143 runs, 20499 measurements

2.1.3.2 Degradation and Measurement Apparatus

Devices are placed into a small custom heating stage equipped with a thermocouple, cartridge heaters, and closed-loop temperature control. The stage is then placed into a custom environmental control chamber equipped with a humidity sensor, inlet and outlet joints for the flowing gas, and feedthroughs for the electrical test leads used to contact the device electrodes. The chamber is transparent, allowing illumination of the device during degradation and characterization (see Figure 5a).

Then, during degradation and during measurements under illumination, the light was focused over the entire active area of one device pixel (of the eight shaped by the evaporation shadow mask) with an Olympus BX53M upright microscope using its 5x-magnification microscope objective. Specifically, a green (542 nm) Lumencor Spectra X Light Engine LED was calibrated to yield the above-bandgap (i.e., absorbed) photon flux equivalent to that under the AM1.5G spectrum (e.g., 1.56×10^{21} photons m^{-2} s^{-1} for $MAPbI_3$). The microscope was also configured to collect re-emitted radiation in reflection geometry, allowing steady-state photoluminescence (SSPL) and dark-field (DF) microscopy images to be collected through placement of the appropriate filter cube in the re-emitted light's optical path to the detector. Specifically, for SSPL, a 665-nm dichroic mirror (Semrock FF665-Di02-25x36) and 664-nm long-pass filter on the filter cube's emission side (Semrock BLP01-664R-25) were used to filter reflected excitation light, allowing the generated PL signal to transmit to the microscope's optical detector. Moreover, for DF microscopy, a standard Olympus U-MDF filter cube was used, and during degradation experiments, the filter cube in use was swapped between the PL and DF cubes automatically using a homemade drive mechanism controlled by an Arduino Uno microcontroller. For electrical measurements, the electrical leads were connected to a Keithley 2400 source/measure unit and the PL cube selected with light measurements conducted under 1 sun-equivalent illumination intensity (see Figure 5).

2.1.3.3 Measurement Process

In the time between measurements (conducted every 15 minutes), devices are biased at the most recently measured maximum power point (MPP) voltage (V_{MPP}) and illuminated with an above-

bandgap photon flux equivalent to that of 1 sun illumination intensity under the AM1.5G solar spectrum. Then, for the $MAPbI_3$ and high-bandgap architectures, measurements include

- Steady-state photoluminescence (SSPL) under 1 sun illumination intensity at open-circuit voltage (V_{oc}) bias
- Dark-field (DF) microscopy under ≈0.01-sun illumination at open-circuit voltage (V_{oc}) bias
- Steady-state (i.e., stabilized) open-circuit voltage (V_{oc}) for 10 seconds
- Short (<0.2 V span) forward J-V scan centered approximately about the maximum power point (MPP) to determine the MPP (i.e., the MPP voltage (V_{MPP}) and current density (J_{MPP})) for setting the between-measurement applied bias.
- Steady-state (i.e., stabilized) MPP for 10 seconds
- Steady-state (i.e., stabilized) short-circuit current (J_{sc}) for 10 seconds
- Reverse and forward current-voltage (J-V) scans (i.e., hysteresis loops) from 1.2 V to 0 V and from 0 V to 1.2 V, respectively, under 1 sun illumination (light) and 0 sun illumination (dark) at 250 mV/s scan rate

In contrast, for the low-bandgap architecture, we only measure the stabilized J_{sc}, stabilized V_{oc}, and MPP (i.e., the J_{MPP} and V_{MPP}) with a forward J-V scan spanning ≈0.2 V and approximately centered about the MPP with a 250 mV/s scan rate. This measurement and degradation procedure was controlled by a custom Python script with MicroManager software controlled as a subprocess for image acquisition. Regarding measurement length, most measurements are continued until T_{80}. Although, some experiments were terminated prior to reaching T_{80}, and the T_{80} values for these experiments were therefore linearly extrapolated from the last 20 PCE values measured before the run's termination. Additionally, in some experiments, temporary malfunctions in electrical equipment or misalignment of filter cubes during filter cube switching invalidated J-V or optical measurements, respectively, and these measurement cycles were thus responsibly neglected. Indeed, the measurements are far beyond the 3.5 standard deviations from the mean required to define an outlier in standard statistical analysis.[70,71] As for all parameters, linear interpolations are used to approximate parameter values between measurement cycles (including these removed cycles) when necessary (e.g., in cumulative sensitivity analyses (CSAs)).

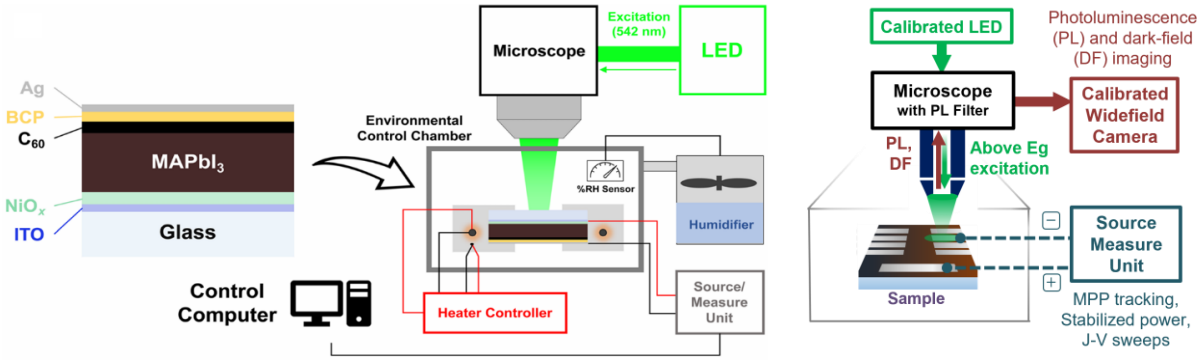

Figure 5. Device Degradation and In Situ Characterization Apparatus. Devices are degraded in (left) an environmental control chamber in which temperature (T), oxygen concentration (C_{O_2}), relative humidity (RH), and illumination intensity (I_{in}) are controlled[17] and (right) characterized under 0-sun- or 1-sun-equivalent illumination (i.e., monochromatic, above-

bandgap photons produced by a calibrated LED) with a microscope for dark-field (DF) microscopy and steady-state photoluminescence (SSPL) imaging and a source measure unit for electronic measurements.[32]

2.1.3.4 General Remarks

This device degradation dataset now consists of 143 runs with 20499 measurement cycles over all three architectures with 61 runs and 3462 measurement cycles for the low-bandgap architecture, 45 runs and 10125 measurement cycles for the medium-bandgap ($MAPbI_3$) architecture, and 37 runs and 6912 measurement cycles for the high-bandgap architecture. Overall, these measurements provide the experimental data necessary for both the mechanistic and predictive modeling of and visualization of degradation processes in this work. Although, as discussed in Section 4.2.1, there are additional measurement techniques we recommend to improve the accuracy, precision, and insights of our results.

2.2 Computational

2.2.1 Solar Cell Parameters

The solar cell parameters are the standard empirical metrics for characterizing solar cell performance (see Table 7 for their names, symbols, and units). The parameters describe device performance at differing levels of applied bias (i.e., short circuit, maximum power point (MPP), and open circuit) and are extracted from current-voltage (J-V) scans as shown in Figure 6. Specifically, in short circuit conditions, the applied bias is zero, and the device thus produces the maximum current of which it is capable under the given illumination intensity. In contrast, under open circuit conditions, the device produces the maximum voltage difference of which it is capable under the given illumination intensity. Equivalently, one may claim the applied bias is chosen such that the current density is zero, perfectly opposing the cell's internal electric field. Although, in each of these conditions, power output ($P = JV$) is zero since either the voltage or current are zero in short circuit or open circuit conditions, respectively. Thus, solar cells are operated at an applied bias between these two conditions which yields maximum power output, known as the maximum power point (MPP). Although, the current and voltage are lower at MPP than in short circuit and open circuit conditions, respectively, and this incentivizes calculation of the fill factor (FF), a parameter which quantifies the ratio of the MPP power output ($P_{MPP} = J_{MPP}V_{MPP}$) to the maximum achievable power ($P_{max} = J_{sc}V_{oc}$). Finally, the power conversion efficiency is simply the MPP power (P_{MPP}) divided by the incident illumination intensity (I_{in}), which for 1-sun-equivalent is approximately 1000 W/m^2.[33]

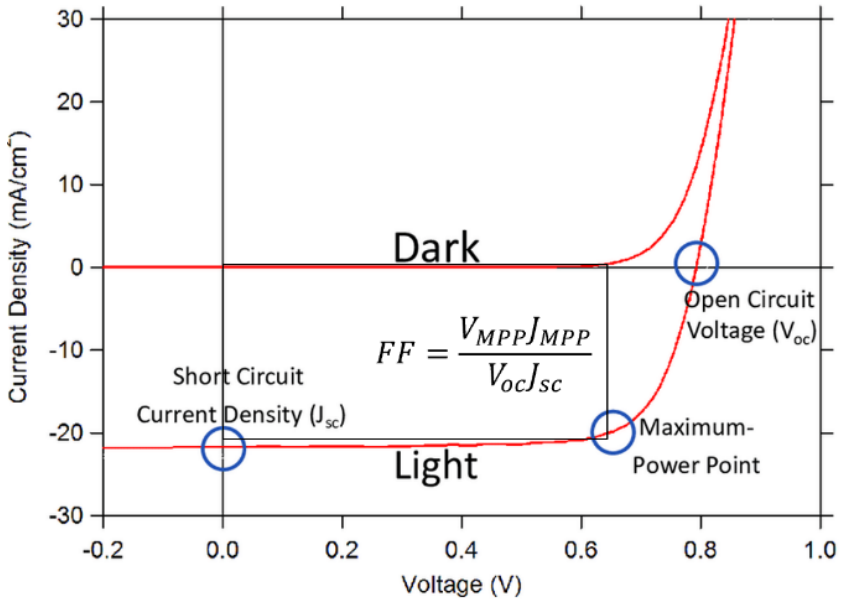

Figure 6. Light and Dark Current-Voltage (J-V) Scans of a Solar Cell with the Key Points and Corresponding Solar Cell Parameters Labeled.

Table 7. Solar Cell Parameters – Names, Symbols, Units

Name	Symbol	Unit
Short Circuit Current Density	J_{sc}	$[A/m^2]$
Open Circuit Voltage	V_{oc}	$[V]$
Fill Factor (FF)	FF	Unitless: fraction or %
Power Conversion Efficiency (PCE)	PCE	Unitless: fraction or %
Maximum Power Point (MPP) Current Density	J_{MPP}	$[A/m^2]$
Maximum Power Point (MPP) Voltage	V_{MPP}	$[V]$

To calculate these parameters, J_{sc} is equated to the current density at zero applied bias and V_{oc} is equated to the voltage at which current density becomes zero. This voltage is calculated by linear interpolation of the given J-V scan between the two points closest to the voltage axis (zero current density), and if the considered J-V scan does not possess a point at zero applied bias, the J_{sc} is calculated by the corresponding linear interpolation at the current density axis (zero applied bias). Moreover, the maximum power point (MPP) is taken to be the point of maximum power output, calculated by cubic interpolation of the J-V curve. The FF and PCE are then calculated accordingly. These are standard, accurate calculation procedures.

In addition to the standard solar cell parameters, we define hysteresis metrics to quantify the level of hysteresis in current-voltage (J-V) hysteresis loops. The first, most common metric is the hysteresis index (HI), expressed as the normalized difference in PCE between forward (PCE_{for}) and reverse (PCE_{rev}) scans, given by

$$HI = \frac{PCE_{for} - PCE_{rev}}{PCE_{rev}}$$

In contrast, we define a second, more precise, integral-based hysteresis metric (HI_{int}) as the difference in power extracted during the forward and reverse current-voltage (J-V) scans ($P_{ion-hys}$) normalized to the MPP power (P_{MPP}) averaged over the forward and reverse scans. Mathematically, this power difference is the integrated difference in the forward and reverse scan current densities, yielding

$$P_{ion-hys} = \int_{V_{min}}^{V_{max}} (J_{for} - J_{rev}) dV$$

$$HI_{int} = \frac{1}{P_{MPP}} \int_{V_{min}}^{V_{max}} (J_{for} - J_{rev}) dV$$

Numerically, we calculate the hysteresis metric by numerically integrating the difference between forward and reverse J-V scans along the applied bias range (0 V to 1.2 V) using adaptive quadrature for accuracy.[72–76] Despite being less common, the evolution in this parameter is much smoother (and its values are thus much more precise) than the standard hysteresis index (HI) since integrating captures hysteresis-based differences in forward and reverse scans at any point, not just at MPP. For quantifying hysteresis in operational performance, the hysteresis index (HI) is of course sufficient since MPP is the operating condition, but for mechanistic modeling of solar cells, this integrated metric is a better metric. Indeed, despite being less common, this idea of quantifying J-V hysteresis by integrating the difference in current densities of the forward and reverse over the entire voltage range was employed in a similar manner by Van Heerden *et al.*[77] Overall, we define multiple hysteresis metrics to strengthen our claims regarding ion migration and potentially identify subtle properties of ion hysteresis from differences in the metrics' evolutions over degradation.

The solar cell parameters serve many purposes in this study. They are the empirical characterizations of device performance to which fitted and derived parameters are compared, the features which yield the most accurate predictive models of operational lifetimes, and the parameters on which we evaluate the influences of fitting parameters in our cumulative sensitivity analysis (CSA). Moreover, for the CSA, quantifying the influences of fitting parameters on all solar cell parameters (not just PCE) provides insights into the influences of each HP film degradation mechanism on each of these standard device performance metrics. Regarding lifetime, operational lifetimes are typically defined as the time required for PCE to reach 80% of its initial value (T_{80}).

2.2.2 Non-Ideal Diode Model

The non-ideal diode equation is a standard and the simplest mechanistic model for a solar cell, modeling current density J as a function of applied voltage V based on the equivalent circuit model for a solar cell. Although, unlike most documentation on the non-ideal diode model, Ortiz-Conde *et al.* present a generalized equivalent circuit model of a single exponential junction with parasitic series resistance (R_s) and parasitic parallel (shunt) resistances (R_{sh}) at the junction (R_{P1}) (in direct parallel with the junction) and periphery (R_{P2}) (in indirect parallel with the junction as the series resistance separates the junction and periphery) (see Figure 7).[78]

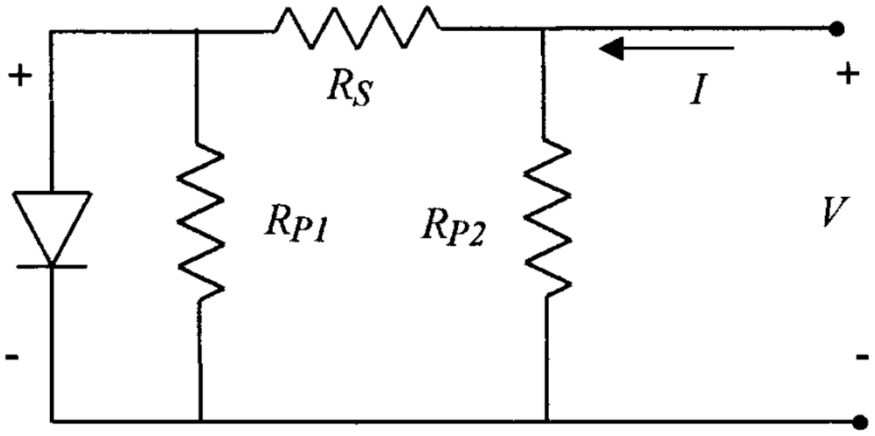

Figure 7. Schematic of a Generalized Equivalent Circuit Model for Solar Cells.[78] This generalized equivalent circuit model consists of a single exponential junction with parasitic series resistance (R_s) and parasitic parallel (shunt) resistances (R_{sh}) at the junction (R_{P1}) (in direct parallel with the junction) and periphery (R_{P2}) (in indirect parallel with the junction as the series resistance separates the junction and periphery).[78]

The non-ideal diode equation for this general circuit model is

$$J = J_0 \left\{ \exp\left[\frac{V\left(1 + \frac{R_s}{R_{P2}}\right) - JR_s}{\eta V_T} \right] - 1 \right\} + \frac{V - JR_s}{R_{P1}} - J_{ph}$$

Then, making the standard assumption of no peripheral shunt resistance losses with series and "junction" shunt resistance losses (i.e., $R_{P2} \to \infty$, $R_{P1} = R_{sh}$), the standard non-ideal diode equation is

$$J = J_0 \left[\exp\left(\frac{V - JR_s}{nV_T} \right) - 1 \right] + \frac{V - JR_s}{R_{sh}} - J_{ph}$$

where J_0 is the dark reverse bias saturation current density, R_s is the series resistance, n is the ideality factor, $V_T = k_B T/q$ is the thermal voltage, k_B is Boltzmann's constant, T is the temperature, R_{sh} is the shunt resistance, and J_{ph} is the photocurrent.[33,78]

Table 8. Non-Ideal Diode Model Fitting Parameters – Names, Symbols, Units

Name	Symbol	Unit
Dark Reverse Bias Saturation Current	J_0	$[A/m^2]$
Ideality Factor	n_{id}	Unitless: fraction or %
Series Resistance	R_s	$[\Omega m^2]$
Shunt Resistance	R_{sh}	$[\Omega m^2]$
Photocurrent	J_{ph}	$[A/m^2]$

Beginning with this more general "lumped" circuit model clarifies the assumption of no peripheral shunt resistance losses not discussed in most embodiments of the model. Beyond the equivalent circuit resistance structure, the model assumes:[33]

- Steady-state approximation – assumes steady-state charge carrier generation, drift, diffusion, recombination, and extraction (i.e., no transient accumulation of charge carriers).
- Uniform excess carrier concentration profiles with infinite carrier mobility and no carrier-generated electric fields – assumes spatial uniformity of carrier concentration, carrier-generated electrostatic potential (i.e., no carrier-generated electric field), and carrier generation, drift, diffusion, trapping, de-trapping, recombination, and extraction (i.e., no carrier accumulation) across all device layers and interfaces. Thus, absorber layer grain boundaries, layer interfaces, and differences between layers are not modeled.
- Recombination may be summarized by a single diode element in the equivalent circuit representing the effective amount of trap-assisted, nonradiative, monomolecular, Shockley-Read-Hall (SRH) recombination – assumes no spatial variation in recombination rates and no bimolecular, Auger, or higher-order recombination.
- Perfect electron-selective anode and hole-selective cathode
- An intrinsic (non-degenerate) absorber layer (i.e., low doping with the Fermi level far from the band edges)
- Low carrier injection

Overall, these model assumptions represent key sources of error in fitting this model to J-V scans. Regarding the solution to the non-ideal diode equation cannot be expressed with elementary functions since the equation is implicit, but it can be expressed with the Lambert W function by

$$J = \frac{nV_T}{R_s} W\left\{\frac{J_o R_s R_{sh}}{nV_T(R_{sh}+R_s)} \exp\left[\frac{R_{sh}\left(V+\left(J_0+J_{ph}\right)R_s\right)}{nV_T(R_{sh}+R_s)}\right]\right\} + \left(\frac{V-\left(J_0+J_{ph}\right)R_{sh}}{R_{sh}+R_s}\right)$$

These are equations 5 and 6 in Ortiz-Conde *et al.*'s work,[78] but note that we added the photocurrent (J_{ph}) term to the dark reverse bias saturation current (J_0) in the locations which account for series and shunt resistance losses. Moreover, since the independent variable is applied bias voltage (V), these terms appear as Ohmic additions to the applied bias voltage: $V \pm \left(J_0 + J_{ph}\right)R_{s,sh}$. Specifically, series resistance is accounted for in the exponent and shunt resistance is accounted for in the term outside the Lambert W function. Although, the factor in front of the exponential term specifically describes diode behavior, meaning it does not involve the applied bias voltage (V) and thus does not receive a photocurrent (J_{ph}) term. Last, for dark current-voltage (J-V) scans, photocurrent (J_{ph}) is set to zero. To simulate and fit current-voltage (J-V) scans with the non-ideal diode model, we utilize Le Corre's open-source "PVLC_Diode_Fit" Python package. Again, as for the drift-diffusion model, the package being open-source and written in a common and accessible language enables easy integration into high-throughput data pipelines for large datasets of PSC degradation data.

Similar to the solar cell parameters, the non-ideal diode model fitting parameters also serve many purposes in this study. First, their evolutions and CSA provide a simpler (although cruder) and more accessible set of predictive modeling features and description of device performance decline than drift-diffusion parameters. Additionally, as the non-ideal diode model is simpler than the drift-diffusion model (i.e. has fewer fitting parameters and cruder

assumptions), its fitting, CSA, and predictive modeling results are effectively a culmination of the corresponding drift-diffusion results. As such, we draw correlations between the two models' results throughout this work (along with the solar cell parameters) to identify how the mechanisms of device performance decline at the drift-diffusion level manifest in the non-ideal diode and solar cell parameters.

2.2.3 Drift-Diffusion Modeling

2.2.3.1 Governing Equations and Simulation Geometry

Drift-diffusion models utilize the set of coupled partial differential equations governing semiconductor devices – the drift-diffusion equation, continuity equation, and Poisson equation – to rigorously model carrier drift and diffusion and the corresponding electrostatic potential profile.[40] The drift-diffusion equation governs charge carrier transport by equating current density to the sum of its drift and diffusion current densities. Assuming one-dimensional (1D) variation along the device thickness (spatial uniformity over cross-sections of the device area), the Boltzmann approximation for intrinsic (non-degenerate) semiconductors (i.e., low doping with the Fermi level far from the band edges),[33,79] and the absence of magnetically induced electric fields (only observed appreciably in organic solar cells, not perovskite solar cells),[80–83] the drift-diffusion equations for electrons and holes, respectively, are

$$J_n(x) = -qn(x)\mu_n(x)\frac{\partial V(x)}{\partial x} + qD_n(x)\frac{\partial n(x)}{\partial x}$$

$$J_p(x) = -qp(x)\mu_p(x)\frac{\partial V(x)}{\partial x} - qD_p(x)\frac{\partial p(x)}{\partial x}$$

where J_n and J_p are the electron and hole current densities, respectively, x is the position coordinate along the device thickness, q is the elementary charge ($q = 1.602 * 10^{-19}\ C$), n and p are the electron and hole concentrations, μ_n and μ_p are the electron and hole mobilities, V is the electrostatic potential, and D_n and D_p are the electron and hole diffusion coefficients, respectively.[33] We assume the diffusion coefficients obey the Einstein relation

$$D_n = \frac{k_B T}{q}\mu_n = V_T\mu_n$$

$$D_p = \frac{k_B T}{q}\mu_p = V_T\mu_p$$

where k_B is Boltzmann's constant, T is the absolute temperature, and V_T is the thermal voltage *w*here $V_T = k_B T/q$.[33,79] Additionally, carrier mobilities are assumed to be independent of electric field strength, treated as an intrinsic material property determined by phonon scattering. Indeed, multiple studies validate this assumption in the low field strengths characteristic of typical solar cell operating conditions.[84–86] These drift-diffusion equations apply to all mobile charge carriers including ions, but care must be taken in ensuring all concentrations, mobilities, and charge types match the considered carrier.

Beyond the drift-diffusion equation, the continuity equation is simply a charge carrier material balance given by

$$\frac{1}{q}\frac{\partial J_n(x)}{\partial x} + G(x) - U(x) = \frac{\partial n(x)}{\partial t}$$

$$-\frac{1}{q}\frac{\partial J_p(x)}{\partial x} + G(x) - U(x) = \frac{\partial p(x)}{\partial t}$$

where G and U are the volumetric free carrier generation and recombination rates, respectively. At steady state, charge carrier concentrations are constant with time and their time derivatives vanish. Additionally, generation and recombination do not occur for mobile ions, meaning their corresponding continuity equations do not contain these terms.

Last, the Poisson equation relates the charge carrier concentration profiles to the electrostatic potential profile by

$$\frac{\partial}{\partial x}\left(\epsilon(x)\frac{\partial V(x)}{\partial x}\right) = -q\left(p(x) - n(x) + \sum_i C_i(x)\right)$$

where ϵ is the material permittivity and C_i represents the concentration profiles of other carriers including dopants, defect ions, and trapped free carriers.[33,40] These additional variables are

$$\sum_i C_i(x) = N_D^+(x) - N_A^-(x) + X_c(x) - X_a(x) + \sum_{j=1}^{M}\left(s_{tb,j}^e(x) - f_{tb,j}(x)\right)N_{tb,j} + \left(s_{ti,j}^e(x) - f_{ti,j}(x)\right)N_{ti,j}$$

where N_D^+ and N_A^- are the donor and acceptor dopant concentrations, X_c and X_a are the cationic and anionic defect concentrations, respectively, M is the number of trap levels, s is the charge type of unoccupied traps, f is the trap occupation probability, and the "tb,j" and "ti,j" denote bulk and interface traps of trap state j, respectively.[40]

The total current density J is the sum of all current densities

$$J(x) = J_n(x) + J_p(x) + J_D(x) + J_{nion}(x) + J_{pion}(x)$$

where J_D is the displacement current and J_{nion} and J_{pion} are the anion and cation current densities, respectively. Although, since the absorber and transport layers possess differing band energies and effective densities of states, each layer possesses its own set of governing equations. Although, to avoid solving a set of governing equations for each layer, Koster *et al.* defined generalized potentials and interfacial current density expressions utilizing finite surface recombination velocities specified as input device parameters.[40] Although, the default values are high (i.e., $10^3\ m/s$) and thus do not affect device characteristics (see Section 6). These equations are the foundation for drift-diffusion modeling of semiconductor devices.

2.2.3.2 Boundary Conditions

Alongside this set of coupled partial differential equations, the following boundary conditions suggested by Koster *et al.* are required to specify their particular solutions. Specifically, the Poisson equation and the combined drift-diffusion and continuity equation are second order and thus each require two boundary conditions. Although, since each charge carrier type obeys its own drift-diffusion and continuity equations, two boundary conditions are required for each carrier type in the combined drift-diffusion and continuity equation. Assuming electron and hole surface recombination velocities are infinite such that electrons and holes are in thermal equilibrium at the transport layers' interfaces with their electrodes, and assuming the Boltzmann approximation,[33,79] the electron and hole concentrations are

$$n_{ETL-anode} = N_c \exp\left(-\frac{\phi_n}{k_B T}\right)$$

$$n_{HTL-cathode} = N_c \exp\left(-\frac{E_g - \phi_p}{k_B T}\right)$$

$$p_{HTL-cathode} = N_v \exp\left(-\frac{\phi_p}{k_B T}\right)$$

$$p_{ETL-anode} = N_v \exp\left(-\frac{E_g - \phi_n}{k_B T}\right)$$

where N_c and N_v are the conduction and valence band effective density of states, respectively, E_g is the bandgap energy, and ϕ_n and ϕ_p are the conduction and valence band energy offsets between the electron transport layer (ETL) and anode and between the hole transport layer (HTL) and cathode, respectively. Additionally, since ionic defects do not appreciably enter the electrodes,[87] their current densities at the transport layers' interfaces with electrodes are equated to zero ($J_{nion,AL-ETL} = J_{nion,AL-HTL} = 0, J_{pion,AL-ETL} = J_{pion,AL-HTL} = 0$). Ion and displacement current densities are thus also zero throughout the device thickness at steady state. Meanwhile, the potential must obey conservation of energy by Kirchoff's voltage law

$$V_a - V_c + V_{app} = V_{bi}$$

$$V_{bi} = \frac{(W_c - W_a)}{q}$$

where V_a and V_c are the anode and cathode potentials, V_{app} is the bias voltage applied across the device electrodes (positive under forward bias), and V_{bi} is the built-in voltage created by the difference in cathode and anode work functions W_c and W_a, respectively. These boundary conditions ensure unique solutions to the governing equations to enable simulation.

2.2.3.3 Simulation Geometry

The drift-diffusion model considers a variable number of device layers, their corresponding interfaces, and evenly-spaced grain boundaries, assuming spatial uniformity of material properties in each region. Although, despite being an available feature, we do not model grain boundaries since our HP film thicknesses (≈300 nm) are roughly equivalent to our grain diameter (≈300 nm), meaning grain boundaries do not exist across the HP film thickness for most of the device area. Overall, the simulation geometry provides the spatial coordinates necessary to specify boundary conditions, again to ensure unique solutions to the governing equations to enable simulation.

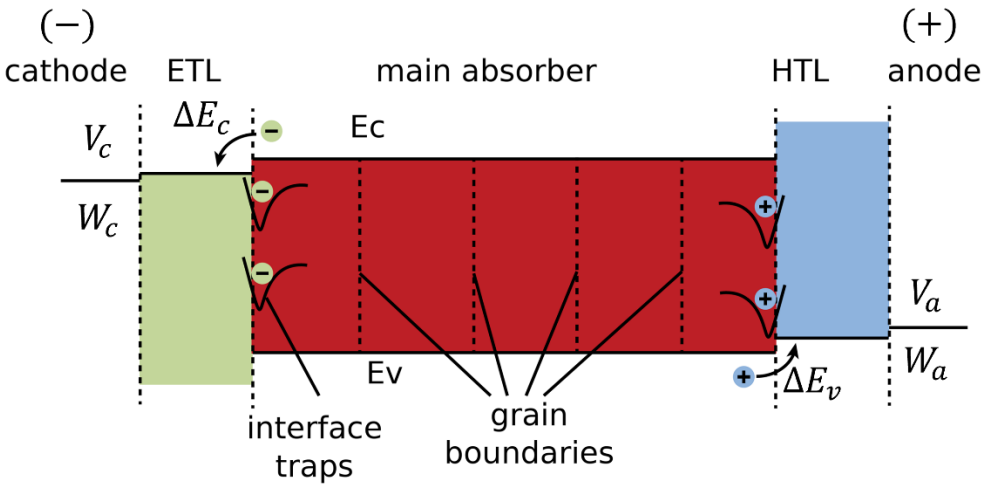

Figure 8. Schematic Band Diagram of a General Thin-Film Solar Cell Which May Be Modeled by the 1D Drift–Diffusion Model (SIMsalabim).[40] SIMsalabim allows specification of properties for a variable number of device layers (e.g., ETLs, absorber layers, and HTLs in thin film PVs), their corresponding interfaces, and evenly-spaced grain boundaries. All variables in this figure are defined in the model formulation above. Additionally, note that despite deep defect (trap) energy wells being shown only at the interfaces joining the absorber layer and transport layers (TLs), such traps also exist at grain boundaries and in the crystal bulk, and as stated above, the model allows specification of unique values for such properties in each region. Last, note that the model assumes assuming spatial uniformity of material properties within each region.

2.2.3.4 Electron-Hole Pair Generation

Electron-hole pairs are generated by excitation of electrons from the valence band to the conduction band, most often by thermal and optical stimuli.[33] Although, for the absorber layer bandgaps relevant for solar cells (e.g., 1.27, 1.61, and 1.65 eV for our low-bandgap, medium-bandgap ($MAPbI_3$), and high-bandgap compositions), carrier concentrations are $\approx 10^{14} - 10^{16}\ cm^{-3}$ for $MAPbI_3$. In contrast, under 1 sun illumination, carrier concentrations range $\approx 10^{19} - 10^{24}\ m^{-3}$, meaning the profile of electron-hole pair generation is effectively equivalent to the optical absorption profile (see Section 6).

SIMsalabim enables calculation of the volumetric electron-hole pair (EHP) generation rate profile $G_{ehp}(x)$ over the active layer thickness (L_{abs}) with the transfer matrix method (TMM). Although, the required data for the wavelength-dependent index of refraction and extinction coefficient are not available for all device layers, preventing use of the TMM. The optimal alternative is a generation profile exhibiting exponential (Beer-Lambert) decay over the active layer thickness (L_{abs}) with a total volumetric generation rate $G_{ehp,tot}$ equal to the specified or fitted value, given by

$$G_{ehp}(x) = \hat{n}_{ph,E>E_g}\alpha e^{-\alpha x}(1-R), L_{ETL} \le x \le L_{ETL} + L_{abs}$$

$$G_{ehp,tot} = \frac{1}{L_{abs}}\int_{L_{ETL}}^{L_{ETL}+L_{abs}} G_{ehp}(x)dx = \frac{\hat{n}_{ph,E>E_g}(1-R)}{L}(1-e^{-\alpha L})$$

where x is the one-dimensional position coordinate along the device thickness, $\hat{n}_{ph,E>E_g}$ is the incident above-bandgap photon flux, α is the active layer's absorption, R is the reflectance, and L_{ETL} is the thickness of the electron transport layer (ETL). These expressions are derived in Section 8.1.1 (Appendix A.1), and they assume:

- Normally incident illumination
- Spatial uniformity of the transmitted above-bandgap photon flux, surface reflectance, and absorption coefficient over the device area
- Exponential attenuation law – a thick, highly absorbing film with insignificant optical interference and thus reflectance dominated by surface reflectivity on the active layer's light-incident side.

The electron-hole pair generation profile can strongly affect electron and hole concentration profiles, especially when diffusion lengths are comparable to or lower than HP film thicknesses (e.g., 900 nm for world-record 26.15% HP device).[88] This affects all device characteristics and phenomena, meaning an accurate electron-hole pair generation model is essential for accurate drift-diffusion modeling.

2.2.3.5 Recombination

Recombination is the process in which electrons and holes react to annihilate one another, effectively by electrons in the conduction band relaxing in energy (through various potential mechanisms) to fill holes in the valence band. This occurs before the electrons and holes may be extracted as electrical current, reducing device performance (i.e., all solar cell parameters). Additionally, recombination is one of the strongest limiters of solar cell performance and, unlike most performance limitations, it is a fundamental limitation to the performance of any solar cell as demonstrated by the Shockley-Queisser theoretical efficiency limit.[33] Accurate recombination models are thus essential for accurate drift-diffusion modeling of solar cells.

This model considers all recombination pathways observed for PSCs under our characterization conditions: bimolecular recombination and Shockley-Read-Hall (SRH) recombination (i.e., trap-assisted, non-radiative, monomolecular recombination). There are other pathways including trimolecular Auger recombination and geminate recombination of excitons, but trimolecular Auger recombination is negligible in the range of simulated carrier concentrations ($\approx 10^{19} - 10^{24}\ m^{-3}$) under 1 sun illumination,[75,76,79,80,123–150] and geminate recombination is also negligible since HPs are non-excitonic materials[103] (i.e., excitons exist in negligible concentrations). A very thorough literature review and discussion of recombination mechanisms and models and their corresponding assumptions will be detailed in a future publication and in a future version of this thesis on our "DegradePV" GitHub repository (see Section 6).[63]

2.2.3.5.1 Bimolecular Recombination

Bimolecular recombination is the process in which exactly one electron and one hole react to annihilate one another.[33] As done by all reviewed models (see Section 6), this is assumed to occur in a single elementary step, meaning its rate law should be the product of a rate constant and the electron and hole concentrations. Although, since thermally generated carriers also recombine through this pathway but are not detrimental to device performance, we exclude their contribution to the recombination rate. Thus, the net bimolecular recombination rate law is

$$R_2 = k_2(np - n_i^2)$$

where R_2 is the net volumetric bimolecular recombination rate, k_2 is the effective bimolecular recombination rate constant, and n_i is the intrinsic carrier concentration. Assuming an intrinsic (non-degenerate) absorber layer (i.e., low doping with the Fermi level far from the band edges), the intrinsic carrier concentration is determined by

$$n_0 = N_c e^{-(E_c - E_i)/k_B T} = N_c \exp\left(-\frac{E_g}{2k_B T}\right)$$

$$p_0 = N_v e^{-(E_i - E_v)/k_B T} = N_v \exp\left(-\frac{E_g}{2k_B T}\right)$$

$$n_i^2 = n_0 p_0 = N_c N_v \exp\left(-\frac{E_g}{k_B T}\right)$$

where N_c and N_v are the conduction and valence band effective densities of states (DOS), E_g is the absorber layer bandgap, k_B is Boltzmann's constant, and T is temperature.

Although, the effective rate constant differs from its true value due to various phenomena which are often not discussed in literature. Specifically, Richter *et al.*[89] and Staub *et al.* (2017)[90] recognize bimolecular recombination may occur through both the well-known direct, band-to-band, radiative pathway and a less-mentioned trap-assisted, nonradiative, Auger pathway, increasing the effective rate constant relative to that determined strictly from measurements of the radiative rate (e.g., through photoluminescence). The effective rate constant thus also depends on deep defect (trap) density. Additionally, photons emitted by the radiative pathway may be reabsorbed (i.e., recycled), decreasing the effective rate constant. Nevertheless, despite these numerous phenomena, bimolecular recombination is still an elementary, bimolecular process and is thus well-modeled by the above rate law. Although, the variation in how and if literature reports account for these phenomena causes wide variation in literature values for the effective and true values for the rate constant. To address this, we perform a thorough literature review of recombination rate constant measurements and models for these various phenomena to inform estimates of the effective and true bimolecular recombination rate constants for our HP films (see Section 6).

Overall, recombination processes all influence device performance by consuming electrons and holes, meaning recombination parameters are highly correlated, and deep defect (trap) densities are thus sensitive to the chosen value for the effective bimolecular recombination rate constant. This value must therefore be accurate to ensure accurate drift-diffusion modeling (and especially fitted deep defect (trap) densities).

2.2.3.5.2 Shockley-Read-Hall (SRH) Recombination (i.e., Trap-Assisted, Nonradiative, Monomolecular Recombination

Shockley-Read-Hall (SRH) recombination is the trap-assisted, nonradiative, monomolecular pathway for recombination. In short, an electron or hole becomes trapped in a deep defect (trap) state near the middle of the HP bandgap, allowing time for the trapped carrier to relax to the opposite band and recombine. Although, since these energy gaps between band edges and trap states are approximately half the bandgap, the emitted radiation is in the infrared range (i.e., essentially absorbed as thermal energy) and thus cannot be recycled for carrier generation. SRH recombination is therefore classified as nonradiative.[33]

For this model, Koster *et al.* present rigorous models for bulk crystals and both sides of interfaces by determining SRH trapping and detrapping rates for a single variable trap energy.[40,52] For a single trap state (t) and position in the device, the trapping and de-trapping rates for electrons and holes in the absorber layer bulk, respectively, are

$$R_{trap,n} = C_n n N_t (1 - f_t)$$

$$R_{detrap,n} = C_n n_1 N_t f_t$$

$$R_{trap,p} = C_p p N_t f_t$$

$$R_{detrap,p} = C_p p_1 N_t (1 - f_t)$$

where C_n and C_p are the electron and hole capture coefficients, n and p are the electron and hole concentrations, N_t is the deep defect (trap) density, f_t is the trap occupation probability, and n_1 and p_1 are the electron and hole concentrations when the quasi Fermi-level matches the trap energy level, respectively.[33,40] Assuming the Boltzmann approximation,[33,79] these concentrations are given by

$$n_1 = N_c \exp\left[-\frac{E_c - E_t}{k_B T}\right] = N_c \exp\left[-\frac{\frac{E_g}{2} - \Delta E_{t,mg}}{k_B T}\right]$$

$$p_1 = N_v \exp\left[-\frac{E_t - E_v}{k_B T}\right] = N_v \exp\left[-\frac{\frac{E_g}{2} + \Delta E_{t,mg}}{k_B T}\right]$$

where N_c and N_v are the conduction and valence band effective densities of states (DOS), E_c and E_v are the conduction band minimum (CBM) and valence band maximum (VBM) energies, E_t is the trap energy, k_B is Boltzmann's constant, T is temperature, and $\Delta E_{t,mg}$ is the difference between the trap energy and mid-gap energy levels. Although, assuming the Fermi level is near mid-bandgap, these concentrations become

$$n_1 = \left[n_i \exp\left(\frac{E_g}{2k_B T}\right)\right] \exp\left[-\frac{E_c - E_t}{k_B T}\right] = n_i \exp\left[-\frac{E_i - E_t}{k_B T}\right]$$

$$p_1 = \left[n_i \exp\left(\frac{E_g}{2k_B T}\right)\right] \exp\left[-\frac{E_t - E_v}{k_B T}\right] = n_i \exp\left[-\frac{E_t - E_i}{k_B T}\right]$$

By material balance, the net SRH recombination rates in the absorber layer bulk are simply the differences in trapping and de-trapping rates, given by

$$R_{SRH,n} = C_n n N_t (1 - f_t) - C_n n_1 N_t f_t$$

$$R_{SRH,p} = C_p p N_t f_t - C_p p_1 N_t (1 - f_t)$$

Assuming a single trap state, these expressions describe the total SRH recombination rate in the absorber layer bulk for a given bulk deep defect (trap) density. For modeling interfacial SRH recombination, similar equations are utilized, but the model is much more extensive. See the SI of Koster *et al.*'s corresponding study[52] for a rigorous derivation of these expressions.

Additionally, we assume the common single mid-gap trap state to model SRH recombination (see Section 8.1.3: Appendix A.3 for a justification of this assumption).

Although, these rate expressions depend on the trap occupation probability (f_t), and this is generally time-dependent. Nevertheless, at steady state, the net SRH recombination rates for electrons and hole must be equivalent to ensure no charge accumulation ($R_{SRH,n} = R_{SRH,p}$), fixing the trap occupation probability (f_t) to

$$f_t = \frac{C_n n - C_p p_1}{C_n(n + n_1) + C_p(p + p_1)}$$

and the bulk SRH recombination rate to

$$R_{SRH} = \frac{C_n C_p N_t (np - n_i^2)}{C_n(n + n_1) + C_p(p + p_1)}$$

Although, this expression contains both capture coefficients and deep defect (trap) density, meaning the fitted deep defect (trap) densities are highly correlated with the chosen values of capture coefficients. In other words, device performance is only appreciably sensitive to the deep defect (trap) density distribution and the effective recombination rate constants and lifetimes, not the specific values of deep defect (trap) densities and capture coefficients. Mathematically, the SRH carrier lifetime for electrons or holes is

$$\tau_{n,p} = \frac{1}{C_{n,p} N_t}$$

However, deep defect (trap) densities vary far more among devices than capture coefficients since deep defect (trap) densities scale with defects introduced during fabrication or handling[67–69] whereas capture coefficients are intrinsic material properties.[33] Of course, the effective DOS and bandgap are also involved, but these are accurately reported in literature[103] and measured in our experiments, respectively. Thus, as for the bimolecular recombination rate constant, we perform a thorough literature review of capture coefficients to determine the capture coefficient values used in this study (see Section 6).

2.2.3.6 Ionic Defects

As stated previously, electric field shielding (i.e., screening) due to ion accumulation at HP-TL interfaces has been observed to significantly decrease device performance,[104] and mobile ion migration has thus been observed to cause significant hysteresis in electronic characterizations of devices, requiring specific procedures to accurately measure PCE.[47] Indeed, over all experiments, our undegraded devices exhibit an average hysteresis index of $\approx -6\%$ and an average hysteresis metric of $\approx -8\ W/m^2$ for our high-bandgap architecture and $\approx -10\ W/m^2$ for our medium-bandgap ($MAPbI_3$) architecture (or $\approx -5\%$ when normalized to the MPP power). Thus, accurate modeling of defect structure and ion migration is essential for accurate drift-diffusion modeling.

Iodide vacancies (V_I) and anions (I^-) are the primary mobile ionic species in halide perovskites (HPs),[105,106] and we thus assume the simulated cations and anions match their properties. Specifically, iodide vacancies (V_I) are not extracted into the transport layers (TLs) because the TLs do not possess halides to donate to the HP film, and iodide anions (I^-) have been observed to enter fullerene-based electron transport layers (ETLs).[55–57] Thus, we assume

cations are restricted to the HP film while anions can move into the ETL. In our thorough literature reviews of device properties (see Section 6), we provide a detailed discussion of defect structure and ion migration in HPs.

2.2.4 Simulation of Current-Voltage (J-V) Scans with the Drift-Diffusion Model

Current-voltage (J-V) scans are simulated by solving discretized, linearized versions of the governing equations through Gummel iteration.[40,43,44] Specifically, the governing equations are discretized with Taylor polynomial expansions of the Bernoulli function $B(x) = x/(e^x - 1)$ about $x = 0$,[40,107] and the governing equations are linearized with expressions derived by Koster *et al.*.[40] Then, the governing equations are solved through Gummel iteration's two-loop structure. First, for a given applied bias voltage, an initial guess is provided for the charge carrier concentration and electrostatic potential profiles, and the Poisson equation is solved at each grid point along the simulation thickness to determine a correction ($\delta V(x)$) to the electrostatic potential profile. The Poisson equation is then repeatedly solved until the correction drops below a set tolerance, resulting in the electrostatic potential profile which corresponds to the guessed carrier concentration profiles. This is the internal iteration loop. Then, in the external iteration loop, these profiles are used to solve the continuity equation for corrections to the carrier concentration profiles. Once corrected, the carrier concentration profiles are then used to recalculate the profiles for electron-hole pair (EHP) generation, free carrier trapping and de-trapping, and recombination rates for the next external iteration loop. The carrier concentration and electrostatic potential profiles are then once again fed into the Poisson equation to determine a new electrostatic potential profile, and this entire process is repeated until all profiles' corrections drop below their set tolerances to yield a final current density. Last, to obtain a simulated current-voltage (J-V) scan, simulations are performed at all relevant applied bias voltages. Outputs from simulations include spatial profiles for all variables explicitly and implicitly present in the governing equations (see Table 9) and current densities for all relevant phenomena versus applied bias voltage (see Table 10).

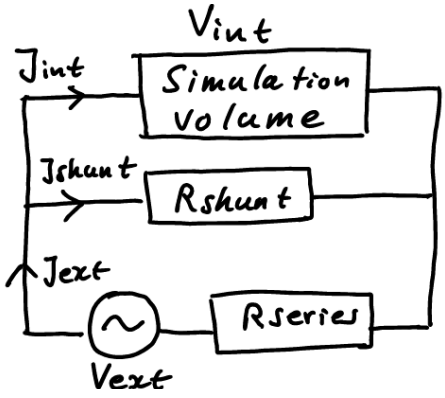

Figure 9. Schematic of the equivalent circuit used for simulation with the SIMsalabim drift-diffusion model.[40]

Both steady-state (SimSS) and transient (ZimT) simulations follow this approach, but for transient simulations, the governing equations include time derivatives and thus require a time step value in addition to the applied bias voltage. Additionally, transient simulations treat the applied bias voltage as the external voltage (V_{ext}), not the internal voltage (V_{int}) across the device as in steady-state simulations, meaning an additional external loop is required to ensure the voltage drop across the series resistor matches the difference between the internal and external voltages for the simulated current density (J_{int}). Finally, note that the steady-state model (SimSS) only depends on the device parameters and applied bias voltage, meaning it may only simulate unidirectional (forward or reverse) scans. In contrast, the transient model (ZimT) also depends on time, meaning it may simulate multidirectional scans (e.g., hysteresis loops). Although, transient simulations require large computation times, and we therefore do not perform transient simulations in this work.

Table 9. Simulated Drift-Diffusion Variables versus Position Along Simulation Thickness – Names, Symbols, Units

Name	Symbol	Unit
Internal Voltages		
Position Along Simulation Thickness	x	$[m]$
External Voltage	V_{ext}	$[V]$
Energetic Quantities		
Internal Electrostatic Potential Energy	V	$[eV]$
Internal Vacuum Energy	E_{vac}	$[eV]$
Conduction Band Minimum (CBM) Energy	E_c	$[eV]$
Valence Band Maximum (VBM) Energy	E_v	$[eV]$
Electron Quasi-Fermi Level	E_{Fn}	$[eV]$
Hole Quasi-Fermi Level	E_{Fp}	$[eV]$
Charge Carrier Concentrations		
Electron Concentration	n	$[m^{-3}]$
Hole Concentration	p	$[m^{-3}]$
Donor Dopant Concentration	N_D	$[m^{-3}]$
Acceptor Dopant Concentration	N_A	$[m^{-3}]$
Anion Concentration	C_{anion}	$[m^{-3}]$
Cation Concentration	C_{cation}	$[m^{-3}]$
Trap Occupation Probabilities		
Bulk Trap Occupation Probability	f_{tb}	Unitless
Interfacial Trap Occupation Probability	f_{ti}	Unitless
Free Carrier Mobilities (in case of mobilities exhibiting field dependence)		
Electron Mobility	μ_n	$[m^2V^{-1}s^{-1}]$
Hole Mobility	μ_p	$[m^2V^{-1}s^{-1}]$
Volumetric Generation and Recombination Rates		
Electron-Hole Pair (EHP) Generation Rate	G_{ehp}	$[m^{-3}s^{-1}]$

Name	Symbol	Unit
Free Carrier Generation Rate	G_{free}	$[m^{-3}s^{-1}]$
Direct Recombination Rate	R_{dir}	$[m^{-3}s^{-1}]$
Bulk Shockley-Read-Hall (SRH) Electron Recombination Rate	$R_{SRH,bulk,n}$	$[m^{-3}s^{-1}]$
Bulk Shockley-Read-Hall (SRH) Hole Recombination Rate	$R_{SRH,bulk,p}$	$[m^{-3}s^{-1}]$
Interfacial Shockley-Read-Hall (SRH) Electron Recombination Rate	$R_{SRH,int,n}$	$[m^{-2}s^{-1}]$
Interfacial Shockley-Read-Hall (SRH) Hole Recombination Rate	$R_{SRH,int,p}$	$[m^{-2}s^{-1}]$
Current Densities		
Electron Current Density	J_n	$[Am^{-2}]$
Hole Current Density	J_p	$[Am^{-2}]$
Internal Current Density	J_{int}	$[Am^{-2}]$

Table 10. Simulated Current Densities versus Applied Bias Voltage – Names, Symbols, and Units

Name	Symbol	Unit
External Voltage	V_{ext}	$[V]$
External Current Density	J_{ext}	$[Am^{-2}]$
Simulation Error in External Current Density	$J_{ext,err}$	$[Am^{-2}]$
Internal Current Density	J_{int}	$[Am^{-2}]$
Photogenerated Current Density	J_{photo}	$[Am^{-2}]$
Bimolecular Recombination Current Density	J_{bi}	$[Am^{-2}]$
Bulk Shockley-Read-Hall (SRH) Recombination Current Density	$J_{SRH,bulk}$	$[Am^{-2}]$
Minority Carrier Current Density at Anode	$J_{min,anode}$	$[Am^{-2}]$
Minority Carrier Current Density at Cathode	$J_{min,cathode}$	$[Am^{-2}]$
Shunt Current Density	J_{shunt}	$[Am^{-2}]$

2.2.5 Fitting Approach

2.2.5.1 Non-Ideal Diode Model

For fitting current-voltage (J-V) scans with the non-ideal diode model, Le Corre utilizes nonlinear least squares regression with the recommended option (which we use) of

logarithmically scaling the current density data and equation prior to fitting. This almost entirely linearizes the exponential shape of current-voltage (J-V) curves, enabling roughly equal weighting to all points in the scan. Specifically, this avoids underweighting dark current densities at low applied bias voltages and avoids overweighting current densities at high applied bias voltages. Although, this requires removal of the zero-voltage point to prevent divergence of the logarithm. Regarding allowed ranges and initial guesses for fitting parameters, the standard allowed ranges are $J_0 \in [10^{-30}, 10^{-3}]$, $n \in [0.8, 3]$, $R_s \in [10^{-8}, 10^{2}]$, and $R_{sh} \in [10^{-3}, 10^{8}]$. The initial guess for the reverse bias dark saturation current (J_0) is equated to the minimum of two values – either $2 * 10^{-30} A\, m^{-2}$ or the minimum absolute current density – and its lower bound is replaced with this initial guess lowered by four orders of magnitude. Moreover, the initial guess for ideality factor is equated to the differential ideality factor

$$n_{diff} = \frac{1}{V_T \frac{d(\ln J)}{dV}}$$

where the derivative is numerically calculated using the differences between adjacent current densities along the entire scan. Similarly, the initial guesses for series and shunt resistance are equated to the numerical derivatives of current density with respect to applied bias voltage at open-circuit and short-circuit conditions, respectively. If a calculated initial guess is outside the parameter's allowed range, the initial guess is set to its respective default value from $n = 1.8$, $R_s = 10^{-3}\ \Omega$, $R_{sh} = 10^{8}\ \Omega$.

2.2.5.2 Drift-Diffusion Model

2.2.5.2.1 Fitting Parameter Selection

As a general principle of fitting models to data, selecting the fitting parameter set is crucial to the accuracy and value of fitting results. Inclusion of parameters which are highly correlated with others can cause excessive volatility in fitted values, and exclusion of essential parameters can cause poor fitting. Thus, we select fitting parameters to avoid both sources of error.

2.2.5.2.1.1 Undegraded Devices

For undegraded devices, fitting parameters include device parameters which are theoretically predicted to vary among samples due to unintended variations in the fabrication process: volumetric electron-hole pair (EHP) generation rate (G_{ehp}), free carrier and ion mobilities, bulk and interfacial deep defect (trap) densities, and ion concentrations). Undegraded device fitting parameters also include device parameters whose range of literature values results in large changes in fitting error and PCE, even if theory suggests low variation among samples (e.g., transport layer (TL) band energies and electrode work functions, specifically). Although, if strong correlations exist among fitting parameters due to their relevant phenomena being related (e.g., deep defect (trap) densities and capture coefficients), their fitted values may lie outside of literature ranges and possibly reach their numerical constraints. In this case, chosen fitting parameters are removed and set to their average literature values while their correlated counterparts remain in the fitting parameter set to model the relevant phenomena (e.g., capture coefficients are fixed while deep defect (trap) densities are allowed to vary).

Although, we do not apply this methodology to TL band energies and electrode work functions. These parameters are highly correlated, and the electrode work functions are especially correlated since their difference (not their individual values) determines the built-in

electric field. Yet, despite these strong correlations, we do not exclude them from the fitting parameter set for initial fits of undegraded devices. These parameters exert great influence on device characteristics by directly affecting electrostatic potential, electric field, and thus open-circuit voltage. Combined with their wide variation of literature values, the use of their literature values often results in nonsensical or difficult fits and high volatility in fitted values, sometimes causing fitting parameters reaching their numerical boundaries. Additionally, their use as fitting parameters yields the same result, but their fitted values are reasonable with low volatility.

Thus, we fit J-V scans for each architecture's undegraded devices in two stages. First, we fit the J-V scans of all undegraded devices with TL band energies and electrode work functions included as fitting parameters. Then, since their values are likely uniform among devices (especially those at equivalent temperatures), we fix them (i.e., excluding them from the fitting parameter set) to their respective averages over all undegraded devices for the given architecture, and we do this for all future fits of undegraded and degraded devices. Although, since many other parameters reach their numerical boundaries in the first stage, it is possible for the TL band energies and electrode work functions to be unjustly influenced by our choices of numerical constraints.

2.2.5.2.1.2 Degraded Devices

For degrading devices, fitting parameters are device parameters which are theoretically predicted to vary over degradation (see Section 6). All remaining device parameters (other than the TL band energies and electrode work functions) are held constant at their literature values. Although, in future work, it is possible parameters fit for undegraded devices are to be held constant for degrading devices. In this case, the parameters' values should be fixed at their average values among the relevant undegraded devices. Specifically, if a parameter is temperature-dependent (see Section 6), only the fitted values for undegraded devices corresponding to the given device's temperature should be averaged. Regarding numerical simulation parameters, default parameters are selected.[40]

Table 11 presents the fitting parameter names, symbols, units, and variation scales, and specifies which parameters are varied when fitting J-V scans for degrading devices. Additionally, in our future publication and on our "DegradePV" GitHub repository published online,[63] we will present a table with the names, symbols, units, and averages and standard deviations among literature values for all device parameters (multiple values specified if multiple materials apply). Last, we have compiled extremely thorough literature reviews for each device parameter with dozens of references and comprehensive tables of reported values, evaluations of the reviewed studies' methodologies, and visualization of the distributions of these reported values (see Section 6).

Table 11. Drift-Diffusion Fitting Parameters – Names, Symbols, Units, Variation Scales

Parameter	Scale	Varied over Degradation?
Electron-Hole Pair (EHP) Generation Rate		
Volumetric Electron-Hole Pair (EHP) Generation Rate (G_{ehp}) [$m^{-3}s^{-1}$]	linear	Yes (automatically with BOAR, manually with OptimPV)
Parasitic Resistances		
Series Resistance R_S [Ω]	log	Yes

Parameter	Scale	Varied over Degradation?
Shunt Resistance R_{sh} [Ω]	log	Yes
Deep Defect (Trap) Densities		
Absorber Layer (AL) Bulk Deep defect (trap) density ($N_{tr,bulk}$) [m^{-3}]	log	Yes
Interfacial Deep defect (trap) density at the AL-ETL Interface ($N_{t,int,AL-ETL}$) [m^{-2}]	log	Yes
Interfacial Deep defect (trap) density at the AL-HTL Interface ($N_{t,int,AL-HTL}$) [m^{-2}]	log	Yes
Free Carrier Mobilities		
Zero-Field Electron Mobility μ_n [$m^2V^{-1}s^{-1}$]	log	Yes
Zero-Field Hole Mobility μ_p [$m^2V^{-1}s^{-1}$]	log	Yes
Ion Mobilities		
Zero-Field Cation Mobility μ_{cation} [$m^2V^{-1}s^{-1}$]	log	Yes (ZimT)
Zero-Field Anion Mobility μ_{anion} [$m^2V^{-1}s^{-1}$]	log	Yes (ZimT)
Band Structure		
Conduction Band Maximum (CBM) of Electron Transport Layer (ETL) $E_{c,ETL}$ [eV]	linear	No
Valence Band Maximum (VBM) of Hole Transport Layer (HTL) $E_{c,HTL}$ [eV]	linear	No
Work Function of Cathode W_c [eV]	linear	No
Work Function of Anode W_a [eV]	linear	No

2.2.5.2.2 Fitting Procedure

As for the simulation procedure and fitting parameter selection, this process is crucial to the accuracy of fitting results. The drift-diffusion model is globally fit to the light (1 sun) and dark (0 sun) current-voltage (J-V) scans for each measurement cycle and scan type. This global fitting over illumination intensities maximizes the experimental data provided to the fit, thus maximizing accuracy and minimizing volatility in the fitted values. First, initial guesses are provided for the fitting parameters based on literature values or previously successful fits (see published code online),[63] and the corresponding current-voltage (J-V) scans are simulated at each illumination intensity (see Section 2.2.4). The chosen error metric (normalized root-mean-squared (RMS) error (NRMSE)) is then calculated globally over both illumination intensities, and the selected fitting parameters are varied on a specified scale (linear or logarithmic, see Table 11) over specified ranges (see published code online)[63] with fitting routines to minimize the error metric.

The variation scales are the scales on which fitting parameters must be varied to cause reasonable changes in basic properties of the J-V curve e.g.., the solar cell parameters), and they are implemented to maximize fitting efficiency. Specifically, varying parameters linearly when they should be varied logarithmically causes little change in the J-V scan and thus the error metric. Conversely, varying parameters logarithmically when they should be varied linearly causes excessive changes in the simulated J-V scan and thus the error metric, and both of these scenarios increase difficulty for the fitting routine by increasing the objective function's nonlinearity.

Regarding fitting parameter bounds, ranges are selected to ensure low computation times while ensuring fitted values lie within the specified ranges (preventing numerical constraint). Specifically, ranges span the maximum set of values which may be simulated in reasonable time. One bound (i.e., the low-sensitivity bound) is the value beyond which changes in the parameter have no effect on the simulated J-V curve, wasting computation time. In contrast, the opposite bound (i.e., the high-sensitivity bound) is the value beyond which simulations exhibit poor convergence, either failing or requiring excessive runtime. All values beyond these bounds are unreasonable and far beyond literature ranges, but these wide bounds were chosen to show the model's ability to isolate accurate fitting parameter values from a vast parameter space.

Regarding fitting routines, Koster *et al.* first developed AutoFit, a Pascal-based random search routine for globally fitting steady-state current-voltage (J-V) scans.[46,49,50] Although, random search is very computationally expensive, despite being accurate. To address this, we use OptimPV, a Python-based optimization program developed by Le Corre to globally fit forward, reverse, and hysteresis loop current-voltage (J-V) scans over varying illumination intensities and scan speeds with the steady-state (SimSS) or transient (ZimT) simulations. The program first performs Bayesian optimization to quickly achieve an error sufficiently to enable gradient descent to a global minimum while avoiding local, non-global minima. Then, the program performs nonlinear least squares (NLLSQ) regression to quickly reach the global minimum. Fitting parameters are varied until changes in all fitting parameters or the error metric are less than a relative tolerance of 10^{-12}. Note that Python's default tolerances (e.g.,$\approx 10^{-8}$) often cause fits to terminate prior to reaching global minima in fitting error, and we thus restrict the tolerance to the highest recommended precision ($\approx 10^{-12}$), indeed resulting in global minima (see below for methodology and see Section 6).

Regarding the objective function, Koster *et al.* and Le Corre *et al.* select the range-normalized root-mean-squared (RMS) error ($NRMSE_{range-norm}$) as the objective function, given by

$$NRMSE_{range-norm} = \frac{RMSE}{J_{max} - J_{min}} = \frac{\sqrt{\frac{1}{n}\sum_i^n (J_i - J_i')^2}}{J_{max} - J_{min}}$$

where $RMSE$ is the root-mean-squared (RMS) error, J_{max} and J_{min} are the maximum and minimum current densities in the range of experimental values, respectively, n is the number of data points considered, i is the summation index, and J_i and J_i' are the ith actual and simulated values, respectively. For global fitting, the values considered are simply the sets of current densities from all scans. This global $NRMSE$ is close to the RMS average (combined uncertainty) of the NRMSEs for each scan, but it differs slightly due to the normalization denominators differing for scans of differing illumination intensities. To verify achievement of global minima in fitting error (i.e., optimal fitting), we perform global, local, and sensitivity

analyses of fitting error relative to changes in each fitting parameter at the calculated optimum (see Section 2.2.6). The near-zero first derivatives (i.e., near-zero gradient) and positive second derivatives resulting from the sensitivity analysis verify optimal fitting within the corresponding local minimum (see Section 6), and the local and global analyses show the calculated optima are indeed the global minima in fitting error.

Regarding fitting parameter error, common statistical practice is to define the fitting parameter variances as the diagonal elements of the covariance matrix (i.e., the inverse of the Hessian matrix).[108–112] Although, the covariance matrix is very time-intensive to compute from our sensitivity analyses for this system due to the long runtimes of objective function evaluations. Specifically, each evaluation requires multiple seconds for steady-state simulations (SimSS) and up to multiple minutes for transient simulations (ZimT). Similarly, Bayesian optimization routines utilize posterior probability distributions of fitting parameters for fitting, and these distributions possess corresponding covariance matrices. Although, fitting errors are insufficiently low following Bayesian optimization to invalidate fitting parameter errors calculated from these distributions. Thus, we use the covariance matrices returned by the final Python-based NLLSQ routine. Additionally, we calculate moving averages of all parameters over degradation time (see Section 2.2.10.2), and their standard deviations accurately estimate for fitting parameter errors. As for all error evaluations, estimation of fitting parameter error is important for scientific responsibility, quantifying the accuracy of results, and providing insights into causes of downstream error. Although, random error in drift-diffusion fitting parameters is especially important because their volatility is large and is the primary source of error for every downstream analysis of these parameters.

2.2.6 Global, Local, and Differential Sensitivity Analyses

In global, local, and differential sensitivity analyses, we vary single fitting parameters about their optimum values, simulate the corresponding current-voltage (J-V) scans, and calculate the corresponding fitting errors and solar cell parameters. Additionally, when varying drift-diffusion model fitting parameters, we also fit the simulated J-V curves with the non-ideal diode model to quantify the sensitivity (and influences, see Section 2.2.7) of diode parameters to the drift-diffusion fitting parameters. Regarding variation ranges, we vary fitting parameters by $\pm 0.1\%$ and 10% for differential and local analyses (centered about the calculated optimum) and by 100% (i.e., the entire range) for global analyses (see Section 6). Additionally, for differential sensitivity analyses, we calculate the first and second derivatives of all outputs (i.e., fitting error, solar cell and diode parameters) with respect to each fitting parameter using finite difference methods. These analyses enable verification of optimal fitting (i.e., achievement of global minima), enable visualization of fitting error landscapes for each parameter, and quantify the general importance of each fitting parameter to device characteristics through the fitting error's second-order sensitivity coefficients. Additionally, these sensitivity coefficients provide a semi-quantitative evaluation of the random error in the corresponding fitting parameters by enabling determination of the Hessian and thus covariance matrices, the diagonal elements of which are the variances in fitting parameters.[108–112]

2.2.7 Cumulative Sensitivity Analysis (CSA)

Although, the evolutions of parameters and their correlations over time do not quantify the exact influences of parameters on device performance. Thus, in a novel approach we term a cumulative sensitivity analysis (CSA) (not to be confused with time-dependent sensitivity analysis (TDSA) or global sensitivity analysis (GSA)),[58–62] we calculate the exact influence of each fitting

parameter on each solar cell parameter over time, quantifying the exact influence of each degradation mechanism on device performance. First, we perform a standard sensitivity analysis (see Section 2.2.6 and Section 6) to obtain the first derivatives of each solar cell parameter with respect to each fitting parameter over time. Then, recognizing the product of each such derivative and the corresponding fitting parameter's first time derivative is the time rate at which a given fitting parameter influences a given solar cell parameter, we integrate all such products over time to calculate the influence of each fitting parameter on each solar cell parameter over time. Specifically, the change $(\Delta Y)_{X_i}$ in a solar cell parameter (Y) caused by a change (ΔX_i) in a fitting parameter X_i between initial (t_i) and final (t_f) times is

$$\Delta Y_{X_i} = \int_{t_i}^{t_f} \frac{\partial Y}{\partial X_i} \frac{dX_i}{dt} dt$$

Additionally, by the definition of the total derivative, the total change (ΔY) in Y is simply the sum of the changes $(\{\Delta Y_{X_i}\})$ caused by the fitting parameters $(\{X_i\})$, given by

$$\Delta Y = \sum_i \int_{t_i}^{t_f} \frac{\partial Y}{\partial X_i} \frac{dX_i}{dt} dt$$

A full derivation of these expressions, a multiplication-based version, and an analytical derivation of the influences of J_{sc}, V_{oc}, and FF on PCE using the product-based variation of this analysis (i.e., the Volterra product integral of the logarithmic derivatives of these influences)[113–115] is provided in Section 8.1.4: Appendix A.4. Although we do not utilize this product-based variation, its production of proportionalities of PCE to J_{sc}, V_{oc}, and FF demonstrates the theoretical robustness of this analysis (see Section 8.1.4.2: Appendix A.4.2).

Regarding computational implementation, we linearly interpolate the sensitivity coefficients (for the drift-diffusion fitting parameters only) and the fitting parameters' first time derivatives, calculate their product over time, and numerically integrate from time zero to a variable time. For integration methods, we utilize the most accurate method with greatest robustness to parameter volatility: adaptive quadrature.[72–76] Since the non-ideal diode model is expressed analytically, we numerically calculate the exact sensitivity coefficients corresponding to the interpolated fitting parameters, eliminating the error of interpolating sensitivity coefficients. Such errors can be quite large when sensitivity coefficients exhibit high concavity with respect to fitting parameters, especially when fitting parameter values cross out of or into a region of near-zero sensitivity (e.g., shunt resistance drops sufficiently low to cause J_{sc} and FF loss).

2.2.8 Derived Drift-Diffusion Parameters

The drift-diffusion fitting parameters are bulk and interfacial electronic properties of the device layers, and they may thus be used to derive (see Section 6) many related properties (see Table 12). In addition to these parameters, the simulated drift-diffusion variables (see Table 9) and simulated current densities (see Table 10) provide a complete electronic description of the device when simulated with the final drift-diffusion fitting parameters. Moreover, we use these simulated current densities to calculate and plot the fractions of current loss (i.e., the ratios of current losses to the difference in photogenerated current (J_{photo}) and J_{MPP}) caused by each loss mechanism over time (see Section 6). These fractional current losses estimate the relative importances of each loss mechanism to device performance, and their evolutions over time

constitute yet another method for quantifying the influences of degradation mechanisms on performance decline. Note that we calculate many of these quantities at each illumination intensity, and we calculate many versions of the ambipolar quantities using different methods for aggregating over the corresponding charge-specific quantities. Additionally, since the drift-diffusion variables vary with position along the simulation thickness, we utilize their spatial averages when deriving parameters from their values. Last, all recombination rate constants are derived by reciprocating their corresponding carrier lifetimes.[33] As for all parameter sets, these derived drift-diffusion parameters provide additional insights into the influences of HP film degradation on device performance. Although, they are also measurable properties of HP films (e.g., ΔE_F and L_d by SSPL and steady-state photoconductivity, respectively),[18,30,31] meaning they are potential objective functions for drift-diffusion modeling of HP films.[116]

Table 12. Derived Drift-Diffusion Parameters – Names, Symbols, and Units

Name	Symbol	Unit
Quasi-Fermi Level Splitting (QFLS)	ΔE_F	$[eV]$
Area-Normalized Bulk Deep defect (trap) density	$N_{tr,bulk}$	$[m^{-2}]$
Total Area-Normalized Deep defect (trap) density	N_{tr}	$[m^{-2}]$
Geometric Mean of the Electron Concentration in the Absorber Layer (AL)	$\overline{n_{AL}}$	$[m^{-3}]$
Geometric Mean of the Hole Concentration in the Absorber Layer (AL)	$\overline{p_{AL}}$	$[m^{-3}]$
Intrinsic Carrier Concentration in the Absorber Layer (AL)	$n_{i,AL}$	$[m^{-3}]$
Ambipolar Ion Concentration	C_{ions}	$[m^{-3}]$
Ambipolar Ion Mobility	μ_{ions}	$[m^2V^{-1}s^{-1}]$
Shockley-Read-Hall (SRH) Electron Recombination Rate	$R_{SRH,n}$	$[m^{-3}s^{-1}]$
Shockley-Read-Hall (SRH) Hole Recombination Rate	$R_{SRH,p}$	$[m^{-3}s^{-1}]$
Mean Electron Quasi-Fermi Level in the Absorber Layer (AL)	$E_{Fn,AL}$	$[eV]$
Mean Hole Quasi-Fermi Level in the Absorber Layer (AL)	$E_{Fp,AL}$	$[eV]$
Ambipolar Carrier Mobility	μ_{np}	$[m^2V^{-1}s^{-1}]$
Minimum Carrier Mobility	μ_{min}	$[m^2V^{-1}s^{-1}]$
Electron Diffusion Coefficient	D_n	$[m^2s^{-1}]$

Name	Symbol	Unit
Hole Diffusion Coefficient	D_p	$[m^2 s^{-1}]$
Ambipolar Diffusion Coefficient	D_{np}	$[m^2 s^{-1}]$
Bimolecular Electron Recombination Lifetime	$\tau_{bi,n}$	$[s]$
Bimolecular Hole Recombination Lifetime	$\tau_{bi,p}$	$[s]$
Ambipolar Bimolecular Recombination Lifetime	τ_{bi}	$[s]$
Bulk Shockley-Read-Hall (SRH) Electron Recombination Lifetime	$\tau_{bulk,SRH,n}$	$[s]$
Bulk Shockley-Read-Hall (SRH) Hole Recombination Lifetime	$\tau_{bulk,SRH,p}$	$[s]$
Ambipolar Bulk Shockley-Read-Hall (SRH) Recombination Lifetime	$\tau_{bulk,SRH}$	$[s]$
Bulk Electron Recombination Lifetime	$\tau_{bulk,n}$	$[s]$
Bulk Hole Recombination Lifetime	$\tau_{bulk,p}$	$[s]$
Ambipolar Bulk Recombination Lifetime	τ_{bulk}	$[s]$
Shockley-Read-Hall (SRH) Electron Surface Recombination Velocity	$S_{SRH,n}$	$[ms^{-1}]$
Shockley-Read-Hall (SRH) Hole Surface Recombination Velocity	$S_{SRH,p}$	$[ms^{-1}]$
Ambipolar Shockley-Read-Hall (SRH) Surface Recombination Velocity	S_{SRH}	$[ms^{-1}]$
Shockley-Read-Hall (SRH) Electron Surface Recombination Lifetime	$\tau_{SRH,surf,n}$	$[s]$
Shockley-Read-Hall (SRH) Hole Surface Recombination Lifetime	$\tau_{SRH,surf,p}$	$[s]$
Ambipolar Shockley-Read-Hall (SRH) Surface Recombination Lifetime	$\tau_{SRH,surf}$	$[s]$
Shockley-Read-Hall (SRH) Electron Recombination Lifetime	$\tau_{SRH,n}$	$[s]$
Shockley-Read-Hall (SRH) Hole Recombination Lifetime	$\tau_{SRH,p}$	$[s]$
Ambipolar Shockley-Read-Hall (SRH) Recombination Lifetime	τ_{SRH}	$[s]$
Effective Electron Recombination Lifetime	τ_n	$[s]$

Name	Symbol	Unit
Effective Hole Recombination Lifetime	τ_p	$[s]$
Ambipolar Effective Recombination Lifetime	τ	$[s]$
Electron Diffusion Length	$L_{D,n}$	$[m]$
Hole Diffusion Length	$L_{D,p}$	$[m]$
Ambipolar Diffusion Length	L_D	$[m]$
Conductivity	σ	$[Sm^{-1}]$
Internal Quantum Efficiency	η_{int}	[%]

2.2.9 Effective Degradation Profile Model

This drift-diffusion modeling of degrading devices to obtain changes in the effective drift-diffusion parameters is informative, but a complete drift-diffusion model of device performance decline would simulate device performance from degradation profiles (i.e., the distribution of degraded products among interfaces, grain boundaries, and crystal bulk). Although, the opaque back-side transport and electrode layers prevent the absorbance measurements used in our previous studies, and we do not perform advanced measurements or simulations to determine degradation profiles over time. Thus, we calculate effective active and degraded HP film areas and thicknesses in a novel approach combining observations from dark-field (DF) microscopy and current-voltage (J-V) scanning.

Specifically, the dark-field (DF) intensity is sensitive to reflectance changes caused by surface roughening or spatial variation in refractive index, both of which occur during HP film decomposition.[17,18] Additionally, the steady-state photoluminescence (SSPL) intensity is sensitive to changes in recombination processes, which also evolve during degradation.[17,18,30,31] This SSPL intensity may be used to directly calculate the photoluminescence quantum yield (PLQY, Φ_{PL}) and, using the method from our previous studies,[17,18,30,31] to calculate the quasi-Fermi level splitting (QFLS, ΔE_F). Thus, changes in DF and PL intensity indicate regions affected by HP film degradation. Although, DF microscopy is primarily sensitive to surface reflectance changes on the device's transparent side (i.e., at the HP-HTL interface for our p-i-n devices), meaning degradation of the HP film thickness caused by photooxidation with gaseous reactants diffusing through the back-side electrode and ETL is not detected until the gaseous reactants reach the HP-HTL interface. Instead, only area extinction caused by photooxidation from the device sides is observed in DF microscopy at early times, and this is because gaseous reactants at the device edges are contacting and thus degrading the entire HP film thickness. Coupled with the total material loss determined from photocurrent decline, this allows clear distinction between area extinction from the device sides and thickness extinction from the HP-ETL interface.

For undegraded devices, DF and PL intensity profiles are uniform and featureless (see Figure 12), indicating the HP films are indeed undegraded with uniform layer morphologies and devoid of macroscopic defects. Then, over degradation, we define the effective active and degraded areas as the device areas with insignificant and significant changes in dark-field (DF) intensity, respectively. Specifically, we define the effective active and degraded areas as the sum of pixel areas which exhibit insignificant ($\left|I_{DF} - I_{DF,avg,t=0}\right| < 2\sigma_{I_{DF}}$) and significant

($\left|I_{DF} - I_{DF,avg,t=0}\right| > 2\sigma_{I_{DF}}$) changes in dark-field (DF) intensity, from the initial average over the entire device area, respectively, where I_{DF} is the dark-field (DF) intensity from a given image pixel at a given time and $I_{DF,avg,t=0}$ and $\sigma_{I_{DF},t=0}$ are the average and standard deviation of the time-zero dark-field (DF) intensity over the entire device area. Next, we numerically solve the equation for the effective active HP film thickness using the calculated electron-hole pair generation rate (G_{ehp}) and an exponential (Beer-Lambert) absorption profile (see Section 8.1.2: Appendix A.2). This approach to calculating degraded thickness is very similar to our previous studies employing absorbance measurements.[16,18–21] Although, the average volumetric electron-hole pair generation rate determined from J_{sc} assuming perfect carrier extraction (i.e., $G_{ehp} \approx J_{sc}/qL_{act}$) is influenced by both active area and thickness extinction, meaning the true average volumetric electron-hole pair generation rate (G_{ehp}) is that obtained from J_{sc} multiplied by the ratio of initial ($A_{active,t=0}$) and current (A_{active}) active areas (see Section 8.1.2: Appendix A.2). The degraded HP film thickness ($L_{abs,deg}$) is then calculated by simply subtracting the remaining active thickness ($L_{abs,active}$) from the initial absorber thickness ($L_{abs,active}\big|_{t=0}$):

$$L_{abs,deg} = L_{abs,active}\big|_{t=0} - L_{abs,active}$$

Although, at later times, the DF intensities change over the entire device area (sometimes as widening spots) as gaseous reactants reach the HP-HTL interface and degrade it along with all remaining grains (see Figure 12).[17] This causes an apparent burn-in of effective active area despite the degradation occurring due to gaseous reactant diffusion through the back electrode and ETL. Thus, we linearly extrapolate the ongoing linear decline of effective active area due to inward degradation of the active area border by linear regression of the 20 points before the beginning of burn-in (defined as the time when the effective active area's time derivative rises by 3.5 standard deviations[70,71] from its initial value) (see Section 8.2.1: Appendix B.1). This causes the effective active thickness to continue declining steadily instead of plateauing upon the apparent burn-in of effective active area. Furthermore, this steady, roughly linear decline implies steady diffusion of gaseous reactants, meaning the exponential-like burn-in behavior of J_{sc} at late times is likely caused by the exponential dependence of film absorptivity on film thickness by the Beer-Lambert law (see Section 8.1.1: Appendix A.1).

Last, we calculate the corresponding fractional quantities relative to their time-zero values, and we plot all considered parameters versus these fractional quantities on filled contour plots to ascertain general, dimensionless relationships between device properties and the effective extents of area and thickness degradation. These effective degradation profile parameters constitute an initial model of degradation profile from experimental data, and their relationships with other parameters over degradation further illuminate mechanisms of device performance decline. They also serve as features in our predictive models of operational lifetime and, furthermore, would enable development of a fully computational model which simulates the evolution of device properties and thus performance during degradation using only undegraded device properties and degradation conditions as inputs (see Section 4.2.2.1.2). This fully computational model would accurately predict operational lifetimes and could thus be used to optimize device design to maximize operational lifetimes without experiments.

2.2.10 General Parameter Transformations

The following transformations are applied to all parameters over degradation time to generate transformed versions of each parameter for both improved analysis of parameter evolutions over time and to serve as additional features for our predictive models of operational lifetimes.

2.2.10.1 Normalization to Time-Zero Values

Parameters are normalized to their initial (time-zero) values to enable comparison across all degradation conditions and architectures by removing random volatility in their time-zero values. Mathematically, this normalization is given by

$$X_{frac} = \frac{X}{X_{t=0}}$$

where X_{frac} is the fractional parameter value, X is the parameter value, and $X_{t=0}$ is the initial parameter value.

2.2.10.2 Moving Averaging

We calculate moving averages by averaging among 0, 5, 10, 15, 20, and 25 points on each side of a given data point. When the considered data point is within the chosen number of points from the first or last measurement, all points between the current data point and the measurement boundary are utilized. Despite including less than the specified number of points in these cases, the parameter's evolution over degradation time is still well-captured by the included points on the unconstrained side. Nevertheless, this error must still be considered. Additionally, since we use moving averages as features in our predictive models, varying the number of points allows us to identify a number of points which optimizes predictive models by optimally reducing volatility while maintaining accuracy (see Section 2.2.12.3.1). Mathematically, the moving average ($\tilde{X}_n$) is

$$\tilde{X}_n = \frac{1}{n}\sum_{j=j_0}^{j=j_f} X|_{t=t_j}$$

$$j_0 = \begin{cases} 0, & i < \left\lfloor \frac{n}{2} \right\rfloor \\ i - \left\lfloor \frac{n}{2} \right\rfloor, & i \geq \left\lfloor \frac{n}{2} \right\rfloor \end{cases}, \qquad j_f = \begin{cases} i + \left\lfloor \frac{n}{2} \right\rfloor, & i \leq N - \left\lfloor \frac{n}{2} \right\rfloor \\ N, & i > N - \left\lfloor \frac{n}{2} \right\rfloor \end{cases}$$

where n is the number of points considered in the moving average, i is the index of the current time point, j is index of the time point considered in the summation, and N is the total number of measurement cycles for the considered experiment.

We utilize moving averages to dampen volatility in drift-diffusion-related parameters and provide powerful features in predictive ML modeling. Specifically, as discussed in Section 3.1 and 4.1.3.5, drift-diffusion-related parameters exhibit moderate volatility over degradation time. Alongside fitting error and correlations among fitting parameters, fitting parameter volatility is primarily due to insufficient sensitivity of fitting parameters to changes in experimental data, or conversely, insufficient information in experimental data to yield high precision in fitting parameters. Moving averages reduce this volatility, enabling use of drift-diffusion-related parameters in all other analyses, enabling visualization of long-term systematic changes over time, and providing an improved measure of parameter volatility with their standard deviations.

Additionally, they are powerful features in our predictive ML models, useful for their ability to dampen sharp changes (including, but not limited to, volatility) which hinder the linear model while maintaining accuracy.

2.2.10.3 Differentiation by Polynomial Fitting

We calculate first and second derivatives of parameters over time to visualize parameters' rates of change over time and to provide additional features to our predictive models. Although, as discussed in Section 2.2.10.3, since even slight volatility can cause very large changes in derivatives calculated by finite difference methods, we differentiate parameters at all time points by fitting linear and quadratic polynomials (see Section 6) to the 0, 5, 10, 15, 20, and 25 points on each side of a given data point. Again, varying the number of points allows us to identify a number of points which yields optimal predictive models by optimally reducing volatility while maintaining accuracy. Additionally, this optimal number provides an estimate for the required number of measurement points to enable accurate differentiation of each parameter set.

2.2.11 Arrhenius Modeling of Parameter Evolutions over Degradation

Traditionally, Arrhenius modeling is performed by linear regression of the natural logarithm of a rate quantity versus absolute temperature with the Arrhenius equation, given by

$$r = Ae^{-\frac{E_a}{k_B T}} \rightarrow \ln(r) = \ln(A) - \frac{E_a}{k_B T}$$

where r is the effective rate for the parameter evolution, A is the pre-exponential frequency factor, E_a is the parameter evolution's effective activation energy, k_B is Boltzmann's constant, and T is temperature. Although, the first time derivatives of parameters vary with time, meaning their Arrhenius behavior evolves with time. Moreover, even small volatility in parameter evolutions can cause poor Arrhenius fits, especially for drift-diffusion-related parameters. Thus, in addition to traditional Arrhenius modeling versus the fraction of T_{80} (see Section 6), we employ another method used by other studies the Arrhenius behavior in degrading solar cells.[117] Specifically, we define the rate quantity as the reciprocal time for the parameter to reach a specified fraction of its initial value (e.g., 80%). For PCE decline, this rate is defined as the reciprocal of operational lifetime, yielding

$$r_{T_{80}} = Ae^{-\frac{E_a}{k_B T}} \rightarrow \ln\left(\frac{1}{T_{80}}\right) = \ln(A) - \frac{E_a}{k_B T}$$

where $r_{T_{80}}$ is the effective rate for the parameter evolution. This modified approach models the temperature dependence of parameter evolutions and thus their associated degradation pathways, illuminating which mechanisms are thermally activated (i.e., demonstrate a statistically significant temperature dependence) and their corresponding activation energies. These activation energies allow us to hypothesize the underlying processes by matching their reported activation energies with the fitted values. Additionally, similarities in activation energies among parameter evolutions indicate which parameters may share a primary degradation mechanism, providing insight into the nature of the mechanism (e.g., FF decline being linked to R_{sh} decline). This analysis thus provides further insights into the mechanisms of device performance decline. Additionally, the identified Arrhenius dependences of parameter evolutions match those identified in predictive ML model feature selection since temperature and temperature-dependent features are often not simultaneously selected. This is due to their primary influences on

operational lifetime occurring through the same set of thermally activated processes are primarily temperature-related. Statistical significance is classified by a p-value of less than 0.05 ($p < 0.05$). Sample plots of parameter evolutions over time for all experiments of a given temperature, along with comprehensive tables and boxplots of the Arrhenius fitting parameters for all architectures and parameter sets, will be provided in a future publication and in a future version of this thesis on our "DegradePV" GitHub repository (see Section 6).[63]

2.2.12 Predictive Modeling of Operational Lifetimes

As in our previous studies,[17,32] we utilize untransformed and transformed versions of the parameters considered in this study as features in predictive models of operational lifetime (T_{80}). These previous works considered the overall solar cell parameters (i.e., not specific to scan direction) at time zero, utilizing first-order and second-order time differentiation of parameters normalized to their time-zero values ($\frac{d(X/X_{t=0})}{dt}$ and $\frac{d^2(X/X_{t=0})}{dt^2}$, respectively) as the parameter transformation. This differentiation was performed by fitting linear and quadratic polynomials, respectively, to each parameter's first seven time points. In this study, we expand this work by constructing models using features from over degradation (not just from time zero) for all architectures, parameter sets, scan directions, and parameter transformation settings considered in this study. We also vary the predictive model specifications (i.e., model type and sparsity) and with and without atmospheric species concentrations and our kinetic rate law models[16,19–21] to develop models which do not depend on architecture-specific transport properties and composition, respectively. Then, we perform a rigorous analysis of model error, predictive ability, selected features, and selected feature coefficients versus each of these variables to optimize the predictive model, identify relationships among selected features, and quantify the importance of these selected features to operational lifetime. This section details our predictive modeling methodology.

2.2.12.1 Recommended Criteria for Predictive Models of Operational Lifetimes

To predict the goal operational lifetime of 30 years with experimental measurements collected over feasible periods (e.g., weeks or less), predictive models must extrapolate by a factor of at least ≈1000. This is done both by optimizing predictive models and enabling accelerated aging (i.e., accelerated degradation). Additionally, beyond predictive ability, the features on which the models depend are constraints to applications of the model. Specifically, including gaseous reactant concentrations as features causes the model to depend on device geometry, mass transport properties, and encapsulation scheme, requiring collection of new datasets for any changes in these variables. Thus, excluding these concentrations from the feature set generalizes the model to variations in these variables, and doing so would dramatically reduce data collection requirements and costs. Alternatively, predictive models may also be constructed from data for many device architectures, geometries, and encapsulation schemes to generalize over these variables. Although, accelerated aging models depend on these variables since degradation conditions are primary features in these models, requiring collection of datasets over the space of degradation conditions. Nevertheless, instead of requiring measurements through T_{80}, an unaccelerated predictive model may be used to extrapolate operational lifetimes from reasonable measurement periods for use in constructing this accelerated model.

Beyond feasible measurement times, degradation acceleration, and generalization over device transport properties, these models should not require expensive, low-throughput measurement and modeling techniques. Instead, inexpensive, high-throughput characterization

techniques should be utilized including current-voltage (J-V) scans and impedance spectroscopy. Moreover, models should not require our kinetic rate law models for material degradation[16,19–21] since, while informative, such models are time-intensive to develop and composition-specific, requiring new data collection and model construction for each unique HP composition. Nevertheless, our kinetic rate law models are invaluable in understanding HP decomposition mechanisms and kinetics and are another strong step toward long-lived device development. Moreover, predictive models must apply to stable, well-encapsulated, single or perovskite-silicon tandem modules with strong commercial relevance (e.g., with our $FA_{0.8}Cs_{0.2}Pb(I_{0.83}Br_{0.17})_3$ composition) under inert atmosphere, not just the unencapsulated devices and unstable compositions ($MAPbI_3$ and $FA_{0.75}Cs_{0.25}Pb_{0.5}Sn_{0.5}I_3$) presented in this study. Regarding accuracy and precision, acceptable ranges for model errors would be economics-dependent, but we suggest models ensure 30-year devices are ensured to exceed a 20-year operational lifetime with 95% certainty, corresponding to a mean-normalized root-mean-squared (RMS) error ($NRMSE_{mean-norm}$) of less than 6%.

In short, the recommended criteria for predictive models of operational lifetime are

- Feasible measurement periods (e.g., weeks or less for 30-year devices).
- Unaccelerated model generalized over gaseous reactant transport properties by either excluding gaseous reactant concentrations from the feature set or including data for many architectures, geometries, and encapsulations.
- Accelerated Aging (i.e., degradation acceleration) – boosts predictive ability.
- High-throughput, inexpensive techniques for device characterization (e.g., J-V scanning) and obtaining model-based features (e.g., not our kinetic rate law models).[16,19–21]
- Relevance – models must apply to devices with strong commercial potential.
- Accuracy and Precision – 30-year devices should be guaranteed to exceed a 20-year operational lifetime with 95% certainty, corresponding to $NRMSE_{mean-norm} \leq 6\%$.

These criteria are essential to the scalable use of these predictive models for the development of long-lived devices.

2.2.12.2 Predictive Ability Metrics

To evaluate the predictive abilities of these models, we define a prediction factor (F_{pred}) quantifying the factor by which models extrapolate experimental data to predict operational lifetimes (we recommend at least ≈1000 as discussed in Section 2.2.12.1). This prediction factor has two contributors: predictive ability for a given set of degradation conditions and accelerated aging. The unaccelerated extrapolation factor (UEF) quantifies the model's ability to predict a device's operational lifetime (T_{80}) in a given set of degradation conditions from measurements collected over the period required to achieve the desired accuracy (t_{meas}) in the same conditions, given by

$$UEF = \frac{T_{80}}{t_{meas}}$$

Additionally, the accelerated aging factor (AAF) is the ratio of a device's operational lifetime in operational conditions (T_{80}) to that in the harshest degradation conditions ($T_{80,accel}$) which may be used to predict the unaccelerated operational lifetime (T_{80}) utilizing only the degradation conditions as features. This quantifies the boost in predictive ability by degradation acceleration and is given by

$$AAF = \frac{T_{80}}{T_{80,accel}}$$

The maximum possible value for this factor (AAF_{max}) is the ratio of the device's operational lifetime (T_{80}) to the minimum operational lifetime ($T_{80,min}$) in maximally harsh degradation conditions, given by

$$AAF_{max} = \frac{T_{80}}{T_{80,min}}$$

Although, AAF may be much less than its maximum value if the model cannot accurately predict the device's lifetime from $T_{80,min}$ and the degradation conditions alone. In standard accelerated aging testing in numerous fields, the AAF is typically expressed by

$$AAF = Q_{10}^{T_{AA}-T_a}$$

where Q_{10} is the accelerated aging factor for each 10°C increase in temperature, T_{AA} is the accelerated aging temperature, and T_a is the ambient temperature.[118–120] For solar cells, accelerated aging models are often more complex and account for other degradation conditions (e.g., relative humidity).[118–123] As for the unaccelerated model, we utilize our predictive machine learning (ML) models since PSC degradation cannot be described by such empirical models based on standard mechanistic dependencies (e.g., Arrhenius dependence)[118–120] or mechanistic models based on standard extrapolations of parameters (see Section 6). Specifically, we construct our accelerated aging model by applying our predictive ML modeling workflow to our device degradation dataset with degradation conditions as the sole features, enabling conversion of operational lifetimes predicted by the unaccelerated model for devices undergoing accelerated aging to the true operational lifetime.

Together, these factors combine to form the overall prediction factor

$$F_{pred} = (UEF)(AAF) = \frac{T_{80}^2}{t_{meas}T_{80,unaccel}}$$

This framework enables maximization of the prediction factor within the precision constraint outlined in Section 2.2.12.1. The prediction factor thus serves as the objective function to maximize while the resulting component factors specify the required measurement time and the experiment to reference for the accelerated aging model. This framework serves as the foundation for development of future predictive models and thus long-lived devices.

2.2.12.3 Predictive Modeling Workflow

2.2.12.3.1 Workflow for the Unaccelerated Predictive Model

As stated above, we improve upon our previous predictive models[17,32] by constructing models using parameters from over degradation (not just from time zero) for all architectures, parameter sets, scan directions, and parameter transformation settings considered in this study. Specifically regarding degradation time, we construct models with parameters evaluated at or up to integer percentages of T_{80} (0, 1, 2 . . ., 10, 20, . . . 100), enabling us to determine how predictive model accuracy and parameters vary with the measurement time considered (normalized to T_{80}). Moreover, to develop models which do not depend on architecture-specific transport properties and composition, we construct models with and without atmospheric species concentrations and

our kinetic rate law models.[16,19–21] We term these variables the feature specifications (see Table 13).

For a given set of feature specifications, we construct the feature set as follows. For each experiment corresponding to the specified architecture, the time corresponding to the specified fraction of T_{80} for the experiment's T_{80} value is calculated, and the parameters corresponding to the specified parameter set, scan direction, and parameter transformation settings are then calculated at this time. This is done for all experiments corresponding to the specified architecture, and the resulting feature set is then utilized for predictive model optimization.

Table 13. Names and Possible Settings for Feature and Predictive Model Specifications

Name	Possible Settings
Device Architecture (i.e., HP composition since we consider one architecture per HP composition)	Low-bandgap, medium-bandgap ($MAPbI_3$), high-bandgap, overall (i.e., all architectures)
Measurement Time (in percentage of T_{80})	$0, 1, 2, \dots, 9$
Parameter Set*	Solar Cell Parameters
Current-Voltage (J-V) Scan Type**	Forward, Reverse, Hysteresis Loop
Drift-Diffusion Simulation Type	Steady-state (SimSS), transient (ZmiT)
Drift-Diffusion Fitting Routine	OptimPV, BOAR, AutoFit
Outlier Removal Boolean	True, False
Set of Degradation Conditions	$T\ [°C]$ only, all degradation conditions except the HP decomposition rate determined by our kinetic rate law model (r_{deg}), and all degradation conditions including r_{deg}
Machine Learning (ML) Model***	Standard linear regression (see Section 2.2.12.4.1) with orthogonal matching pursuit (OMP) feature selection
Model Sparsity (number of selected features)	$0, 1, 2, \dots, 20$

* The results for the diode parameters, drift-diffusion fitting parameters, derived drift-diffusion parameters, and degradation profile parameters will be reported in a future publication and on our "DegradePV" GitHub repository published online,[63] but we nevertheless order these parameter sets by accuracy in Section 3.2.1.

** The hysteresis loop scan type is only relevant for transient drift-diffusion simulations since the solar cell and diode parameters are specific to forward or reverse scan directions.

*** There are many variations of this standard linear regression model and feature selection method which include additional terms (e.g., penalizing excessive feature selection). In our group's recent work, Sunkari *et al.* compiled these models and developed the corresponding

programs, and we will publish the corresponding results in a future publication and on our "DegradePV" GitHub repository published online, see Section 6).[63]

Following construction of the feature set, for each set of predictive model specifications, we optimize the predictive model for the given feature set (see Section 3.2.1) and compare the set of predicted lifetimes with the experimental set on a parity plot. This is done on a logarithmic scale since T_{80} values span multiple orders of magnitude for the wide space of degradation conditions considered in this study. Additionally, the error in the predictive model appears to grow with operational lifetime on a linear scale while appearing uniform on a logarithmic scale (as shown by all parity plots in Section 3.2.1), meaning the logarithmic scale also enables consistent and reasonable error across a wide range of operational lifetimes. Moreover, since inaccurate features often cause a few experiments to exhibit unrealistic lifetime predictions, we perform standard outlier removal by classifying points which deviate from the parity line by more than 3.5 standard deviations as outliers.[70,71] This standard deviation is calculated based on the deviations of all remaining predicted values from their respective experimental values. This process is standard statistical practice[70,71] and results in occasional removal of single experiments which yield unrealistic predictions due to a combination of either outliers in measurement or poor modeling parameters, meaning its systematic error is minimal (see Section 4.1.8). Note that outlier removal is also performed on this logarithmic scale to prevent irresponsible removal of points which appear as outliers on a linear scale but not on a logarithmic scale.

For generality, we calculate many error metrics, but we utilize the mean-normalized RMS error ($NRMSE_{mean-norm}$) to calculate the corresponding confidence intervals in operational lifetime for a hypothetical 30-year device. The $NRMSE_{mean-norm}$ is expressed by

$$NRMSE_{mean-norm} = \frac{RMSE}{\overline{T_{80}}} = \frac{\sqrt{\frac{1}{n}\sum_i^n [(T_{80})_i - (T_{80})_i']^2}}{\overline{T_{80}}}$$

where $RMSE$ is the RMS error, $\overline{T_{80}}$ is the average operational lifetime among the considered degradation experiments, n is the number of considered degradation experiments, and $(T_{80})_i$ and $(T_{80})_i'$ are the experimental and predicted operational lifetimes for the ith degradation experiment, respectively. This is the RMS average of the standard deviation about the parity line normalized by the dataset mean, meaning if the range of possible T_{80} values is normally distributed about a given device's predicted T_{80} value, the 95% confidence interval limits are given by

$$T_{80,\pm} = 10^{(\log_{10} T_{80})(1 \pm 1.96 * NRMSE_{mean-norm})}$$

where the $\pm$ subscript represents the upper and lower bounds of the confidence interval, respectively, and the value 1.96 is the z-score corresponding to two standard deviations (1.96). Alternatively, this may written as

$$T_{80,\pm} \approx T_{80} * 91.2^{NRMSE_{mean-norm}}$$

With this NRMSE, we recommend calculating the corresponding confidence intervals of the predicted operational lifetimes since the confidence interval's lower limit is the key metric of interest for quantifying the accuracy and precision of predictive models.

With this framework, the predictive model is then optimized for the given feature set and predictive model specifications by repeating this process while varying the model's parameters (i.e., empirical coefficients) (if any) to minimize a chosen error metric. Specifically, mechanistic

(non-ML) models utilize standard optimization methods (e.g., nonlinear least squares regression (NLLSQ) for ours) whereas ML models are trained on the set of experimental operational lifetimes and feature set. This process is then repeated for all feature and predictive model specifications and the predictive model optimized over all permutations of these specifications to minimize a chosen error metric. Furthermore, with this expansive set of results, we perform a rigorous analysis of model error, selected features, and selected feature coefficients versus each of the feature and predictive model specifications to identify how error metrics and predictive model parameters change with these specifications, identify relationships among selected features, and quantify the importance of these selected features to operational lifetime. Additionally, since our machine learning (ML) models treat all features agnostically without recognizing relationships among them, we may also construct machine learning (ML) models with features corresponding to any combination of multiple specifications, meaning the passed feature table contains features calculated with each subset of the considered specifications. This enables further optimization by allowing selection of features with different specifications. Although, unlike feature specifications, ML model specifications are not used in constructing feature tables and thus cannot be given multiple settings. Additionally, increasing the number of potential features can reduce training quality, and consideration of all combinations of these multiple specifications adds great computational expense for very little improvement. Nevertheless, we do construct feature tables containing the operational lifetimes and features for all architectures to develop an overall model generalized over architectures and for all parameter sets to allow selection of features from multiple parameter sets. Indeed, the overall model exhibits strong accuracy and the use of multiple parameter sets further verifies the identified relationships among selected features. These are the only instances of multiple specifications we consider.

Regarding visualization, we construct boxplots (with scattered points) and histograms of error metrics and selected feature coefficients versus each of the feature and predictive model specifications, and we then plot the error metrics, selected feature coefficients, and operational lifetime confidence intervals corresponding to the optimal specifications on bar charts versus each specification. Note that for a given choice of error metric to optimize, the other error metrics are often higher than their optimum values, and the optimal feature and predictive model specifications slightly change. Indeed, the reported R^2 values for our $NRMSE_{mean-norm}$-optimized models are lower than the maximum R^2 values achieved. The results corresponding to optimization of error metrics other than the $NRMSE_{norm-mean}$ will be provided in a future publication and in a future version of this thesis on our "DegradePV" GitHub repository (see Section 6).[63] Last, since the maximum T_{80} value which may be accurately predicted by the model increases with T_{80} fraction, and since the extrapolation factor simultaneously decreases due to increased measurement time, we calculate the corresponding prediction factors and report the maximum value achieved. These optimized factors quantify our predictive model's maximum overall predictive ability.

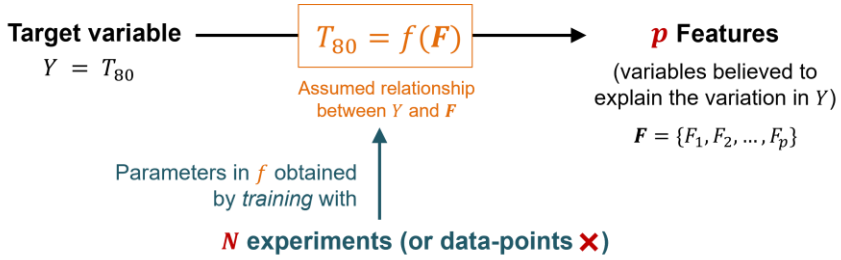

Figure 10. Schematic of the General Predictive Machine Learning (ML) Modeling Workflow.[124] The employed machine learning (ML) model (i.e., the assumed relationship between Y and $\boldsymbol{F}$) is trained on N device degradation experiments each with $\boldsymbol{p}$ features and an operational lifetime (T_{80}), which is the target variable.

2.2.12.3.2 Workflow for the Accelerated Aging Model

After optimizing the unaccelerated predictive model, predictive ability may be further extended by accelerated aging models. In standard accelerated aging testing, devices are degraded in harsh conditions to accelerate degradation and thus lower the measurement time required to reach T_{80}. Then, after reaching T_{80}, each operational lifetime and the corresponding degradation conditions are inserted into the accelerated aging model to predict the device's true lifetime in standard operating conditions. Although, to further reduce the required measurement time, we predict the T_{80} values for the devices degrading under accelerated aging using measurements only to the fraction of T_{80} necessary for accurate lifetime prediction. Specifically, we recommend estimating the fraction of T_{80} in real time with the unaccelerated model or with experimental or predicted values for devices degraded under similar conditions, followed by continuing the measurement until the corresponding fraction of T_{80} reaches the value required to achieve accurate T_{80} predictions.

Regarding construction of the accelerated aging model, standard accelerated aging models employ an Arrhenius term to model temperature dependence and potentially terms to model the influence of all other degradation inducers.[118–120] In contrast, we construct the accelerated aging model by applying the predictive ML modeling workflow to the device degradation dataset using only the degradation conditions and specific, physics-inspired transformations of them as features (including the terms in standard accelerated aging models). Thus, excluding degradation conditions from the predictive model may only be done for the unaccelerated model. Additionally, accelerated predictions are specific to the gaseous reactant transport properties of the devices, and they are subject to the inaccuracies of modeling the device degradation dataset with only degradation conditions. Again since the error is relatively uniform over the space of T_{80} values on a logarithmic scale for the accelerated aging model as well, the NRMSEs of the unaccelerated and accelerated models yield the combined NRMSE

$$NRMSE_{mean-norm} = \sqrt{(NRMSE_{mean-norm})^2_{unaccel} + (NRMSE_{mean-norm})^2_{accel}}$$

where the "unaccel" and "accel" subscripts denote the errors for the unaccelerated and accelerated models, respectively. As for the unaccelerated model, the error grows with operational lifetime on a linear scale but appears uniform on a logarithmic scale, again justifying use of a logarithmic scale. Last, to calculate the confidence intervals of operational lifetimes predicted with the accelerated aging model, this combined error should be employed.

Overall, as for all accelerated aging models, this allows translation among T_{80} values over varying degradation conditions and thus extension of the prediction factor. Although, our use of T_{80} values predicted by the unaccelerated model in constructing the accelerated aging model further extends the prediction factor, and as for the unaccelerated model, the application of our predictive ML modeling workflow enables improved modeling of the complex influences of degradation conditions in PSC degradation not attainable with traditional accelerated aging models.

2.2.12.3.3 Additional Details for Feature and Predictive Model Specifications

2.2.12.3.3.1 Parameter Sets

In our previous study, we constructed models with the solar cell parameters, and we now do so for each parameter set developed in this study, classified into the following groups: the solar cell parameters, non-ideal diode fitting parameters, non-ideal diode fitting parameters' influences on solar cell parameters, drift-diffusion fitting parameters, drift-diffusion fitting parameters' influences on solar cell parameters, derived drift-diffusion parameters, and degradation profile parameters. We also construct a model containing all parameter sets to improve model accuracy and determine which parameter sets should be prioritized in future predictive models. These new parameter sets provide additional features with which to improve model accuracy and enable us to identify correlations among selected features and their coefficients. Indeed, the results match those obtained in our cumulative sensitivity analysis (CSA).

2.2.12.3.3.2 Degradation Conditions

Considered degradation conditions include temperature (T), oxygen partial pressure or concentration (P_{O_2} or C_{O_2}), water vapor partial pressure (P_{H_2O}) (or equivalently, concentration (C_{H_2O}) or relative humidity (RH)), and AM1.5G illumination intensity (I_{in}). Additionally, we also consider the material degradation rate (r_{deg}) predicted by our kinetic rate law models for each composition.[16,19,20] Our previous ML model considered all degradation conditions and r_{deg},[17] but as discussed in Section 2.2.12 and 3.2.1, it is favorable to exclude gaseous reactant concentrations and r_{deg} from the feature set. Thus, we consider the following combinations of these quantities in our ML models:

- All degradation conditions and the material degradation rate (r_{deg}) predicted by the kinetic rate law model: $T, C_{O_2}, RH, I_{in}, r_{deg}$
- All degradation conditions without r_{deg}: T, C_{O_2}, RH, I_{in}
- Non-chemical degradation conditions only: T, I_{in}

Naturally, excluding degradation conditions slightly reduces model accuracy since they are sometimes selected features, but in addition to generalizing the model to device geometries, mass transport properties, and encapsulation schemes, this exclusion illuminates the relative importances of degradation conditions to model accuracy and their relationships with J-V features. Additionally, although not considered in this study, iodine vapor ($I_{2(g)}$) also degrades HPs,[19] and its concentration should be included as a degradation condition in these predictive models and incorporated into our previous kinetic rate law models for our medium-bandgap ($MAPbI_3$) and high-bandgap ($FA_{0.8}Cs_{0.2}Pb(I_{0.83}Br_{0.17})_3$) materials[16,20,21] (as done by Meng *et al.*[19] for our low-bandgap ($FA_{0.75}Cs_{0.25}Pb_{0.5}Sn_{0.5}I_3$) material). Last, we degrade devices at their current maximum power point (MPP) voltage as in operating conditions, but the MPP voltage evolves differently among all degradation experiments, meaning these devices degrade under differing electrical biases. Indeed, varying bias in degradation experiments and including it as a feature would be useful for assessing its influence on device performance decline. Note that temperature is the only degradation condition valid for mechanistic models while all degradation conditions are valid for ML models.

2.2.12.4 Predictive Models

Regarding model types, we consider both machine learning (ML) and mechanistic (non-ML) models. Mechanistic models utilize classical predictive modeling techniques (e.g., polynomial extrapolation) without using machine learning (ML) (which is training-based), relying instead on theory-based relationships among parameters. Although, as is characteristic of HPs, many parameters vary nonlinearly due to many phenomena including early short-circuit current (J_{sc}) burn-in, deep defect (trap) reduction at interfaces and grain boundaries, and grain isolation (see Section 3.1 and Figure 36). Additionally, phenomena such as early-time deep defect (trap) can cause PCE to increase at early times, causing initial linear extrapolations to predict indefinite PCE increase. To address this, machine learning (ML) methods agnostically treat parameters as features in training an ML model, removing the assumption of polynomial behavior, neglecting relationships among parameters, and enabling higher accuracy and shorter measurement periods even with early-time PCE increases and other nonlinear parameter evolutions. Although, many parameters exhibit relatively linear behavior for our devices at moderate and late degradation times after the early-time nonlinear behavior (but before the late-time burn-in of the short-circuit current density (J_{sc})), and many publications studying PSC degradation report smooth, monotonically decreasing solar cell parameters for stable (and possibly encapsulated) devices. This would likely improve the performance of both model types and allow mechanistic (non-ML) models to yield similar accuracy at early times (as opposed to our scaled polynomial extrapolation model, see Section 6),[63] lending both model types even stronger potential.

2.2.12.4.1 Small-Dataset Machine Learning (ML) – Leave-One-Out (LOO) Linear Regression

Traditional machine learning (ML) models typically employ neural networks, but such models require datasets much larger than the number of selected features (e.g., by a factor of ten according to Hastie *et al.*[125] as cited by Sunkari *et al.* in his PhD thesis).[32] Specifically, our models typically consider a set of ≈50-100 features, and use of neural networks would thus require more than ≈500-1000 degradation experiments to accurately resolve each feature. Moreover, with each device fabrication cycle requiring ≈ 11 hours, constructing such a traditional machine learning (ML) model would require ≈1.25 years to collect the necessary data. Additionally, this data would be specific to the device geometry, mass transport properties, and encapsulation scheme. To address these issues, we instead utilize specialized leave-one-out (LOO) linear regression models developed specifically for small-dataset machine learning (ML). Sunkari *et al.*[32] developed such models to enable a data-feature ratio as low as ≈10, and with 37-61 degradation experiments for each architecture, we may reliably construct models with 3-6 features. Although, note that our dataset sizes are at or near the lower limit of this recommended ratio, and expansion of the utilized datasets would both increase model accuracy and enable ML methods which require larger datasets (e.g., neural networks).

The base model is a standard linear regression of operational lifetimes on a natural logarithm scale and with features centered on their means and normalized by their standard deviations:

$$\ln(T_{80}) = c + \sum_i \beta_i \frac{x_i - \bar{x_i}}{\sigma_{x_i}}$$

where c is the vertical axis intercept (i.e., the $\ln(T_{80})$ value when all features assume their mean values), β_i is the feature coefficient for the ith feature, x_i is the ith feature's value in a given experiment, and $\bar{x}_i$ and σ_{x_i} are the average and standard deviation of the ith feature over the considered experiments. With features normalized to their standard deviations, these feature

coefficients are dimensionless numbers quantifying the importance of a feature to operational lifetime. Moreover, operational lifetimes are modeled on a logarithmic scale since operational lifetimes (T_{80}) span multiple orders of magnitude for the various degradation conditions and architectures tested in our experiments. There are many variations of this base model which include additional terms (e.g., penalizing excessive feature selection), and in our group's recent work, Sunkari *et al.* compiled these models and developed the programs we utilize in this study (an analysis of how results vary with modeling method[32] will be provided in a future publication and in a future version of this thesis on our "DegradePV" GitHub repository (see Section 6)).[63]

To implement this model, we utilize a leave-one-out (LOO) training procedure to predict operational lifetimes. Specifically, for each experiment, we remove the experiment (i.e., the test point) from the feature table and train the ML model (using the "sklearn" package in Python) on the remaining experiments' operational lifetimes and feature values (i.e., the training set) to predict the removed experiment's operational lifetime, yielding a corresponding set of feature coefficients. This training process is similar fitting a regression model by varying the coefficients to minimize an error metric using standard optimization routines (e.g., NLLSQ). Then, over all experiments, we compute the averages and standard deviations of the feature coefficients and report only those with averages at least one standard deviation from zero (i.e., the error bars do not cross the horizontal axis). Nevertheless, it is still worthwhile to consider the values and relative order of selected features within one standard deviation from zero, and we will therefore provide equivalent bar charts on our "DegradePV" GitHub repository (see Section 6).[63] For a full description of our original ML model types (including their loss functions) and pseudocode for the LOO workflow, see the Supporting Information (SI) of our $MAPbI_3$ device degradation study. Moreover, for a comprehensive description of all ML modeling methods considered in this study, see Sunkari *et al.*'s thesis[32] and future publication.

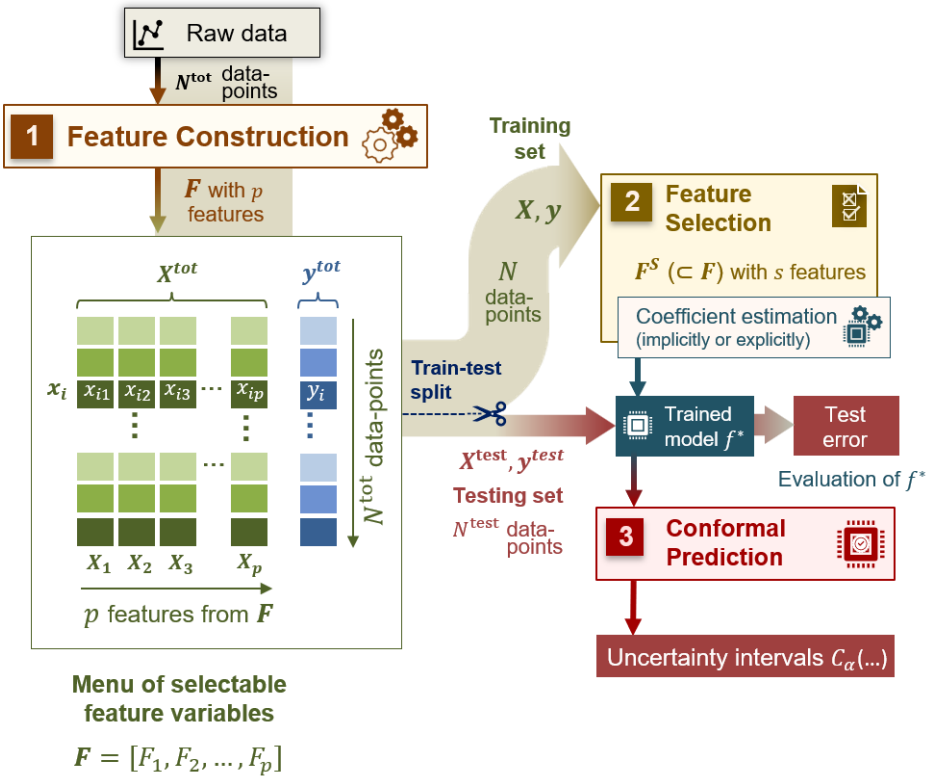

Figure 11. Schematic of Leave-One-Out (LOO) Machine Learning (ML) Modeling Workflow. (1) A set $\boldsymbol{F}$ of p feature values and corresponding operational lifetime (T_{80}) are collected into a feature table for each of the N_{tot} device degradation experiments to form the feature dataset ($\boldsymbol{X_{tot}}$) and operational lifetime dataset (y_{tot}). Then, (2) the operational lifetime (y_{test}) and corresponding feature values ($\boldsymbol{X_{test}}$) for a single experiment (i.e., the testing set) are removed from the feature table and used to train the ML model on the remaining experiments' operational lifetimes (y_{train}) and feature values ($\boldsymbol{X_{train}}$) (i.e., the training set) to predict the removed experiment's operational lifetime, yielding a corresponding test error and set of selected features ($\boldsymbol{F^S}$) and their coefficients. This is repeated for all N_{tot} device degradation experiments to yield an overall error metric and averages and standard deviations for the selected feature coefficients.[124]

2.2.12.5 Summary of Methodology for Predictive Modeling of Operational Lifetimes

We establish a machine-learning (ML) and mechanistic (non-ML) modeling workflow to predict operational lifetimes of degrading PSCs using the empirical and fitted parameters determined from our degrading device time-series data. Building upon our previous ML model, we construct both ML and mechanistic (non-ML) models for each combination of architectures, parameter sets, J-V scan directions, parameter transformations, and predictive model specifications. We also construct models which exclude atmospheric species concentrations and our previous kinetic rate law models to generalize models over device geometries, mass transport properties, and encapsulation schemes, and we establish criteria for accuracy, generalizability, and feasibility. Finally, we perform a rigorous analysis of model error, predictive ability, selected features, and selected feature coefficients over these variables to optimize the predictive model, quantify the importance of the selected features, and identify relationships among them.

3 RESULTS

3.1 Mechanistic Modeling

3.1.1 Dark-Field (DF) Microscopy and the One-Dimensional (1D) Effective Degradation Profile Model

For undegraded devices, DF and SSPL intensity profiles are uniform and featureless (see Figure 12), indicating the HP films are indeed undegraded with uniform layer morphologies and devoid of macroscopic defects. Then, for $MAPbI_3$ devices at early times, DF intensity increases at and outside the contact perimeter as gaseous reactants degrade the exposed perovskite surrounding the cell (i.e., no ETL or back electrode due to evaporation masking). During this time, the effective active area may remain briefly constant (see Figure 12) as gaseous reactants must degrade and diffuse downward through the surrounding perovskite before degrading active area (see Figure 13). Although, once this is done, gaseous reactants then steadily diffuse through degraded perovskite at the device edges to degrade the outermost surface of undegraded perovskite along its entire thickness, leading to a linear decline in active area for the remainder of degradation in $MAPbI_3$ devices. This is indicated by the steady ingress of increased DF intensity and decreased PL intensity from the device edges. Moreover, the DF intensity at the active area border rapidly increases and plateaus while the PL intensity rapidly increases, decreases, and plateaus when affected,[17] indicating rapid and full degradation of the entire HP film thickness at the active area border. Although, no significant changes in DF intensity are observed for our high-bandgap devices, meaning there are also no significant changes observed for the effective active area. Additionally, we do not consider DF and SSPL imaging for the low-bandgap architecture, but this is recommended in future work.

Meanwhile, the PL intensity increases rapidly and uniformly over the device area for all architectures,[16] implying gaseous reactants readily diffuse through the back electrode and ETL to degrade the HP-ETL interface and nearby grain boundaries. Although, no significant changes in DF intensity are observed in the device interior as gaseous reactants have not yet diffused to the HP-HTL interface. This yields a steady decline in the effective active perovskite thickness (see Figure 12). Last, at later times, the DF intensities change over the entire device area (sometimes as widening spots) as gaseous reactants reach the HP-HTL interface and degrade it along with all remaining grains (see Figure 12). After some time, the PL intensity then decreases and plateaus as the remaining grains are extinguished, again suggesting gaseous reactants diffuse along grain boundaries and degrade the HP-HTL interface prior to full extinction of the HP film, meaning the remaining undegraded perovskite exists as isolated grains. These observations are obtained both in this study, our previous device degradation study,[17] and our previous studies on HP film degradation.[16,18–21,30,31] This causes an apparent burn-in of effective active area despite the degradation occurring due to gaseous reactant diffusion through the back electrode and ETL. Thus, we linearly extrapolate the ongoing linear decline of effective active area due to inward degradation of the active area border by linear regression of the 20 points before the beginning of burn-in (defined as the time when the effective active area's time derivative rises by 3.5 standard deviations[70,71] from its initial value) (see Section 8.2.1: Appendix B.1). This causes the effective active thickness to continue declining steadily instead of plateauing upon the apparent burn-in of effective active area. This steady, roughly linear decline implies steady diffusion of gaseous reactants, meaning the exponential-like burn-in behavior of J_{sc} at late times is likely caused by the exponential dependence of film absorptivity on film thickness by the Beer-Lambert law (see Section 8.1.1: Appendix A.1). Additionally, the effective active thickness is almost always a

significant fraction of its initial value upon degradation of the HP-HTL interface over all experiments, again indicating gaseous reactant diffusion along grain boundaries. Although, the systematic error in the thickness calculation is high since the exponential attenuation law (i.e., Beer-Lambert law) does not account for optical interference effects, and such effects are especially present since the HP film thicknesses (≈300 nm) are well below the illuminating wavelengths (≈542 nm for $MAPbI_3$). Thus, we only consider thicknesses at early times, before J_{sc} and active area burn-in.

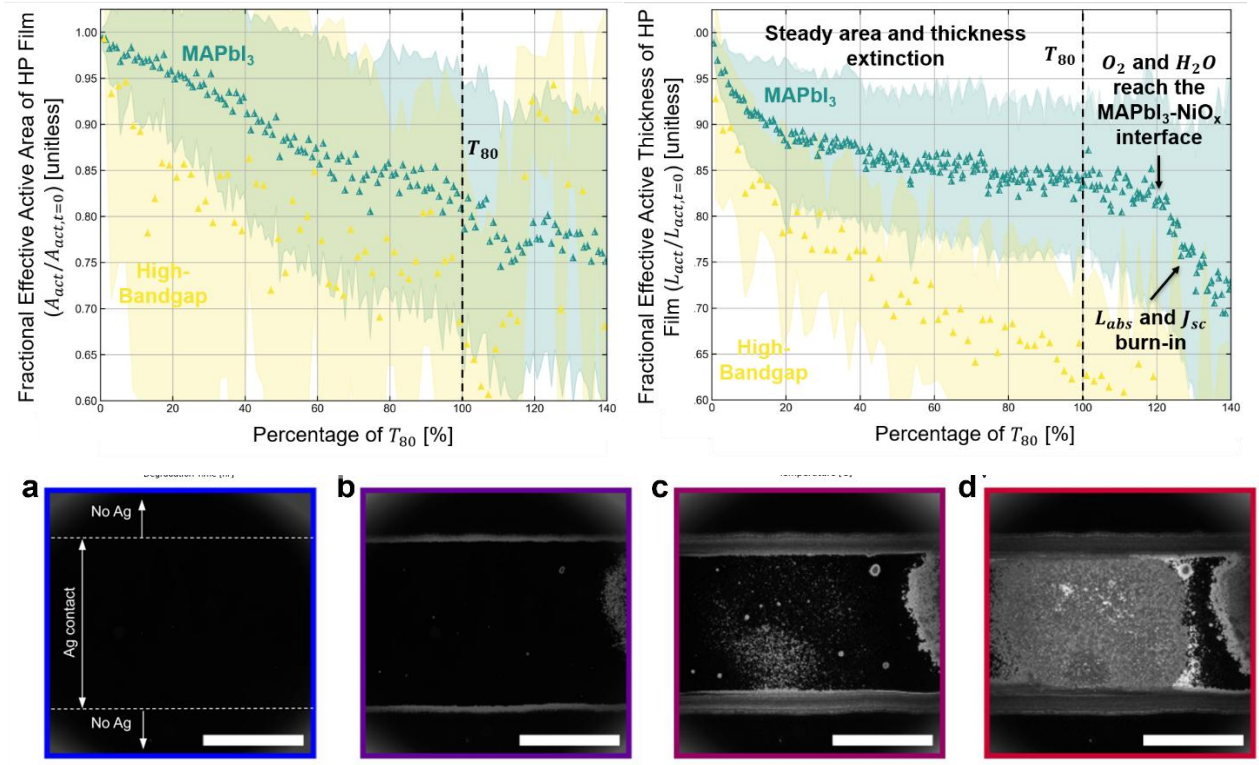

Figure 12. The Evolution of Dark-Field (DF) Microscopy Images and the Corresponding Effective Degradation Profile Parameters over Degradation. (top left and top right) Scatterplots of the averages (shown as points) and standard deviations (shown as faded regions) of the fractional effective active (top left) area and (top right) thickness of HP films in our devices over time (measured as a percentage of T_{80} for each device to enable comparison across all degradation conditions) for our medium-bandgap ($MAPbI_3$) (green) and high-bandgap (yellow) architectures degrading in the conditions outlined in Table 6 (encoded according to the grid legend in Figure 4). Important features of parameter evolutions are labeled with bolded text and arrows, and operational lifetime (T_{80}) is indicated by the labeled dashed black line at 100% of T_{80}.

Regarding differences among architectures, $MAPbI_3$ is known to be unstable to photooxidation relative to the more stable higher-bandgap HPs. Indeed, the fractional effective active area and thickness (and thus total material volume) decrease much more rapidly (and are therefore much lower by T_{80}) for $MAPbI_3$ devices than for our high-bandgap devices (see Figure 12). In combination with the J_{sc} decline behavior of these architectures (Figure 18(b)), we conclude perovskite compositions become increasingly unstable to photooxidation with lowering bandgap, causing the fractional effective degradation profile parameters at T_{80} to increase with bandgap and

an increasing portion of PCE loss to be attributable to loss mechanisms other than absorptivity loss (e.g., effective mobility decreases during grain isolation). This bandgap-based stability trend is observed in both our film[16,18–21,30,31] and device studies.[17] Additionally, the ratio of fractional effective area to thickness at T_{80} decreases with bandgap. Specifically, gaseous reactant diffusion is more rapid at the exposed device edges compared with the HP film thickness covered by the back electrode and ETL, and this exaggerates differences in area and thickness extinction for materials increasingly unstable to photooxidation (e.g., lowering bandgap). Nevertheless, despite these differences, the relationships among the solar cell, fitted, and derived parameters, degradation profile parameters, and DF and SSPL images are consistent across architectures, suggesting an improved postulated HP film degradation scheme in both films and devices as shown in Figure 13.

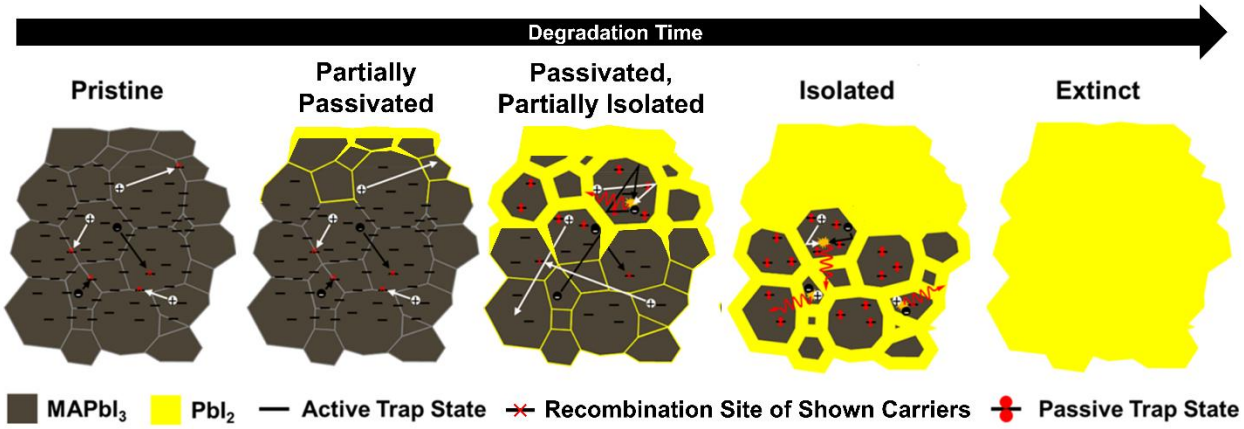

Figure 13. Postulated HP Film Degradation Scheme.[18] Gaseous reactants readily diffuse through the back electrode and ETL and into surface-exposed grain boundaries, photooxidizing both the grain boundaries and the HP-ETL interface. This slight degradation of interfaces and grain boundaries passivates the associated deep defect (trap) states (see Section 3.1.4), causing the observed steady, early-time decrease in the fitted HP-ETL interfacial deep defect (trap) density and the corresponding increase in fitted electron mobility, QFLS in SSPL images, and in V_{oc}, FF, and PCE. No significant changes are observed in DF intensity at this stage since the measured side (i.e., the HP-HTL interface) has not been degraded. Gaseous reactants then continue steadily diffusing through the back electrode, ETL, and degraded perovskite (especially along grain boundaries), shrinking isolated grains and degrading pristine grain boundaries as the gases penetrate deeper into the film. This causes simultaneous passivation of deep defects (traps) at newly degraded grain boundaries (toward the HTL) alongside carrier mobility losses (and thus increased SRH recombination) at the boundaries of isolated grains (toward the ETL). The result is local extrema in these V_{oc}-related and FF-related quantities as grain isolation begins to outweigh the initial passivation effects. Finally, near T_{80}, all grains become isolated as the gaseous reactants reach and degrade the HP-HTL interface (observed as a rapid, uniform increase in DF intensity over the device area), causing all of these quantities to plateau at roughly their original values. Deep defect (trap) densities and carrier mobilities are thus not significant drivers of PCE decline, further establishing HP film absorptivity loss (caused by its chemical decomposition) as the primary driver of performance decline.

This degradation scheme is specific to unencapsulated devices, but nevertheless, the causal relationships between solar cell, fitted, and derived parameters and measures of the degradation

profile (i.e., both the degradation profile parameters and the DF and SSPL images) demonstrate the utility of determining the degradation profile and mechanistically modeling the corresponding effects on device performance. Additionally, the plateau of many V_{oc}- and FF-related parameters near their original values further establishes HP film absorptivity loss (caused by its chemical decomposition) as the primary driver of PCE decline.

Although, in addition to studying how the fractional effective degradation profile parameters evolve over time for each architecture, we also study how they vary with degradation conditions. $MAPbI_3$ devices exhibit decreases in both the fractional effective active area and thickness with increasing temperature at low temperatures (i.e., 25°C to ≈45°C) followed by a sharp increase between 45°C and 55°C. Similarly, high-bandgap devices seem to exhibit local minima in these parameters around 40°C while values at 25°C and 55°C are similar to each other. There are many possible explanations for these results, but the similarity between the two parameters suggests these trends are caused by similar HP decomposition behavior at the HP-ETL interface and device edges, and the similarity across both architectures suggests this behavior is observed for both architectures. Moreover, the observed minimum near 40-45°C in both parameters at T_{80} for both architectures further suggests this common phenomenon, and the minimum suggests HP decomposition is influenced by two competing temperature-dependent processes.

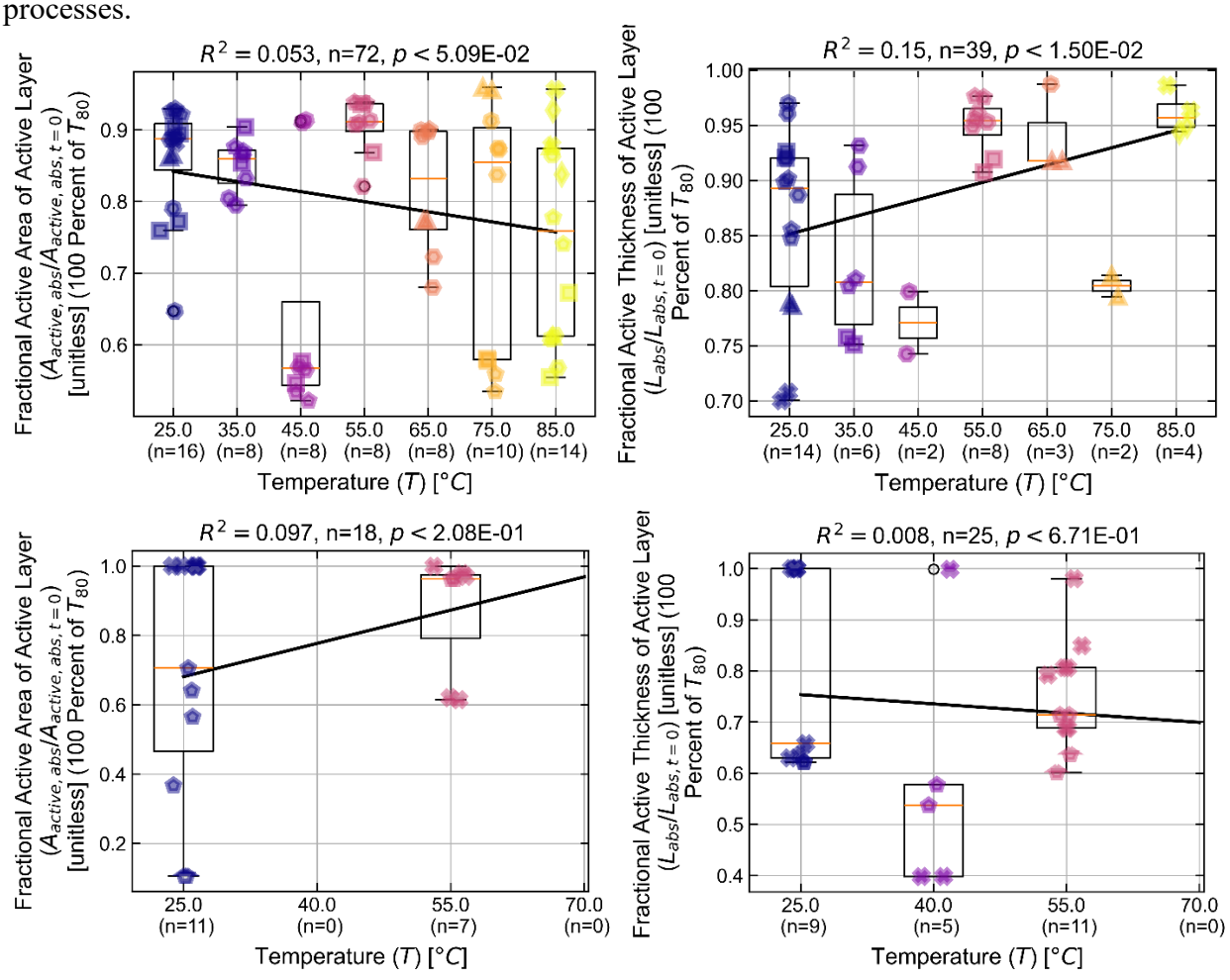

Figure 14. Boxplots of Fractional Effective Degradation Profile Parameters at T_{80} versus Temperature by Architecture. Boxplots of fractional effective active (left column) area and

(right column) thickness at T_{80} versus temperature for our (top row) $MAPbI_3$ and (bottom row) high-bandgap devices. As above, degradation conditions are tabulated for each architecture in Table 6 and encoded according to the grid legend in Figure 4. Additionally, we show the R^2 value for a linear or quadratic polynomial fit which captures general trends of parameter values at T_{80} with degradation conditions, and we report the p-value from a linear regression to determine the significance of changes with degradation conditions.

Initially, we postulated the two competing phenomena are the thermal acceleration of gaseous reactant diffusion through the back electrode and ETL relative to that at the device edges and the thermal acceleration of photooxidation, respectively. Specifically, the only diffusion barrier present for ingress of gaseous reactants from the device edges is the bordering layer of degradation products (e.g., PbI_2 for $MAPbI_3$). Although, this layer is porous due to the constant diffusion of gaseous reactants and products through the layer, enabling rapid diffusion relative to the device's back side. Thus, increasing temperature would be postulated to accelerate the back-side diffusion process more than ingress at the device edges. Although, note that both diffusion processes are still accelerated under elevated temperature. Meanwhile, based on our kinetic rate law models, temperature also accelerates decomposition of the HP film (dominated by photooxidation)[16,19,21] at a combination of higher temperatures (i.e., > 50-60°C for $MAPbI_3$) and lower humidities (i.e., < 20-30% for $MAPbI_3$),[16] and we thus postulated temperature elevation could accelerate photooxidation more than diffusion processes at the above lower temperatures (i.e., 25°C to ≈45°C for $MAPbI_3$ devices) and vice versa at higher temperatures (i.e., ≈45°C to 85°C for $MAPbI_3$ devices), leading to the observed local extrema near 40-45°C.

Although, the temperatures and relative humidities among these experiments span far wider than these thresholds (i.e., > 50-60°C and < 20-30% RH for $MAPbI_3$), allowing the decomposition rate to increase or decrease with temperature among these experiments and thus invalidating this initial theory. Thus, we postulated these two competing phenomena to simply be the opposing Arrhenius dependences (i.e., opposite signs of the effective activation energies) of the dry photooxidation (DPO) pathway and combined dry and wet photooxidation (WPO) pathway (DPO+WPO) observed for all of our HP compositions. Specifically, temperature elevation accelerates the dry photooxidation (DPO) pathway and decelerates the combined dry and wet photooxidation (WPO) pathway (DPO+WPO) for all HP compositions through Arrhenius terms with positive and negative effective activation energies (i.e., those which include and thus are convolved with the adsorption enthalpies of O_2 and H_2O), respectively (see Table 14). These effective activation energies for the DPO+WPO pathway are negative due to the negative adsorption enthalpies of O_2 and H_2O outweighing the small, positive values of the pathway's true activation energies, meaning increasing temperature slightly decreases its rate by inhibiting O_2 and H_2O adsorption more than accelerating the photooxidation reactions. This leads to the observed increase in total photooxidation rate at lower temperatures (i.e., approximately < 60°C for $MAPbI_3$) and the observed increase at higher temperatures (i.e., approximately > 60°C for $MAPbI_3$ in the presence of water vapor) (see Figure 15).[16]

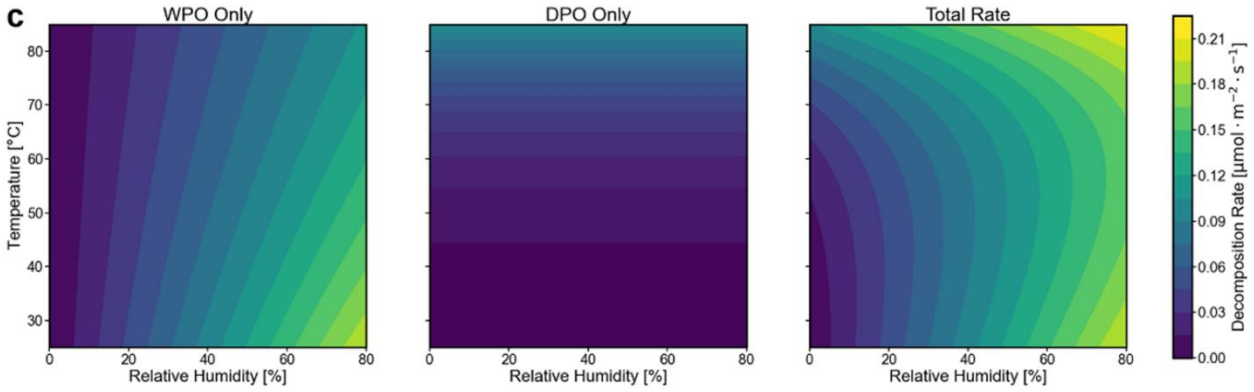

Figure 15. Filled Contour Plots of $MAPbI_3$ Chemical Decomposition Rates Predicted by Our Kinetic Rate Law Model for the Dry Photooxidation (DPO) and Water-Accelerated Photooxidation (WPO) Pathways and Overall Decomposition. (left) Dry Photooxidation (DPO), (middle) Water-Accelerated Photooxidation (WPO), and (right) Total $MAPbI_3$ Decomposition Rates Predicted by Our Kinetic Rate Law Model.[16]

Now, for the devices in this study, we postulate the increase in photooxidation rate with temperature at lower temperatures causes the rate of photooxidation mediated by back-side diffusion to increase more than that for the device sides (since O_2 and H_2O concentrations and thus photooxidation rate are lower following back-side diffusion), causing the observed increase in effective active area and decrease in effective active thickness by T_{80}. Then, as temperature is further increased (i.e., approximately > 45°C for our $MAPbI_3$ devices), gaseous reactant adsorption is sufficiently decreased due to their negative adsorption enthalpies (i.e., $\Delta H_{ads,O_2}, \Delta H_{ads,H_2O} < 0$) to decrease the total photooxidation rate. By the above logic, this decreases the rate of photooxidation mediated by back-side diffusion more than that for the device sides and thus the observed decrease in effective active area and increase in effective active thickness by T_{80} at higher temperatures (i.e., approximately > 45°C for our $MAPbI_3$ devices). Note that the local extrema in these quantities at T_{80} versus temperature are located at a temperature (i.e., ≈45°C for our $MAPbI_3$ devices) similar to the local extremum observed for the $MAPbI_3$ photooxidation rate predicted by our kinetic rate law model (i.e., approximately 50-60°C), further suggesting this conclusion. Nevertheless, note that this reasoning is speculative and only one of many possible explanations.

Table 14. Effective Activation Energies (E_A^{eff}), Adsorption Enthalpies of O_2 and H_2O, and Estimated True Activation Energies (E_A) for the Dry Photooxidation (DPO) and Combined Dry and Wet Photooxidation (WPO) Pathways (DPO+WPO) by Architecture

	Low-Bandgap	Medium-Bandgap	High-Bandgap
Effective Activation Energy (E_A^{eff}) for the Dry Photooxidation (DPO) Pathway [eV]	0.50±0.02, Ref: 19	0.62±0.05, Ref: 16	0.56±0.02, Ref: 21
Effective Activation Energy (E_A^{eff}) for the Combined Dry and Wet Photooxidation (WPO) Pathway [eV]	-0.21±0.08, Ref: 19	-0.09±0.06, Ref: 16	-0.12±0.12, Ref: 21

Given the strong effect of temperature and our knowledge of material decomposition activation energies, we perform an Arrhenius analysis (see Section 2.2.12) of the decays in fractional effective active area and thickness (along with all other parameters throughout this text) to determine if the activation energies are similar. The analysis suggests both parameters decay with similar frequency factors (i.e., pre-exponential coefficients) and with similar activation energies near those for the respective materials' photooxidation pathways (denoted by dashed lines) (see Section 6).

These effective degradation profile parameters constitute an initial model of degradation profile from experimental data, and their evolutions thus provide a rough quantification of the degradation profile throughout degradation. Furthermore, their correlations and dimensionless relationships with other parameters over degradation represent an initial attempt at relating device properties with degradation profile parameters, further illuminating mechanisms of device performance decline. Last, the effective degradation profile parameters also serve as features in our predictive models of operational lifetime. Overall, this approach is a strong step toward modeling degradation profile from experimental data and thus toward the aforementioned complete drift-diffusion model of device performance decline which simulates device performance from degradation profile.

3.1.2 Current-Voltage (J-V) Scans and the Solar Cell Parameters over Time

Following this use of DF and SSPL imaging to model the HP film degradation profile, we consider the evolution of current-voltage (J-V) scans and their corresponding solar cell parameters over time, along with their relationships with architecture and degradation conditions. As shall be continuously seen, it is the evolutions of and correlations among DF and SSPL imaging, the effective degradation profile parameters, and these solar cell, fitted, and derived parameters which illuminates the mechanisms through which HP film degradation influences device performance.

Specifically, for all architectures at early times, J_{sc} exhibits a steady, linear decrease (see Figure 18) nearly proportional to the steady declines in fractional effective HP film area and thickness (see Figure 12), as shown in at 0%, 100%, 200%, and 300% of T_{80} and (right) a single high-bandgap device degrading in air (i.e., 21% O_2, 50% RH) at 25°C under 1 sun illumination intensity at 0%, 40%, 80%, and 130% of T_{80}. In both devices (and generally across both architectures), J_{sc} undergoes a steady, monotonic decline while V_{oc} and FF increase at early times followed by a decrease at later times.. Specifically, the 2D linear polynomial regression yields partial derivatives of the fractional J_{sc} with the fractional effective area and thickness which are nearly equal (i.e., approximately 3.0 and 3.7, respectively), aligning with the known volumetric nature of the volumetric electron-hole pair generation rate (G_{ehp}). Moreover, the intercept is near zero relative to most J_{sc} values (i.e., approximately -5.89 $\mathrm{A/m^{-2}}$), and this matches the expected result in the limit of vanishing area or thickness.

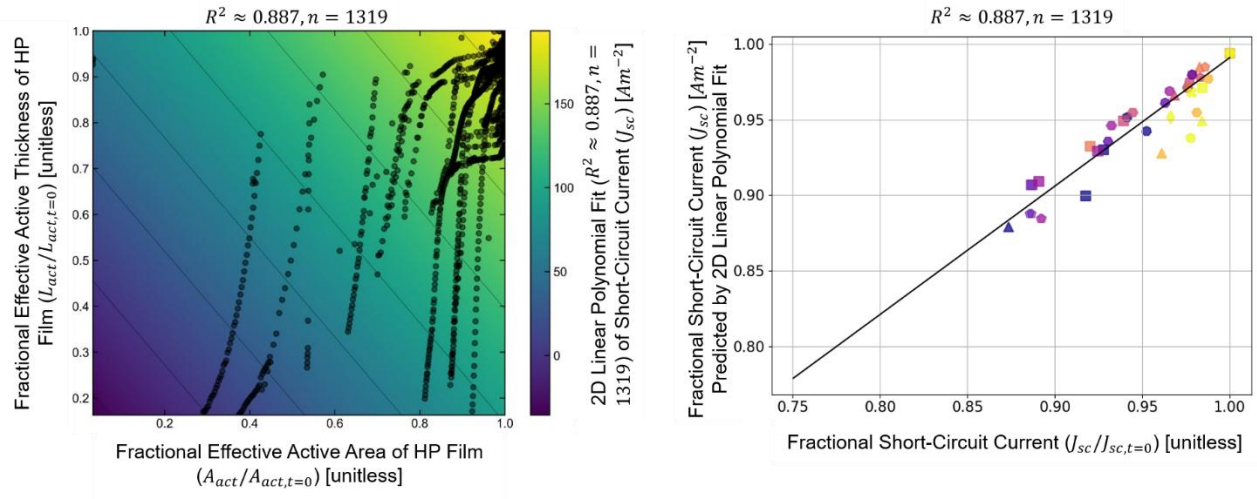

Figure 16. The Proportionality Between J_{sc}-Related Quantities and Effective Active Area, Thickness, and Volume of the HP Film Throughout Degradation. (left) Filled contour plot and (right) the corresponding parity plot for a 2D linear polynomial fit to J_{sc} versus the fractional effective active area and thickness for the $MAPbI_3$ device degradation dataset. Of the 10125 measurement cycles, only 1319 lie in the early-time region of linear decline in J_{sc} and fractional effective degradation profile parameters. The parity plot error metric is calculated for all 1319 points, but only the time averages for each experiment are plotted to avoid clutter.

Then, at moderate and late times, the J_{sc} sometimes exhibits a burn-in (i.e., rapid decline) with near-equivalent fractional change to the apparent active area burn-in (if it exists). Among other reasons, these strong correlations between J_{sc} and the effective HP film area and thickness primarily exist because the HP film is responsible for light absorption and thus electron-hole pair (EHP) generation (see Section 3.1.3). Indeed, in our $MAPbI_3$ device degradation study, we reported a strong Pearson correlation coefficient of $\rho \approx -0.7332$ the logarithm of the time at which J_{sc} declines to 80% of its time-zero value ($T_{80,J_{sc}}$) and the degradation rate (r_{deg}) predicted by our kinetic rate law model[16]. Additionally, the J_{sc} has a significant value at the start of J_{sc} burn-in, and the burn-in occurs after the gaseous reactants reach and degrade the HP-HTL interface. This implies gaseous reactants diffuse along the HP film grain boundaries, degrading both HP-TL interfaces and GBs while leaving a significant fraction of perovskite undegraded as isolated grains. Additionally, in many experiments (including the standard $MAPbI_3$ degradation in Figure 18), the J_{sc} burn-in exhibits an exponential shape. To explain this, we consider the properties which influence J_{sc}. Indeed, we demonstrate short-circuit current (J_{sc}) decline is almost exclusively caused by decline in the volumetric electron-hole pair (EHP) generation rate (G_{ehp}), exclusively due to loss of perovskite material and thus absorptivity. Additionally, we assume an exponential (Beer-Lambert) absorption profile, and the effective active thickness is modeled to continue steadily declining during J_{sc} burn-in. Thus, we thus postulate J_{sc} burn-in occurs when a sufficient thickness of the HP film (≈35-40% remaining, see Section 6) degrades to cause film absorptivity profile to reach its exponential knee (e.g., remaining absorptivity of $1/e \approx 36.8\%$), causing the film's absorptivity to decay exponentially as the thickness steadily declines. Although, it is also possible for the arrival of the gaseous reactants at the HP-HTL interface to cause accumulation of gaseous reactants in the HP film and thus accelerated photooxidation. Thus, despite being probable, our hypothesis is speculative. Additionally, J_{sc} may be influenced by other properties in

different architectures, especially those with standard thicknesses (e.g., 900 nm for world-record 26.15% HP device)[88] comparable to or larger than free carrier diffusion lengths (measured to be ≈1800 nm for high-bandgap films).[30,31] In such cases, J_{sc} burn-in could occur earlier due to band misalignment of device layers with degradation products at isolated grains, reducing carrier mobilities quickly as degradation product thicknesses become sufficient to prohibit the quantum tunneling allowed at single-nanometer thicknesses. Additionally, despite these J_{sc} burn-ins occurring when or after our devices have reached their operational lifetimes (T_{80}), such additional J_{sc} limitations could cause J_{sc} burn-in earlier and thus significantly contribute to short operational lifetimes.

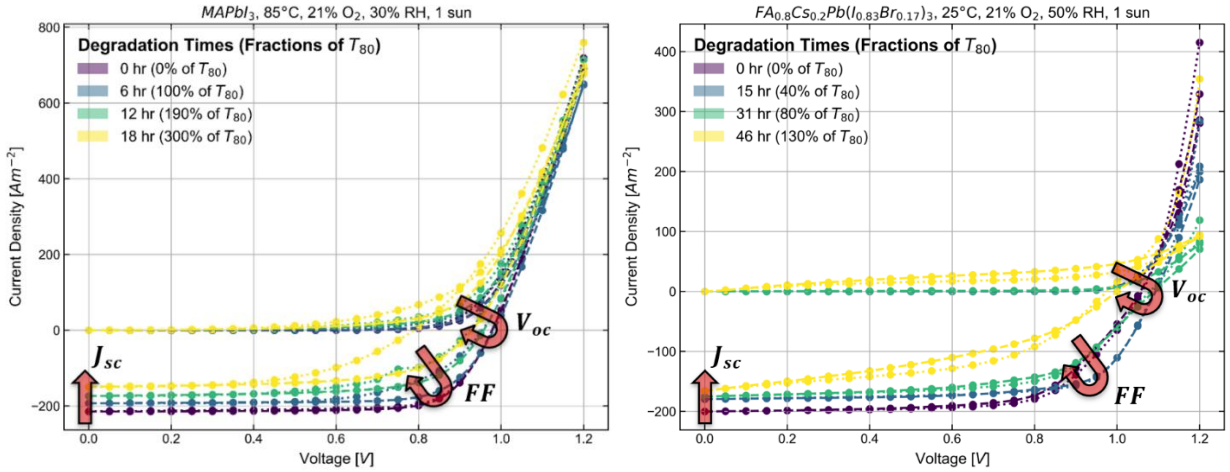

Figure 17. Current-Voltage (J-V) Hysteresis Loop Scans over Time for Single Devices Degrading in Standard Conditions. Current-voltage (J-V) hysteresis loop scans for (left) a single $MAPbI_3$ device degrading in air (i.e., 21% O_2, 30% RH) at 85°C under 1 sun illumination intensity at 0%, 100%, 200%, and 300% of T_{80} and (right) a single high-bandgap device degrading in air (i.e., 21% O_2, 50% RH) at 25°C under 1 sun illumination intensity at 0%, 40%, 80%, and 130% of T_{80}. In both devices (and generally across both architectures), J_{sc} undergoes a steady, monotonic decline while V_{oc} and FF increase at early times followed by a decrease at later times.

Regarding V_{oc} and FF, $MAPbI_3$ and high-bandgap devices exhibit similar, shallow increases at early times, slight and moderate decreases at moderate times before T_{80}, and plateaus when gaseous reactants reach and degrade the HP-HTL interface (i.e., when the DF intensity rapidly and uniformly increases). Although, V_{oc} and FF evolutions over the experiments for a given architecture are similar, and this implies a common phenomenon affecting both parameters. We determine this to be deep defect (trap) passivation at the HP-ETL interface and grain boundaries at early times and subsequent grain isolation at later times (see Section 3.1.4). This grain isolation causes band misalignment between the device layers and degradation products, decreased effective carrier mobilities, increased trapping and SRH recombination, and potentially causing the apparent increase in deep defect (trap) density. Moreover, the plateau of the V_{oc} and FF when gaseous reactants reach and degrade the HP-HTL interface implies most defects exist at HP-TL interfaces and grain boundaries, suggesting significant fitting parameter changes should only occur for J_{ph} and G_{ehp} after this point (see Figure 18). Last, the more rapid decrease of FF relative to V_{oc} implies an additional phenomenon contributing to FF decline, which we determine to be decreasing shunt resistance (R_{sh}) due to shunt pathway formation (see

Figure 32). We therefore again recognize the evolutions and correlations among DF and SSPL imaging, effective degradation profile parameters, and the solar cell, fitted, and derived parameters illuminate the mechanisms of device performance decline.

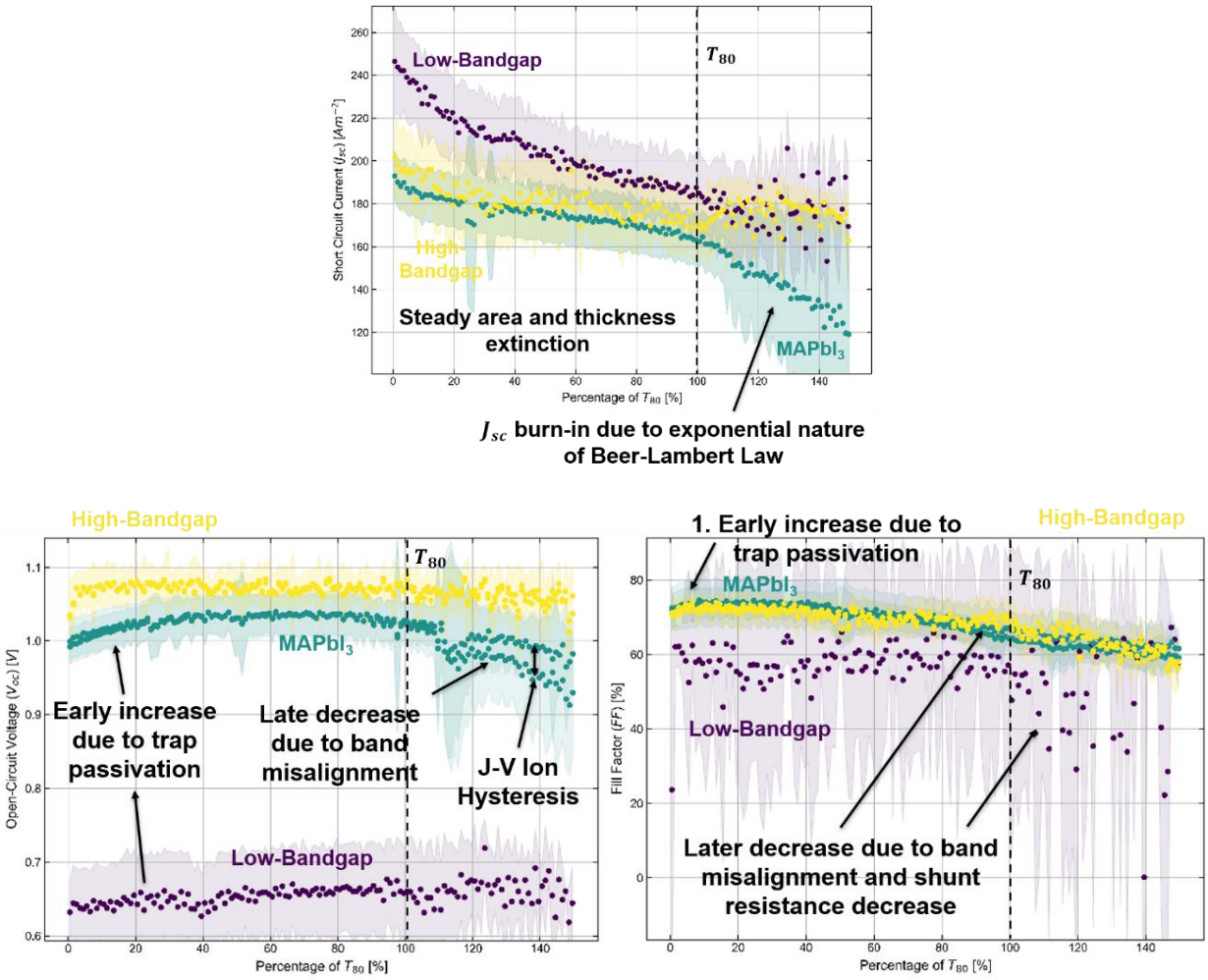

Figure 18. Scatterplots of Solar Cell Parameters over Degradation Averaged over All Experiments for Each Architecture. Scatterplots of the averages (shown as points) and standard deviations (shown as faded regions) of the (top) J_{sc}, (bottom left) V_{oc}, and (bottom right) FF over time (measured as a percentage of T_{80} for each device to enable comparison across all degradation conditions) for all three architectures (low-bandgap in purple, $MAPbI_3$ in green, and high-bandgap in yellow) degrading in the conditions outlined in Table 6 (encoded according to the grid legend in Figure 4). Important features of parameter evolutions are labeled with bolded text and arrows, and operational lifetime (T_{80}) is indicated by the labeled dashed black line at 100% of T_{80}.

Nevertheless, despite the evolutions in V_{oc} and FF illuminating such mechanisms and contributing to PCE changes, the PCE decline is proportional to and thus primarily attributable to J_{sc} decline due to HP film absorptivity loss (caused by its chemical decomposition), yielding a very strong correlation with Pearson correlation coefficient of $\rho \approx 0.884$ and coefficient of determination ($R^2 \approx 0.782$) for nearly all time points (i.e., ≈10021 of the total 10125) and both forward and reverse scan directions (i.e., $n = 20043$) (see Figure 19).

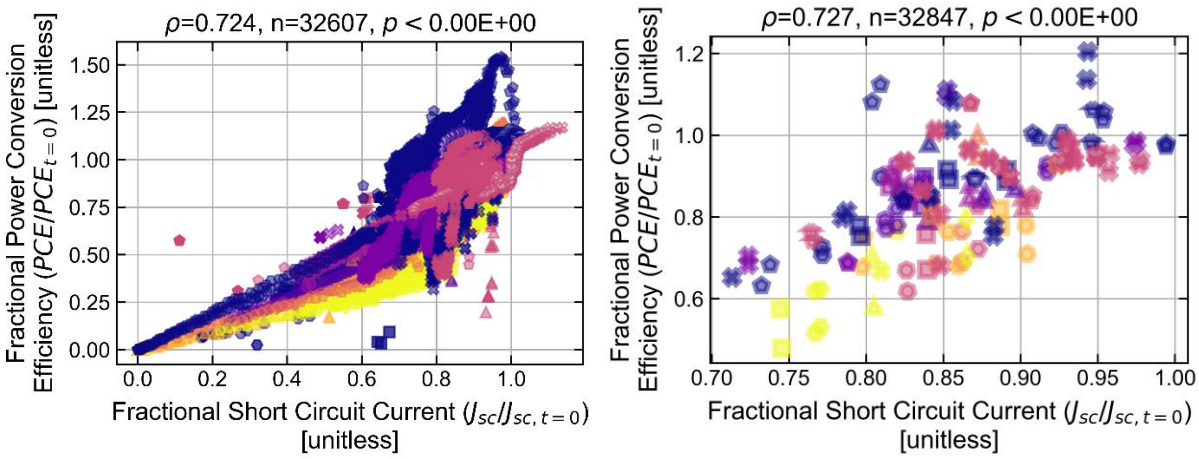

Figure 19. Correlation Plot of Power Conversion Efficiency (PCE) versus Short-Circuit Current (J_{sc}) over All Measurements (i.e., The Study-Wide Dataset). We present correlation plots showing (left) points for each J-V scan and (right) the averages over all time points in each experiment to avoid clutter. Nearly all time points (e.g., ≈10021 of the total 10125 for $MAPbI_3$ devices) and both forward and reverse scan directions (e.g., $n = 20043$ for $MAPbI_3$ devices) are considered, yielding 32607 total measurements with a very strong Pearson correlation coefficient of $\rho \approx 0.724$and a p-value of essentially zero. As above, degradation conditions are tabulated for each architecture in Table 6 and encoded according to the grid legend in Figure 4. Last, note that the metrics reported at the top of (right) are calculated using all measurements in (left), causing them to be equivalent.

For the corresponding boxplots and histograms of the fractional solar cell parameters at T_{80} over all experiments and for each architecture, see Section 6. For all architectures, the primary driver of PCE decline to T_{80} are J_{sc} decline due to HP film absorptivity loss (caused by its chemical decomposition), and FF loss is shown to be a secondary loss mechanism in our $MAPbI_3$ and high-bandgap devices due to decreased shunt resistance (see Figure 37). Meanwhile, the V_{oc} increases slightly in our $MAPbI_3$ and high-bandgap devices due to deep defect (trap) passivation and a corresponding carrier mobility increase at the HP-ETL interface and nearby grain boundaries (see Section 3.1.4). Note that these phenomena to which changes in solar cell parameters are primarily attributed are demonstrated to do so by our mechanistic modeling results below. Furthermore, note that these observations hold across all architectures, despite variation in the relative contribution of J_{sc} and FF in our previous studies.[17,18] Additionally, since our architectures are degraded in a variety of conditions, a wide range of degradation profiles, parameter evolutions, and operational lifetimes are observed (see Table 6).

Now, as the solar cell parameters are the standard empirical metrics for characterizing solar cell performance from current-voltage (J-V) scans, they may be nearly completely described by mechanistic model parameters, and we thus analyze how the mechanistic model parameters independently influence (through our unique cumulative sensitivity analysis (CSA)) and correlate with each solar cell parameter, quantifying the exact influence of each degradation mechanism on device performance decline. Specifically, the phenomena observed are J_{sc} decline due to HP film absorptivity loss (caused by its chemical decomposition), deep defect (trap) passivation (i.e., reduction) and a corresponding carrier mobility increase, shunt resistance decrease (i.e., increased shunting), and a gradual transition from the initial n-type self-doping

behavior (characteristic of HPs) to p-type behavior as halide anions are liberated as halogen gas during film decomposition.

3.1.3 The Robust Proportionality Among Short-Circuit Current (J_{sc}), Photocurrent (J_{ph}), and the Volumetric Electron-Hole Pair Generation Rate (G_{ehp}) Throughout Degradation

3.1.3.1 Summary

We first demonstrate that the J_{sc} and the fitted photocurrent (J_{ph}) in the diode model are almost exclusively determined by and proportional to the drift-diffusion model's electron-hole pair generation rate (G_{ehp}) over all times, degradation conditions, and architectures. Equivalently, this implies such J_{sc}-related quantities are not limited by other phenomena including carrier transport (as suggested in our previous study[17]), recombination, extraction barriers, or parasitic resistances, despite being common in solar cell physics.[33] Additionally, we show how the evolutions of J_{sc}-related quantities depend on degradation conditions in a similar manner as the fractional effective degradation profile parameters and the material degradation rate (r_{deg}) predicted from our kinetic rate law models (e.g., similar activation energies in Arrhenius modeling).

Overall, these results suggest the short-circuit current (J_{sc}) decline is almost exclusively (> 90% at T_{80}) caused by the proportional decline in electron-hole pair generation rate (G_{ehp}) due to HP film absorptivity loss (caused by its chemical decomposition), where decreased shunt resistances and increased series resistances can cause small, fictitious gains in J_{ph} in the non-ideal diode model. J_{sc} limitations caused by carrier transport, recombination, or extraction barriers are not detected on our devices, but we expect standard-thickness (e.g., 900 nm for world-record 26.15% HP device)[88] HP films to exhibit diffusion length limitations of J_{sc}, again without recombination or extraction barrier limitations. This near-perfect extraction of free carriers causes J_{sc}-related quantities to be equally proportional to HP film area and thickness and thus volume, but we expect these proportionalities to vanish if other J_{sc} limitations appear. Additionally, J_{sc} decline due to HP film absorptivity loss (caused by its chemical decomposition) and thus carrier generation rate is the primary driver of PCE decline in our devices, increasing in importance with decreasing bandgap due to a corresponding decrease in stability to photooxidation. Regarding J_{sc} dependence on degradation conditions, J_{sc}-related quantities exhibit similar Arrhenius behaviors to J_{MPP} and PCE, suggesting J_{MPP} primarily depends on J_{sc} instead of FF and again that J_{sc} loss is the primary driver of PCE decline. Additionally, J_{sc} exhibits a local minimum with temperature, a linear decline with oxygen concentration, and insignificant correlation with humidity.

3.1.3.2 Evolution of J_{sc}-Related Quantities over Degradation and the Corresponding Integrated Influences of Mechanistic Model Parameters Determined through Cumulative Sensitivity Analysis (CSA)

Specifically, J_{sc}-related quantities include J_{sc}, J_{ph}, G_{ehp} fitted with Koster *et al.*'s BOAR or AutoFit routines (which allow fitting of G_{ehp}), and G_{ehp} assuming perfect extraction of all generated carriers (i.e., $J_{sc} = qG_{ehp}L$). Indeed, all J_{sc}-related quantities evolve along near-proportional trajectories for all times, degradation conditions, and architectures. This suggests the short-circuit current (J_{sc}) decline is almost exclusively caused by the proportional decline in HP film electron-hole pair generation rate (G_{ehp}), not by changes in other potentially limiting phenomena including carrier transport (as predicted in our previous study[17]), recombination, extraction barriers, or parasitic resistances, despite such phenomena being common in solar cell

physics.[33] Additionally, of these phenomena, we only observe decreased shunt resistance and increased series resistance to contribute appreciably to J_{sc} decline, and even this contribution is almost negligible (i.e., < 10% of the J_{sc} change by T_{80} for $MAPbI_3$ devices) despite heavily degraded edges in $MAPbI_3$ devices. These claims are supported by the observed proportionality of J_{sc} with G_{ehp} when G_{ehp} is included as a fitting parameter in Koster *et al.*'s BOAR or AutoFit routines, or conversely, by the preservation of low fitting error when assuming perfect carrier extraction (i.e., $J_{sc} = qG_{ehp}L$) and excluding G_{ehp} as a fitting parameter in the OptimPV routine. We only report results from the OptimPV routine in this text, but we will provide the corresponding results for the standard $MAPbI_3$ device degradation run considered in Figure 12 with G_{ehp} as a fitting parameter in the AutoFit routine in a future publication and in a future version of this thesis on our "DegradePV" GitHub repository (see Section 6).[63] Additionally, in the following SI section, we show assuming constant G_{ehp} over degradation results in poor fits, indicating the fitted influence of G_{ehp} on J_{sc} is a physical result, not a hypothetical artifact of systematic error in the model or insufficient experimental data to isolate such phenomena in fitting results. Last, since electrons and holes are generated almost exclusively by light absorption (see Section 2.2.3.4), these declines in J_{sc}-related quantities are thus almost exclusively caused by HP film absorptivity loss (due to its chemical decomposition). This directly supports the observed proportionality of J_{sc} with the fractional effective area and thickness of the HP film (see Figure 12) and the strong correlation between J_{sc} and the rate-law-predicted degradation rate (r_{deg}) for our $MAPbI_3$ devices.[17]

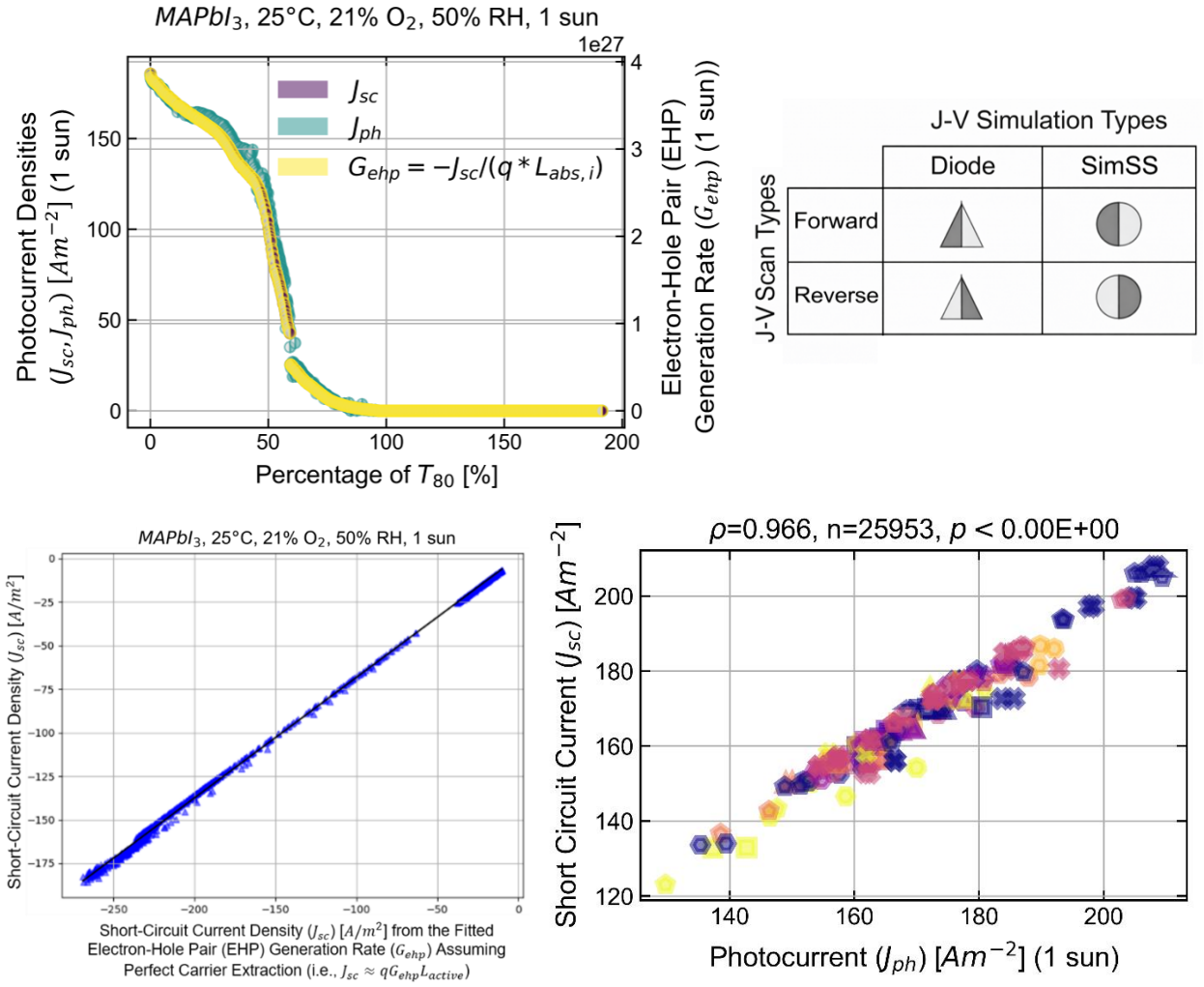

Figure 20. The Robust Proportionality Among J_{sc}-Related Quantities over Degradation for All Degradation Conditions and Architectures. (top left) Scatterplot of the fractional J_{sc} (purple), J_{ph} (green), and G_{ehp} fitted with AutoFit (yellow) over degradation time (measured as a percentage of T_{80}) for a single $MAPbI_3$ device degrading in air (21% O_2, 50% RH) at 25°C under 1 sun illumination. (top right) Grid legend showing marker shape and fill style encodings for simulation types (i.e., diode or steady-steady drift-diffusion (SimSS)) and J-V scan types (i.e. forward or reverse) for calculating parameters. (bottom row) Correlation plots of the J_{sc} versus (bottom right) J_{ph} over all $MAPbI_3$ and high-bandgap device degradation runs and versus (bottom left) J_{sc} determined from the fitted G_{ehp} (fitted with AutoFit) assuming perfect carrier extraction (i.e., $J_{sc} \approx qG_{ehp}L_{act,t=0}$) for the $MAPbI_3$ device in (top). The low-bandgap dataset is not included because full J-V scans are not performed for low-bandgap devices, preventing fitting with the diode and drift-diffusion models. Additionally, as above, degradation conditions are tabulated for each architecture in Table 6 and, for the plot above involving multiple experiments (i.e., bottom right), markers are encoded according to the grid legend in Figure 4.

Although, despite these strong proportionalities among the J_{sc}, J_{ph}, G_{ehp} fitted with BOAR or AutoFit, fractional effective degradation profile parameters, we still must consider the nature and importance of the decreased shunt resistance and increased series resistance contributions to J_{sc}

decline. Specifically, J_{ph} diverges slightly above the J_{sc} and G_{ehp} trajectories in all experiments where this phenomenon occurs (often near T_{80}, see Figure 20(a)) while G_{ehp} near-perfectly matches the J_{sc} trajectory. Indeed, the drift-diffusion model yields lower error in the simulated J_{sc} than the non-ideal diode model. The reason for this difference is shown in Figure 20. During the period J_{ph} diverges slightly above J_{sc}, the shunt resistance (R_{sh}) and series resistance (R_s) are much lower than its original value, causing increased shunt and series resistance losses and thus small influences on J_{sc} as determined by applying our CSA to the diode fitting results. Although, the fitted parasitic resistances are near-equivalent for the diode and drift-diffusion models, meaning the observed influences of R_{sh} and R_s on J_{sc} is a fictitious result of the diode model's cruder assumptions. Indeed, the normalized integrated influences of J_{ph} on J_{sc} for the single $MAPbI_3$ device in Figure 12 at T_{80} is lower (on average, ≈95.5% at T_{80}) than those for the fitted G_{ehp} (i.e., $\approx 97.2\%$, see Section 6). Although, note that G_{ehp} was only fitted for the single $MAPbI_3$ device in Figure 12, meaning performing the CSA for all experiments with G_{ehp} included as a fitting parameter (i.e., with BOAR or AutoFit) may yield equivalent normalized influences of J_{ph} and G_{ehp} on J_{sc}. Nevertheless, even if the series and shunt resistances fitted with the drift-diffusion model contribute equally to J_{sc} loss relative to the diode-fitted series and shunt resistances, their contribution are also minor in either case over all architectures, degradation conditions, and degradation extents, even with heavily degraded device edges. Specifically, the diode fit for the single $MAPbI_3$ device in Figure 12 yields influences of R_s and R_{sh} on J_{sc} of ≈1% and ≈3.5%, respectively, while the drift-diffusion fit yields influences of ≈0.2% and ≈2.4%, respectively (see Section 6). Overall, as suggested by the evolution of fitting parameters over degradation, the CSA suggests J_{sc} decline is almost exclusively driven by the near-proportional declines in J_{ph} and G_{ehp} due to HP film absorptivity loss (caused by its chemical decomposition) with minor contributions from R_s and R_{sh}. Furthermore, this rough similarity among the influences of the diode and drift-diffusion fitting parameters further affirms these conclusions. Although, as discussed in Section 4.1.4, the high volatility in drift-diffusion fitting parameter values over time causes excessive error in the calculated parameter sensitivity coefficients and thus influences on higher-level parameters (i.e., both the diode and solar cell parameters).

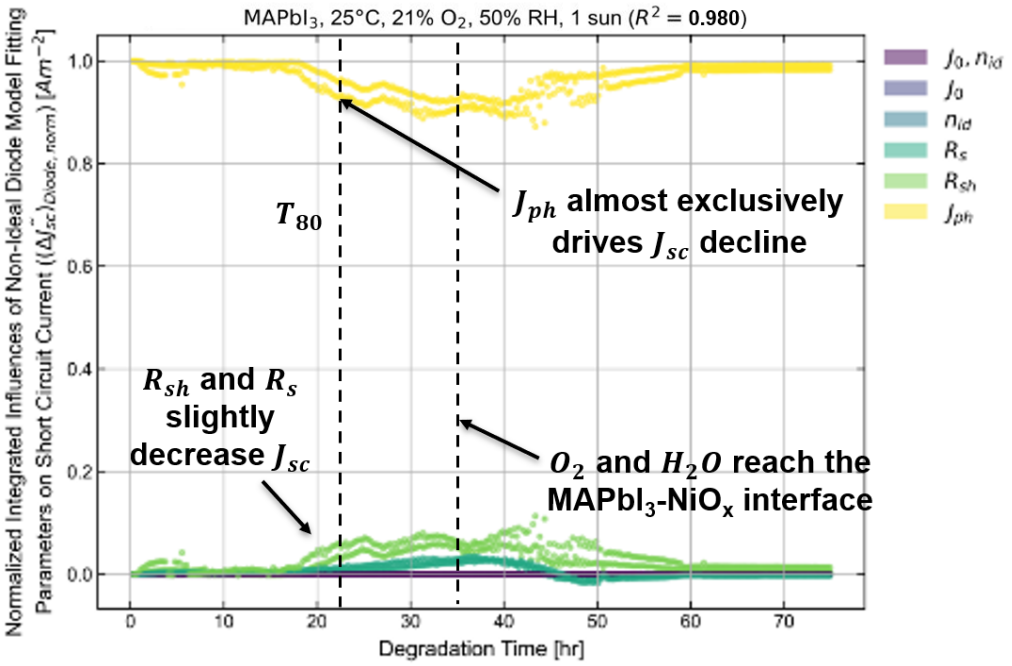

Figure 21. Normalized Integrated Influences of Diode Fitting Parameters on J_{sc} over Time for a Single MAPbI3 Device. Scatterplot of the normalized integrated influences of the diode fitting parameters on J_{sc} over time (measured as a percentage of T_{80}) for the $MAPbI_3$ device degradation in Figure 12. Normalization is performed by dividing each respective integrated influence by the sum of the absolute values of integrated influences for all parameters. Additionally, as above, simulation type and scan type are encoded for single experiments according to the grid legend in Figure 20.

Other than parasitic resistances, we observe no significant contributions of carrier transport, recombination, or extraction barriers to J_{sc} loss, despite being common in solar cell physics.[33] Specifically, as discussed in this section above, our HP film thicknesses (≈300 nm) are comparable to our measured (≈1800 nm for high-bandgap films)[30,31] and derived ambipolar diffusion lengths, enabling diffusion of electrons and holes throughout the HP film before significant recombination losses and preventing diffusion length limitations of J_{sc}. Although, HP film thicknesses in high-efficiency devices are significantly higher (e.g., 900 nm for world-record 26.15% HP device)[88] than our HP film thicknesses and their diffusion lengths, meaning carrier diffusion lengths may limit J_{sc} during degradation for devices with thicker HP films. Indeed, the robustness of these proportionalities over all architectures, degradation conditions, and degradation extents implies these other expected limitations are not present due to a common trait among architectures, which we hypothesize is their relatively low HP film thicknesses (≈300 nm). Regarding other potential sources of J_{sc} loss, we expect diffusion length limitations will affect J_{sc} more than other possible sources of J_{sc} loss since diffusion lengths are observed to be more sensitive to HP film degradation than carrier lifetimes in this study and our previous studies.[30,31]

To support these claims, we simulate our degradation experiments for many initial HP film thicknesses assuming a G_{ehp} predicted with the Beer-Lambert Law and equivalent degradation rates of fractional effective area and thickness (not normalized). Indeed, diffusion length will be limiting for thicknesses above 1/3 or 1/2 of the diffusion length, with its influence

on J_{sc} increasing exponentially with increasing thickness. These facts are in accordance with the definition of characteristic length. Additionally, in such cases of diffusion length limitations, we expect the proportionalities of J_{sc}-related quantities with the fractional effective degradation profile parameters to become invalid. As such, these mechanistic and predictive models are specific to these architectures and their properties, including layer compositions and thicknesses. Thus, general models applicable for various architectures are an object for future research, as is enabling OptimPV to fit G_{ehp} as is done by BOAR and AutoFit (see Section 6).

Regarding the effect on PCE, the primary driver of PCE decline in our devices (see Figure 19 and Figure 37) is J_{sc} decline due to the loss in HP film absorptivity and thus carrier generation rate caused by its chemical decomposition, increasing in importance with decreasing bandgap due to a corresponding decrease in stability to photooxidation. Indeed, as stated previously, PCE and J_{sc} are strongly correlated over all architectures and experiments with a Pearson correlation coefficient of $\rho \approx 0.884$ and coefficient of determination of $R^2 \approx 0.782$ (see Figure 19). Additionally, this again explains the strong correlation ($\rho = -0.73$) between the logarithm of the time at which J_{sc} declines to 80% of its time-zero value ($T_{80,J_{sc}}$) and the $MAPbI_3$ degradation rate predicted by our kinetic rate law model[16] in our predictive ML modeling study.[17]

3.1.3.3 Relationships of J_{sc}-Related Quantities at T_{80} with Degradation Conditions

Last, we investigate the relationships of J_{sc} at T_{80} with degradation conditions (see Figure 22). Specifically, the fractional J_{sc} exhibits a temperature dependence very similar to that of the fractional effective active area (see Figure 14), exhibiting a steady decrease in the low-temperature region (i.e., 25-45°C) and a sharp increase between 45°C and 55°C. This suggests the temperature dependence of the J_{sc} is subject to the same two competing phenomena as the fractional effective active area, postulated above to be the positive and negative Arrhenius dependences of the DPO and WPO pathways (see Section 3.1.1).

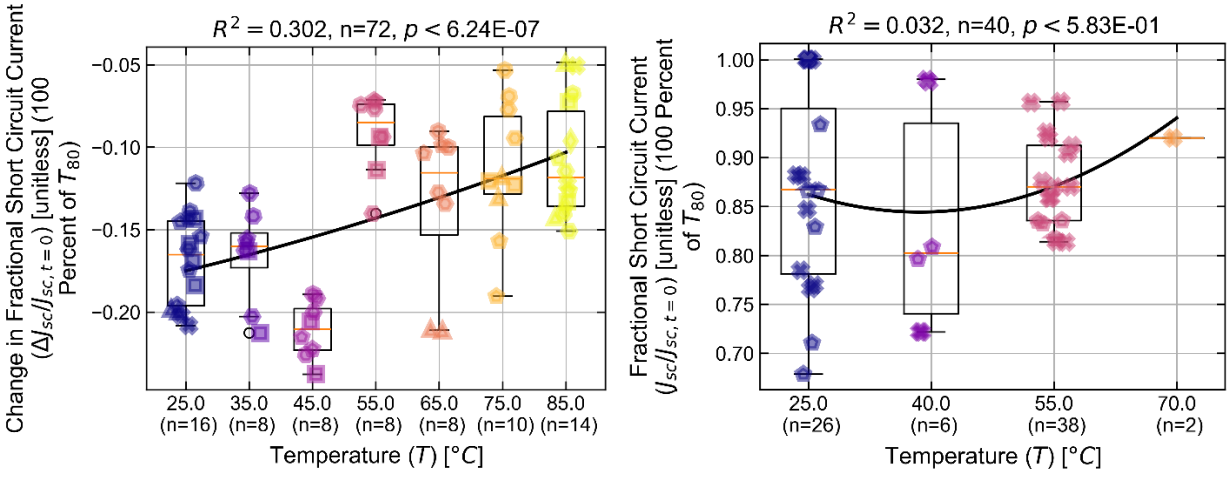

Figure 22. Boxplots of Fractional Short-Circuit Current ($J_{sc}/J_{sc,t=0}$) at T_{80} versus Temperature by Architecture. (left) $MAPbI_3$ and (right) high-bandgap. As above, degradation conditions are tabulated for each architecture in Table 6 and encoded according to the grid legend in Figure 4. Additionally, we show the R^2 value for a linear or quadratic polynomial fit which captures general trends of parameter values at T_{80} with degradation conditions, and we report the

p-value from a linear regression to determine the significance of changes with degradation conditions.

Now, to determine if there exist similarities in the Arrhenius behavior of the decline in J_{sc}-related parameters and the fractional effective active area, we again perform an Arrhenius analysis. Specifically, the decline in the fractional J_{sc}, J_{ph}, G_{ehp}, J_{MPP}, and PCE exhibit Arrhenius behavior ($R^2 \approx 0.43 - 0.49$) with activation energies very similar to one another (≈0.14-0.18 eV). The similarity of the fractional PCE decline's activation energy with those of the fractional J_{sc}-related parameters is a result of the PCE's primary dependence on (i.e., proportionality with) the J_{sc}. Although, the similarity in the Arrhenius behavior of J_{sc} and J_{MPP} suggests the J_{MPP} depends on J_{sc} more than on FF, and by logical extension, that FF changes primarily affect V_{MPP}, and that V_{MPP} is more dependent on FF than on V_{oc} (see Section 6). Although, the activation energies for the fractional effective active area and thickness are much higher and lower, respectively, than those for the above parameters, indeed indicating the activation energies for the declines of the above parameters are the result of contributions from the Arrhenius dependence of the fractional effective degradation profile parameters. Although, as for the effective degradation profile parameters, this reasoning is speculative and only one of many possible explanations.

Regarding the remaining degradation conditions, the fractional J_{sc} at T_{80} in $MAPbI_3$ devices exhibits no significant change with relative humidity, and trends with oxygen concentration and illumination intensity cannot be analyzed since all $MAPbI_3$ device experiments involve single values for these degradation conditions (i.e., 21% O_2 and 1 sun, respectively). Similarly, the fractional J_{sc} at T_{80} in low-bandgap devices also exhibits no significant trends with degradation conditions other than temperature despite the experiments spanning multiple values for each variable (see Table 6). Although, the fractional J_{sc} at T_{80} in high-bandgap devices exhibits a steady decline with oxygen concentration (see Figure 23(left)) and an initial decrease with relative humidity from ≈2-15% followed by a plateau from ≈15-50% (see Figure 23(right)). We postulate high-bandgap devices exhibit trends of the fractional J_{sc} at T_{80} with these degradation conditions while low-bandgap and $MAPbI_3$ devices do not because high-bandgap devices are inherently more stable to photooxidation,[16,19–21] meaning chemical decomposition of the HP film is likely increasingly limited by chemical kinetics (alongside mass transport) and the kinetic rate law model's concentration dependence manifests in J_{sc} decline. Additionally, the fractional J_{sc} at T_{80} decreases with illumination intensity as expected, but no further information may be extracted since 0 sun and 1 sun are the only illumination intensities tested. Overall, all of the above observations are sensible given the mechanistic relationships among parameters discussed above, again demonstrating the utility of combining degradation profile analysis with mechanistic modeling. All boxplots of the fractional J_{sc} at T_{80} versus degradation conditions for each architecture will be provided in a future publication and in a future version of this thesis on our "DegradePV" GitHub repository (see Section 6)).[63]

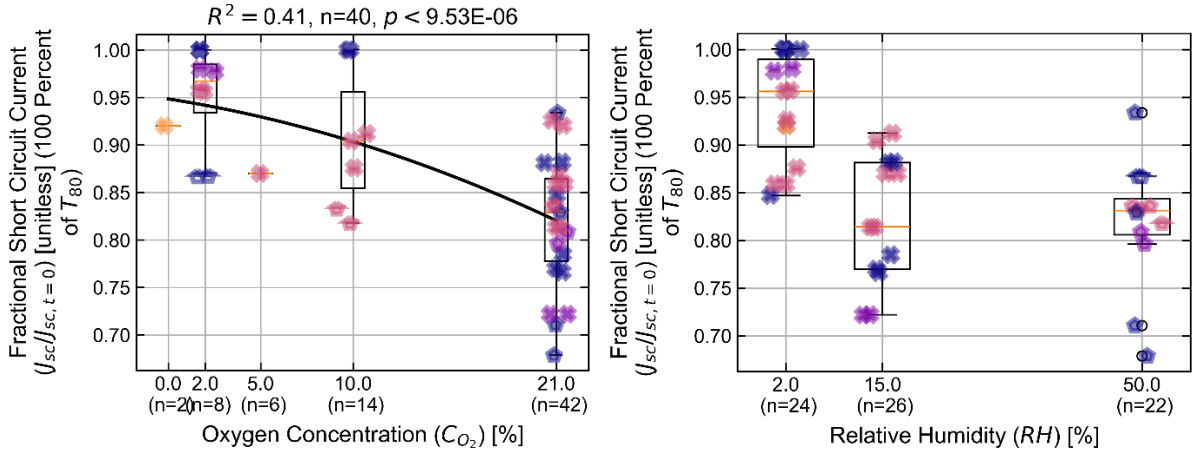

Figure 23. Boxplots of Fractional Short-Circuit Current ($J_{sc}/J_{sc,t=0}$) at T_{80} versus (left) Oxygen Concentration (C_{O_2}) and (right) Relative Humidity (RH) for the High-Bandgap Device Dataset. As above, degradation conditions are tabulated for each architecture in Table 6 and encoded according to the grid legend in Figure 4. Additionally, we show the R^2 value for a linear or quadratic polynomial fit which captures general trends of parameter values at T_{80} with degradation conditions, and we report the p-value from a linear regression to determine the significance of changes with degradation conditions.

3.1.4 Deep Defect (Trap) Reduction and Band Misalignment at Degrading HP-TL Interfaces and Grain Boundaries

Although, many phenomena discussed above which do not affect J_{sc} do affect PCE through the V_{oc} and FF, and we first discuss our discovery of early-time deep defect (trap) reduction and later-time band misalignment at degrading HP interfaces and grain boundaries as observed in our previous film studies.[30,31]

3.1.4.1 Summary

Specifically, we discover the fitted HP-ETL deep defect (trap) density ($N_{tr,HP-ETL}$) and electron mobility (μ_n) are inversely correlated due to the electrostatic barriers posed by deep defect space charge, decreasing and increasing (respectively) at early times due to deep defect reduction at the HP-ETL interface and grain boundaries followed by increasing and decreasing (respectively) at later times due to band misalignment of HP with degradation products at these locations. We postulate this occurs at later times since sufficient thicknesses of degradation products must be developed to prevent tunneling through the original, thin potential barriers, thus causing classical band misalignment. This decreases carrier mobilities and increases SRH recombination (which manifests as an apparent increase in HP-ETL interfacial deep defect (trap) density). Furthermore, we observe no significant changes in the fitted HP-HTL interfacial deep defect (trap) density and hole mobility, supporting our hypothesized degradation scheme in which degradation begins at the HP-ETL interface and ingresses along grain boundaries, reaching the HP-HTL interface only after significant degradation of the HP-ETL interface and grain boundaries.

Additionally, regarding the non-ideal diode model, the parameters which are theoretically described by the deep defect (trap) densities and carrier mobilities (i.e., essentially all parameters other than G_{ehp}, R_{sh}, and R_s) are the dark reverse bias saturation current (J_0) and ideality factor (n_{id}). Indeed, in observing their evolutions with time, we discover the times at which noticeable

changes occur align with those of the HP-ETL interfacial deep defect (trap) density and electron mobility. Although, J_0 and n_{id} exhibit an incredibly strong inverse correlation which dominates their evolutions, meaning the combination of their influences on solar cell parameters is most relevant. We thus consider the influences of these phenomena on V_{oc} and FF through CSA of both the diode and drift-diffusion fitting results. Indeed, these phenomena exclusively drive the early-time increases in and are primary contributors to the later-time decreases in V_{oc}, FF, and PCE (alongside all phenomena discussed in this work). Additionally, as stated in Section 3.1.3, these phenomena would likely influence J_{sc}-related parameters in a similar manner as for the V_{oc} and FF in devices with HP film thicknesses sufficiently large to cause diffusion length limitations to carrier extraction.

3.1.4.2 Evolution of Deep Defect (Trap) Densities, Carrier Mobilities, Dark Reverse Bias Saturation Current, and Ideality Factor over Degradation and the Corresponding Integrated Influences of Fitting Parameters on V_{oc} Determined Through Our Unique Cumulative Sensitivity Analysis (CSA)

For $MAPbI_3$ devices, we immediately observe the fitted HP-ETL deep defect (trap) density ($N_{tr,HP-ETL}$) to decrease and the fitted electron mobility (μ_n) to increase at early times. We also observe these changes for single high-bandgap devices, but to much less of an extent, and since the evolutions of drift-diffusion fitting parameters exhibit large volatility over time and across experiments, aggregating over all high-bandgap experiments yields seemingly insignificant changes (i.e., the yellow points in Figure 24). In other words, the volatility in the drift-diffusion fitting parameters over time and experiments masks the evolutions observed in single experiments. Furthermore, evolutions related to these changes are also observed for the related higher-level parameters (i.e., J_0, n_{id}, V_{oc}, FF) as shown in Figure 27 and Figure 32, further indicating this phenomenon's existence in high-bandgap devices alongside $MAPbI_3$ devices. To illustrate this, we show the evolutions of $N_{tr,HP-ETL}$ and μ_n for the standard $MAPbI_3$ device first presented in Figure 12. Indeed, we observe the trends described for the $MAPbI_3$ devices for the single high-bandgap device as well, but to less of an extent. We postulate this far lower sensitivity of such parameters to degradation in high-bandgap devices is attributable to a combination of either lower deep defect (trap) densities (as shown in Figure 24) or lower sensitivity of defect structure at interfaces and grain boundaries upon degradation compared with $MAPbI_3$ (see Section 6). Additionally, we note this is likely not due to the high-bandgap architecture's greater stability to photooxidation[21] since a similar level of loss in J_{sc}-related quantities is still observed for high-bandgap devices (which is known to be well-correlated with the decomposition rate).

Moreover, beyond their evolutions, the fitted HP-ETL deep defect (trap) density ($N_{tr,HP-ETL}$) and electron mobility (μ_n) appear inversely correlated throughout degradation, and since no other parameters are involved in this correlation, we postulate this correlation is the result of an underlying, physical ability of deep defects (traps) to inhibit carrier movement. Indeed, such defects in the crystal lattice could scatter carriers by collision as observed for any microscopic particles moving through a solid medium. Although, defect states exist in concentrations ranging order of $\approx 10^{15}$ to $\approx 10^{17}\ cm^{-3}$,[126–129] and the number density of atoms in the lattice is on the order of $\approx 10^{21}\ m^{-3}$ (see Section 6). Thus, changes in defect densities likely do not appreciably affect carrier movement through lattice scattering. Although, defect states are often charged depending on the nature of the defect and whether the defect is occupied by an electron or hole, and both positively or negatively charged defects represent space charges which

affect carrier movement through electrostatic forces (with a much larger radius of influence compared with lattice scattering).[33] Indeed, Nelson explains the impedance of carrier movement by charged defects at grain boundaries in polycrystalline materials. This concept applies everywhere in the film, but as noted by Nelson, it is most prevalent at interfaces and grain boundaries due to their higher defect densities.[33] Indeed, the immediate beginning of these changes at time zero aligns with the observation of deep defect (trap) densities being concentrated at interfaces and grain boundaries both in this work and in other experimental and computational studies.[46,52] Moreover, of the fitted deep defect (trap) density and carrier mobility parameters, only the HP-ETL interfacial deep defect (trap) density ($N_{tr,HP-ETL}$) and electron mobility (μ_n) exhibit significant changes while no significant changes are observed for the fitted HP-HTL interfacial deep defect (trap) density and hole mobility. Thus, since electrons are concentrated near the HP-ETL interface and holes are concentrated near the HP-HTL interface, this supports our postulated degradation scheme (see Figure 13) in which degradation begins at the HP-ETL interface and ingresses along grain boundaries, reaching the HP-HTL interface only after significant degradation of the HP-ETL interface and grain boundaries. Additionally, since the fitted HP-ETL interfacial deep defect (trap) density ($N_{tr,HP-ETL}$) continues decreasing far into degradation (i.e., approximately 80% of T_{80} for both the $MAPbI_3$ and high-bandgap architectures), a significant portion of deep defects likely exist at grain boundaries, passivated as gaseous reactants ingress along and degrade the grain boundaries until reaching the HP-HTL interface.

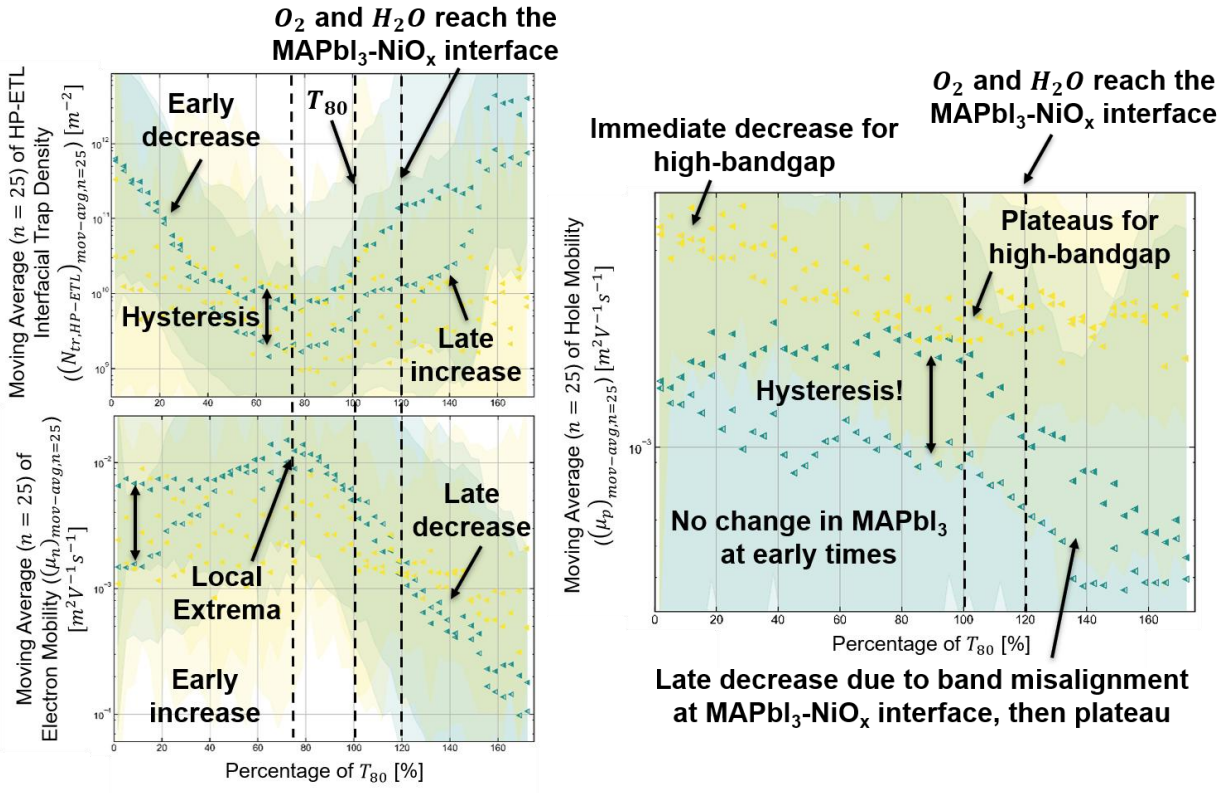

Figure 24. The Evolution of the Interfacial Deep defect (trap) densities ($N_{tr,HP-ETL}$ and $N_{tr,HP-HTL}$) and Carrier Mobilities (μ_n and μ_p) over Time Averaged over All Experiments for Each Architecture. Scatterplots of the averages (shown as points) and standard deviations

(shown as faded regions) of the (top) HP-ETL interfacial deep defect (trap) density ($N_{tr,HP-ETL}$), (bottom left) electron mobility (μ_n), and (bottom right) hole mobility (μ_p) over degradation time (measured as a percentage of T_{80}) for our medium-bandgap ($MAPbI_3$) (green) and high-bandgap (yellow) architectures degrading in the conditions outlined in Table 6 (encoded according to the grid legend in Figure 4). Important features of parameter evolutions are labeled with bolded text and arrows, and operational lifetime (T_{80}) is indicated by the labeled dashed black line at 100% of T_{80}.

Then, as degradation progresses, the HP-ETL interfacial deep defect (trap) density ($N_{tr,HP-ETL}$) reaches a local minimum at approximately 75% of T_{80} for both $MAPbI_3$ and high-bandgap architectures, Meanwhile, the electron mobility (μ_n) reaches a local maximum at approximately 75% of T_{80}, again for both architectures. Although, as the HP-ETL interface and grain boundaries are degraded, increasing thicknesses of solid degradation products accumulate, isolating and shrinking grains. It is thus logical to postulate sufficient thicknesses of degradation products impede carrier movement and extraction due to a combination of lower carrier mobility and band misalignment with (i.e., differing band energies than) the adjacent perovskite (see Caputo *et al.* for a band energy comparison of $MAPbI_3$ with its degradation product PbI_2),[130] thus leading to an increased SRH recombination rate. At very low thicknesses (i.e., single-nanometer thicknesses), carriers should easily tunnel through such barriers, but once thicknesses reach the order of ≈10 nm, they would be expected to begin impeding carrier movement. This explains why the phenomenon is not immediately observed but outlasts deep defect (trap) passivation. Additionally, based on the review of interfacial defect physics which will be provided in a future publication and on our "DegradePV" GitHub repository published online,[63] the defect structure and densities should not change appreciably following degradation of the given interface or grain boundary. Furthermore, this process is passivating, and these facts further suggest an unexplained increase in deep defect (trap) densities at later times does not occur. Instead, degradation products simply accumulate at interfaces and grain boundaries as they are degraded, impeding carrier movement due to lower mobility and/or band misalignment relative to the adjacent perovskite. Although, all parameters other than J_{sc}-related parameters plateau after gaseous reactants reach the HP-HTL interface (indicated by the rapid, uniform increase in DF intensity over the device area as shown in Figure 12), implying band misalignment is the dominant mobility impedance mechanism. This is because an increasing thickness of lower mobility material would cause a continued decrease in effective (i.e., fitted) carrier mobilities even after gaseous reactants have contacted all interfaces and grain boundaries, reaching the average mobility of the degradation products in the limit of full extinction. Nevertheless, this is still a possibility due to the systematic and large random errors of drift-diffusion fitting results. Last, since the HP-ETL interfacial deep defect (trap) density ($N_{tr,HP-ETL}$) and electron mobility (μ_n) reach their local extreme approximately halfway to their plateau (i.e., when gaseous reactants reach the HP-HTL interface and the DF intensity exhibits a rapid, uniform increase), grain isolation effects likely begin shortly after passivation of a given interface or grain boundary surface, intensifying over time.

Now, with these observed changes in drift-diffusion fitting parameters, we also observe corresponding changes in the corresponding derived parameters (see Section 6) which align with our previous studies measuring optoelectronic properties of degrading HP films.[18,30,31] Specifically, in these studies, we determined the quasi-Fermi level splitting (QFLS, ΔE_F) from the photoluminescence quantum yield (PLQY, ϕ_{PL}) in steady-state photoluminescence (SSPL)

measurements and ambipolar diffusion length (L_D) through photoconductivity measurements. In these previous studies and this study, we observe the QFLS and L_D to rapidly and steadily increase, respectively, during deep defect (trap) reduction at early times, the ambipolar diffusion length (L_D) to steadily and then rapidly decay to a plateau during grain isolation while the QFLS increases at a reduced rate, and finally a rapid QFLS decrease to slightly lower than its initial value at very late times (see Figure 25 for our previous study results). This increased sensitivity of L_D to HP film degradation relative to the QFLS has been observed in these previous studies, and we attributed the decays of J_{sc} and FF and the concurrent, steady increase in V_{oc} in a corresponding $MAPbI_3$ device to this observation.

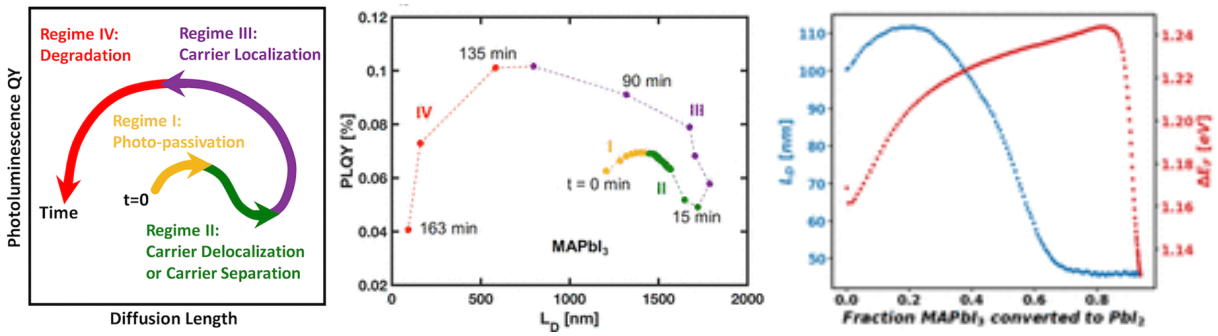

Figure 25. The Evolution of Photoluminescence Quantum Yield (PLQY), Quasi-Fermi Level Splitting (QFLS, ΔE_F), and Ambipolar Diffusion Length (L_D) over Time for Single $MAPbI_3$ Devices Degrading in Humid Air. (left) Semi-quantitative depiction of the evolution of PLQY versus L_d with characteristic regimes labeled.[30] (middle) Experimental evolution of PLQY versus L_d for a single $MAPbI_3$ device degrading in humid air.[30] (right) Experimental evolution of L_d (blue) and ΔE_F (red) versus the fractional degraded thickness for a different $MAPbI_3$ device degrading in humid air.

Although, we observe the QFLS to transition from increasing rapidly to increasing steadily well before the local extrema in the fitted HP-ETL interfacial deep defect (trap) density ($N_{tr,HP-ETL}$) and fitted electron mobility (μ_n), and we observe $N_{tr,HP-ETL}$ to increase instead of continuing to steadily decrease as would be expected from the QFLS's steady increase. To determine the source of these discrepancies, we consider the difference between our film and device degradation experiments. Indeed, the primary difference is the presence of the transport layers (TLs), electrodes, and applied bias in device experiments. Applied bias may accelerate degradation throughout the HP film as opposed to HP-TL interfaces and GBs which dominate photooxidation and thus lead to other phenomena. Although, we have not modeled this, and we expect the effects of the back electrode and ETL on gaseous reactant diffusion to be far more responsible for this discrepancy since all parameter evolutions are directly related to the diffusion behavior of gaseous reactants through the HP film along GBs. Indeed, HP films on glass substrates possess no encapsulating barrier to mass transport, allowing gaseous reactants to readily diffuse to the glass-side interface of the HP film. Additionally, in our photoconductivity measurements, the photocurrent flows laterally between two top-side contacts, meaning photogenerated carrier fluxes (and thus the importance of grain boundary (GB) properties) increase toward the film surface. This and the hastened diffusion of gaseous reactants through the HP film quickly reduces deep defect (trap) densities and isolates grains, causing the observed rapid increase in QFLS and L_D and early beginning of L_D decay to a plateau. Additionally, the rapid initial increase in QFLS concurrent with the rapid L_D increase again implies nearly all

defects exist at HP-TL interfaces and GBs, and the slow, steady increase in QFLS during and after L_D decay implies either slow removal of remaining deep defects (traps) at less accessible regions of HP-TL interfaces or GBs which require longer diffusion times for gaseous reactants to reach, or implies removal of deep defects (traps) in the bulk crystal of each grain as the isolated grains shrink. Last, the QFLS rapidly decays (i.e., SRH recombination increases significantly) after ≈80% extinction of HP film thickness, and this could occur due to both low mobilities allowing for greater trapping or creation of cationic deep defects (traps) due to the p-type stoichiometric shift during degradation.

Beyond the evolutions of fitted and derived drift-diffusion parameters, we also consider the evolutions of higher-level parameters (i.e., the diode fitting parameters and the solar cell parameters) and the influences of mechanistic modeling parameters on their higher-level parameters (e.g., the influences of diode parameters on the solar cell parameters) through our unique CSA to quantify the influence of each degradation mechanism on device performance decline. Specifically, the diode parameters which are theoretically described by deep defect (trap) densities and carrier mobilities (i.e., essentially all parameters other than G_{ehp}, R_{sh}, and R_s) are the dark reverse bias saturation current (J_0) and ideality factor (n_{id}). Indeed, in observing their evolutions with time (see Figure 26), we discover the times at which noticeable evolution changes occur align with those of the interfacial deep defect (trap) densities and carrier mobilities. Although, J_0 and n_{id} are highly correlated parameters since they both exist in and scale the exponential diode term in the non-ideal diode equation, causing them to exhibit an incredibly strong correlation which dominates their evolutions. Thus, despite exhibiting noticeable changes in evolution at similar times as the interfacial deep defect (trap) densities and carrier mobilities, their individual influences on V_{oc} and FF are much more exaggerated than their combined influences (see Figure 27 and Figure 32). These combined influences are thus a far more interpretable measure of the influences of deep defect (trap) densities and carrier mobilities on device performance. Now, regarding the evolutions of J_0 and n_{id}, J_0 and n_{id} both immediately undergo a rapid decrease at early times (i.e., before approximately 40% of T_{80}, enter a region of slow decline starting around 40-60% of T_{80}, and finally increase starting between 90% and 100% of T_{80}. Again, trends are clear when aggregating over all $MAPbI_3$ devices while large volatility among high-bandgap experiments masks these trends when considering the aggregation over all high-bandgap experiments (i.e., Figure 24 and Figure 26). Thus, we again show the evolutions of the volatile parameters (i.e., J_0 and n_{id} in this case) for the standard $MAPbI_3$ device first presented in Figure 12. Indeed, we observe the trends described for the $MAPbI_3$ devices for the single high-bandgap device considered, but to less of an extent. In sum, the similarity in the times at which appreciable changes in the evolution of these parameters occur compared with the interfacial deep defect (trap) densities and carrier mobilities aligns with the known relationship of these quantities with J_0 and n_{id}, and the repeated observation of higher volatility in these parameters for high-bandgap devices again implies either lower deep defect (trap) densities (as shown in Figure 24) or lower sensitivity of defect structure at interfaces and grain boundaries upon degradation compared with $MAPbI_3$ (see Section 6). We again note this is likely not due to the high-bandgap architecture's greater stability to photooxidation observed in our studies presenting kinetic rate law models for our three HP compositions.[16,19–21]

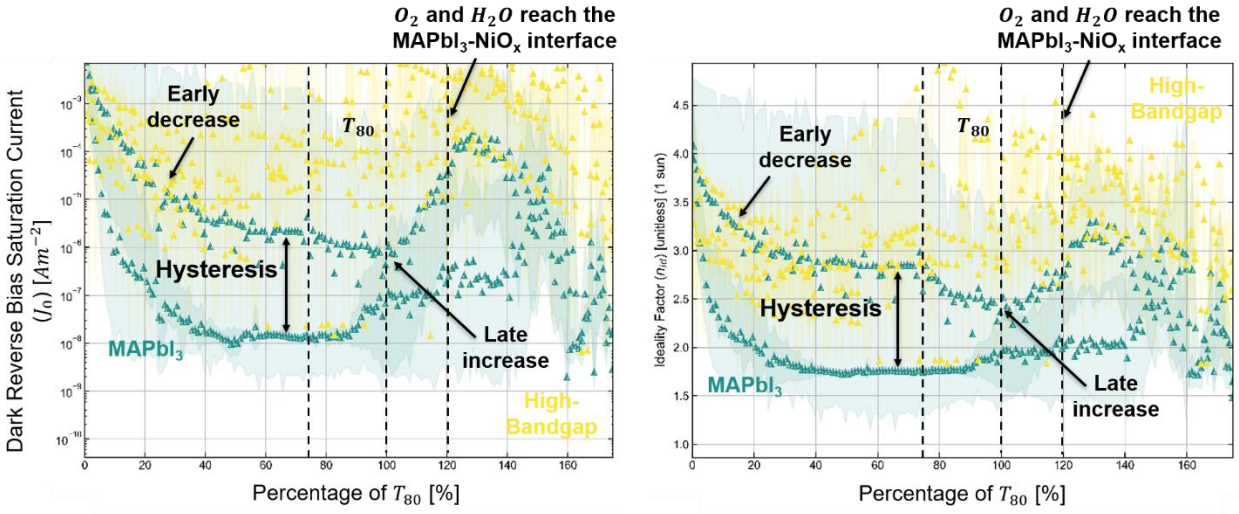

Figure 26. The Evolution of the Dark Reverse Bias Saturation Current (J_0) and Ideality Factor (n_{id}) over Time Averaged over All Experiments for Each Architecture. Scatterplots of the averages (shown as points) and standard deviations (shown as faded regions) of the (left) dark reverse bias saturation current (J_0) and (right) ideality factor (n_{id}) over degradation time (measured as a percentage of T_{80}) for our medium-bandgap (MAPbI$_3$) (green) and high-bandgap (yellow) architectures degrading in the conditions outlined in Table 6 (encoded according to the grid legend in Figure 4). Important features of parameter evolutions are labeled with bolded text and arrows, and operational lifetime (T_{80}) is indicated by the labeled dashed black line at 100% of T_{80}.

Now, as stated previously, we determine the influences of mechanistic modeling parameters on their higher-level parameters (e.g., the diode fitting parameters' influences on the solar cell parameters) through our unique CSA to quantify the influence of each degradation mechanism on device performance decline. Although, as discussed in Section 4.1.4, the high volatility in drift-diffusion fitting parameter values over time causes excessive error in the calculated parameter sensitivity coefficients and thus influences on higher-level parameters (i.e., both the diode and solar cell parameters). Nevertheless, despite the larger error, we observe the HP-ETL interfacial deep defect (trap) density ($N_{tr,HP-ETL}$) and electron mobility (μ_n) to be the primary drivers of V_{oc} changes (≈61.3% and ≈21.3% of V_{oc} changes by T_{80}, respectively) with a light decrease caused by shunt resistances ($\approx -4.4\%$ of V_{oc} changes by T_{80}) and moderate decreases caused by G_{ehp} at later times ($\approx -7.1\%$ of V_{oc} changes by T_{80}, similar to that for J_{ph} in Figure 27 below) for the single MAPbI$_3$ device in Figure 12. Very minor influences are reported for the remaining drift-diffusion fitting parameters (see Section 6). Moreover, as expected, the influences of J_0 and n_{id} are nearly symmetric (i.e., near equal and opposite with a strong negative correlation), but their combined influence (≈76.4% of V_{oc} changes by T_{80}) logically accounts for almost all V_{oc} changes up to T_{80}. Additionally, their combined influence is similar to that of $N_{tr,HP-ETL}$ and μ_n, further supporting our attribution of J_0, n_{id}, and V_{oc} changes primarily to deep defect (trap) passivation and band misalignment at the HP-ETL interface and grain boundaries. This exhibits the power of our unique CSA in comparison with analyzing parameter evolutions over time alone. Regarding photogenerated current, the electron-hole pair (EHP) generation rate (G_{ehp}) and photocurrent (J_{ph}) cause a slow, accelerating decrease in V_{oc} at late times ($\approx -7.1\%$ from G_{ehp} and $\approx -13.8\%$ for J_{ph} by T_{80}, strong after 250% of T_{80}) concurrent

with J_{sc} burn-in. This is logical since J_{sc}-related quantities should not limit V_{oc} until decreasing sufficiently to be outweighed by recombination losses at V_{oc}. Additionally, the similar order of magnitude of the influences of G_{ehp} and J_{ph} on V_{oc} further suggest this mechanism. Last, series resistance exerts an insignificant influence and V_{oc} for the diode and drift-diffusion fits while shunt resistances exert ≈ 9.7% and ≈ 4.4% of V_{oc} changes by T_{80} for the diode and drift-diffusion fits, respectively. Indeed, these phenomena exclusively drive the early-time increases in and are primary contributors to the later-time decreases in V_{oc}, FF, and PCE (alongside all phenomena discussed in this work). Additionally, as stated in Section 3.1.3, these phenomena would likely influence J_{sc}-related parameters in a similar manner as for the V_{oc} and FF in devices with HP film thicknesses sufficiently large to cause diffusion length limitations to carrier extraction. Overall, the unique CSA supports the proposed mechanisms for V_{oc} changes during degradation including the strong negative correlation between J_0 and n_{id} and between their influences, the dominating influences of J_0 and n_{id} or $N_{tr,HP-ETL}$ and μ_n on V_{oc} with moderate contributions from J_{sc}-related quantities (i.e., J_{ph} and G_{ehp}) and R_s and R_{sh}. Additionally, this rough similarity among the influences of the diode and drift-diffusion fitting parameters further affirms these conclusions.

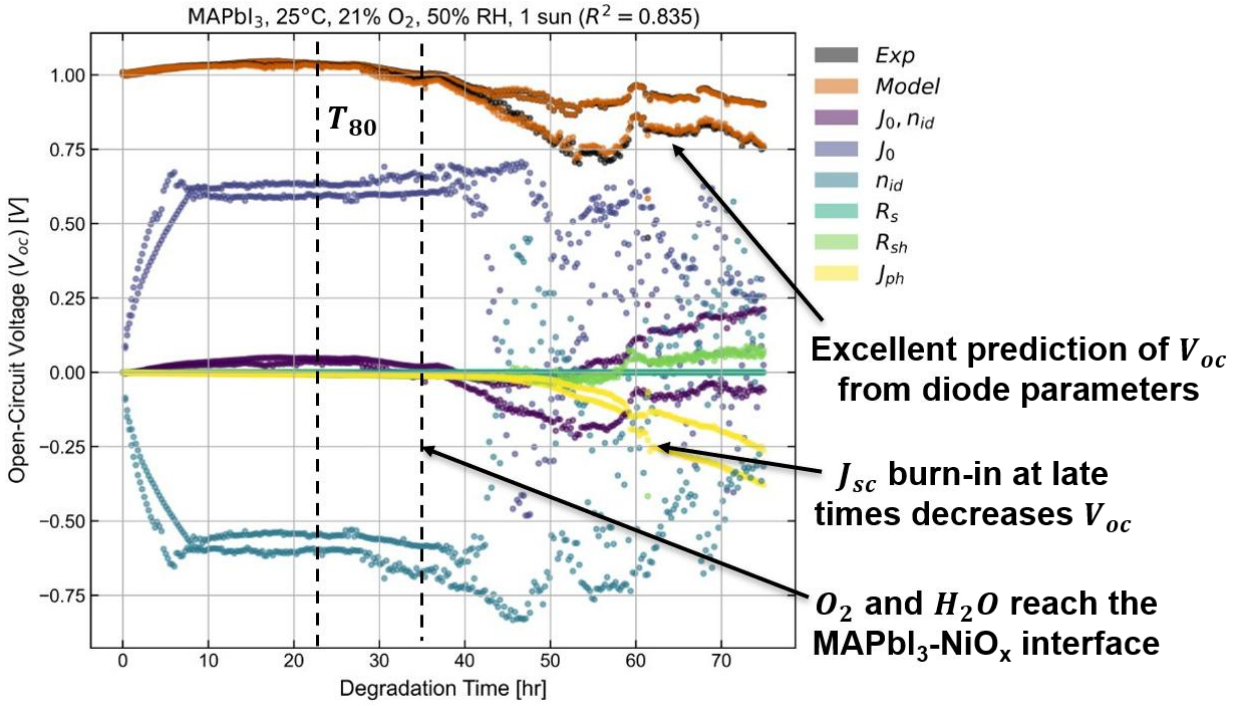

Figure 27. Integrated Influences of Diode Fitting Parameters on V_{oc} over Time for a Single $MAPbI_3$ Device. Scatterplot of the unnormalized integrated influences of the diode fitting parameters on V_{oc} over time (measured as a percentage of T_{80}) for the $MAPbI_3$ device degradation in Figure 12. As above, simulation type and scan type are encoded for single experiments according to the grid legend in Figure 20.

Regarding these parameters' relationships with degradation conditions, in $MAPbI_3$ devices, the fractional V_{oc} at T_{80} exhibits a quadratic dependence on temperature with a local maximum at the same temperature at which a sharp rise is observed for the fractional effective degradation profile parameters and J_{sc}-related quantities: ≈45°C (see Figure 28(middle row)). As for the J_{sc}-related

parameters, this similarity in temperature dependence with that of the fractional effective degradation profile parameters again implies the fractional V_{oc} and thus the combined influences of its lower-level parameters are also subject to the same two competing phenomena, postulated above to be the positive and negative Arrhenius dependences of the DPO and WPO rates predicted by our kinetic rate law model. In contrast, the fractional V_{oc} at T_{80} for high-bandgap devices steadily declines with temperature, and we attribute this to the monotonic decrease in hole mobility (see Figure 24). Last, low-bandgap devices exhibit no significant change in fractional V_{oc} with temperature, likely due to the overwhelming dependence of performance decline on the decline in J_{sc}-related parameters due to HP film absorptivity loss (caused by its chemical decomposition). Regarding the nonfractional V_{oc} at T_{80}, its values exhibit negative, linear dependences with temperature for all architectures (very strong for $MAPbI_3$), and we attribute this to the general, strong temperature dependence of V_{oc} in solar cells independent of degradation. Specifically, increasing temperature increases recombination rate, decreasing the quasi-Fermi level splitting (QFLS) and thus V_{oc}. The strong, negative dependence observed for the nonfractional V_{oc} at T_{80} therefore masks the weaker dependence of the fractional V_{oc} at T_{80} in $MAPbI_3$ devices (see Figure 28(middle row)).

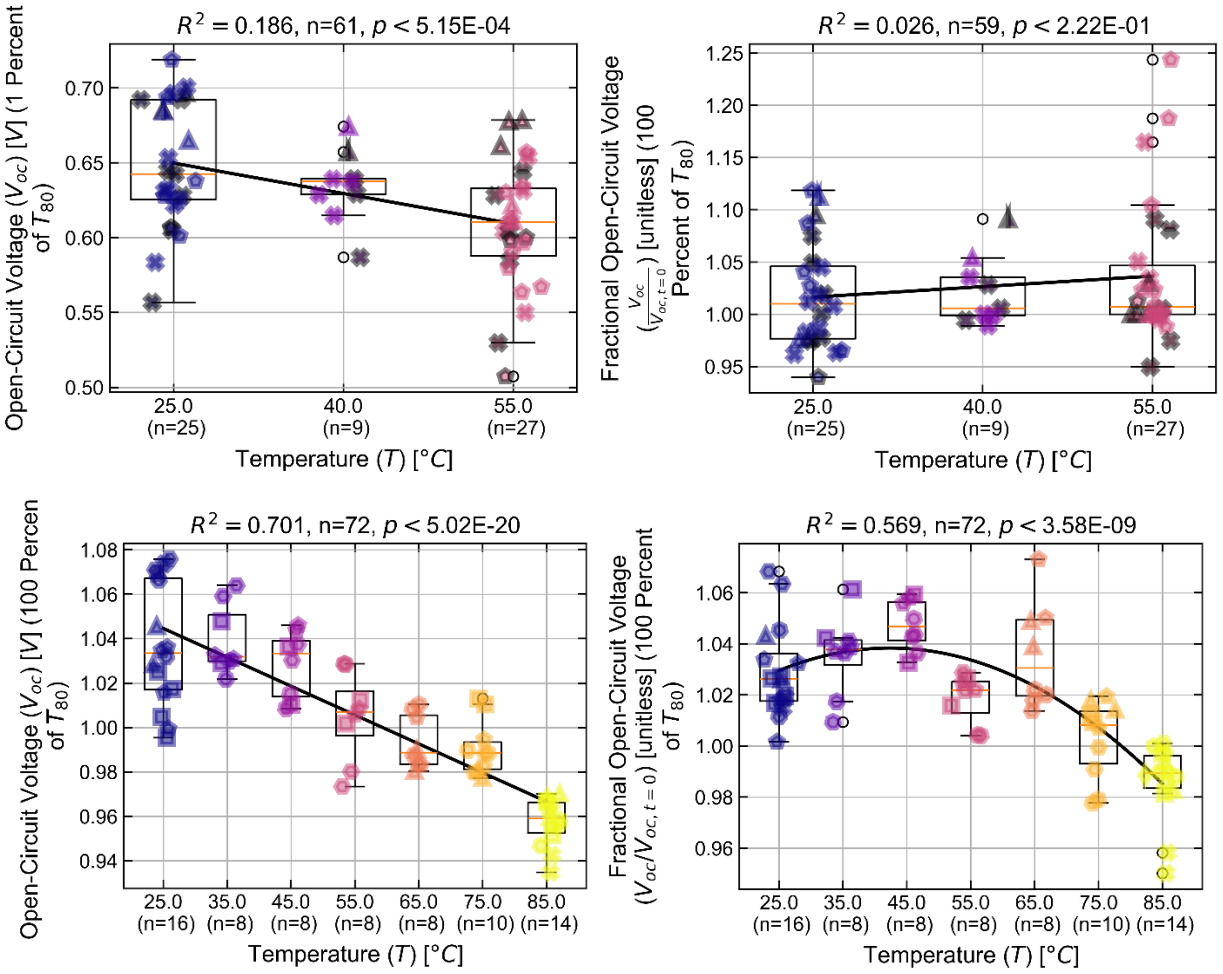

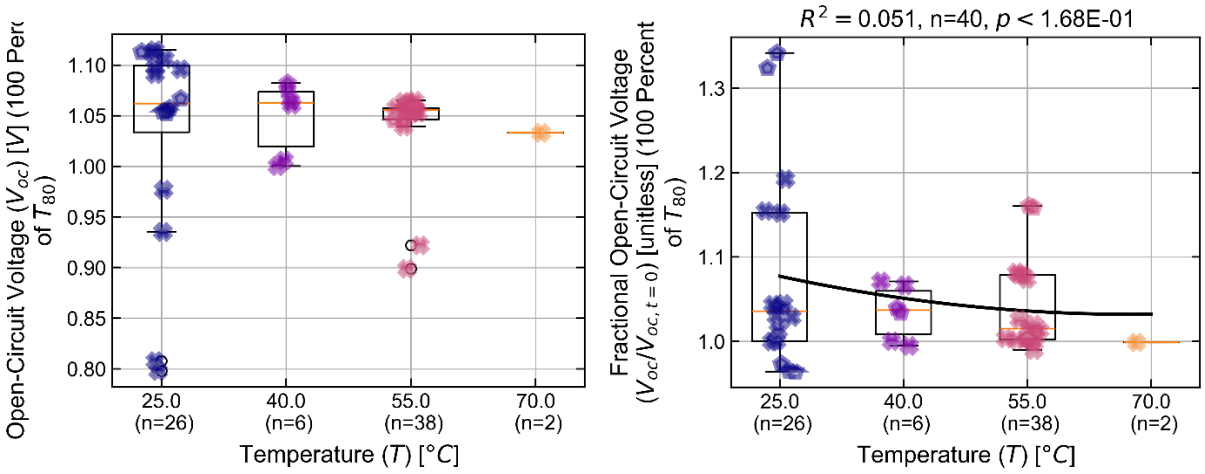

Figure 28. Boxplots of Nonfractional (V_{oc}) and Fractional Open-Circuit Voltage ($V_{oc}/V_{oc,t=0}$) at T_{80} versus Temperature for Each Architecture. Specifically, we present the (left column) nonfractional and (right column) fractional V_{oc} at T_{80} versus temperature for the (top row) low-bandgap, (middle row) $MAPbI_3$ and (bottom row) high-bandgap architectures. As above, degradation conditions are tabulated for each architecture in Table 6 and encoded according to the grid legend in Figure 4. Additionally, we show the R^2 value for a linear or quadratic polynomial fit which captures general trends of parameter values at T_{80} with degradation conditions, and we report the p-value from a linear regression to determine the significance of changes with degradation conditions.

Meanwhile, the fractional J_0 (on a logarithmic scale) and fractional n_{id} at T_{80} exhibit strong, positive, near-linear relationships with temperature for $MAPbI_3$ devices and insignificant relationships with temperature for high-bandgap devices (shown only for $MAPbI_3$ in Figure 29 for concision). Although, their values at early times are highly temperature-dependent (not shown) and change rapidly with degradation, and their values at moderate and late times are much more similar to one another and slower-changing across experiments (see Figure 26). Thus, we postulate the temperature dependence of the fractional J_0 and n_{id} at T_{80} in $MAPbI_3$ devices results from the temperature dependence of their initial values instead of their rates of change caused by degradation. Indeed, the nonfractional J_0 and n_{id} at T_{80} exhibit only weak, negative temperature dependences for both $MAPbI_3$ and high-bandgap architectures. These observations align with the strong, negative temperature dependence of the nonfractional V_{oc} at T_{80}. Although, since these parameters are highly correlated, only their combined influence (see Section 2.2.7 and Figure 27) is meaningful for analyzing the diode parameters' influences on V_{oc}. Indeed, their combined influence at T_{80} is near-equivalent to the V_{oc} change throughout degradation (see Figure 27) and thus shares a near-equivalent temperature dependence (see Section 6).

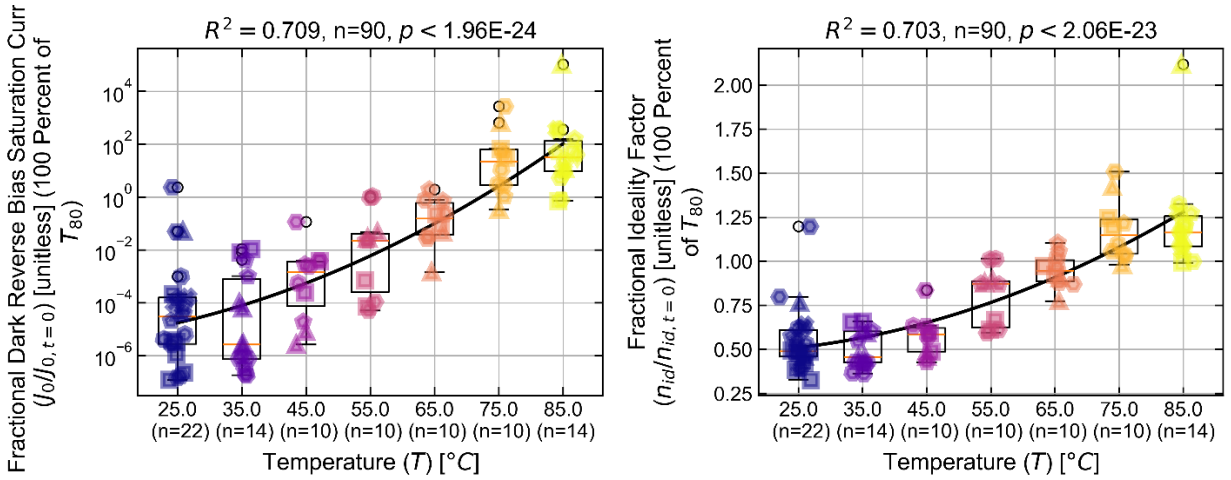

Figure 29. Boxplots of Fractional Dark Reverse Bias Saturation Current (J_0) and Ideality Factor (n_{id}) at T_{80} versus Temperature for the $MAPbI_3$ Device Degradation Dataset. Specifically, we present the (left) fractional J_0 and (right column) fractional n_{id} at T_{80} versus temperature for the $MAPbI_3$ device degradation dataset. As above, degradation conditions are tabulated for each architecture in Table 6 and encoded according to the grid legend in Figure 4. Additionally, we show the R^2 value for a linear or quadratic polynomial fit which captures general trends of parameter values at T_{80} with degradation conditions, and we report the p-value from a linear regression to determine the significance of changes with degradation conditions.

Last, of the fitted deep defect (trap) densities and carrier mobilities, only the fractional $N_{tr,HP-ETL}$ and μ_p (nonfractional for $MAPbI_3$ and fractional for high-bandgap) at T_{80} exhibit temperature dependences. Specifically, the fractional $N_{tr,HP-ETL}$ at T_{80} exhibits monotonic, positive temperature dependences while μ_p (nonfractional for $MAPbI_3$ and fractional for high-bandgap) at T_{80} exhibits monotonic, negative temperature dependences (see Figure 30). Based on our postulated degradation scheme and the evolutions of the fitted interfacial deep defect (trap) densities and carrier mobilities, we postulate the HP-ETL interface and its nearby grain boundaries are fully degraded by T_{80} in every experiment, meaning temperature would not affect their values at T_{80}. Although, since temperature accelerates gaseous reactant diffusion and HP decomposition, and since gaseous reactants reach the HP-HTL interface around T_{80}, the extent to which the HP-HTL interface and its grain boundaries (which still may manifest changes in $N_{tr,HP-ETL}$) degrade likely increases with temperature, potentially causing the observed linear declines of $N_{tr,HP-ETL}$ and μ_p at T_{80} with temperature. Indeed, $N_{tr,HP-ETL}$ plateaus (near its original value) far after T_{80} for $MAPbI_3$ devices and near T_{80} for high-bandgap devices, meaning $N_{tr,HP-ETL}$ is still lower than its initial value by T_{80} for low-temperature (e.g., 25°C) experiments and is able to further increase by T_{80} with increasing temperature, leading to its observed positive temperature dependence in both $MAPbI_3$ and high-bandgap devices. Regarding the hole mobility (μ_p) at T_{80}, the fractional μ_p at T_{80} only exhibits temperature dependence in high-bandgap devices, and this aligns with the immediately observed decrease in high-bandgap devices and lack of change until $\approx T_{80}$ in $MAPbI_3$ devices (see Figure 24).

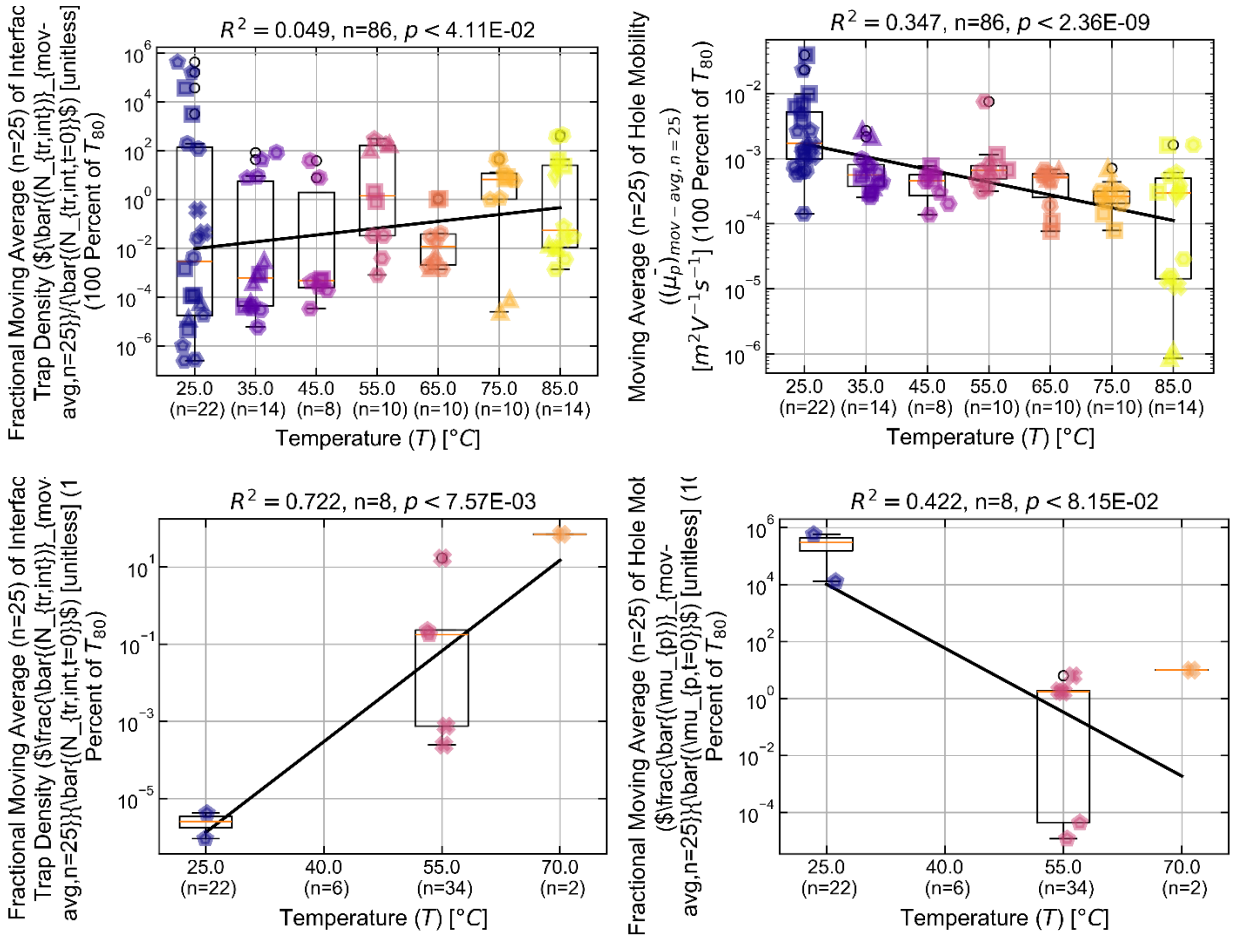

Figure 30. Boxplots of Deep Defect (Trap) Densities and Carrier Mobilities at T_{80} versus Temperature for the $MAPbI_3$ and High-Bandgap Architectures. Specifically, we present the (top left) nonfractional V_{oc}, (top right) fractional V_{oc}, (middle left) fractional J_0, (middle right) fractional n_{id}, (bottom left) fractional moving average (n=25) of $N_{tr,HP-ETL}$, and (bottom right) nonfractional moving average (n=25) of μ_p at T_{80} versus temperature. As above, degradation conditions are tabulated for each architecture in Table 6 and encoded according to the grid legend in Figure 4. Additionally, we show the R^2 value for a linear or quadratic polynomial fit which captures general trends of parameter values at T_{80} with degradation conditions, and we report the p-value from a linear regression to determine the significance of changes with degradation conditions.

Regarding the remaining degradation conditions, these V_{oc}-related parameters at T_{80} exhibit no significant trends in $MAPbI_3$ devices (noting that parameter relationships with oxygen concentration and illumination intensity are not considered), but we observe the fractional $N_{tr,HP-ETL}$ at T_{80} to decrease monotonically with oxygen concentration (not shown for concision). There are many possible explanations for this, but we postulate increasing oxygen concentration accelerates photooxidation and thus deep defect (trap) passivation before T_{80}. These boxplots are not shown for concision (see Section 6)). Overall, all of the above observations are sensible given the mechanistic relationships among parameters discussed above, again demonstrating the utility of combining degradation profile analysis with mechanistic modeling.

3.1.5 Shunt Resistance (R_{sh}) Decline Driving Fill Factor (FF) Decline

The last fitting parameters in the diode and drift-diffusion models which have not yet been discussed are the series resistance (R_s) and shunt resistance (R_{sh}). In our previous study of the evolutions of optoelectronic properties in degrading high-bandgap films[18] and in our $MAPbI_3$ device degradation study,[17] we postulated the primary driver of FF decline to be decreasing shunt resistance (R_{sh}) corresponding to shunt pathway formation during degradation. Indeed, we observe this phenomenon to occur in a remarkably similar manner for both $MAPbI_3$ and high-bandgap architectures (see Figure 31). Additionally, although full J-V scans were not collected for our low-bandgap devices, FF exhibits a similar evolution in our low-bandgap devices as in our $MAPbI_3$ and high-bandgap devices, and we thus postulate low-bandgap devices exhibit a similar decline in shunt resistance. Specifically, R_{sh} values begin at large, volatile values ranging from 1 to $10^4\ \Omega m^2$, decreasing rapidly until approximately 20% of T_{80} for both architectures and plateauing in high-bandgap devices at approximately $10^{-1}\ \Omega m^2$ (see Figure 31). Then, R_{sh} continues decreasing steadily until approximately 40% of T_{80} for $MAPbI_3$ devices followed by also plateauing around $10^{-1}\ \Omega m^2$. Then, around 60% of T_{80}, R_{sh} begins very slowly decreasing for both architectures, continuing far past T_{80} for high-bandgap devices while increasing steadily for $MAPbI_3$ devices. Although, since formed shunt pathways likely are not passivated during degradation, we postulate this final increase is caused by a sufficient loss in photogenerated current during J_{sc} burn-in (which is observed for MAPbI3 devices but not high-bandgap devices) to sufficiently reduce the shunting current such that the sensitivity of the simulated J-V curve (and thus fitting error metric) nearly vanishes, causing the shunt resistance to assume large, volatile values which are equivalent to negligible shunting current losses. This theory is primarily supported by this phenomenon's observation in $MAPbI_3$ devices (which experience J_{sc} burn-in) and not in high-bandgap devices. Meanwhile, the series resistance slowly increases for $MAPbI_3$ devices while remaining relatively constant in high-bandgap devices, increasing rapidly for $MAPbI_3$ devices beginning around 130% of T_{80}. A common explanation for series resistance increase in PSCs is the reaction of the silver (Ag) electrode with liberated iodine gas ($I_{2(g)}$) to form resistive silver iodide ($AgI_{(s)}$) salt,[131–134] and this potentially occurs faster in our $MAPbI_3$ devices due to the higher iodine concentration in the perovskite film and faster HP decomposition rate. Although, this is simply one of many possible explanations. Note that the series and shunt resistances shown in Figure 31 are the results of the diode model, not the drift-diffusion model, and that high volatility in drift-diffusion modeling results achieves only moderate correlation of the resistances between the two models (see Section 6). Last, regarding our low-bandgap devices, FF remains relatively constant throughout degradation and is volatile, implying both series and shunt resistances also exhibit this behavior throughout degradation (not shown since full J-V scans are not collected for low-bandgap devices). Last, with only the slight, volatile increase in V_{oc} for our degrading low-bandgap devices, PCE decline in our low-bandgap devices is also almost exclusively driven by J_{sc} decline.

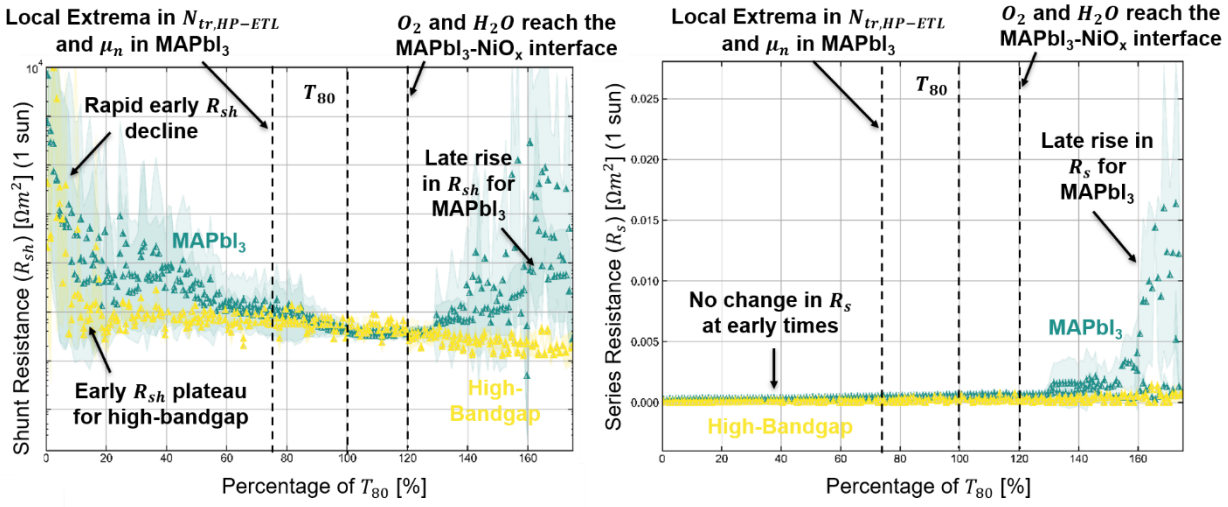

Figure 31. The Evolution of Series Resistance (R_s) and Shunt Resistance (R_{sh}) over Time Averaged over All Experiments for Each Architecture. Scatterplots of the averages (shown as points) and standard deviations (shown as faded regions) of the (left) shunt resistance (R_{sh}) and (right) series resistance (R_s) over degradation time (measured as a percentage of T_{80}) for our medium-bandgap ($MAPbI_3$) (green) and high-bandgap (yellow) architectures degrading in the conditions outlined in Table 6 (encoded according to the grid legend in Figure 4). Important features of parameter evolutions are labeled with bolded text and arrows, and operational lifetime (T_{80}) is indicated by the labeled dashed black line at 100% of T_{80}.

Regarding these parameters' influences on solar cell parameters, R_s and R_{sh} are well-known sources of FF losses in solar cells[33] and FF decline in degrading solar cells.[135–137] Specifically, R_s and R_{sh} are roughly equal to the J-V curve's slope at open-circuit and short-circuit conditions, respectively, meaning they directly influence FF alongside other parameters (namely carrier mobilities according to Le Corre *et al.*[51]). Indeed, according to our unique CSA, R_s and R_{sh} are the primary drivers of FF decline, contributing to roughly ≈20.9% and ≈33.9%, respectively, of the FF's change by T_{80} for the single $MAPbI_3$ device in Figure 12 as determined through our unique CSA (see Figure 32). Although, the decrease in J_0 due to early-time deep defect (trap) reduction (i.e., $N_{tr,HP-ETL}$ decrease) is the primary driver of FF change at early times and a secondary contributor by T_{80} (i.e., ≈ 42.3% by T_{80}). Last, n_{id} and J_{ph} contribute ≈ 3.2% and ≈ 0.3% to FF changes by T_{80}. Regarding the CSA of the drift-diffusion fit, the HP-ETL interfacial deep defect (trap) density ($N_{tr,HP-ETL}$) contributes ≈ 12.5% of the FF changes by T_{80} while carrier mobilities contribute ≈ 37.5%, supporting Le Corre et. al's observations of the FF's strong dependence on carrier mobilities.[51] Although, as discussed in Section 4.1.4, the high volatility in drift-diffusion fitting parameter values over time causes excessive error in the calculated parameter sensitivity coefficients and thus influences on higher-level parameters (i.e., both the diode and solar cell parameters). Overall, the unique CSA of FF changes during degradation which are not provided by analyzing the evolutions and correlations among parameters over degradation alone. Specifically, the decrease in J_0 and the corresponding decrease in $N_{tr,HP-ETL}$ and increase in μ_n during deep defect (trap) reduction are the primary drivers of FF change at early times and in FF increase over degradation. Then, as degradation

progresses, R_s and R_{sh} are the primary drivers of FF decline as expected from their standard effects on FF. This again demonstrates the utility of our unique CSA in understanding mechanisms of device performance decline compared with the evolutions and correlations among parameters over degradation. Furthermore, this rough similarity among the influences of the diode and drift-diffusion fitting parameters further affirms these conclusions.

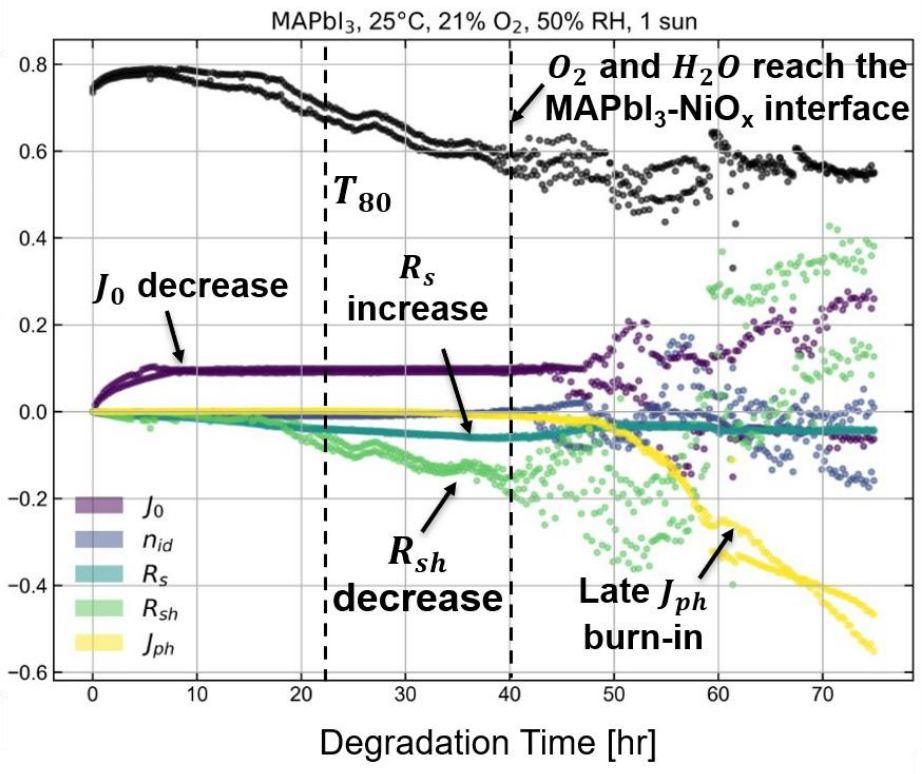

Figure 32. Integrated Influences of Diode Fitting Parameters on FF over Time for All Degradation Conditions and Architectures. Scatterplot of the unnormalized integrated influences of the diode fitting parameters on FF over time (measured as a percentage of T_{80}) for the $MAPbI_3$ device degradation in Figure 12. Additionally, as above, simulation type and scan type are encoded for single experiments according to the grid legend in Figure 20.

Regarding these parameters' relationships with degradation conditions, the fractional FF at T_{80} exhibits a nearly opposite trend compared with the fractional J_{sc} in $MAPbI_3$ devices, implying the FF declines independently of the J_{sc} decline (e.g., due to shunt pathway formation) where the opposing temperature dependence is only an artifact of the temperature dependence of T_{80} caused by that of the J_{sc} decline. In contrast, high-bandgap devices exhibit no temperature dependence of the fractional FF at T_{80} (see Figure 33), and the nonfractional FF at T_{80} exhibits a quadratic-like, positive temperature dependence in all architectures due to the temperature dependence of the relevant nonfractional diode and drift-diffusion parameters (e.g., R_{sh}).

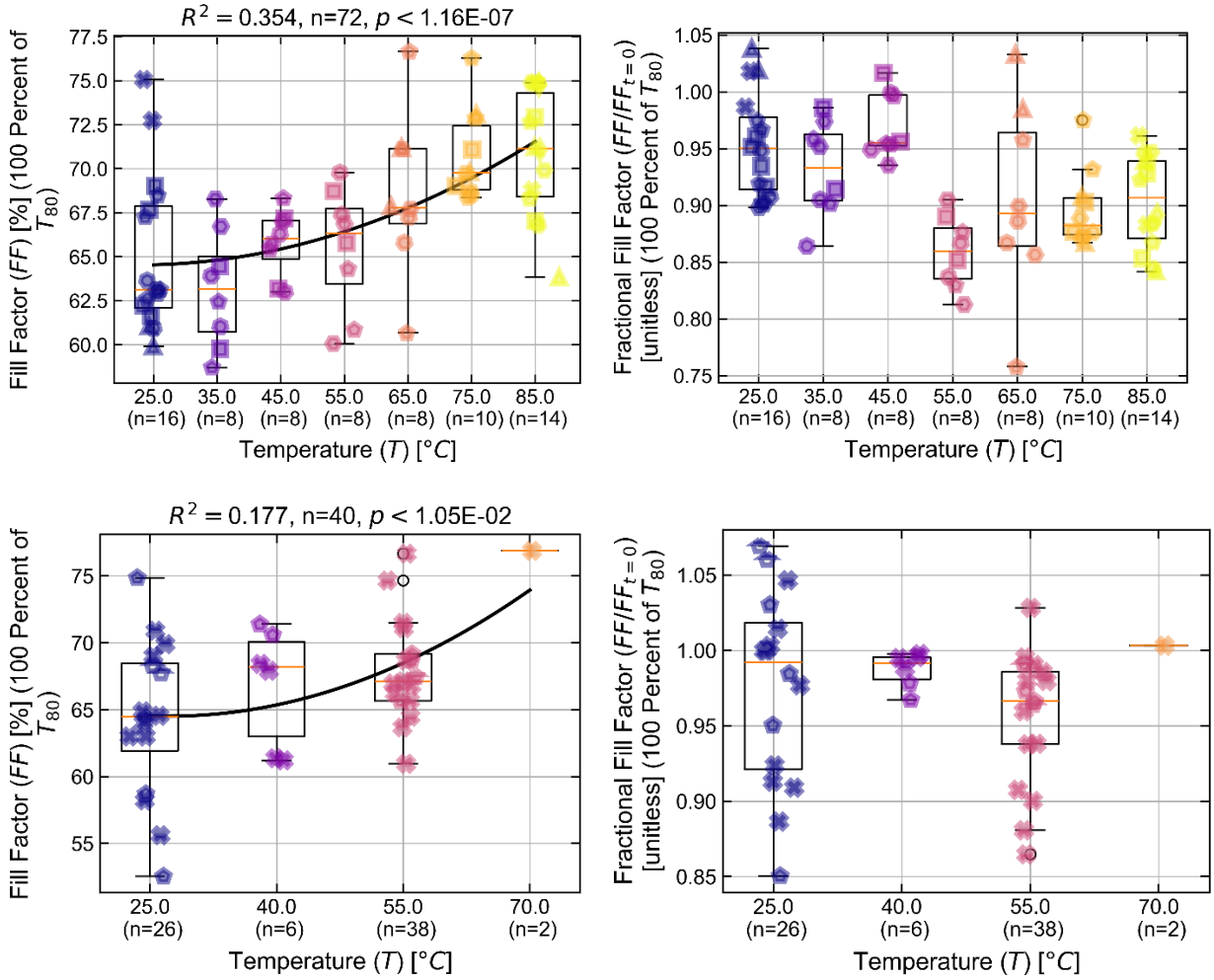

Figure 33. Boxplots of Nonfractional and Fractional Fill Factor (FF) at T_{80} versus Temperature for the MAPbI$_3$ and High-Bandgap Architectures. Specifically, we present the (left column) nonfractional FF and (right column) fractional FF at T_{80} versus temperature for the (top row) MAPbI$_3$ and (bottom row) high-bandgap architectures. The low-bandgap architecture is not shown since their fractional FF at T_{80} exhibits no significant temperature dependence. As above, degradation conditions are tabulated for each architecture in Table 6 and encoded according to the grid legend in Figure 4. Additionally, we show the R^2 value for a linear or quadratic polynomial fit which captures general trends of parameter values at T_{80} with degradation conditions, and we report the p-value from a linear regression to determine the significance of changes with degradation conditions.

Indeed, the primary diode and drift-diffusion parameters related to FF decline according to our unique CSA (see Figure 32) are J_0, R_s, and R_{sh}, and none of their fractional values at T_{80} correlate well with temperature. Additionally, the positive temperature dependence of the nonfractional FF is easily explained with the corresponding positive dependence of the nonfractional R_{sh}. The temperature dependence for the fractional J_0 at T_{80} is shown in Figure 29, and the temperature dependences of R_s and R_{sh} are not shown for concision (see Section 6). Last, no significant relationships are observed with the remaining degradations (see Section 6). Overall, all of the above observations are sensible given the mechanistic relationships among

parameters discussed above, again demonstrating the utility of combining degradation profile analysis with mechanistic modeling.

3.1.6 Postulating the Mechanisms Underlying the Evolutions of the Current-Voltage (J-V) Scan Hysteresis Metrics

As discussed in Section 1.3.2, drift-diffusion models were originally applied to PSCs to develop a mechanistic model of current-voltage (J-V) scan hysteresis caused by the migration of mobile ions (especially halide-based defects such as iodide anions (I^-) and vacancies (V_I^+) in $MAPbI_3$). Additionally, as stated previously, this phenomenon was discovered by Henry Snaith and coworkers HP PVs)[47] in 2014 and is now a widely accepted barrier to the scalability of HP PVs (alongside instability). Thus, this work's mechanistic modeling would be most complete with application of Koster *et al.*'s transient drift-diffusion model to all collected J-V hysteresis loops with ion concentrations and mobilities becoming important fitting parameters with clear evolutions describing the changes in the corresponding J-V hysteresis metrics. Although, as explained in Section 2.2.4, the transient model was not utilized in this study and is thus recommended as a primary avenue for future work in improving these mechanistic models for degrading PSCs. Nevertheless, we combine our analysis of the HP film degradation profile and mechanistic modeling of J-V scans over time to explain the observed evolutions in hysteresis metric and their relationship with degradation conditions for all architectures.

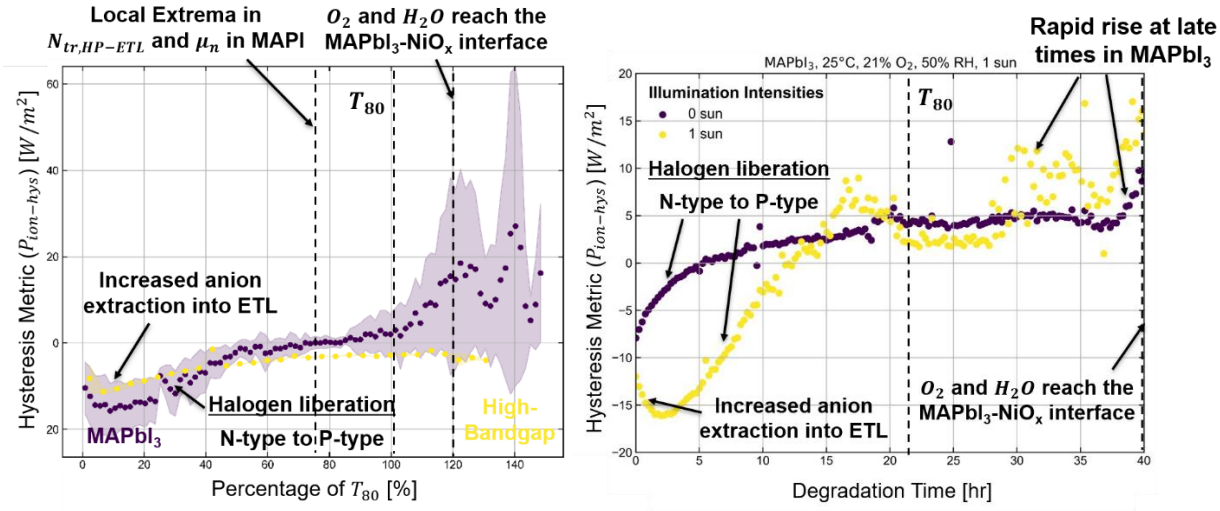

Figure 34. The Evolution of the Hysteresis Metric ($P_{ion-hys}$) over Time over All Experiments for Each Architecture or Illumination Intensity. (left) Scatterplot of the averages (shown as points) and standard deviations (shown as faded regions) of the hysteresis metric ($P_{ion-hys}$) over degradation time (measured as a percentage of T_{80}) for our medium-bandgap ($MAPbI_3$) (purple) and high-bandgap (yellow) architectures degrading in the conditions outlined in Table 6 (encoded according to the grid legend in Figure 4). (right) Scatterplot of the hysteresis metric ($P_{ion-hys}$) over degradation time for the single $MAPbI_3$ device in Figure 12 at 0 sun and 1 sun illumination intensities.

3.1.6.1 Analysis of Hysteresis Metric Sign and Magnitude at Early Times in Light and Dark Conditions

On average over all $MAPbI_3$ and high-bandgap devices, hysteresis metric values begin at around -10 W/m^2 and -8 W/m^2 at 1 sun illumination intensity and around -7 W/m^2 and -5 W/m^2 at 0 sun illumination intensity, respectively (see Figure 34 and Section 6).[63] Then, at early times, the 1-sun hysteresis metric decreases (increases in magnitude) slightly for both $MAPbI_3$ and high-bandgap devices (with the decrease for $MAPbI_3$ devices slightly larger on average than the high-bandgap devices), reaching local minima at approximately 10% of T_{80}. Similarly, for MAPbI3 devices, the 1-sun hysteresis index (HI) decreases slightly and reaches a local maximum around 20% of T_{80}, and high-bandgap devices exhibit no significant changes in hysteresis index (HI) at early times. In contrast to the 1-sun hysteresis metric, the 0-sun hysteresis metric steadily increases (decreases in magnitude) and finally plateaus around 100% of T_{80} when the gaseous reactants reach the HP-HTL interface. Note that no 0-sun hysteresis index (HI) exists because PCE is not a valid quantity in dark conditions. Additionally, given these differences in the evolutions of the hysteresis metric and hysteresis index (HI), it is important to consider their relative accuracy. Specifically, the hysteresis index (HI) is more volatile than the hysteresis metric over all time and experiments, and this is due to the hysteresis index's limited consideration of only the PCE (which corresponds only to MPP) whereas the hysteresis metric accounts for changes in J-V hysteresis along the entire curve through integration. The hysteresis metric is thus a more precise measure of J-V hysteresis, but we nonetheless consider the evolutions in both given their similarities.

At all times before the 1-sun evolutions plateau to the 0-sun evolutions and possibly change sign, the 1-sun hysteresis metric is larger in magnitude than the 0-sun metric, implying greater ion accumulation at interfaces and thus greater ion concentrations under illumination than in dark conditions. Indeed, this aligns with experimental observations and computational predictions of greater ionic defect concentrations under illumination due to reaction of photoexcited carriers with lattice elements (see Section 6).[138–142] Indeed, we reference this fact to postulate the role of iodide vacancies (V_I^+) as the primary adsorption sites for gaseous oxygen in photooxidation of $MAPbI_3$.[16] Additionally, regarding sign, the hysteresis metric and index subtract the forward scan from the reverse scan, meaning the initially negative hysteresis metric suggests forward scans exhibit greater power than reverse scans. Moreover, since forward scans are performed after reverse scans in our measurement cycles, and since we expect ions to migrate further toward interfaces in the later (sub-V_{MPP}) portion of the reverse scan (see Figure 18 and Figure 36, we expect ion migration to inhibit performance of the forward scan relative to the reverse scan and thus yield a positive hysteresis metric. Although, since we observe a negative hysteresis metric, another ionic phenomenon must be occurring. Specifically, we recognize the 1-sun hysteresis metric undergoes this initial decrease with a similar profile as the HP-ETL interfacial deep defect (trap) density ($N_{tr,HP-ETL}$) and electron mobility (μ_n), implying the carrier mobilities at the HP-ETL interface could cause this decrease in an already negative 1-sun hysteresis metric. Specifically, the primary mobile ion in HPs (interstitial iodide anion (I^-)) has been shown to enter fullerene-based electron transport layers (ETLs),[55–57] meaning the mid-scan regions of applied biases less than V_{MPP} may cause these anions to enter the ETL, reducing interfacial ion accumulation. This would improve performance for the forward scan and lead to the observed negative hysteresis metric. Additionally, the primary mobile defect ions in $MAPbI_3$ are iodide vacancies (V_I^+) and interstitial iodide (I^-), and since the mobility of iodide vacancies (V_I^+) has been reported to be a factor of ≈1000 lower than interstitial iodide (I^-), the negative

effect of ion accumulation at the HP-TL interfaces is likely outweighed by anion extraction into the ETL (i.e., not due to a large excess of cations compared with anions). Furthermore, this theory suggests the initial decrease in the 1-sun hysteresis metric is due to increased anion extraction into the ETL due to increased carrier mobilities at the HP-ETL interface during deep defect (trap) reduction upon its degradation (see Figure 24). Although, this decrease (increase in magnitude) is not observed for the 0-sun hysteresis metric (i.e., in dark conditions), meaning the increase in anion extraction into the ETL due to increased carrier mobilities at the HP-ETL interface does not outweigh standard ion accumulation at the HP-TL interfaces in dark conditions. Since the only difference in this case is the lack of illumination, this is likely due to an insufficient concentration of photoexcited carriers in dark conditions. Specifically, under illumination, photogenerated carriers react with the perovskite to form additional mobile ionic defects (see Section 6).[138–142] Additionally, since the trap occupation probability is high > 90%) for the HP-ETL interface under 1 sun illumination intensity (see Section 6), we postulate the photogenerated free carriers fill and neutralize most remaining deep defect states, increasing free carrier and ion mobilities across the HP-ETL interface. Thus, both mobile ionic defect formation and filling of HP-ETL interface deep defect states by photogenerated carriers may increase the hysteresis effect of the anion extraction into the ETL enough for it to appear in the hysteresis metric evolution. Regarding the hysteresis index (HI), its inability to show this phenomenon suggests the hysteresis is observed in a range of the J-V curve displaced from MPP, again illustrating the advantage of the hysteresis metric over the hysteresis index (HI).

In sum, standard electric field screening and anion extraction into the ETL are therefore primary, competing contributors to J-V scan hysteresis for both $MAPbI_3$ and high-bandgap architectures, and given the similarity between the two architectures, we expect the low-bandgap devices to exhibit similar behavior. Additionally, at early times, anion extraction into the ETL likely outweighs ion accumulation at the HP-TL interfaces, yielding the observed negative hysteresis metric and index.

Following these local minima, the 1-sun hysteresis metric and hysteresis index steadily increase (decrease in magnitude) and plateau roughly to the value of the 0-sun hysteresis metric plateau value (i.e., about +2 W/m^2 for $MAPbI_3$ devices and -3 W/m^2 for high-bandgap devices) at about 60% of T_{80}. Based on the above logic, this steady increase (decrease in magnitude) in the hysteresis metric implies the ratio of mobile anion to cation concentration may decrease over degradation time. Alternatively, anion extraction into the ETL may become outweighed by ion accumulation at interfaces due to decreased carrier mobilities at the HP-ETL interface caused by band misalignment of grains with bordering degradation products. Indeed, during degradation, halogen gases (e.g., iodine gas ($I_{2(g)}$) in $MAPbI_3$) are liberated from the HP film,[16,19–21] leaving the film halogen-deficient, metal-rich, and removing anionic defects (namely mobile interstitial iodide anions (I^-) in $MAPbI_3$) while creating additional cationic defects (namely mobile iodide vacancies (V_I^+) in $MAPbI_3$) (see Section 6). The film thus transitions from slightly n-type or intrinsic behavior to p-type during degradation, but note that both cationic and anionic defects are present. Thus, both decreased carrier mobilities due to band misalignment and a gradual shift from slightly n-type to p-type behavior due to halogen gas liberation are possible contributors to the 1-sun and 0-sun hysteresis metric and hysteresis index (HI) increases (decreases in magnitude). Although, the hysteresis metric for high-bandgap devices increases (decreases in magnitude) much more than the corresponding hysteresis index while the changes are similar for $MAPbI_3$ devices. This implies this phenomenon is observed in a range of the J-V curve displaced from MPP, again illustrating the advantage of the hysteresis metric over the hysteresis index

(HI). A detailed review of defect physics in HPs and the corresponding effects of degradation will be provided in a future publication and in a future version of this thesis on our "DegradePV" GitHub repository (see Section 6).[63]

Last, as for all parameters other than J_{sc}, J_{ph}, and G_{ehp}, the hysteresis metric and hysteresis index (HI) will have plateaued when the gaseous reactants reach the HP-HTL interface and complete grain isolation. This implies the changes in mobile ion concentrations due to deep defect (trap) reduction and material degradation cease changing after all grains have been isolated, and this further implies most defects creating mobile ions (e.g., iodide vacancies (V_I^+) and interstitial iodide anions (I^-) in $MAPbI_3$) exist at HP-TL interfaces and grain boundaries[46,52] (see Section 6). Additionally, there is no statistically significant difference between the 0-sun and 1-sun hysteresis metrics after the plateau, implying the interfacial accumulation of ions indeed dominates J-V hysteresis while anion extraction into the ETL is independent of photogenerated carriers. Additionally, we have postulated band misalignment with degradation products causes the observed mobility reductions for all electrons and anions, and this phenomenon is independent of carrier charge, where it occurs for all carriers. Thus, when gaseous reactants degrade the HP-HTL interface, we expect cation mobilities and thus their ability to accumulate at the HP-HTL interface to slow, causing a decrease in hysteresis metric (and its magnitude). Although, the hysteresis metric and hysteresis index (HI) plateau roughly concurrently with the HP-HTL interface degradation (i.e., at ≈100% of T_{80}), meaning the corresponding decrease in hysteresis metric decrease likely manifests as a lower plateau value.

Thus, despite the lack of transient drift-diffusion modeling of our J-V scans, the combination of our degradation profile analysis, evolutions of the presented parameters, and evolution of the hysteresis metric under light and dark conditions enabled postulation of the mechanisms in which ion-based J-V hysteresis evolves over degradation. As a key barrier to HP PV scalability and a contributor to instability,[104] such mechanisms are crucial to modeling device performance decline.

3.1.6.2 Analysis of the Relationships of Parameter Values at T_{80} with Degradation Conditions

Regarding the relationships of the hysteresis metric and hysteresis index (HI) at T_{80} with degradation conditions, the fractional and nonfractional 1-sun hysteresis metrics at T_{80} follow a positive quadratic relationship with temperature in $MAPbI_3$ devices and a positive linear relationship in high-bandgap devices. Specifically, in $MAPbI_3$ devices, the fractional and nonfractional 1-sun hysteresis metrics at T_{80} are approximately constant with temperature from 25°C to 55°C for $MAPbI_3$ followed by increasing at an increasing rate for temperatures higher than ≈55°C. Moreover, based on the above discussion, the hysteresis metric increases (decreases in magnitude) by and plateaus around T_{80}, and since increasing temperature shortens the time required to reach this plateau due to increased gaseous reactant diffusion rate, we postulate the final plateau values are the source of the observed positive temperature dependence. Mechanistically, this corresponds to a deeper shift into p-type behavior by T_{80}, and we postulate this is due to an increased degradation rate. Note that greater ion concentrations exist at higher temperatures since defect formation is governed by thermally-activated Boltzmann factors of formation energies, but this would not explain the temperature dependence being equally strong for the fractional hysteresis metric (which is normalized and thus not dependent on the initial hysteresis metric and thus ion concentrations). Last, no significant relationships with the remaining degradation conditions were identified for either architecture. Last, no significant relationships are observed with the remaining degradations (see Section 6). Overall, all of the

above observations are sensible given the mechanistic relationships among parameters discussed above, again demonstrating the utility of combining degradation profile analysis with mechanistic modeling.

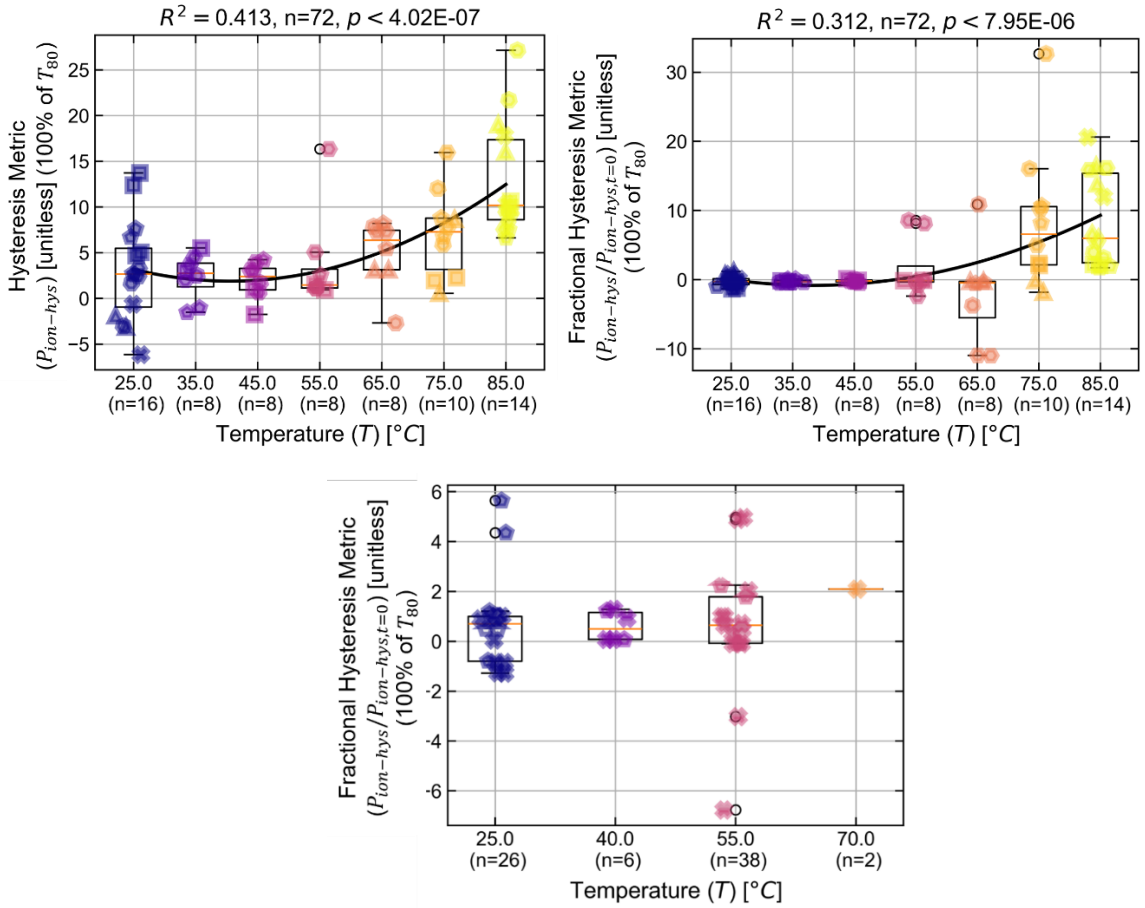

Figure 35. Boxplots of the Nonfractional and Fractional Hysteresis Metric (HI_{int}) versus Temperature for the $MAPbI_3$ and High-Bandgap Architectures. Specifically, we present the (left column) nonfractional HI_{int} and (right column) fractional HI_{int} at T_{80} versus temperature for the (top row) $MAPbI_3$ and (bottom row) high-bandgap architectures. Again, the low-bandgap architecture is not considered since full J-V hysteresis loop scans are not collected for these devices. As above, degradation conditions are tabulated for each architecture in Table 6 and encoded according to the grid legend in Figure 4. Additionally, we show the R^2 value for a linear or quadratic polynomial fit which captures general trends of parameter values at T_{80} with degradation conditions, and we report the p-value from a linear regression to determine the significance of changes with degradation conditions.

*3.1.7 Concluding Remarks – Influences of Mechanistic Modeling Parameters on Power Conversion Efficiency (**PCE**) Over Degradation Through CSA and a Novel PSC Device Degradation Scheme*

The phenomena discussed above are the primary mechanisms for device performance decline for our devices, and with their complete understanding, we propose the following overall PSC degradation scheme based on our original HP film degradation scheme posed in Figure 13.

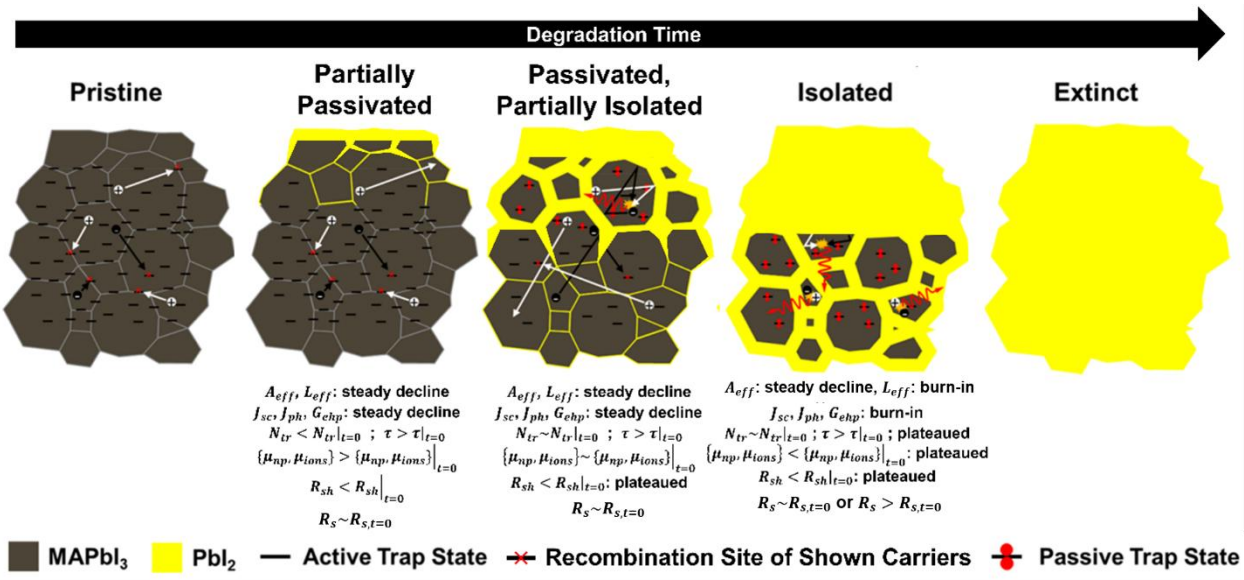

Figure 36. Postulated Device Degradation Scheme. This is the HP film degradation scheme introduced in Figure 13 noting the values of all relevant parameters in each degradation regime with respect to their initial values.

Additionally, having quantified the integrated influences of these phenomena (i.e., the diode parameters) on J_{sc}, V_{oc}, and FF with our unique CSA, we collect these influences to quantify the integrated influences and normalized integrated influences of the diode parameters (and thus the underlying drift-diffusion phenomena discussed above) on PCE at T_{80}. Specifically, Figure 37 plots these quantities over time for the single $MAPbI_3$ device in Figure 12.

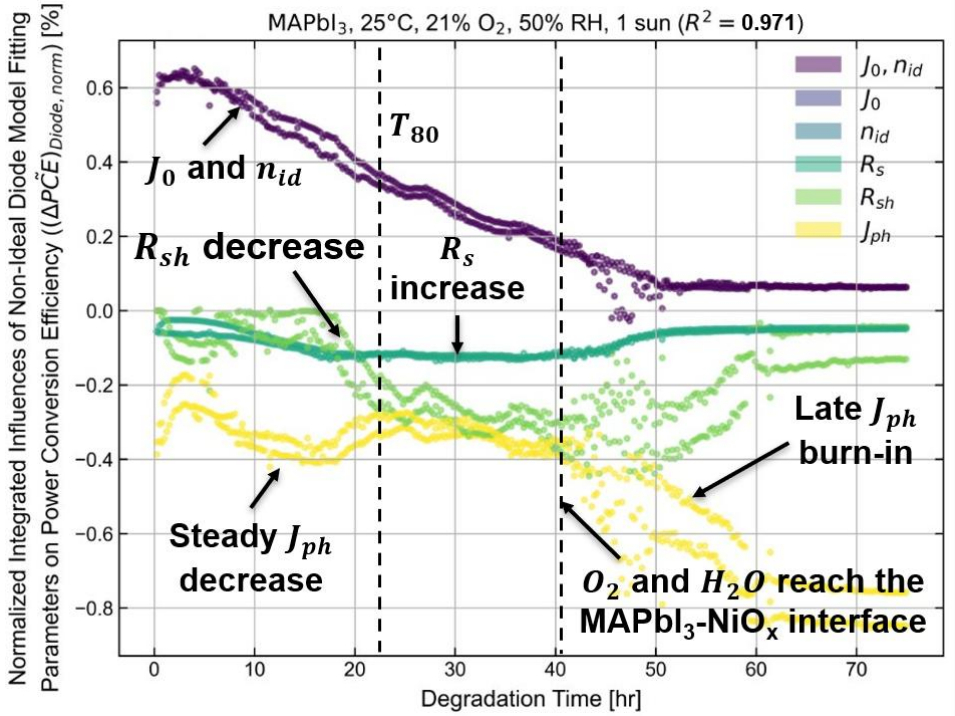

Figure 37. Normalized Integrated Influences of Diode Fitting Parameters on PCE over Time for a Single $MAPbI_3$ Device. Scatterplot of the normalized integrated influences of the diode fitting parameters on PCE over time (measured as a percentage of T_{80}) for the single $MAPbI_3$ device in Figure 12. Normalization is performed by dividing each respective integrated influence by the sum of the absolute values of integrated influences for all parameters. Additionally, as above, simulation type and scan type are encoded for single experiments according to the grid legend in Figure 20.

On average over all $MAPbI_3$ devices, the J_{sc}, V_{oc}, and FF evolve by factors of 0.867, 0.905, and 1.023, respectively,[17] constituting ≈53%, 9%, and 38% of the PCE changes. Thus, the primary drivers of PCE decline to T_{80} are the decreases in J_{sc} and FF while the small V_{oc} increase slightly increases the PCE by T_{80}.[17] Regarding the influences of the diode fitting parameters on PCE, PCE changes are dominated by the combined influence of J_0 and n_{id} at early times, followed by J_{ph}, R_s, and finally R_{sh} (see Figure 37). Although, over degradation, PCE changes become dominated by both J_{ph} ($\approx -34.9\%$ of PCE changes by T_{80}) and the combined influence of J_0 and n_{id} ($\approx +32.6\%$ combined influence on PCE changes by T_{80}), followed by moderate contributions from R_s ($\approx -12.0\%$ of PCE changes by T_{80}) and R_{sh} ($\approx -20.5\%$ of PCE changes by T_{80}) for the single $MAPbI_3$ device in Figure 12. Regarding the drift-diffusion fitting parameters' influences on solar cell parameters, the high volatility of the drift-diffusion fitting parameters causes excessive volatility in the calculated sensitivity coefficients and thus influences. Nevertheless, even in high-error results, we observe the expected result. The fitted HP-ETL interfacial deep defect (trap) density ($N_{tr,HP-ETL}$) and fitted electron mobility (μ_n) dominate PCE changes at early times (corresponding to J_0 and n_{id}) with moderate contributions from G_{ehp}, R_s, and R_{sh}. Then, over degradation, PCE changes again become dominated by both G_{ehp} ($\approx -35.6\%$ of PCE changes by T_{80}) and $N_{tr,HP-ETL}$ and μ_n ($\approx +15\%$ and $\approx +25\%$, respectively, of PCE changes by T_{80}), again followed by moderate contributions from R_s and R_{sh} ($\approx -15\%$ and $\approx -10\%$, respectively, of PCE changes by T_{80}) and minor contributions from all remaining parameters. Again, this rough similarity among the influences of the diode and drift-diffusion fitting parameters which we postulate relate to common degradation phenomena further affirm these postulated relationships of parameters with such degradation phenomena. Additionally, much of the differences in such influences are likely due to the excessive volatility in drift-diffusion fitting parameters and thus the calculated sensitivity coefficients and integrated influences. In short, the primary drivers of PCE changes at early times are the performance-improving deep defect (trap) reduction at HP-TL interfaces and grain boundaries and the performance-degrading steady decline in J_{sc}-related parameters due to HP film absorptivity loss (caused by its chemical decomposition). Then, at later times, band misalignment with degradation products at the HP-TL interfaces and grain boundaries, the continued decline in J_{sc}-related parameters, R_{sh} decline, and R_s increase contribute to PCE decline (see Figure 37).

The primary relationships among the various parameters discussed in this study are summarized in the following causality tree of the hierarchy of parameters. As discussed in Section 3.1.3, G_{ehp} generally depends on both the fractional effective area and thickness of the HP film (proportionally in this study) while all other drift-diffusion parameters depend appreciably on only the fractional effective active thickness. Additionally, also discussed in Section 3.1.3, all J_{sc}-related parameters are roughly proportional, determined almost exclusively by electron-hole pair (EHP) generation based on the remaining film absorptivity while relatively invariant with all other electronic parameters. Although, as discussed in Section 3.1.3, J_{sc} may be

influenced by other properties in different architectures, especially those with standard thicknesses comparable to or larger than free carrier diffusion lengths. Beyond the J_{sc}-related parameters, J_0 and n_{id} are determined by the deep defect (trap) densities and carrier mobilities, and for our devices, primarily the HP-ETL interfacial deep defect (trap) density ($N_{tr,HP-ETL}$) and electron mobility (μ_n). Note that deep defect (trap) densities should primarily influence J_0 while carrier mobilities primarily influence n_{id} (based on our analysis in Section 2.1.4), but due to their incredibly strong correlation, both parameters are heavily influenced by deep defect (trap) densities and carrier mobilities. Additionally, R_s and R_{sh} in the drift-diffusion and diode models should correlate well, but the high volatility in the drift-diffusion parameters yields only a moderate correlation (see Section 6). Last, J_0 and n_{id} dominate V_{oc} changes at early times while J_{ph} also contributes to V_{oc} decline during J_{sc} burn-in, and J_0, R_s, and R_{sh} dominate V_{oc} changes.

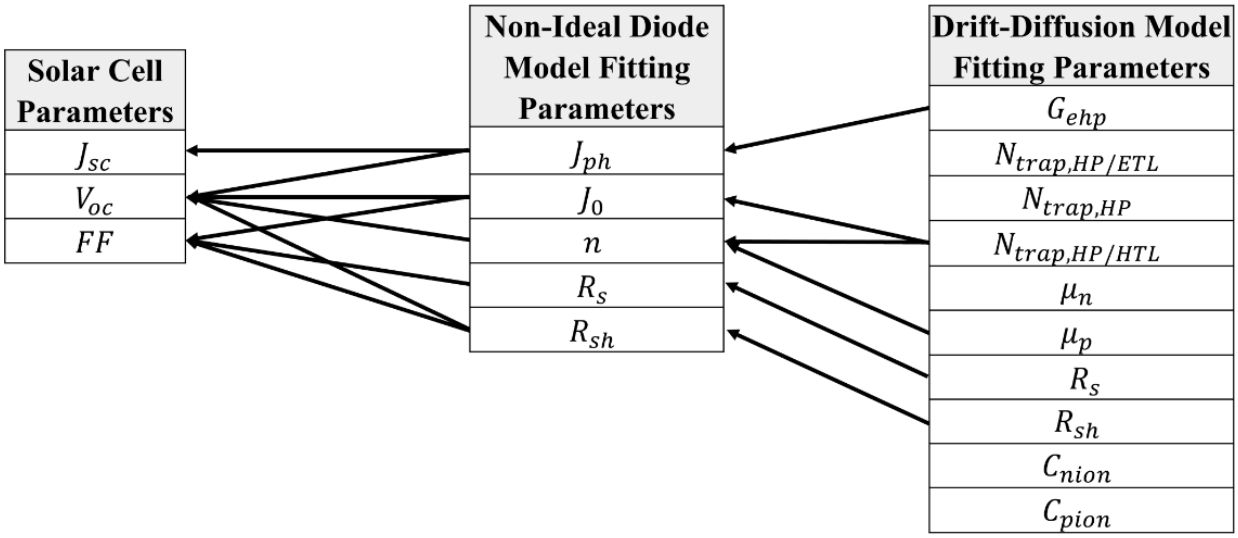

Figure 38. Causality Tree of the Hierarchy of Parameters. Parameter sets are arranged from higher-level (i.e., less fundamental, more empirical) toward the left to lower-level (i.e., more fundamental, less empirical) toward the right.

These quantitative relationships among parameters quantify the influences of each device degradation mechanism on device performance decline, and it is the combination of our degradation profile analysis, mechanistic modeling of J-V data over degradation, and unique CSA which enables this achievement. As in this study, such mechanistic models provide valuable information for both informing predictive models of operational lifetimes and design of long-lived devices.

3.2 Predictive Machine Learning (ML) Modeling of Operational Lifetime (T_{80})

With these mechanistic models, we calculate transformed versions of the parameters as described in Section 2.2.10 and use both the untransformed and transformed parameters as features in predictive machine learning (ML) models of operational lifetime (T_{80}), as described in Section 2.2.12. ML model errors generally increase with model complexity, appearing lowest for the solar cell parameters, increasing for degradation profile parameters due to their neglect of J-V data, increasing further for the diode parameters due to their moderate systematic and random volatility, and maximizing for drift-diffusion parameters due primarily to their high random volatility (alongside their moderate systematic volatility similar to the diode parameters).

Additionally, ML model errors also follow a general trend with the combinations of device architectures considered. Ordered from lowest to highest, this list is, respectively, $MAPbI_3$, overall (i.e., all architectures) or low-bandgap, and high-bandgap. Note that this overall model generalizes over architectures and is the target model to optimize in this field of work. Last, note that the relatively high errors of the high-bandgap architecture's ML models are likely due to its lower range of operational lifetimes (i.e., ≈1-70 hours as compared with ≈0.9-70 hours for low-bandgap and ≈0.5-100 hours for $MAPbI_3$). Thus, as stated in Section 4.2.1, we recommend maximization of degradation condition ranges to maximize the ranges of operational lifetimes and thus predictive model accuracy.

Regarding feature selection, it is most common for features to be selected which describe the device degradation phenomena investigated above which are not primarily described by the other selected features. In other words, as expected, selected features are often maximally independent to describe the various device degradation phenomena with the lowest possible number of selected features (i.e., sparsity). Indeed, we find the selected features, their weighting coefficients, and their correlations amongst each other align well with our mechanistic modeling results, including our unique CSA. Additionally, regarding the mathematical meaning of selected features, undifferentiated values are often not selected for individual architectures since such values are relatively uniform across devices and thus provide little information on the difference in operational lifetimes. Although, for the overall model (i.e., over all architectures), undifferentiated features are often selected since they are strong identifiers of composition. However, we do not derive physical meaning from such selections since the variations in parameters across architectures are similar and any differences are often described by the parameter's Arrhenius behavior and thus the selection of temperature (see below). Now, beyond undifferentiated features, the first and second time derivatives (i.e., dX/dt and d^2X/dt^2, respectively, for a general feature X) are often selected since they effectively describe the rates of processes and rates at which competing processes transition between dominant phenomena, respectively. Additionally, selection of the nonfractional derivative (e.g., d^2X/dt^2) alongside its fractional counterpart (e.g., $d^2(X/X_{t=0})/dt^2$) is common and emphasizes the importance of the derivative to modeling operational lifetime. Specifically, the decline in J_{sc}-related parameters is primarily described by the first time derivative of J_{sc} (i.e., dJ_{sc}/dt) or, because PCE and J_{sc} are nearly proportional (see Figure 19), the first time derivative of PCE (i.e., $d(PCE)/dt$). Regarding deep defect (trap) passivation and band misalignment between perovskite and degradation products at grain boundaries, this is often described by any features not related to J_{sc}, R_s, or R_{sh}. Although, since these processes primarily affect V_{oc} while FF is influenced less, these competing phenomena are often described by the first and second derivatives of parameters describing these phenomena (again any features not related to J_{sc}, R_s, or R_{sh}). Indeed, since these phenomena exert competing influences on V_{oc}, it is sensible for the second derivative to be a selected feature. Moreover, since V_{oc} and V_{MPP} are strongly correlated throughout degradation and over all architectures (see Section 6), dV_{MPP}/dt and d^2V_{MPP}/dt^2 are also often selected. Next, regarding R_s increase and R_{sh} decrease, these phenomena are logically described by their first time derivatives (i.e., dR_s/dt and dR_{sh}/dt, respectively). Although, there are many instances of other features being selected to describe the V_{oc}-related and FF-related phenomena which are not in direct causal relationship with the expected features but are sufficiently correlated to serve as substitutes for the expected features (e.g., $P_{ion-hys}$ to describe these V_{oc}-related phenomena). Specifically, as showcased in the causality tree of the hierarchy of parameters (Figure 38), parameters which describe the same underlying phenomena are

correlated. In our mechanistic modeling analysis, this causes parameter evolutions to exhibit similarities in shape and in times at which evolutions undergo large changes in character (i.e., enter a new regime). Similarly, in these predictive ML models, these correlations manifest as the selection of features correlated (but not causally related) to the given underlying phenomenon. Last, degradation conditions are often selected in place of electronic parameters when included in the feature set. This is enabled by strong relationships between the parameters describing the relevant phenomenon and the selected degradation condition. The strongest example of this is the selection of temperature over the first time derivatives of parameters with strong Arrhenius dependences, namely the J_{sc}-related derivatives (i.e., dJ_{sc}/dt, dJ_{ph}/dt, dG_{ehp}/dt) related to material decomposition or FF-related derivatives (i.e., $d(FF)/dt$ and dR_{sh}/dt) related to the shunt pathway formation rate. Mathematically, with temperature selected, the standard linear regression model becomes

$$\ln(T_{80}) = c + \beta_T \left(\frac{T - \bar{T}}{\sigma_T} \right) + \sum_i \beta_i \frac{x_i - \bar{x_i}}{\sigma_{x_i}}$$

Although, as done by many studies,[117] we quantify the Arrhenius dependence of parameter evolutions by defining the Arrhenius rate as the reciprocal time for the parameter to reach a specified fraction of its initial value (e.g., 80%), as outlined in Section 2.2.11. For PCE decline, this rate is defined as the reciprocal of operational lifetime, yielding

$$r_{T_{80}} = Ce^{-\frac{E_a}{k_B T}} \rightarrow \ln\left(\frac{1}{T_{80}}\right) = \ln(C) - \frac{E_a}{k_B T}$$

where $r_{T_{80}}$ is the effective rate for the parameter evolution, C is the pre-exponential frequency factor, E_a is the parameter evolution's effective activation energy, k_B is Boltzmann's constant, and T is temperature. Despite this expression differing from the standard linear regression model, the effect of temperature is functionally similar: increasing temperature decreases operational lifetime on a logarithmic scale. Thus, temperature's selection roughly implies an Arrhenius behavior of the underlying phenomenon's influence on PCE decline rate and operational lifetime. As stated above, this is most prominent for the J_{sc}-related derivatives (i.e., dJ_{sc}/dt, dJ_{ph}/dt, dG_{ehp}/dt) describing material decomposition or FF-related derivatives (i.e., $d(FF)/dt$ and dR_{sh}/dt) describing the shunt pathway formation rate. Although, as discussed above, selected features often describe distinct phenomena to minimize the number of selected features (i.e., sparsity). Thus, if temperature is selected alongside a feature known to exhibit Arrhenius behavior, temperature should primarily describe the remaining phenomenon.

Although, the inclusion of gaseous reactant concentrations causes the ML modeling results to depend on device geometry and mass transport properties while including material decomposition rate (r_{deg}) causes the ML modeling results to depend on HP composition. As such, it is beneficial to exclude these features such that the ML models are generalized to device architectures. Additionally, the number of points utilized in parameter transformations (n_{pt}) may affect the model accuracy through a combination of the accuracy of differentiating features by polynomial fitting and providing additional measurement time to improve the model's predictive ability. In other words, the utilized measurement time and unaccelerated extrapolation factor are limited by n_{pt}. Thus, in future studies, we also recommend shorter times between measurement cycles (i.e., increasing measurement frequency) and incorporating devices with longer operational lifetimes to decouple the effect of n_{pt} on the accuracy of polynomial fitting from its

improvement of predictive ability by incorporating additional measurement time. Last, the percentage of T_{80} at which features are calculated is a direct measure of the utilized measurement time, and since these predictive models must be accurate with low utilized measurement times (e.g., 0-1% of T_{80} according to Section 2.2.12.1 and 2.2.12.1), we recommend evaluating a model's predictive ability using only such early-time measurements.

Given the effects these specifications have on the generality and efficacy of these models, we identify the best-performing models for numerous subsets of specifications which adhere to one or more of the above restrictions, thus enabling evaluation of model error and results (i.e., selected features and their coefficients) under these varying levels of generality. Specifically, the specifications we vary include the number of points utilized in performing parameter transformations (n_{pt}) (i.e., moving averaging and differentiation by polynomial fitting), measurement time (t_{meas}) measured in percentage of T_{80}, which degradation conditions (DCs) to include, and whether the material decomposition rate (r_{deg}) predicted by the considered architecture's kinetic rate law model. See our GitHub webpage published online[63] for parity plots and feature coefficient bar charts for each model, boxplots and histograms depicting the distribution of error metric and feature coefficient values versus any specification over all other specifications in the chosen subset, and the corresponding bar charts of error metrics and feature coefficients (analogous to those below). Specifically, for the bar charts of feature coefficients, it is valuable to study the features selected and their coefficients by architecture, but it is also valuable to do so across parameter sets (see our GitHub webpage published online)[63] to ascertain relationships among features (which are expected to align with those of our unique CSA). Additionally, in our $MAPbI_3$ device degradation study, we displayed feature coefficients only with magnitudes larger than their standard deviations. Although, in this study, we observe models with very different error metrics may have the same features whose means outweigh their standard deviations, and we thus show all selected features in our bar charts to ascertain the distinguishing features. Last, we present the coefficient of determination (R^2) due to its standard use in defining model accuracy, but the corresponding mean-normalized root-mean-squared (RMS) error (m-NRMSE) is still used in calculating confidence intervals for predicted T_{80} values. The corresponding plots for all such other error metrics are also published on our GitHub webpage online.[63]

3.2.1 Presentation of Best-Performing Machine Learning (ML) Models for Various Sets of Featurization and Predictive Model Specifications

3.2.1.1 Specification Subset 1 – Five Points for Parameter Transformations at 0% of T_{80} with Temperature as the Only Degradation Condition and Excluding r_{deg}

First, we consider the strictest set of specifications in which all degradation conditions other than temperature are excluded to generalize over device geometries and mass transport properties (e.g., encapsulation schemes), features are calculated at time zero only (i.e., 0% of T_{80}), and in which only the first five points (where the options are 0, 5, 10, 15, 20, or 25) of each relevant parameter's evolution are used for differentiation by polynomial fitting (minimizing the measurement time utilized in calculating features and thus maximizing the extrapolation factor) (see Section 2.2.10.3). For the low-bandgap, $MAPbI_3$, high-bandgap, and overall models, the measurement times utilized by these first five points are ≈62%, ≈6%, ≈12%, and ≈14% of T_{80}, respectively, and the corresponding unaccelerated extrapolation factors are ≈1.6, ≈15, ≈8, and ≈6, respectively. These values are unrealistic for practical use of these models, but as stated

above, if accuracy is sufficiently maintained when measurement frequency or operational lifetimes are increased, this model's use of only time-zero features may enable full extrapolation of 30-year device operational lifetimes with only days to weeks of measurement time since features are calculated at 0% of T_{80}. Additionally, as is generally observed, the architecture combinations in order of increasing error are $MAPbI_3$, low-bandgap, overall (i.e., all architectures), and high-bandgap. Moreover, for this subset, the low-bandgap, $MAPbI_3$, and overall models exhibit moderate error while the high-bandgap model exhibits large error (see Figure 39). These moderate-to-high errors are due to the above-described restriction of specifications, and as stated at the beginning of Section 3.2, the relatively high error for the high-bandgap architecture across all models is likely due to its lower range of operational lifetimes. Last, regarding the effective percentage of T_{80} (or equivalently, the unaccelerated extrapolation factor), if accuracy is sufficiently maintained when measurement frequency or operational lifetimes are increased, this model's use of only time-zero features may enable full extrapolation of 30-year device operational lifetimes with only days to weeks of measurement time since features are calculated at 0% of T_{80}.

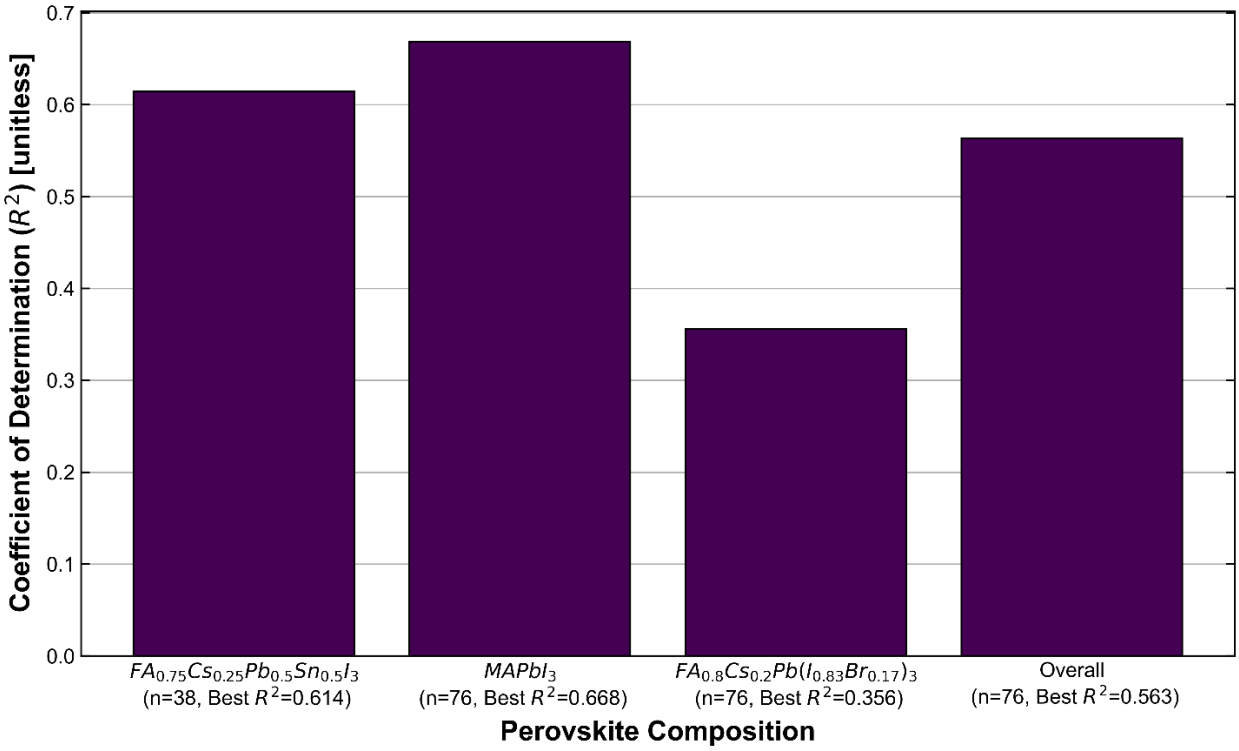

Figure 39. Bar Chart of the Coefficients of Determination (R^2) versus Architecture Combination for the Best-Performing ML Models Under Specification Subset 1 . As stated above, Specification Subset 1 is the set of specifications which uses only the first five measurements following time zero and temperature as the only degradation condition. Additionally, the number of models corresponding to a given architecture for this subset is given by "n" (e.g., $n = 76$).

For this champion model, the weighting coefficients of selected features are displayed in Figure 40. First, we postulate the fractional J_{sc} and first time derivatives of J_{sc} and PCE (i.e., dJ_{sc}/dt, $d(PCE)/dt$, and $d(PCE/PCE_{t=0})/dt$) describe the decline in electron-hole pair (EHP) generation rate (G_{ehp}) due to HP film absorptivity loss caused by its chemical decomposition.

Specifically, the first time derivatives of PCE (i.e., $d(PCE)/dt$ and $d(PCE/PCE_{t=0})/dt$) are the only features selected for the high-bandgap architecture, likely due to its high error preventing other feature coefficients from having significant values. $d(PCE)/dt$ is also the primary selected feature in the overall model, and its lack of selection for the low-bandgap and $MAPbI_3$ architectures implies its presence in the overall model is driven by its importance to the high-bandgap architecture, especially given the high-bandgap model's high error. Additionally, since PCE and J_{sc} are nearly proportional throughout degradation (see Figure 19), the time derivative likely primarily describes the decline in electron-hole pair (EHP) generation rate (G_{ehp}) due to loss of HP film absorptivity caused by its chemical decomposition (i.e., is roughly proportional to the first time derivative of J_{sc}-related parameters). Moreover, the first time derivative of J_{sc} (i.e., dJ_{sc}/dt) is selected for the low-bandgap composition, and the fractional J_{sc} (i.e., $J_{sc}/J_{sc,t=0}$) is also selected in the overall model. This fractional J_{sc} is the average dJ_{sc}/dt at the considered time and thus also represents dJ_{sc}/dt, and its selection alongside $d(PCE)/dt$ implies $d(PCE)/dt$ incorporates information regarding the remaining phenomena. Indeed, the high-bandgap architecture is more stable to photooxidation, and the evolution of PCE is thus convolved with other phenomena and thus less with HP film absorptivity loss (i.e., J_{sc}-related parameters). Last, as noted at the beginning of Section 3.2, selection of the nonfractional derivative alongside its fractional counterpart is common and emphasizes the importance of the derivative to modeling operational lifetime.

As discussed in the mechanistic modeling results in Section 3.1.4, one such phenomenon is deep defect (trap) passivation and band misalignment between perovskite and degradation products at HP-TL interfaces and grain boundaries. Indeed, we postulate the first time derivative of the hysteresis index (HI) (i.e., $d(HI)/dt$) and second time derivatives of the fractional and nonfractional maximum power point (MPP) voltage (V_{MPP}) (i.e., $d^2(V_{MPP}/V_{MPP,t=0})/dt^2$ and d^2V_{MPP}/dt^2) describe these phenomena as discussed in Sections 3.1.4 and 3.1.5. Specifically, the hysteresis metric and index evolve in a similar shape to V_{oc}-related and FF-related parameters at early times due to deep defect (trap) passivation and proceed to evolve steadily for the remainder of degradation. Thus, their first time derivatives may incorporate information of these phenomena as well as HP film absorptivity loss (i.e., J_{sc}-related parameters). Indeed, J_{sc}-related parameters are not selected for the $MAPbI_3$ architecture, but given their importance to degradation, they must be strongly represented by either temperature or $d(HI)/dt$. Additionally, as discussed above at the beginning of Section 3.2, second derivatives of V_{oc}-related parameters at early times represent the rate at which band misalignment between perovskite and degradation products outweighs deep defect (trap) passivation, and its selection supports this hypothesis.

Regarding the contributions of series resistance (R_s) increase and shunt resistance (R_{sh}) decrease to FF decline, features containing FF are not selected. Although, since the declines of FF and R_{sh} exhibit one of the strongest Arrhenius behaviors of the studied parameters, we postulate temperature is selected to describe this as well as HP film absorptivity loss (i.e., J_{sc}-related parameters). Specifically, temperature (T) is a significant feature for the low-bandgap and $MAPbI_3$ architectures and is the strongest feature for $MAPbI_3$, likely selected to encapsulate the Arrhenius dependence of both material decomposition and shunt pathway formation (see Figure 14, Figure 22, Figure 33, and Figure 33) by the T_{80}-temperature relationship discussed at the beginning of Section 3.2. As stated previously, all bar charts of Arrhenius modeling errors and parameters will be provided in a future publication and in a future version of this thesis on our "DegradePV" GitHub repository (see Section 6).[63] Although, temperature's selection alongside a feature known to exhibit Arrhenius behavior (e.g., the first time derivatives of J_{sc}-related

parameters, FF, or R_{sh}) suggests temperature describes the remaining temperature-dependent phenomenon. Thus, the temperature feature likely describes the Arrhenius behavior of FF and R_{sh} decline due to shunt pathway formation for the low-bandgap model and both material decomposition (i.e., J_{sc}-related parameters) and shunt pathway formation for $MAPbI_3$.

Last, as stated at the beginning of Section 3.2, numerous additional features are selected in the overall model which are not selected in their exact or similar form (e.g., dJ_{sc}/dt and $J_{sc}/J_{sc,t=0}$) in the models for individual architectures which, as expected, characterize the key differences among architectures. Specifically, for this subset, these bandgap (E_g) and V_{oc} are selected. Bandgap does not evolve over degradation, and its selection therefore represents the general stability of our HP compositions. Bandgap is thus a metric which may be roughly mapped to an HP composition's general stability in predictive models of operational lifetime. Moreover, V_{oc} does evolve over degradation, but the selection of its undifferentiated value at time zero implies it provides another metric for a device's general stability, as stated above at the beginning of Section 3.2. Although, the feature coefficients of E_g and V_{oc} are opposite in sign, and since the average bandgap ($\overline{E_g}$) over all experiments is 1.48 eV, the negative sign of its coefficient implies low-bandgap devices are more stable than $MAPbI_3$ and high-bandgap devices. We know this is not true, and this illustrates the empirical nature of these ML models. Specifically, as stated at the beginning of Section 3.2, many features are highly correlated, and this can cause two positively correlated features to be selected with offsetting coefficients. Furthermore, these correlations allow models to maintain their accuracy upon removing selected features due to correlated features replacing the removed ones. Last, note that six more features are selected (i.e., $d(PCE)/dt$, $d(J_{MPP}/J_{MPP,t=0})/dt$, dJ_{sc}/dt, $PCE/PCE_{t=0}$, T, J_{MPP}), but their feature coefficients are near zero and thus deemed insignificant. Although, their relationships with selected features among architectures nonetheless demonstrate their relevance to the overall model as well, and it is thus recommended to view the feature coefficient bar charts on our "DegradePV" GitHub repository (see Section 6).[63]

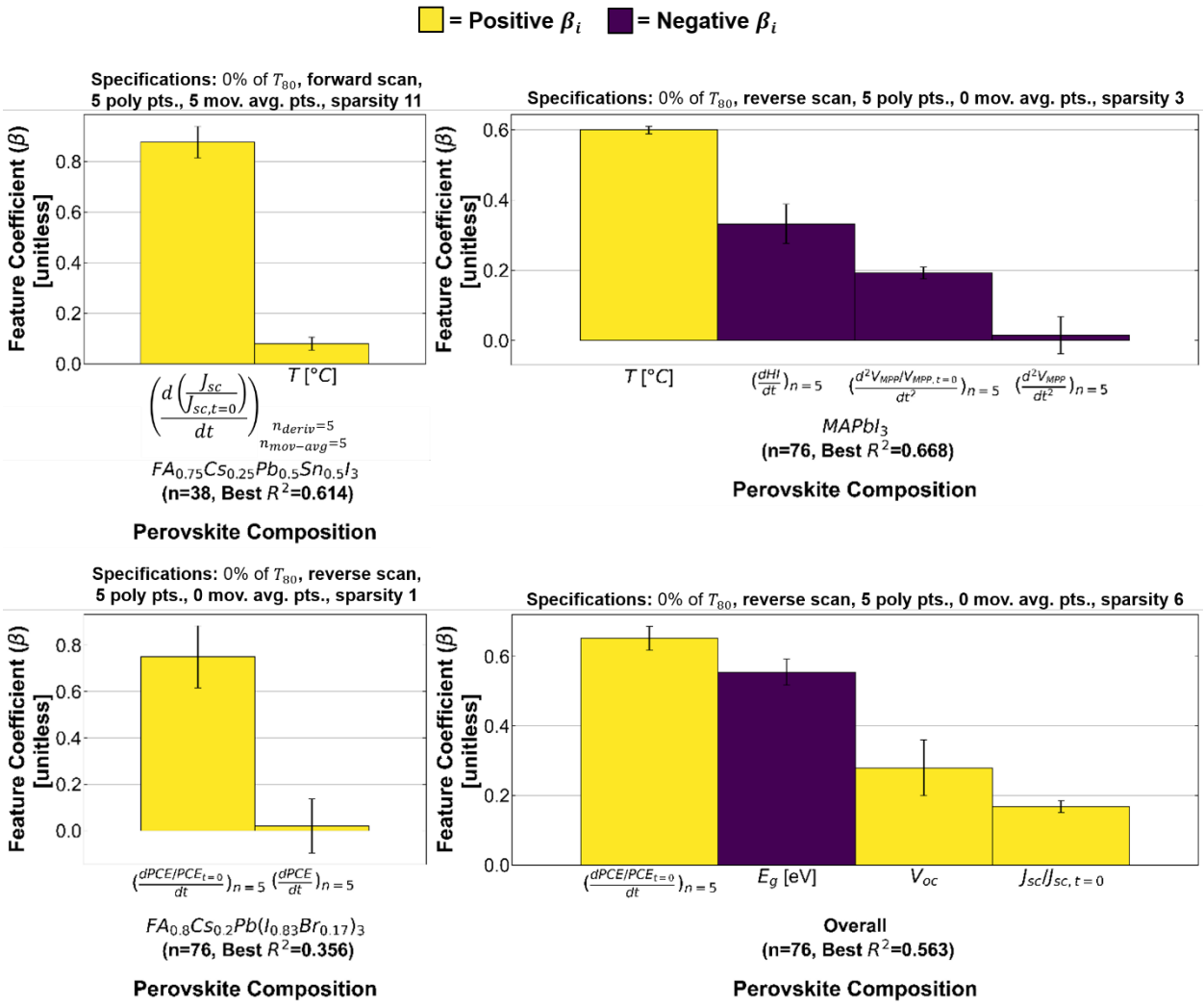

Figure 40. Bar Charts of Selected Feature Coefficients for Each Architecture Combination for the Best-Performing ML Models Under Specification Subset 1. The architecture combinations include (top left) low-bandgap, (top right) $MAPbI_3$, (bottom left) high-bandgap, and (bottom right) overall (i.e., all architectures). Additionally, as stated above, Specification Subset 1 is the set of specifications which uses only the first five measurements following time zero and temperature as the only degradation condition. The number of models corresponding to each given architecture for this subset is given by "n" (e.g., $n = 76$) in the architecture combination label, and the corresponding best R^2 value is also denoted. Moreover, the variable n_d (or "n") and n_{ma} in the subscripts of feature abbreviations refer to the number of points used in polynomial fitting and moving averaging of the respective parameter. Last, the corresponding optimal featurization and predictive model specifications for each architecture combination are listed above each chart.

3.2.1.2 Specification Subset 2 – Any Number of Points for Parameter Transformations at 0% of T_{80} with Temperature as the Only Degradation Condition and Excluding r_{deg}

To improve these results, we sequentially relax restrictions in order of least to greatest importance to maintain maximum generality. First, we relax the restriction on the number of points used in moving averaging and differentiation by polynomial fitting, considering models

regardless of these numbers (i.e., any of 0, 5, 10, 15, 20, 25 for moving averaging and 5, 10, 15, 20, 25 for differentiation by polynomial fitting). As expected, this significantly improves model accuracy since these additional points utilize a greater measurement period and thus provide more accurate features (see Figure 41). Specifically, for the low-bandgap, $MAPbI_3$, high-bandgap, and overall models, the measurement times utilized by 25 points if used in calculating transformed parameters are ≈310%, ≈30%, ≈60%, and ≈70%, and the corresponding unaccelerated extrapolation factors are 1, 3, 1.6, and 1.2. Although, for this subset, the low-bandgap and $MAPbI_3$ models now exhibit low error, the overall model again exhibits moderate error, and the high-bandgap model again exhibits large error (see Figure 41). Additionally, as is generally observed, the architecture combinations in order of increasing error are again $MAPbI_3$, low-bandgap, overall (i.e., all architectures), and high-bandgap. Of the overall models constructed for this subset, the champion model is displayed in Figure 42.

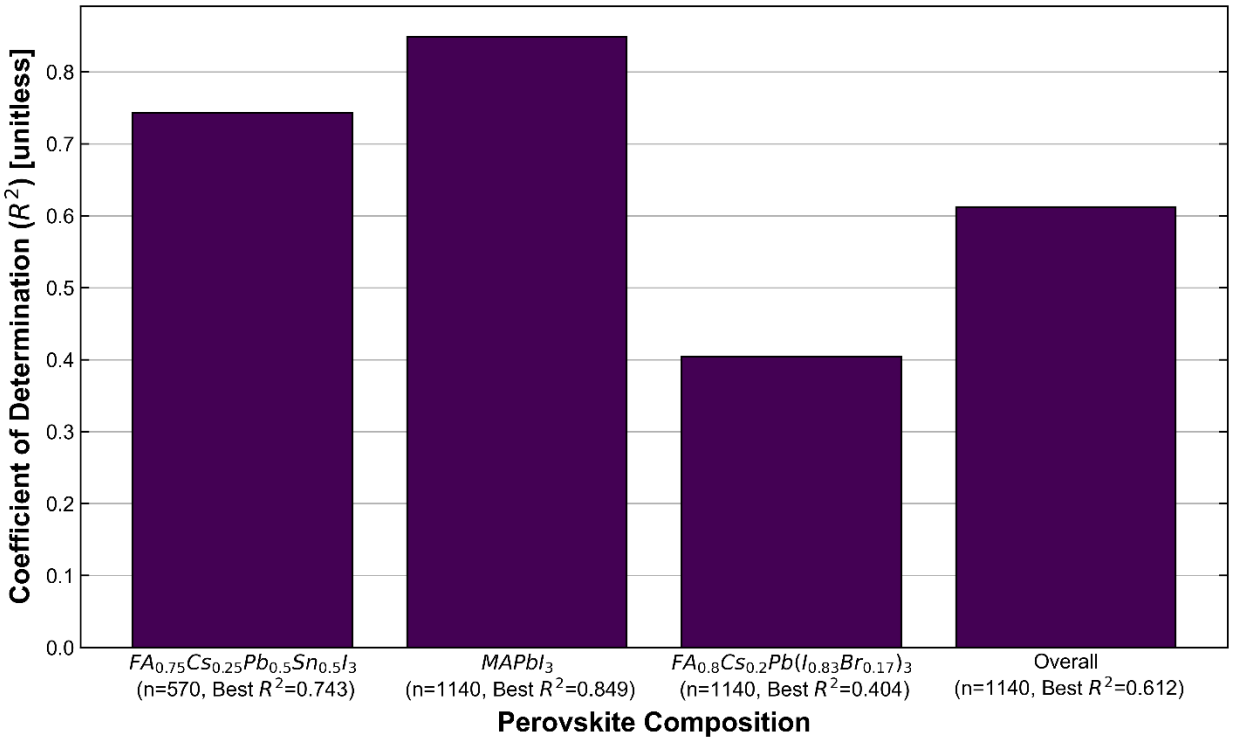

Figure 41. Bar Chart of Coefficients of Determination (R^2) versus Architecture Combination for the Best-Performing ML Models Under Specification Subset 2. As stated above, Specification Subset 2 is the set of specifications which uses any number (i.e., 5, 10, 15, 20, or 25) of measurements following time zero and uses temperature as the only degradation condition. Additionally, the number of models corresponding to a given architecture for this subset is given by "n" (e.g., $n = 1140$).

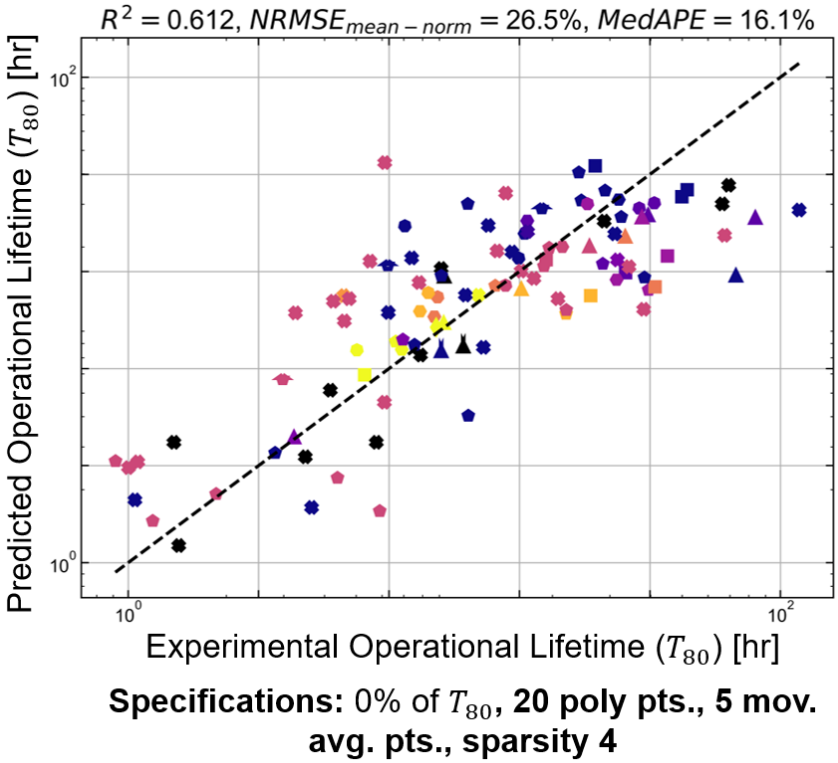

Figure 42. Champion ML Model Parity Plot Under Specification Subset 2. Parity plot of the champion ML model under Specification Subset 2 (i.e., the set of specifications which uses any number (i.e., 5, 10, 15, 20, or 25) of measurements following time zero and uses temperature as the only degradation condition). The corresponding optimal featurization and predictive model specifications are listed below the parity plot.

Regarding the selected features and their coefficients for this champion model, many are very similar to those corresponding to subset 1, but with a few differences. Specifically, dJ_{sc}/dt is again selected as the primary feature for the low-bandgap architecture, and temperature is again selected as the secondary feature, but the magnitude of its mean dropped below its standard deviation. Additionally, temperature is no longer selected for the $MAPbI_3$ architecture, but $d(HI)/dt$ and d^2V_{MPP}/dt^2 are still selected as features in the same order of importance. Although, their feature coefficients signs are opposite, and both V_{oc} and the fractional fill factor ($FF/FF_{t=0}$) are selected as positive-contributing features for the $MAPbI_3$ architecture. Again, since fractional parameters are proportional to the average time derivative of the fractionalized quantity (i.e., $d(FF)/dt$ here), we postulate the temperature's contribution in subset 1 is replaced by $FF/FF_{t=0}$ given the fill factor's strong temperature dependence. Regarding V_{oc}, such undifferentiated parameters vary among devices of a single architecture only due to small, random error in device fabrication and temperature, and this fact coupled with the strong Arrhenius dependence of the untransformed V_{oc} suggests the selection of V_{oc} also encapsulates the contribution of temperature observed for subset 1. Again, $d(PCE)/dt$ is the sole selected feature with a mean greater in magnitude than its standard deviation for the high-bandgap architecture, and we again postulate this is due to the high-bandgap model's high error preventing other feature coefficients from having significant values. Although, all features for the overall model with means greater in magnitude than their standard deviations are still selected,

but with means within a standard deviation of zero. Additionally, the only feature with a mean greater in magnitude than its standard deviation is the temperature, and with all four features in Figure 40d removed from the selected feature set, we postulate temperature replaced V_{oc} and $FF/FF_{t=0}$ due to their strong Arrhenius dependence.

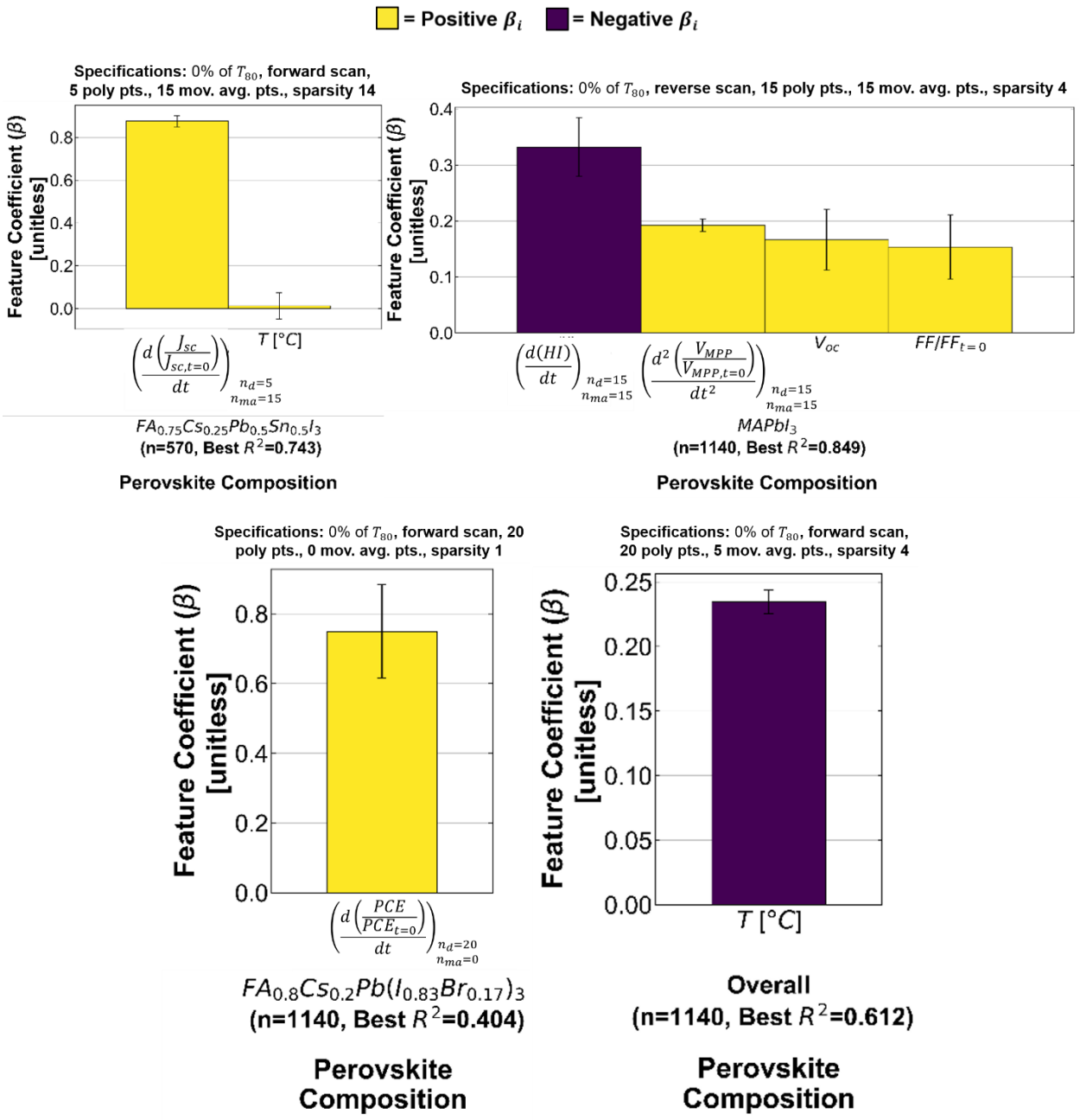

Figure 43. Bar Charts of Selected Feature Coefficients for Each Architecture Combination for the Best-Performing ML Models Under Specification Subset 2. The architecture combinations include (top left) low-bandgap, (top right) $MAPbI_3$, (bottom left) high-bandgap, and (bottom right) overall (i.e., all architectures). Additionally, as stated above, Specification Subset 2 is the set of specifications which uses any number (i.e., 5, 10, 15, 20, or 25) of measurements following time zero and uses temperature as the only degradation condition. The

number of models corresponding to each given architecture for this subset is given by "n" (e.g., $n = 1140$) in the architecture combination label, and the corresponding best R^2 value is also denoted. Moreover, the variable n_d (or "n") and n_{ma} in the subscripts of feature abbreviations refer to the number of points used in polynomial fitting and moving averaging of the respective parameter. Last, the corresponding optimal featurization and predictive model specifications for each architecture combination are listed above each chart.

3.2.1.3 Specification Subset 3 – Any Number of Points for Parameter Transformations at 0-9% of T_{80} with Temperature as the Only Degradation Condition

Next, we relax the restriction on measurement time, considering models including features calculated at any integer percentage from 0-9% of T_{80}. As expected, this results in an even greater increase in model performance since utilization of a greater proportion of measurement time yields more accurate features (see Figure 44). Specifically, all architectures models now exhibit low error at certain, often later percentages of T_{80} (see Figure 41). Additionally, the architecture combinations in order of increasing error are now $MAPbI_3$, overall (i.e., all architectures), low-bandgap, and high-bandgap. This follows the general observation, but the overall model is now (on average) lower in error, and this is likely due to the dramatic increase in accuracy for the high-bandgap architecture in including measurements slightly after time zero. Although, the utilized measurement times (in percentage of T_{80}) represent lower limits on the effective measurement time utilized and upper limits on the unaccelerated extrapolation factor (i.e., $UEF = T_{80}/t_{meas}$) when increasing measurement frequency or operational lifetimes. This incentivizes the increase in measurement frequency and incorporation of longer-lived devices into these predictive models to distinguish between accuracy contributed by the number of points in polynomial fitting and by measurement time. Regarding the selected features and their coefficients, we omit these results for this subset due to their similarity to those in Specification Subset 4.

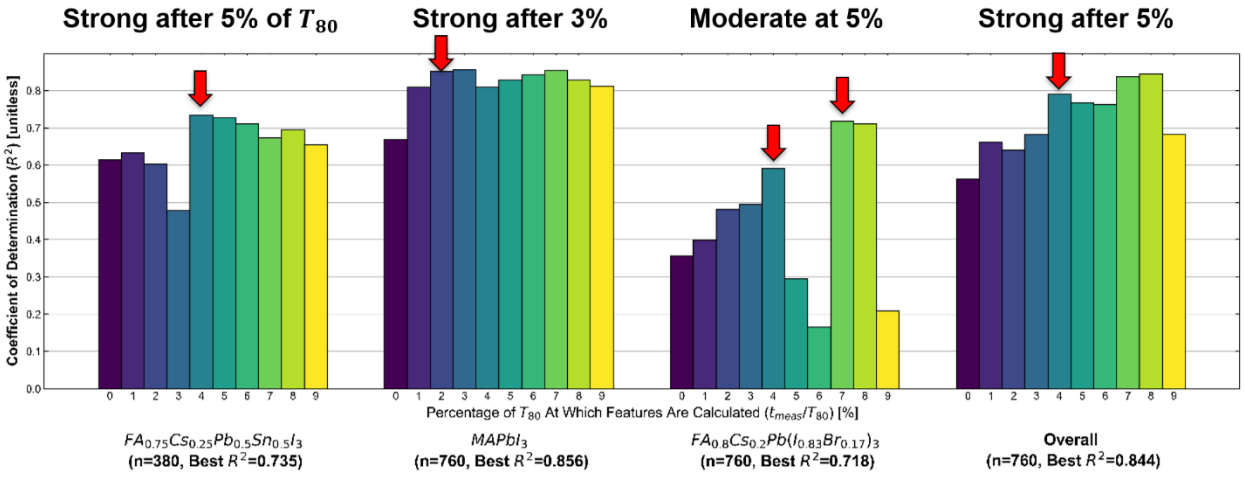

Figure 44. Bar Chart of Coefficients of Determination (R^2) versus Architecture Combination and Measurement Time (in Percentage of T_{80}) for the Best-Performing ML Models Under Specification Subset 3. As stated above, Specification Subset 3 is the set of specifications which uses any number (i.e., 5, 10, 15, 20, or 25) of measurements following time zero and uses temperature as the only degradation condition. Additionally, the number of models corresponding to a given architecture for this subset is given by "n" (e.g., $n = 760$), and the

corresponding best R^2 value is also reported. Last, each bar is colored and labeled corresponding to the measurement time (i.e., 0, 1, 2, …, 9 % of T_{80}) at which features are calculated for the models each bar represents, and red block arrows with labels are added to indicate optimal measurement times.

3.2.1.4 Specification Subset 4 – Any Number of Points for Parameter Transformations at 0-9% of T_{80} with All Degradation Conditions Except Material Decomposition Rate

Last, we relax the restriction on degradation conditions, considering models with degradation condition sets of temperature only, or all degradation conditions other than the HP decomposition rate predicted by our kinetic rate law models for each architecture's HP composition.[16,19–21] This yields only a slight improvement since degradation conditions sometimes capture their related phenomena with more accuracy and concision than features derived from J-V curves (see Figure 45). This concision is key since increasing the number of features (i.e., the sparsity) increases random error and is discouraged in ML models with penalties discouraging high sparsities (see Sunkari *et al.*'s review of ML models).[32] Although, as discussed in Section 2.2.12.1 and the beginning of Section 3.2, including gaseous reactant concentrations as features causes the models to depend on device geometry and mass transport properties, requiring collection of new datasets for each architecture. Nevertheless, it is useful for examining relationships among degradation conditions and J-V features, and as seen above, degradation conditions provide only a slight improvement and are not necessary to achieve accurate models. This is contrast to the results in Section 3.2.1.2 relative to Section 3.2.1.1 where degradation conditions yield a moderate improvement due to the limited information in J-V features at time zero. Of the overall models constructed for this subset, the champion model is displayed in Figure 47.

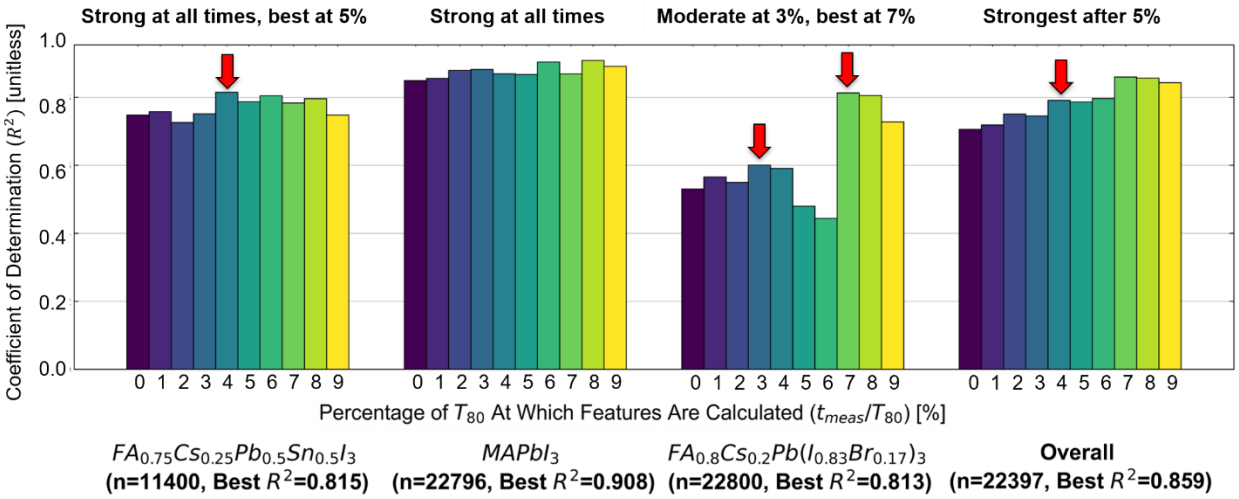

Figure 45. Bar Chart of Coefficients of Determination (R^2) versus Architecture Combination and Measurement Time (in Percentage of T_{80}) for the Best-Performing ML Models Under Specification Subset 4. As stated above, Specification Subset 4 is the set of specifications which uses any number (i.e., 5, 10, 15, 20, or 25) of measurements following time zero and uses all degradation conditions except for the HP chemical decomposition rate predicted by our kinetic rate law *models.[16,19–21] Additionally, the number of models corresponding to a given architecture for this subset is given by* "n" (e.g., $n = 22397$), and the corresponding best R^2 value is also reported. Last, each bar is colored and labeled corresponding to the measurement time (i.e., 0, 1, 2, …, 9 % of

T_{80}) at which features are calculated for the models each bar represents, and red block arrows with labels are added to indicate optimal measurement times.

Regarding the selected features and their coefficients, many are again very similar to those corresponding to subsets 1 and 2, but the inclusion of additional measurement time enables resolution of additional features, especially in the overall model (i.e., that for all architectures). Specifically, dJ_{sc}/dt is again selected as the primary feature for the low-bandgap architecture, and temperature is again selected as the secondary feature, but the magnitude of its mean is again below its standard deviation (hence it is not shown). Moreover, for $MAPbI_3$ devices, $d(HI)/dt$ and d^2V_{MPP}/dt^2 are still selected as features, but the three additional features are now selected (as opposed to just V_{oc} and $FF/FF_{t=0}$ in Specification Subset 2) including T, $J_{sc}/J_{sc,t=0}$, and RH. As discussed above, we postulate the selection of temperature replaces $FF/FF_{t=0}$ in Specification Subset 2 and describes the Arrhenius dependence of R_{sh} and thus FF decline. Although, the V_{oc} is now replaced with $J_{sc}/J_{sc,t=0}$, and RH, both of which are most related to photooxidation and thus J_{sc} decline. This demonstrates the empirical nature of these models, meaning the strong correlations among features can cause unexpected feature results while producing strong models. Now, regarding the high-bandgap architecture, the additional measurement time enables resolution of the five features shown, yielding the corresponding increase in accuracy. Specifically, $d(PCE)/dt$ is still the primary feature selected but is now accompanied by V_{oc}, C_{O_2}, d^2J_{MPP}/dt^2, and RH. The selection of V_{oc} and RH implies these features describe phenomena common to both $MAPbI_3$ and high-bandgap devices, and since MPP is strongly related to FF, d^2J_{MPP}/dt^2 likely provides a similar description as d^2V_{MPP}/dt^2. Last, for the overall model, many of these and similar features are selected, but the important conclusion is the increased number of resolved features due to the increased experiment number and the selection of features distinguishing HP compositions (e.g., bandgap (E_g) and V_{oc}).

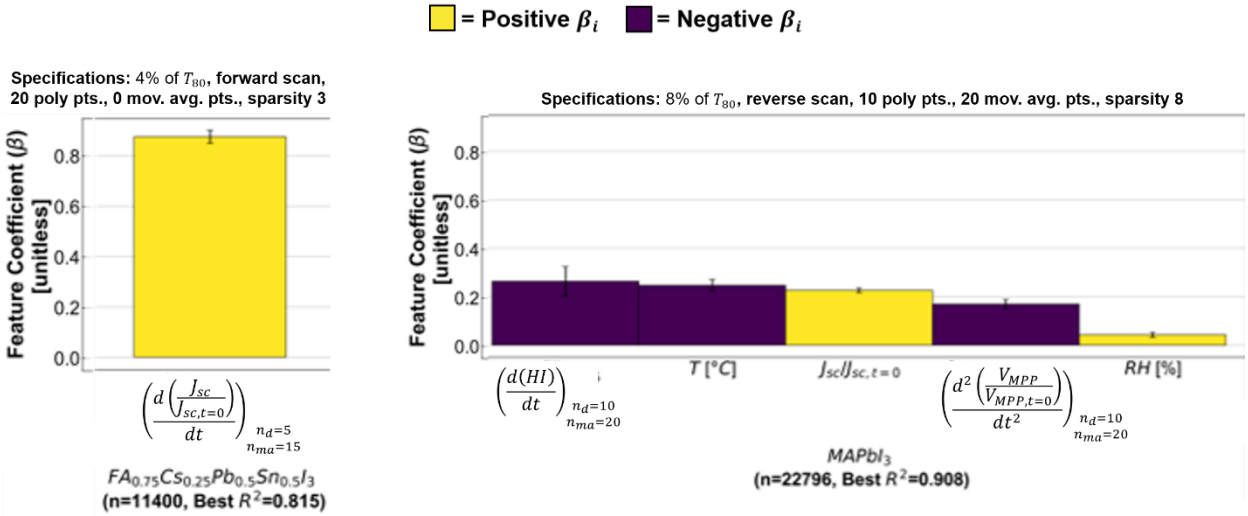

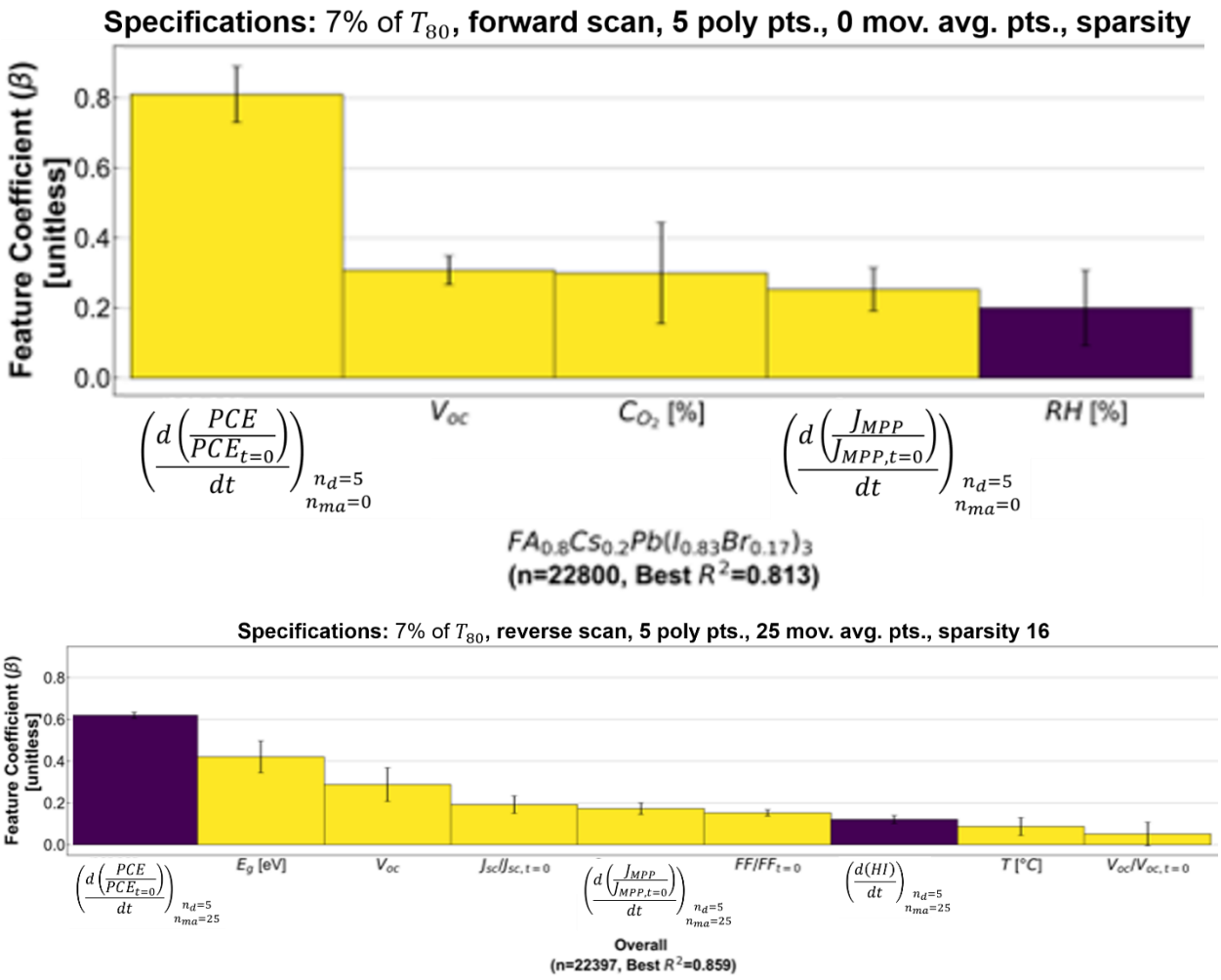

Figure 46. Bar Charts of Selected Feature Coefficients for Each Architecture Combination for the Best-Performing ML Models Under Specification Subset 4. The architecture combinations include (top left) low-bandgap, (top right) $MAPbI_3$, (bottom left) high-bandgap, and (bottom right) overall (i.e., all architectures). Additionally, as stated above, Specification Subset 4 is the set of specifications which uses any number (i.e., 5, 10, 15, 20, or 25) of measurements following time zero and uses all degradation conditions except for the HP chemical decomposition rate predicted by our kinetic rate law models.[16,19–21] The number of models corresponding to each given architecture for this subset is given by "n" (e.g., $n = 22397$) in the architecture combination label, and the corresponding best R^2 value is also denoted. Moreover, the variable n_d (or "n") and n_{ma} in the subscripts of feature abbreviations refer to the number of points used in polynomial fitting and moving averaging of the respective parameter. Last, the corresponding optimal featurization and predictive model specifications for each architecture combination are listed above each chart.

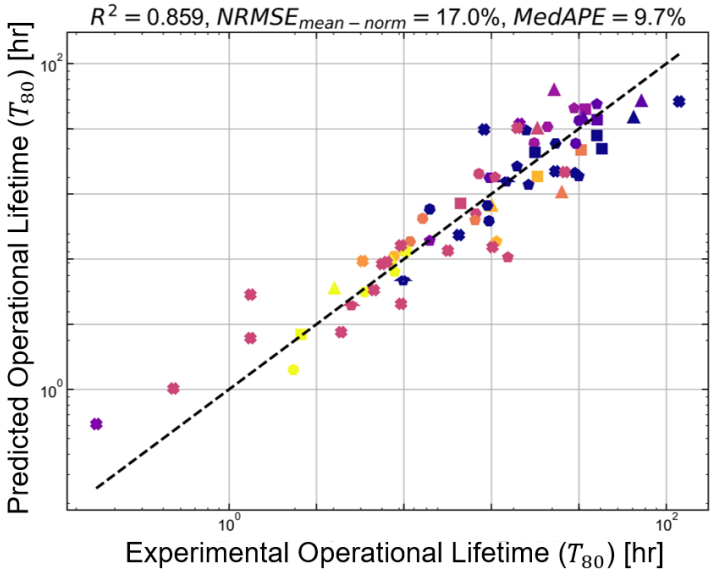

Figure 47. Champion ML Model Parity Plot Under Specification Subset 4. Parity plot of the champion ML model under Specification Subset 4 (i.e., the set of specifications which uses any number (i.e., 5, 10, 15, 20, or 25) of measurements following time zero and uses all degradation conditions except for the HP chemical decomposition rate predicted by our kinetic rate law models).[16,19–21] The corresponding optimal featurization and predictive model specifications are listed below the parity plot.

3.2.2 Degradation Acceleration (i.e., Accelerated Aging) Model – Presentation of Best-Performing Machine Learning (ML) Models with Only Degradation Conditions as Features

As discussed in Section 2.2.12.3.2, degradation acceleration (i.e., accelerated aging) models are extremely powerful in extending the predictive ability of models. Indeed, our unaccelerated model studies integer percentages of T_{80} since the order of magnitude of the number of measurements per experiment is ≈100, meaning differences among fractional changes in the percentage of T_{80} cannot be resolved. In other words, the frequency and number of measurements cycles per experiment before T_{80} are sufficient to resolve differences among integer percentages of T_{80} but cannot resolve differences at finer resolution. Additionally, as stated at the beginning of Section 3.2, this prohibits knowledge of whether the source of improvement when increasing the number of points utilized in parameter differentiation is additional measurement time or reduced error in polynomial fitting. Thus, we cannot quantify the relationship between model error and measurement time with sufficient resolution to optimize this number of points and determine the minimum measurement time required to ensure accurate models with these methods. Although, since accelerated aging models are standard for other solar cell technologies,[22–26] its utility likely applies to PSCs, meaning this minimum measurement time is likely greater than required to achieve a prediction factor of ≈1000.

Although, in combining an unaccelerated model above with an accelerated aging model, the combined model's error is constrained to be above the highest error between the unaccelerated and accelerated models. Specifically, the combined uncertainty (NRMSE) is

simply additive on the natural logarithmic scale used to calculate the error metrics for the individual models ($NRMSE_{unaccel}$ and $NRMSE_{accel}$), given by

$$NRMSE = \sqrt{NRMSE_{unaccel}^2 + NRMSE_{accel}^2}$$

and yielding a confidence interval for the predicted T_{80} value using the original expression in Section 2.2.12.3.1, given by

$$T_{80,\pm} \approx T_{80} * 91.2^{\pm NRMSE_{mean-norm}}$$

$$T_{80,-} \approx 10^{\log_{10} T_{80} - 1.96 * NRMSE} \approx \frac{T_{80}}{91.2^{NRMSE}}$$

$$T_{80,-} \approx 10^{\log_{10} T_{80} + 1.96 * NRMSE} \approx T_{80} * 91.2^{NRMSE}$$

Indeed, if the accelerated aging model exhibits comparable or less error than the unaccelerated model, its acceleration factor may be utilized with little consequence. Results for this model will be published in a future publication and a future version of this thesis on our "DegradePV" GitHub repository (see Section 6).[63]

3.2.3 Concluding Remarks – Best-Performing Model Generalized over Architectures and HP Compositions

As stated in Section 2.2.7.3.1 and the beginning of Section 3.2, we construct models for the above subsets of specifications to identify the best-performing models under varying levels of generality. Thus, as an evaluation of this work's ability to generate a predictive model of operational lifetime which is general to architectures and HP compositions and requires only early-time data from common, low-cost electronic measurements (e.g., J-V scans), we recommend the champion model over all architectures (i.e., overall) which considers all possible n_{pt} but considers temperature as the only degradation condition (i.e., excludes gaseous reactant concentrations and r_{deg} from the feature set) and calculates features only at time zero (i.e., 0% of T_{80} while excluding 1-9% of T_{80}). The parity plot, feature coefficient bar chart, and list of corresponding specifications for this champion model are shown in Figure 42 and Figure 43 in Section 3.2.1.2. Beyond this model, relaxing all restrictions on specifications other than the exclusion of $\mathrm{r_{deg}}$ as in Section 3.2.1.4 yields its champion model in Figure 42 in Section 3.2.1.4. Regarding feature selection, the selected features often describe unique phenomena observed in our mechanistic modeling study, but it is essential to note these models are empirical, and the strong correlations among features cause the selection of many different features across models. As such, models of similar accuracy may be constructed from various possible sets of features, and this eases generalization of these models by exclusion of certain features (e.g., degradation conditions).

Overall, we have achieved a champion model applicable to all three of our PSC architectures with a mean-normalized root-mean-squared (RMS) error (NRMSE) of 26.5% using features derived only from temperature and the first 20 J-V measurements, without requiring other degradation conditions or the composition-specific kinetic rate law models necessary for our previous predictive ML model. The models in this study are therefore the strongest predictive ML models for operational lifetimes we have produced in both accuracy and applicability, and we thus demonstrate the ability to use standard parameters from common, low-cost electronic measurements (e.g., J-V scans) as features to construct accurate, general small-dataset ML

models for PSC operational lifetimes. This establishes a strong foundation for and represents a powerful step toward high-throughput device testing and thus long-lived device development.

4 DISCUSSION

4.1 Evaluation of Error Sources

4.1.1 Experiment

4.1.1.1 Device Fabrication

Regarding experimental error, all instruments were calibrated according to the procedures which will be outlined in a future publication and on our "DegradePV" GitHub repository published online,[63] meaning experimental measurements primarily possess random error and little systematic error. Specifically, sources of random error include both fabrication and characterization processes. Fabrication sources include variation in layer thicknesses, crystal structures (including microscopic defects), and crystal morphologies (including macroscopic defects) due to variation in layer deposition (e.g., spin coating, thermal evaporation) and post-deposition processes (e.g., antisolvent treatment, annealing) including variation of material amounts, flow rates, temperatures, and process times. For our fabrication process, the greatest sources of variation are temperature and the amount, flow rate, timing, and duration of antisolvent deposition during perovskite spin coating. Moreover, additional defects may be introduced due to imperfect sample handling during fabrication or characterization. Although, variations in layer thicknesses are the most important source of experimental error since drift-diffusion simulations (and thus devices) are sensitive to thickness variations as small as ≈10 nm according to Le Corre. Nevertheless, variations in our film thicknesses are on this order, and the expected variation in J_{sc} among devices is correspondingly low. Regarding variations in crystal structure, morphology, and the corresponding defects, such are likely the primary source of variation among undegraded devices other than layer thicknesses since such properties are highly sensitive to fabrication process parameters for solution-processed perovskites.[67–69] Indeed, the random variation of fitted deep defect (trap) densities and carrier mobilities among undegraded devices is greater than for single devices while they degrade, meaning variations in fabrication cause significant variations among devices. These variations are accounted for since these properties are fit for each device at each time point, but the error manifests as random error in their initial fitted values among devices. This creates additional difficulty in analyzing drift-diffusion parameter values over multiple experiments.

4.1.1.2 In Situ Characterization of Devices Degrading in Controlled Environment

4.1.1.2.1 Current-Voltage (J-V) Scanning

Regarding characterization, variations in series resistance may occur due to variations in contact area, pressure, and positioning of the needle probes on device electrodes. Specifically, insufficient contact area (potentially due to insufficient contact pressure) may increase series resistance. Additionally, the cathode needle probe contacts the indium tin oxide (ITO) near the edge of the substrate area with a varying distance (a few mm to 1 cm) to the anode contact, and since ITO exhibits higher sheet resistance than metal electrodes (e.g., ≈100 for ITO versus silver (Ag)), this may also cause appreciable variation in series resistance. Although, as for defect densities and carrier mobilities, variations in series resistance are accounted for by fitting series resistance for each device at each time point, but this again causes the random error to manifest in its initial fitted values among devices.

Beyond electrical contacts, small variations in scan speed and intended applied biases by the Keithley 2400 source-measure unit may cause small errors in reported applied biases and

measured current densities. Additionally, variation in the illumination intensity profile (e.g., nonuniform, elliptical shape) and its total value may cause minor changes in degradation rate and photogeneration. Although, these instruments are calibrated and rated with very low tolerances, and these tolerances are insignificant relative to the observed random error. However, we did not employ a shadow mask to restrict the illuminated device area since such prevents microscopy of the device edges, and we thus assume the active area to be the overlap area between the ITO and Ag electrodes. Although, this assumption may cause minor inaccuracies in J_{sc} estimation due to light piping (undesired light exposure) at the device edges and fluctuations in substrate-mask alignment among samples for Ag contact deposition.[17]

4.1.1.2.2 Dark-Field (DF) Microscopy and Steady-State Photoluminescence (SSPL)

Regarding dark-field (DF) microscopy and steady-state photoluminescence (SSPL), these illumination intensity variations also apply, and additional error sources include ambient illumination penetrating small gaps in the light cover enclosing the characterization apparatus, unintended reflection of light within the enclosed apparatus, and small variations in exposure time and duration. Although, our light cover is functional, and microscope exposure timing and duration also have low tolerances. These variations are also accounted for by determining J_{sc}-related parameters for each device at each time point, but the errors again manifest as variation among devices' initial values.

4.1.1.3 Summary

All experimental errors other than variation in layer thicknesses are either insignificant or accounted for by fitting the related parameters for each device at each time point. Although, variation in layer thicknesses among devices is the most important source of experimental error, and we recommend determining the extent of its effects on modeling results (see Section 4.1.1.1).

4.1.2 Solar Cell Parameters

Regarding the solar cell parameters, the J_{sc}, V_{oc}, J_{MPP}, and V_{MPP} are subject to cubic interpolation error between the two points surrounding each relevant condition (i.e. short circuit, MPP, open circuit). Thus, according to their expressions, PCE is subject only to the interpolation error of J_{MPP} and V_{MPP}, and FF is subject to the interpolation errors of all four parameters (i.e., J_{sc}, V_{oc}, J_{MPP}, and V_{MPP}). Although, these errors are low for our applied bias voltage step of 0.05 V (see Figure 18). Last, the hysteresis metric is subject to both cubic interpolation error and integration error, but integration error is also minimal, especially with adaptive quadrature.

4.1.3 Mechanistic Models

4.1.3.1 Summary

Errors in fits, their corresponding fitting parameters, and their corresponding current-voltage (J-V) scan simulations are caused by inaccuracies in model assumptions (see Section 4.1.3.2 and Section 4.1.3.3), literature-based device parameters (see Section 6), experimental data, and suboptimal fitting. Both model assumptions and inaccuracies in literature-based device parameters are moderate sources of systematic (not random) error, but only model assumptions contribute appreciably to fitting error since fitting parameters likely adjust for inaccuracies in literature-based device parameters. In contrast, experimental errors and suboptimal fitting errors are negligible as explained in Section 4.3.1 and 4.1.3.5, respectively. Additionally, the simulation

errors (not fitting) of both the non-ideal diode and drift-diffusion models are negligible as they are caused only by machine error and the drift-diffusion simulation's default convergence criteria.[40] Thus, the primary sources of mechanistic modeling error are model assumptions and inaccuracies in literature-based device parameters, providing an explanation for fitting error and any systematic errors in fitting parameter values identified in future work and representing areas for improvement in future studies.

4.1.3.2 Non-Ideal Diode Model

All of the non-ideal diode model's assumptions are moderately inaccurate and thus sources of error. Specifically, the non-ideal diode model assumes steady state, neglecting transience in all phenomena (i.e., carrier generation, drift, diffusion, recombination, extraction, and accumulation in device layers and their interfaces). Additionally, unlike the drift-diffusion model, the non-ideal diode model makes cruder assumptions for all such phenomena, exhibiting larger fitting error for dark current-voltage (J-V) scans and similar error for light J-V scans. Specifically, carrier concentration profiles are nonuniform with a corresponding electric field contribution, radiative recombination dominates over nonradiative recombination, and carrier mobilities are finite (especially at interfaces and grain boundaries due to defect-generated space charge). Regarding carrier extraction, the assumption of perfectly selective transport layers (TLs) is valid since our simulations exhibit very high electron and hole extraction selectivities (i.e., greater than factors of 10 at minimum, respectively. This is enabled by sufficient energy differences between the perovskite and TL band energies (e.g., > 0.2 eV) (see Section 6). Last, assuming an intrinsic (non-degenerate) absorber layer (i.e., low doping with the Fermi level far from the band edges) with low injection is well-supported by literature (see Section 6). Regarding the similar error for light J-V scans, this occurs since the near-perfect extraction of free carriers is a good approximation for our devices and since dark J-V scans are much more sensitive to all phenomena other than photogeneration. Although, we expect non-ideal diode fits of light J-V scans will also exhibit larger error than drift-diffusion fits for devices with standard-thickness HP films as the HP film thickness becomes significantly larger than diffusion lengths, enabling appreciable trapping and recombination. In short, the assumptions of the non-ideal diode model with noteworthy inaccuracy are assuming steady-state, total absorption, no radiative recombination, and uniform carrier concentration profiles with infinite carrier mobilities and no electric fields.

4.1.3.3 Drift-Diffusion Model

4.1.3.3.1 Governing Equations and Simulation Geometry

In contrast, the drift-diffusion model allows one-dimensional (1D) variation along the device thickness, assuming spatial uniformity over cross-sections of the device area instead of throughout the entire device volume. This enables modeling of carrier concentrations, electrostatic potential and electric field, and carrier generation, drift, diffusion, recombination, and extraction along the device thickness, unlike the non-ideal diode model. This model also uniquely considers the absorber layer grain boundaries, each device layer, and each interface, assuming spatial uniformity in each region. This geometric layout is a strong choice since variations throughout each region would be difficult to model and are likely random and low, especially because grain boundaries in the perovskite film are the largest source of inhomogeneity of all layers. Additionally, this model assumes grain boundaries are evenly spaced, and this is true for most perovskite films (including ours).[17] Although, despite being an

available feature, we do not model grain boundaries since our HP film thicknesses (≈300 nm) are roughly equivalent to our grain diameter (≈300 nm), meaning grain boundaries do not exist across the HP film thickness for most of the device area (see SEM cross-sections of our HP films, see Section 6). Nonetheless, grain boundaries exist along the film thickness in some device regions, and carriers may laterally diffuse to, collide with, and undergo trapping, de-trapping, or SRH recombination at vertical grain boundaries, especially since ambipolar diffusion lengths (measured to be ≈1800 nm for high-bandgap films)[30,31] are much larger than grain diameters (≈300 nm). These effects are not modeled, but the model likely compensates by adjusting interfacial deep defect (trap) densities during fitting. This is acceptable for our conclusions, but we recommend modeling grain boundaries for devices with standard HP film thicknesses (e.g., 900 nm for world-record 26.15% HP device)[88] since grain boundaries do exist along the thickness of such films over most or all of the device area. Regarding the remaining assumptions, we assume the Boltzmann approximation,[33,79] and this is literature-supported (see Section 6).[143–145] Additionally, we assume no magnetically induced electric fields since such are only appreciable in organic solar cells (OSCs), not perovskite solar cells (PSCs).[80–83] We also assume the Einstein relation relating diffusion coefficient to mobility,[33,79] but this assumption may become inaccurate at high carrier concentrations under high illumination intensities.[146] Nevertheless, this is a strong assumption since such concentrations are not reached in this study.

4.1.3.3.2 Boundary Conditions

Additionally, it is common to assume electron and hole surface recombination velocities are infinite such that electrons and holes are in thermal equilibrium at the transport layers' interfaces with their electrodes.[33] Regarding ions, we assume ions cannot enter electrodes based on literature findings.[87] Although, in long-lived devices where reaction of iodide anions (I^-) in the electron transport layer (ETL) with the silver (Ag) electrode to form silver iodide (AgI) is a significant degradation mechanism,[131–134] it may be necessary to equate ion current densities to their known reaction rates (if significant) at the interfaces joining transport layers (TLs) with their electrodes.

4.1.3.3.3 Free Carrier Generation

The assumptions of normally incident illumination and spatial uniformity of optical phenomena across the device area are experimentally satisfied by utilizing normally incident illumination and fabricating devices to possess spatially uniform properties over the device area. Although, our absorber layer thicknesses are thin (≈300 nm) relative to high-performance devices (e.g., 900 nm for world-record 26.15% HP device),[88] and the resulting optical interference effects weaken the validity of the exponential (Beer-Lambert) absorption profile. Instead, the transfer matrix method (TMM) may be utilized to model interference effects, but this may result in different evolutions of fitted parameters (especially the G_{ehp}) over degradation time. Additionally, the TMM is known to overestimate interference effects,[147–149] and incorporating a method for dampening the predicted effects to a reasonable scale should also be considered. The derivation of the generation profile's exponential form and the resulting expression for the total generation rate will be provided in a future publication and in a future version of this thesis on our "DegradePV" GitHub repository (see Section 6).[63]

Regarding excitons and free electron-hole pairs (EHPs), light absorption in HPs produces both,[103,150] but HPs are non-excitonic materials possessing low exciton binding energies on the order of milli electron volts (meV).[103] Thus, excitons rapidly separate into electron-hole pairs (EHPs), validating our assumption that each absorbed photon creates an electron-hole pair

(EHP). A detailed discussion of exciton formation, dissociation, and decay models which could be employed in future work will be provided in a future publication and in a future version of this thesis on our "DegradePV" GitHub repository (see Section 6).

4.1.3.3.4 Free Carrier Recombination

Regarding free carrier recombination, we neglect trimolecular Auger recombination and geminate recombination losses. Indeed, HPs do not exhibit appreciable trimolecular Auger recombination in the range of simulated carrier concentrations ($\approx 10^{19} - 10^{24}\ m^{-3}$, to be provided in a future publication and in a future version of this thesis on our "DegradePV" GitHub repository (see Section 6))[63] under 1 sun illumination,[75,76,79,80,123–150] and since HPs are non-excitonic materials (i.e., excitons exist in negligible concentrations),[103] geminate recombination losses are also negligible (see Section 6). Additionally, we again assume the Boltzmann approximation[33,79] in all recombination models, and as stated previously, it is well-supported by literature (see Section 6).[143–145]

4.1.3.3.4.1 Bimolecular Recombination

A detailed overview of theoretical models and experimental results for bimolecular recombination in HPs will be provided in a future publication and on our "DegradePV" GitHub repository (see Section 6).[63] Regarding trap-assisted, bimolecular Auger recombination, Shockley-Read-Hall (SRH) recombination dominates trap-assisted recombination. Additionally, short-circuit current density (J_{sc}) is not diffusion-length-limited, meaning carrier concentration profiles are roughly symmetric (see Section 6). Thus, simply accounting for the rate of this Auger pathway without locational dependence is an accurate approach. Nevertheless, accounting for these phenomena may be prudent in cells with high deep defect (trap) densities, poor carrier mobilities and extraction efficiencies, and high carrier concentrations enabled by high illumination intensities or low bandgap.

4.1.3.3.4.2 Nonradiative, Monomolecular, Shockley-Read-Hall (SRH) Recombination

Regarding the steady-state approximation, free carrier trapping and de-trapping occur on similar time scales (seconds)[151] to J-V scans, meaning the steady-state approximation is a source of error, but only when employing the steady-state model. Additionally, regarding the assumption of a single mid-gap trap state for modeling SRH recombination, a detailed theoretical justification recombination is provided in Section 8.1.3: Appendix A.3. Although, defect energy levels, formation energies, and thus concentrations may evolve with quasi-Fermi levels when applied bias and illumination are changed,[152–155] and while this model can technically model this by simulations at each applied bias with unique, user-specified trap energy structures, but such structures are difficult to obtain as they require density functional theory (DFT) simulations,[156–161] and they are thus not modeled. The inaccuracy of this assumption would increase with increasing applied bias and illumination intensity since reported defect structures are simulated assuming zero applied bias and dark conditions, and it would appear at and after the knee of the current-voltage (J-V) scan (i.e., when recombination becomes significant). Although, under the single mid-gap trap assumption, this assumption would be insignificant as long as shallow defect levels (outer ≈20% on each side of the bandgap, see Section 6) do not shift into the deep defect region (middle ≈60% of bandgap, see Section 6).

4.1.3.3.5 Device Parameters Determined by Literature Review

Although, despite exhibiting lower fitting error, the drift-diffusion model also suffers from inaccuracies in literature-based device parameters. Such parameters vary due to variation among literature reports and with degradation conditions (see Section 6), and since the parameters reviewed are highly correlated with fitting parameters, we again expect fitting parameters to adjust accordingly to maintain low fitting error. This again causes systematic errors in fitting parameter values, but the drift-diffusion model accurately models device behavior, and the general trends of the evolutions of drift-diffusion fitting parameters over time are thus unaffected.

4.1.3.4 Summary of Mechanistic Model Assumptions

In short, the drift-diffusion model improves upon the following assumptions of the non-ideal diode model, enabling the drift-diffusion model's higher accuracy:

- Steady-state approximation – assumes steady-state charge carrier generation, drift, diffusion, recombination, and extraction (i.e., no transient accumulation of charge carriers). The drift-diffusion model enables both steady-state (SimSS) and transient simulations (ZimT).
- Uniform excess carrier concentration profiles with infinite carrier mobility and no carrier-generated electric fields – the drift-diffusion model allows one-dimensional (1D) modeling of free carrier and ion concentration, electrostatic potential, and electric field profiles and carrier generation, drift, diffusion, trapping, de-trapping, recombination, extraction, and accumulation at absorber layer grain boundaries and in each device layer and interface.
- Only trap-assisted, nonradiative, monomolecular, Shockley-Read-Hall (SRH) recombination – the drift-diffusion model considers trap-assisted, nonradiative bimolecular Auger recombination, direct (band-to-band), radiative bimolecular recombination, and trap-assisted, non-radiative, monomolecular Shockley-Read-Hall (SRH) recombination in the bulk, at grain boundaries, and at interfaces with transport layers.
- Perfect electron-selective anode and hole-selective cathode – the drift-diffusion model exhibits strong carrier selectivity at HP-TL interfaces and electrodes.

Although, the following items remain unaccounted for and are thus recommendations for future model improvement:

- Steady-state approximation – we perform steady-state fits for all experiments, but due to the large computation times of transient simulations, we only fit the transient drift-diffusion model to one experiment per architecture.
- Model grain boundaries for standard-thickness HP films since such films contain GBs along the HP film thickness in most or all regions of device area.
- Utilize a generalized form of the Einstein relation[146] for higher carrier concentrations under higher illumination intensities.
- Model defect ion extraction into and reaction with electrodes (e.g., iodide anions (I^-) with the silver (Ag) electrode to form silver iodide (AgI)).[131–134]
- Model optical interference effects with the transfer matrix method (TMM), perhaps with a method for dampening the TMM's characteristic overestimation of interference effects.[147–149]

- Model trap-assisted, bimolecular Auger recombination and possibly trimolecular Auger recombination, especially in cells with high deep defect (trap) densities, poor carrier mobilities and extraction efficiencies, and high carrier concentrations.
- Develop computational models for defect structure (i.e., defect energy levels, formation energies, and thus concentrations) under varying applied biases and illumination intensities and enable implementation with changing applied bias in drift-diffusion simulations.

4.1.3.5 Fitting

Fits are successful with final fitting parameter values lying within the allowed ranges. Thus, as stated previously, fitting error is almost exclusively due to model assumptions. Although, removal of the zero-bias measurement for non-ideal diode fitting is a source of error, especially for the J_{sc}. Nevertheless, since J-V curves are relatively flat near the current density axis (zero bias), this removal likely has minimal effect. Additionally, large volatility is observed in drift-diffusion-related parameters due to insufficient sensitivity of fitting parameters to changes in current-voltage (J-V) scans, or conversely, insufficient information in current-voltage (J-V) scans to yield high precision in fitting parameters.

4.1.4 Cumulative Sensitivity Analysis (CSA)

Error sources in the cumulative sensitivity analysis (CSA) include differentiating solar cell parameters with respect to fitting parameters to determine sensitivity coefficients using finite difference methods, linear interpolation in modeling derivatives between measurements, and numerical integration. Although, these calculation steps all depend on fitting parameter values, meaning fitting parameter error propagates through these error sources. As stated in Section 2.2.10.3, finite difference methods are very sensitive to random error due to the low number of considered points, but the sensitivity coefficients of solar cell parameters to fitting parameters are smooth since these models involve well-behaved equations. Although, since such sensitivity coefficients vary with fitting parameter values (e.g., sensitivity of V_{oc} to deep defect (trap) densities increases with increasing deep defect (trap) density), high volatility in fitting parameters may cause inaccuracies. Regarding fitting parameter time derivatives, our measurement frequency is sufficiently high to enable relatively smooth evolutions for low-volatility parameters, and thus low error in time derivatives and their interpolation. Although, high volatility in fitting parameters again increases these errors. Last, numerical integration errors are very low across many methods, but we utilize the method with greatest accuracy and robustness to parameter volatility: adaptive quadrature.[72–76]

Indeed, the non-ideal diode model CSA exhibits low error while the drift-diffusion model CSA exhibits moderate error, indicating these error sources are low when fitting parameter volatility is low and that fitting parameter error is the primary source of error for CSA. To address this, we perform drift-diffusion CSAs with the moving averages of drift-diffusion fitting parameters for varying numbers of moving average points and present results for the lowest CSA error (see Section 6). Nevertheless, we recommend decreasing the drift-diffusion CSA's error by decreasing drift-diffusion fitting parameter volatility.

4.1.5 Derived Drift-Diffusion Parameters

Derived drift-diffusion parameters are susceptible to the error sources of their constituent parameters, and especially high volatility in drift-diffusion fitting parameters. Although, high volatility is sometimes reduced when combining charge-specific quantities into ambipolar

quantities since such removes correlations between the parameters. Such correlations may exist since such quantities may have similar effects on device characteristics (e.g., cation and anion concentration). However, volatility may also increase when combining parameters of differing type (e.g., diffusion constants and carrier lifetimes to calculate diffusion lengths) due to combined uncertainty.

4.1.6 Effective Degradation Profile Model

The primary error sources for the effective degradation profile model are also model assumptions, meaning the effective degradation profile parameters are indeed effective, not the actual active area and thickness of a shrinking HP film. Specifically, this parameterization neglects the distribution of degraded product at interfaces with transport layers (TLs), grain boundaries, and in the crystal bulk in any number of dimensions. Nevertheless, these parameters are useful in describing the effective extents of area and thickness degradation and their differing effects on device properties, producing expected results.

4.1.7 General Parameter Transformations

4.1.7.1 Normalization to Time-Zero Values

Regarding normalization of parameters over degradation time to their time-zero values, the resulting fractional parameters are subject to the error of their untransformed parameters. Although, the fractional parameters directly depend on their time-zero parameter values. Thus, among multiple experiments, fractional parameters may exhibit a far wider range of values than their untransformed counterparts if the parameters exhibit high volatility, and we thus report nonfractional parameters in such cases. For example, ideality factor begins at values far above two (e.g., ≈3-4 in Figure 26) and rapidly declines to between one and two, evolving slowly for the remainder of degradation. These initial values are highly temperature-dependent, and this causes the fractional ideality factor to exhibit a strong, linear temperature dependence not caused by Arrhenius behavior of the relevant degradation mechanisms over time (see Section 6).

4.1.7.2 Moving Averaging

Moving averaging removes large volatility at the cost of systematic error by aggregating local variation. This causes adjacent points to average to similar values with lower volatility, requiring longer-term, systematic changes in parameter values to cause significant changes in moving averages. Although, this causes systematic changes in parameter values to manifest late in moving averages (by the number of moving average points), causing systematic errors in parameter values and their rates of change. Additionally, small errors are also caused by the bounding of moving average intervals near the first and last measurements. These errors are small, estimated by the small moving average errors of low-volatility parameters. Although, parameter volatility far outweighs these systematic errors for drift-diffusion-related parameters (see Section 3.1 and 4.1.3.5), incentivizing our use of moving averages for these parameters.

4.1.8 Predictive Modeling of Operational Lifetime (T_{80})

Error sources in our predictive models include model assumptions (see Section 4.1.3.2 and Section 4.1.3.3), feature (parameter) inaccuracies, experimental errors in measured operational lifetimes, and model training error. Although, experimental errors are low as above, meaning the primary sources of predictive model error other than feature inaccuracies are model assumptions and model training. Overall, the machine learning (ML) models assume features linearly

contribute to the natural logarithm of operational lifetime. Even with the additional correction terms in variations of the linear model, model assumptions are the largest source of error but are nevertheless accepted since all predictive models suffer from such assumptions. Regarding model training, training error decreases with increasing experimental dataset size and fewer features. For small datasets, the lower theoretical limit for the ratio of between dataset size and sparsity (number of selected features) is ≈10 (see Section 6). With the number of experiments (and thus operational lifetime values) limited to 61, 45, 37, and 143 for the low-bandgap, MAPbI3, high-bandgap, and overall models (see Table 6), respectively, and the typical number of significant selected features ranging from 1 to ≈15, our models are very close to the lower limit of acceptable dataset size. Last, the outlier removal process described in Section 2.2.12.3.1 (i.e., removing points greater than 3.5 standard deviations from their respective experimental values) is standard statistical practice and only occasionally removes single experiments, meaning its systematic error is minimal. Overall, the primary sources of predictive modeling error for parameter sets with low-volatility features (e.g., solar cell parameters) are model assumptions, and for high-volatility parameter sets (e.g., drift-diffusion-related parameters), parameter volatility causes the increased error.

Beyond the error of single predictive models, sequentially applying predictive models (e.g., when applying the accelerated aging model to unaccelerated model results) yields a greater error due to combined uncertainty (see Section 3.2.2). Specifically, the accelerated aging models exhibit much greater errors than the optimized unaccelerated models for each architecture (well above the recommended 6% maximum $NRMSE_{mean-norm}$), meaning the errors of our accelerated aging models must be significantly decreased to maintain accuracy when extending the prediction factor with accelerated aging (see Section 6). This may be done by extending the range of degradation conditions studied, and namely by enabling temperatures up to the perovskite's thermal decomposition temperature. Specifically, $MAPbI_3$ exhibits general decomposition at low temperatures (≈80-100°C) and, in thermogravimetric analyses (TGA), rapid chemical decomposition around ≈250-300°C.[162–165] Similarly, our low-bandgap perovskite and its variations also exhibit general thermal decomposition at low temperatures but volatilization of organics (e.g., MA and FA) at ≈125°C and hydrogen iodide (HI) volatilization at ≈170°C.[166–168] In contrast, our high-bandgap perovskite and its variations ($FA_xCs_{1-x}Pb(I_yBr_{1-y})_3$) exhibit general thermal decomposition but successful operation up to higher temperatures (≈150-200°C, stronger thermal decomposition above 200°C, and complete thermal breakdown above ≈300°C.[169–172] Thus, we recommend extending device degradation experiments up to the complete thermal breakdown temperatures with an analysis of the variation in ML modeling error with increasing temperature. Specifically, the strong thermal decomposition regime with organics volatilization would not be observed in operating conditions and is not necessarily related to the device degradation mechanisms, meaning ML modeling error will increase after an upper temperature threshold. Determination of such thresholds is thus a key priority for future research to provide recommended temperature ranges for device degradation experiments used for the development of predictive models for operational lifetimes.

4.1.9 Summary of Error Source Evaluation

Solar cell parameters are subject to negligible cubic interpolation error while mechanistic model fitting error almost exclusively due to the overviewed model assumptions (Section 4.1.3.2 and 4.1.3.3). Additionally, the drift-diffusion fitting parameters exhibit large volatility due to insufficient sensitivity of fitting parameters to changes in current-voltage (J-V) scans, or

conversely, insufficient information in current-voltage (J-V) scans to yield high precision in fitting parameters. This volatility is the largest/primary source of error for every downstream analysis involving these parameters. Although, moving averages reduce this volatility at the expense of low systematic error. Regarding the effective degradation profile model, its primary error sources are also model assumptions, but these parameters are nevertheless useful in describing the effective extents of area and thickness degradation and their differing effects on device properties. Last, predictive models are primarily subject to inaccuracies in feature values and model assumptions. Errors in experimental measurements, suboptimal fitting, interpolation, and numerical integration are negligible in all cases.

4.2 Recommendations

Regarding future work, we recommend addressing key sources of error and expanding scope to improve both our mechanistic models for device performance decline and our predictive models of operational lifetime, ultimately to enable the development of long-lived devices.

4.2.1 Experimental

4.2.1.1 Techniques for Characterization of Electronic Properties

As discussed in Section 3.1 and 4.1.3.5, large volatility is observed in drift-diffusion-related parameters due to insufficient sensitivity of fitting parameters to changes in current-voltage (J-V) scans, or conversely, insufficient information in current-voltage (J-V) scans to yield high precision in fitting parameters. We thus recommend varying scan speeds alongside illumination intensities and incorporating additional measurement techniques, especially transient techniques which capture ion migration effects. Specifically, in the only other known study applying drift-diffusion modeling to PSC degradation (although computational), Clarke *et al.* demonstrated impedance spectroscopy simulations to exhibit far greater sensitivity to the simulated linear increase in SRH recombination rate compared with current-voltage (J-V) scans,[53] suggesting impedance spectroscopy as the next logical addition to the present work. Additionally, other electronic device characterization techniques include fluence-dependent transient photocurrent (TPC), transient photovoltage (TPV), and time-resolved microwave photoconductance (TRMC).[33] Overall, it is the transient and alternating nature of these techniques which provides valuable new information for fitting and thus improves fitting parameter precision. Beyond electronic device characterization, many other techniques which are also applicable to non-device structures may be performed. Such techniques performed in our previous studies include spatially resolved steady-state photoluminescence (SSPL), time-resolvent photoluminescence (TRPL), and steady-state photoconductivity (PC), and many other techniques are discussed in our literature review for device parameters (see Section 6). These techniques may allow spatial or spectral resolution, where spatial resolution would enable visualization of corresponding drift-diffusion parameters over the device area during degradation (potentially to inform improved degradation profile models) and spectral resolution would provide information on the films' energetic structure throughout degradation. Additionally, these techniques may be performed on many structures including single device layers on glass, single device layers sandwiched between electrodes, incomplete device architectures after deposition of each layer, and completed devices, and such consideration of multiple structures would provide direct information on how individual layers affect device characteristics. Regarding the utility of such techniques in modeling, these techniques often yield drift-diffusion-related parameters through simplified models or use of a drift-diffusion model (e.g., Koster *et al.*'s),[34,37,39–42] and these parameters may be introduced as fitting constraints to improve

fitting parameter precision. Specifically, if the measurement yields drift-diffusion fitting parameters throughout degradation, the parameters may be fixed as device parameters and excluded from the fitting parameter set (fitting parameter constraint). Instead, if the measurement yields drift-diffusion fitting parameters at time-zero or derived drift-diffusion parameters, the values may simply be introduced as fitting constraints.

Of these options, we recommend performing current-voltage (J-V) scans and impedance spectroscopy during degradation along with spatially resolved SSPL and TRPL after deposition of each layer and during degradation. These techniques are relatively common, inexpensive, and may be performed on devices after deposition of each layer (rather than requiring fabrication of non-device architectures) and throughout degradation. Moreover, we recommend these measurements be performed at varying scan speeds and under varying illumination intensities (especially in the dark) to maximize the experimental information provided in fitting. We also recommend incorporating spatial resolution whenever possible to visualize evolutions of the corresponding drift-diffusion parameters over the device area during degradation, potentially to inform improved degradation profile models. Last, if incorporating non-device architectures, we recommend steady-state photoconductivity (PC) through the thickness and laterally across film area to determine ambipolar diffusion lengths of the given film along two differing current flow paths. Since these two paths would have differing numbers of grain boundaries, the grain boundary (GB) deep defect (trap) density in undegraded films may be fitted and set as a fitting constraint in fitting degrading device data.

4.2.1.2 Imaging Techniques

Beyond characterization of electronic properties, we recommend performing the considered imaging techniques (DF and SSPL) for the low-bandgap architecture since these measurements were not included, and more generally, we recommend additional imaging techniques to improve degradation profile models. Such techniques could include various forms of microscopy including bright-field (BF), dark-field (DF), and scanning/tunneling electron microscopy (SEM/TEM) of degraded devices' cross-sections. These measurements would aim to visualize the distribution of degradation products at the HP-TL interfaces and along grain boundaries, potentially at varying fractions of T_{80} for varying degradation conditions. The estimated distribution of degradation products could then be utilized as an accurate (not just effective as in this study) degradation profile model and inserted in one or more dimensions to drift-diffusion models for fitting, representing the first mechanistic model for PSC degradation which considers an accurate HP film degradation profile.

4.2.1.3 Architectures

Regarding architectures, all three architectures considered in this study exhibit the proportionality between J_{sc}, J_{ph}, and G_{ehp} with no other sources of J_{sc} loss (e.g., parasitic resistances, diffusion lengths, ion migration). We thus recommend investigation of combinations of architectures and degradation conditions which do not obey this proportionality due to these other contributors to J_{sc} loss. Additionally, all architectures considered in this study are unencapsulated, meaning the predictive model performance and feature coefficients apply only to unencapsulated devices. We therefore also recommend generalize these models to include encapsulated devices with encapsulation properties (e.g., diffusion constants) and geometric properties (e.g., layer thicknesses) as features, culminating with formation of a global database of PSC degradation data continuously used to train small-dataset (e.g., our models) and large-dataset (physics-informed neural network) predictive models.

Beyond modeling degradation of completed devices, we also suggest modeling devices fabricated from degraded HP films. Specifically, we recommend fabricating incomplete device architectures without the back electrode to enable degradation of the HP-ETL interface as in a device (i.e., with both the HP and ETL present), degrading the incomplete devices in varying degradation conditions for varying time periods while performing optical characterizations (e.g., spatially resolved SSPL and TRPL) throughout degradation, and finally depositing the back electrode and performing electronic characterization of the completed devices. This enables characterization of the device during degradation from the back side (which cannot be done with the back electrode present), enabling better characterization of the HP-ETL interface degradation's influence on device performance. These additional measurements may then be included as experimental data to be globally fit alongside current-voltage (J-V) scans of the completed devices. Although, bias cannot be applied uniformly over the device area without the back electrode, meaning the effects of applied bias on degradation are unaccounted for. Nevertheless, the degradation profile is likely similar and may still be varied by varying temperature and atmospheric concentrations, flow rates, and flow velocities.

4.2.2 Computational

4.2.2.1 Mechanistic Modeling

4.2.2.1.1 Addressing Sources of Error

Regarding experimental data, we recommend decreasing the voltage (and thus time) step of current-voltage (J-V) scans and simulations (e.g., from 0.05 V to 0.005 eV) to both reduce interpolation error in calculating solar cell parameters and to increase accuracy of transient drift-diffusion modeling where the profile of applied bias over time is important. Additionally, we recommend varying scan speed and expanding the scan voltage range (but not to unmodeled regions (e.g., the breakdown point)) for lower volatility in fitting parameters. Additionally, to reduce error caused by variation in literature-based device parameters, we recommend measuring all possible parameters (see Section 6) for each device, and if not for each device, averaging measurements across multiple samples and batches. Although, this does not include transport layer (TL) band energies and electrode work functions since ultraviolet photoelectron spectroscopy (UPS) results are error-prone.[173–177] This is demonstrated by the high variation of these quantities in literature reports (see Section 6).

Regarding model assumptions, we recommend fitting the transient drift-diffusion model (ZimT) to experimental data to eliminate the steady-state approximation in all fits. Such would be achievable with larger supercomputer clusters or accelerated optimization (e.g., improved initial guesses). Additionally, we recommend modeling grain boundaries in one dimension for standard-thickness HP films and utilizing the transfer matrix method (TMM) to account for optical interference. For fitting, we recommend both including the zero-voltage measurement and expanding the scan voltage range (but not to unmodeled regions (e.g., the breakdown point)) to match the expanded experimental scan range, again for both accuracy and lower volatility in fitting parameters. Additionally, to reduce the errors in the cumulative sensitivity analysis (CSA) and derived drift-diffusion parameters, we recommend reducing volatility in drift-diffusion fitting parameters, in addition to continued use of moving averages. Last, for the inaccuracies of effective degradation profile model and predictive models for operational lifetime, we recommend developing the new models discussed below.

4.2.2.1.2 Expanding the Scope of Mechanistic Modeling

Beyond addressing these sources of error, we recommend various additional modeling techniques to expand scope. First, we recommend incorporating traditional statistical analyses (e.g., principal component analysis (PCA)) and traditional local and global sensitivity analyses (e.g., Sobol method) to complement our local, derivative-based sensitivity analysis and CSA, provide additional ML features, and potentially inform ML feature selection with novel ML models dependent on sensitivity coefficients. Additionally, we recommend developing fully computational models for device performance decline. Such a model would be created by developing a mass transport model for gaseous reactant and product transport throughout the device (i.e., through device layers and along grain boundaries) and combining it with a kinetic rate law model for HP decomposition (e.g., those developed in our previous studies)[16,19–21] to simulate degradation profiles and feeding these profiles into the complete drift-diffusion model to simulate device performance.

Specifically, we recommend sealing device edges (e.g., with Kapton tape as in our previous study)[17] to allow uniform degradation of only the HP film thickness (not the device edges) and varying species concentrations, flow rates, and flow velocities to create a comprehensive space of mass transport conditions through device layers (including along grain boundaries). We would describe these conditions with the dimensionless numbers describing the competition between convective and diffusive mass transport (i.e., Sherwood number) and between mass transport and chemical reaction rates (i.e., Damkohler number). Empirical models of device characteristics over time versus degradation conditions and these dimensionless numbers could then be constructed. Although, these models would be specific to device geometry and encapsulation scheme (if any), and we therefore recommend creating a one-dimensional (1D) model for degradation profile based only on degradation conditions and atmospheric flow conditions (expressed by the dimensionless numbers for generality). Such a 1D model would be created by developing a 1D mass transport model for gaseous reactant and product transport throughout the film (e.g., along grain boundaries) and combining it with a kinetic rate law model for HP decomposition (e.g., those developed in our previous studies).[16,19–21] This fully computational model would be an effective first step, but future models should account for additional complexity including three-dimensional (3D) mass transport and drift-diffusion simulations with a 3D grain boundary (GB) structure, likely incorporated with a finite element analysis (FEA) software (e.g., COMSOL). This model could then be fit to degradation profiles estimated from advanced cross-sectional imaging to determine unknown mass transport properties (e.g., gas diffusion constants along grain boundaries) or used to simulate degradation profiles for insertion into the drift-diffusion model (without experiments). Moreover, these degradation profile and drift-diffusion models could then be used to fit device degradation datasets by varying both mass transport and drift-diffusion fitting parameters, or to simulate device characteristics over degradation for any device geometry, encapsulation scheme, and set of degradation and atmospheric flow conditions without requiring experiments.

This fully computational model would accurately predict operational lifetimes and could thus be used to optimize device design to maximize operational lifetimes without experiments. Such designs could then be fabricated and tested under accelerated aging conditions with our predictive models to validate simulated results. Thus, despite requiring a kinetic rate law model for HP decomposition (composition-specific and expensive), such a fully computational model would be very powerful. Indeed, fully computational degradation models have been developed

for other PV technologies, and since the primary barrier to HP PV scalability is their degradation, such models are an even greater priority for HP PV.

4.2.2.2 Predictive Modeling of Operational Lifetimes (T_{80})

There are various possible expansions to the scope of predictive modeling. First, any new mechanistic model parameters should be included as new features, and we recommend further identification of shortened feature sets containing only important features to potentially reduce random error in training. Beyond mechanistic models, we recommend continued development of small-dataset ML methods (based on the foundation built by Sunkari *et al.*)[32] to improve predictive accuracy and ability. Additionally, we envision a global database of HP PV degradation data continuously used to train small-dataset (e.g., our models) and large-dataset (e.g., physics-informed neural networks) predictive models, possibly by expansion of the existing "Perovskite Database" compiling all HP PV degradation studies before 2020.[178] Such a vast, open-source collection of data would provide the dataset size necessary to develop the accurate and general predictive models required for long-lived device development.

4.2.3 Summary of Recommendations

Future work should both reduce error sources and expand modeling scope. Experimentally, we recommend varying scan speeds and illumination intensities, measuring literature-based device parameters, and incorporating additional measurement techniques (namely impedance spectroscopy as recommended by Clarke *et al.*)[53,54] to reduce drift-diffusion fitting parameter volatility. We also recommend additional imaging techniques to improve degradation profile modeling. For modeling, we recommend utilizing Koster *et al.*'s grain boundary, transfer matrix method, and transient drift-diffusion models for all experiments. We also recommend developing fully computational models accounting for both mass transport and HP decomposition kinetics to enable optimization of device design to maximize operational lifetimes without experiments. Regarding predictive modeling, we recommend investigating other architectures, degradation conditions, and encapsulation schemes, along with developing new ML features and models, to generalize and improve our predictive models. Ultimately, we envision a global database of HP PV degradation data used to train small-dataset (e.g., our models) and large-dataset (e.g., physics-informed neural networks) predictive models for long-lived device development.

5 CONCLUSIONS

In this study, we have successfully identified and modeled the mechanisms of halide perovskite (HP) film degradation's influence on device performance in degrading perovskite solar cells (PSCs) through a combination of degradation profile modeling, mechanistic modeling of current-voltage (J-V) scans, and a unique cumulative sensitivity analysis (CSA) for three architectures of PSCs degrading in various conditions. We then use the various sets of parameters as features in a small-dataset machine learning (ML) model for successful predictive modeling of operational lifetimes.

5.1 Mechanism of Halide Perovskite (HP) Film Degradation's Influence on Device Performance in Degrading Perovskite Solar Cells (PSCs)

5.1.1 Linear Active Area Extinction and J_{sc} Decline Due to Photooxidation at Device Edges

Gaseous reactants first degrade the exposed perovskite at and around the device edges. Then, after steady diffusion through this degraded perovskite, the gaseous reactants degrade the outermost surface of undegraded perovskite along the entire HP film thickness. This causes a linear decline in the effective active area derived from our effective degradation profile analysis and in J_{sc}-related quantities for the remainder of degradation, contributing appreciably to the J_{sc} decline in our $MAPbI_3$ device dataset and negligibly in our high-bandgap dataset.

5.1.2 Deep Defect (Trap) Reduction and Band Misalignment at Degrading HP-TL Interfaces and Grain Boundaries

Gaseous reactants then reach and degrade both the HP-ETL interface and its surface-exposed grain boundaries after diffusing through the back electrode and ETL, reducing its deep defect (trap) density ($N_{tr,HP-ETL}$) (see Figure 24). Then, since defects are often charged and thus act as space charge which electrostatically inhibits carrier movement, this deep defect (trap) passivation causes the concurrent increase in the fitted electron mobility (μ_n). These changes together then cause the expected concurrent decrease in dark reverse bias saturation current (J_0) and correlated decrease in ideality factor (n_{id}), and increases in quasi-Fermi level splitting (QFLS, ΔE_F) in steady-state photoluminescence (SSPL) imaging, open-circuit voltage (V_{oc}), fill factor (FF), and power conversion efficiency (PCE). Additionally, the increased mobility of carriers at the HP-ETL interface enables increased anion extraction into the ETL, reducing ion-based electric field shielding near the HP-ETL interface, increasing carrier extraction, and thus improving performance. Although, the corresponding decrease (increase in magnitude) in hysteresis metric ($P_{ion-hys}$) only applies under illumination such that a sufficient number of mobile defects exist to outweigh the steady increase (decrease in magnitude) caused by the steady transition from slightly n-type to p-type behavior through the liberation of gaseous halogens. Additionally, it is noted these changes in deep defect (trap) densities and carrier mobilities may affect J_{sc}-related quantities in many devices with thicker HP films (e.g., 900 nm for world-record 26.15% HP device),[88] in which diffusion length limits carrier extraction. Although, since our devices possess relatively thin HP films (≈300 nm), their J_{sc} and the diode model's photocurrent (J_{ph}) are roughly proportional to the electron-hole pair (EHP) generation rate (G_{ehp}) throughout degradation, not appreciably affected by any other optoelectronic properties including deep defect (trap) densities, diffusion lengths, parasitic resistances, and ion concentrations. Thus, at early times, J_{sc} exhibits a steady, linear nearly proportional to the steady declines in fractional effective HP film area and thickness followed by a possible exponential-like burn-in (i.e., rapid decline) we attribute to the

exponential nature of the Beer-Lambert absorption profile coupled with the steady decline of effective active thickness.

Gaseous reactants then continue steadily diffusing through the back electrode, ETL, and degraded perovskite (especially along grain boundaries), shrinking grains and degrading additional grain boundaries as gaseous reactants penetrate deeper into the film. This causes the accumulation of solid degradation products at the HP-TL interfaces and grain boundaries, and this accumulation causes subsequent band misalignment of the HP and TLs with the degradation products which impede carrier movement. As such, we observe decreases in both the fitted electron mobility (μ_n) and hole mobility (μ_p), and due to the decreased extraction of carriers, an increase in SRH recombination rate and thus a perceived increase in the fitted interfacial deep defect (trap) densities. Ultimately, this competition of deep defect (trap) passivation and band misalignment of the HP and TLs with accumulating degradation products results in local extrema in all related parameters listed above.

Finally, near T_{80}, degradation products have accumulated at both HP-TL interfaces and all grain boundaries as the gaseous reactants reach and degrade the HP-HTL interface (observed as a rapid, uniform increase in DF intensity over the device area), causing all of these V_{oc}-related and FF-related properties to plateau at roughly their original values, further exaggerating the importance of HP film absorptivity loss (caused by its chemical decomposition) to device performance decline. Last, shunt resistance (R_{sh}) is observed to steadily decrease and series resistance (R_s) to steadily increase over degradation.

Overall, the extracted diode and drift-diffusion fitting parameters and their corresponding derived parameters are mechanistic properties of the device, and coupled with our effective degradation profile parameters, the evolutions of and correlations among parameters over degradation illuminate the mechanisms of device performance decline. This work thus constitutes the most advanced mechanistic model of PSC performance decline to date, and in quantifying the exact influence of each fitting parameter on each solar cell parameter over time in our unique cumulative sensitivity analysis (CSA), this work enables evaluation of the influence of each degradation mechanism on device performance decline.

5.2 Predictive Machine Learning (ML) Modeling of Operational Lifetime (T_{80})

Beyond mechanistic modeling, we utilize the untransformed and transformed versions of the considered parameters as features in predictive machine learning (ML) models of operational lifetime (T_{80}).

5.2.1 The Dependence of Predictive ML Model Error on Architecture, Model Complexity, and Measurement Time

For our datasets, we generally observe the architectures in order of lowest-to-highest model errors to be $MAPbI_3$, low-bandgap or overall (i.e., all architectures), and high-bandgap, where the high-bandgap architecture's relatively large errors are likely due to its lower range of operational lifetimes compared with the low-bandgap and $MAPbI_3$ datasets. Additionally, we observe ML model errors to generally increase with model complexity, appearing lowest for the solar cell parameters, increasing for the degradation profile parameters due to their neglect of J-V data, increasing further for the diode parameters due to their moderate systematic and random volatility, and maximizing for drift-diffusion parameters due primarily to their high random volatility (alongside their moderate systematic volatility similar to the diode parameters). Last, we observe

a general increase in model accuracy with increasing measurement time (in percentage of T_{80}) with a local maximum often at 5% of T_{80}.

5.2.2 General Observations of Feature Selection, Coefficients, and Correlations

Regarding feature coefficients, we find the selected features are often maximally independent to describe the various device degradation phenomena with the lowest possible number of selected features (i.e., sparsity). Additionally, we find the selected features, their weighting coefficients, and their correlations align well with our mechanistic modeling results (i.e., the evolutions of and correlations among parameters, their relationships with degradation conditions, and our unique CSA). We further find first and second time derivatives are often selected since they effectively describe the rates of processes and rates at which competing processes transition between dominant phenomena, respectively. Last, degradation conditions are sometimes selected when included in the feature set for low incorporated measurement times, implying degradation conditions can provide useful empirical measures for the influences of certain degradation phenomena on operational lifetimes for models utilizing low measurement times.

5.2.3 Identification of Best-Performing Machine Learning (ML) Models for Various Sets of Featurization and Predictive Model Specifications to Establish Baselines for Model Development in Future Work

Finally, we utilize the solar cell, fitted, derived, and degradation profile parameters as features in predictive machine learning (ML) models of operational lifetime (T_{80}), achieving a mean-normalized root-mean-squared (RMS) error (NRMSE) of 26.5% with time-zero measurements using only temperature and the first J-V measurements, without requiring degradation conditions or the composition-specific kinetic rate law model necessary for our previous model. With the further improvements recommended in this study, this could enable predictive modeling of 30-year devices in just days or weeks of common, low-cost electronic measurements, providing a strong foundation for and powerful step towards high-throughput testing and development of long-lived devices. Additionally, we establish that the scope of application of these models is determined by four key specifications: the number of points utilized in calculating parameter transformations (n_{pt}), considered measurement time (in percentage of T_{80}), and inclusion or exclusion of gaseous reactant concentrations and the HP decomposition rate predicted by the kinetic rate law model. Furthermore, given the effects these specifications have on the generality and efficacy of these models, we identify the best-performing models for numerous subsets of specifications which adhere to certain restrictions on these specifications, thus enabling evaluation of model error and results (i.e., selected features and their coefficients) under these varying levels of generality. In fact, these cases represent realistic scenarios which may be encountered by research or companies developing such models for high-throughput testing and development of long-lived devices, and this analysis thus provides the first baselines for model errors, feature selection, and feature coefficients in each of these cases and thus guides the development of these models in such work.

6 DATA AND CODE AVAILABILITY AND FUTURE SUPPLEMENTARY MATERIAL

In this work, I constructed a data pipeline which performs all relevant processing, modeling, analysis, and visualization of data in this study. I will publish this pipeline as a Python package (currently to be named "DegradePV") along with all associated data and visualizations both on my personal GitHub webpage[63] and our group's GitHub webpage.[179] This pipeline enables modeling, analysis, and visualization of any dataset describing degrading solar cells with the measurement techniques employed in this study and both steady-state and transient drift-diffusion simulations with SIMsalabim. Additionally, the pipeline is easily generalized to other measurement techniques including those recommended in Section 4.2.1 (e.g., impedance spectroscopy), and I am happy to collaborate in generalizing the package for such uses upon request. Regarding previous pipelines, the experimental data collection and analysis pipeline utilized in many of our previous film and device degradation studies along with the corresponding data is available in our "perovskite-ML" GitHub repository.[179] Last, the machine learning (ML) modeling, analysis, and visualization pipelines developed by Dr. Wiley Dunlap-Shohl for our initial $MAPbI_3$ device degradation study and in Dr. Preetham Sunkari's PhD dissertation of small-data machine learning (ML) modeling are available in our "small-data-ml" GitHub repository.[124]

Regarding data, all film and device degradation experiment and modeling data and visualizations will be published in the "DegradePV" repository both for viewing by other researchers and as an illustration of the DegradePV package's application to generic datasets. Additionally, there are many references to this section (i.e., Section 6) throughout this work, and such references refer to the additional writing and data visualizations from this work which will be made available in a future publication and on our "DegradePV" GitHub repository[63] within the weeks following publication of this thesis.

7 REFERENCES

(1) *U.S. Energy Information Administration - EIA - Independent Statistics and Analysis*. https://www.eia.gov/outlooks/aeo/electricity_generation.php (accessed 2024-05-16).

(2) Powell, D. M.; Fu, R.; Horowitz, K.; Basore, P. A.; Woodhouse, M.; Buonassisi, T. The Capital Intensity of Photovoltaics Manufacturing: Barrier to Scale and Opportunity for Innovation. *Energy Environ. Sci.* **2015**, *8* (12), 3395–3408.

(3) *Materials and Devices | Photovoltaic Research | NREL*. https://www.nrel.gov/pv/materials-devices (accessed 2025-08-18).

(4) Powalla, M.; Bonnet, D. Thin-Film Solar Cells Based on the Polycrystalline Compound Semiconductors CIS and CdTe. *Adv. Optoelectron.* **2007**, *2007*, 1–6. https://doi.org/10.1155/2007/97545.

(5) Yang, F.; Jang, D.; Dong, L.; Qiu, S.; Distler, A.; Li, N.; Brabec, C. J.; Egelhaaf, H. Upscaling Solution-Processed Perovskite Photovoltaics. *Adv. Energy Mater.* **2021**, *11* (42), 2101973. https://doi.org/10.1002/aenm.202101973.

(6) Pitaro, M.; Tekelenburg, E. K.; Shao, S.; Loi, M. A. Tin Halide Perovskites: From Fundamental Properties to Solar Cells. *Adv. Mater.* **2022**, *34* (1), 2105844. https://doi.org/10.1002/adma.202105844.

(7) *Best Research-Cell Efficiency Chart*. National Renewable Energy Laboratory (NREL), Photovoltaic Research. https://www.nrel.gov/pv/cell-efficiency.html (accessed 2024-05-16).

(8) Chang, N. L.; Ho-Baillie, A. W. Y.; Vak, D.; Gao, M.; Green, M. A.; Egan, R. J. Manufacturing Cost and Market Potential Analysis of Demonstrated Roll-to-Roll Perovskite Photovoltaic Cell Processes. *Sol. Energy Mater. Sol. Cells* **2018**, *174*, 314–324. https://doi.org/10.1016/j.solmat.2017.08.038.

(9) Mathews, I.; Sofia, S.; Ma, E.; Jean, J.; Laine, H. S.; Siah, S. C.; Buonassisi, T.; Peters, I. M. Economically Sustainable Growth of Perovskite Photovoltaics Manufacturing. *Joule* **2020**, *4* (4), 822–839. https://doi.org/10.1016/j.joule.2020.01.006.

(10) Al-Ashouri, A.; Köhnen, E.; Li, B.; Magomedov, A.; Hempel, H.; Caprioglio, P.; Márquez, J. A.; Morales Vilches, A. B.; Kasparavicius, E.; Smith, J. A.; Phung, N.; Menzel, D.; Grischek, M.; Kegelmann, L.; Skroblin, D.; Gollwitzer, C.; Malinauskas, T.; Jošt, M.; Matič, G.; Rech, B.; Schlatmann, R.; Topič, M.; Korte, L.; Abate, A.; Stannowski, B.; Neher, D.; Stolterfoht, M.; Unold, T.; Getautis, V.; Albrecht, S. Monolithic Perovskite/Silicon Tandem Solar Cell with >29% Efficiency by Enhanced Hole Extraction. *Science* **2020**, *370* (6522), 1300–1309. https://doi.org/10.1126/science.abd4016.

(11) Mazzarella, L.; Lin, Y.; Kirner, S.; Morales-Vilches, A. B.; Korte, L.; Albrecht, S.; Crossland, E.; Stannowski, B.; Case, C.; Snaith, H. J.; Schlatmann, R. Infrared Light Management Using a Nanocrystalline Silicon Oxide Interlayer in Monolithic Perovskite/Silicon Heterojunction Tandem Solar Cells with Efficiency above 25%. *Adv. Energy Mater.* **2019**, *9* (14), 1803241. https://doi.org/10.1002/aenm.201803241.

(12) Yoo, J. J.; Seo, G.; Chua, M. R.; Park, T. G.; Lu, Y.; Rotermund, F.; Kim, Y.-K.; Moon, C. S.; Jeon, N. J.; Correa-Baena, J.-P.; Bulović, V.; Shin, S. S.; Bawendi, M. G.; Seo, J. Efficient Perovskite Solar Cells via Improved Carrier Management. *Nat. Lond.* **2021**, *590* (7847), 587–593.

(13) Meng, L.; You, J.; Yang, Y. Addressing the Stability Issue of Perovskite Solar Cells for Commercial Applications. *Nat. Commun.* **2018**, *9* (1), 5265. https://doi.org/10.1038/s41467-018-07255-1.

(14) *First Solar, Inc., Financials - Quarterly Results*. https://investor.firstsolar.com/financials/quarterly-results/default.aspx (accessed 2025-08-21).
(15) *The Sunshot 2030 Goals: 3 Cent per Kilowatt Hour for PV and 5 Cent per Kilowatt Hour for Dispatchable CSP*; Whitepaper DOE/EE-1501; United States (US) Department of Energy (DOE), Office of Energy Efficiency and Renewable Energy (EERE), Solar Energy Technologies Office (SETO), 2017. https://www.energy.gov/sites/prod/files/2020/09/f79/SunShot%202030%20White%20Paper.pdf (accessed 2024-05-16).
(16) Siegler, T. D.; Dunlap-Shohl, W. A.; Meng, Y.; Yang, Y.; Kau, W. F.; Sunkari, P. P.; Tsai, C. E.; Armstrong, Z. J.; Chen, Y.-C.; Beck, D. A. C.; Meilă, M.; Hillhouse, H. W. Water-Accelerated Photooxidation of $CH_3NH_3PbI_3$ Perovskite. *J. Am. Chem. Soc.* **2022**, *144* (12), 5552–5561. https://doi.org/10.1021/jacs.2c00391.
(17) Dunlap-Shohl, W. A.; Meng, Y.; Sunkari, P. P.; Beck, D. A. C.; Meilă, M.; Hillhouse, H. W. Physiochemical Machine Learning Models Predict Operational Lifetimes of CH3NH3PbI3 Perovskite Solar Cells. *J. Mater. Chem. A* **2024**, *12* (16), 9730–9746. https://doi.org/10.1039/D3TA06668A.
(18) Stoddard, R. J.; Dunlap-Shohl, W. A.; Qiao, H.; Meng, Y.; Kau, W. F.; Hillhouse, H. W. Forecasting the Decay of Hybrid Perovskite Performance Using Optical Transmittance or Reflected Dark-Field Imaging. *ACS Energy Lett.* **2020**, *5* (3), 946–954. https://doi.org/10.1021/acsenergylett.0c00164.
(19) Meng, Y.; Sunkari, P. P.; Meilă, M.; Hillhouse, H. W. Chemical Reaction Kinetics of the Decomposition of Low-Bandgap Tin–Lead Halide Perovskite Films and the Effect on the Ambipolar Diffusion Length. *ACS Energy Lett.* **2023**, *8* (4), 1688–1696.
(20) Cira, S. G.; Dunlap-Shohl, W. A.; Meng, Y.; Sunkari, P. P.; Folch, J. H.; Hillhouse, H. W. Light-Induced Degradation of Mixed-Cation, Mixed-Halide Perovskite: Observed Rates and Influence of Oxygen. *J. Mater. Chem. A* **2025**, *13* (7), 5033–5044. https://doi.org/10.1039/D4TA07807A.
(21) Cira, S. G.; Meng, Y.; Sunkari, P. P.; Hillhouse, H. W. Photooxidation Reaction Kinetics of Mixed-Cation Mixed-Halide Perovskite. *J. Mater. Chem. A* **2025**, *13* (44), 38436–38445. https://doi.org/10.1039/D5TA05228A.
(22) *Terrestrial Photovoltaic (PV) Modules. Design Qualification and Type Approval Test Procedures*, Under Review.; 2021.
(23) Cheacharoen, R.; Boyd, C. C.; Burkhard, G. F.; Leijtens, T.; Raiford, J. A.; Bush, K. A.; Bent, S. F.; McGehee, M. D. Encapsulating Perovskite Solar Cells to Withstand Damp Heat and Thermal Cycling. *Sustain. Energy Fuels* **2018**, *2* (11), 2398–2406. https://doi.org/10.1039/C8SE00250A.
(24) Shi, L.; Young, T. L.; Kim, J.; Sheng, Y.; Wang, L.; Chen, Y.; Feng, Z.; Keevers, M. J.; Hao, X.; Verlinden, P. J.; Green, M. A.; Ho-Baillie, A. W. Y. Accelerated Lifetime Testing of Organic–Inorganic Perovskite Solar Cells Encapsulated by Polyisobutylene. *ACS Appl. Mater. Interfaces* **2017**, *9* (30), 25073–25081. https://doi.org/10.1021/acsami.7b07625.
(25) Bush, K. A.; Palmstrom, A. F.; Yu, Z. J.; Boccard, M.; Cheacharoen, R.; Mailoa, J. P.; McMeekin, D. P.; Hoye, R. L. Z.; Bailie, C. D.; Leijtens, T.; Peters, I. M.; Minichetti, M. C.; Rolston, N.; Prasanna, R.; Sofia, S.; Harwood, D.; Ma, W.; Moghadam, F.; Snaith, H. J.; Buonassisi, T.; Holman, Z. C.; Bent, S. F.; McGehee, M. D. 23.6%-Efficient Monolithic Perovskite/Silicon Tandem Solar Cells with Improved Stability. *Nat. Energy* **2017**, *2* (4), 17009. https://doi.org/10.1038/nenergy.2017.9.

(26) Bella, F.; Griffini, G.; Correa-Baena, J.-P.; Saracco, G.; Grätzel, M.; Hagfeldt, A.; Turri, S.; Gerbaldi, C. Improving Efficiency and Stability of Perovskite Solar Cells with Photocurable Fluoropolymers. *Science* **2016**, *354* (6309), 203–206. https://doi.org/10.1126/science.aah4046.

(27) Haryński, Ł.; Trocki, K.; Bykkam, S.; Pozo, G. del; Romero, B.; Bochentyn, B.; Glowienka, D. Degradation of Perovskite Solar Cells: Insights from Accelerated Testing versus Outdoor Aging in Two Climate Zones. *Sol. Energy* **2026**, *303*, 114131. https://doi.org/10.1016/j.solener.2025.114131.

(28) Khenkin, M. V.; Katz, E. A.; Abate, A.; Bardizza, G.; Berry, J. J.; Brabec, C.; Brunetti, F.; Bulović, V.; Burlingame, Q.; Di Carlo, A.; Cheacharoen, R.; Cheng, Y.-B.; Colsmann, A.; Cros, S.; Domanski, K.; Dusza, M.; Fell, C. J.; Forrest, S. R.; Galagan, Y.; Di Girolamo, D.; Grätzel, M.; Hagfeldt, A.; Von Hauff, E.; Hoppe, H.; Kettle, J.; Köbler, H.; Leite, M. S.; Liu, S.; Loo, Y.-L.; Luther, J. M.; Ma, C.-Q.; Madsen, M.; Manceau, M.; Matheron, M.; McGehee, M.; Meitzner, R.; Nazeeruddin, M. K.; Nogueira, A. F.; Odabaşı, Ç.; Osherov, A.; Park, N.-G.; Reese, M. O.; De Rossi, F.; Saliba, M.; Schubert, U. S.; Snaith, H. J.; Stranks, S. D.; Tress, W.; Troshin, P. A.; Turkovic, V.; Veenstra, S.; Visoly-Fisher, I.; Walsh, A.; Watson, T.; Xie, H.; Yıldırım, R.; Zakeeruddin, S. M.; Zhu, K.; Lira-Cantu, M. Consensus Statement for Stability Assessment and Reporting for Perovskite Photovoltaics Based on ISOS Procedures. *Nat. Energy* **2020**, *5* (1), 35–49. https://doi.org/10.1038/s41560-019-0529-5.

(29) Jacobsson, T. J.; Hultqvist, A.; García-Fernández, A.; Anand, A.; Al-Ashouri, A.; Hagfeldt, A.; Crovetto, A.; Abate, A.; Ricciardulli, A. G.; Vijayan, A.; Kulkarni, A.; Anderson, A. Y.; Darwich, B. P.; Yang, B.; Coles, B. L.; Perini, C. A. R.; Rehermann, C.; Ramirez, D.; Fairen-Jimenez, D.; Di Girolamo, D.; Jia, D.; Avila, E.; Juarez-Perez, E. J.; Baumann, F.; Mathies, F.; González, G. S. A.; Boschloo, G.; Nasti, G.; Paramasivam, G.; Martínez-Denegri, G.; Näsström, H.; Michaels, H.; Köbler, H.; Wu, H.; Benesperi, I.; Dar, M. I.; Bayrak Pehlivan, I.; Gould, I. E.; Vagott, J. N.; Dagar, J.; Kettle, J.; Yang, J.; Li, J.; Smith, J. A.; Pascual, J.; Jerónimo-Rendón, J. J.; Montoya, J. F.; Correa-Baena, J.-P.; Qiu, J.; Wang, J.; Sveinbjörnsson, K.; Hirselandt, K.; Dey, K.; Frohna, K.; Mathies, L.; Castriotta, L. A.; Aldamasy, Mahmoud. H.; Vasquez-Montoya, M.; Ruiz-Preciado, M. A.; Flatken, M. A.; Khenkin, M. V.; Grischek, M.; Kedia, M.; Saliba, M.; Anaya, M.; Veldhoen, M.; Arora, N.; Shargaieva, O.; Maus, O.; Game, O. S.; Yudilevich, O.; Fassl, P.; Zhou, Q.; Betancur, R.; Munir, R.; Patidar, R.; Stranks, S. D.; Alam, S.; Kar, S.; Unold, T.; Abzieher, T.; Edvinsson, T.; David, T. W.; Paetzold, U. W.; Zia, W.; Fu, W.; Zuo, W.; Schröder, V. R. F.; Tress, W.; Zhang, X.; Chiang, Y.-H.; Iqbal, Z.; Xie, Z.; Unger, E. An Open-Access Database and Analysis Tool for Perovskite Solar Cells Based on the FAIR Data Principles. *Nat. Energy* **2021**, *7* (1), 107–115. https://doi.org/10.1038/s41560-021-00941-3.

(30) Stoddard, R. J.; Eickemeyer, F. T.; Katahara, J. K.; Hillhouse, H. W. Correlation between Photoluminescence and Carrier Transport and a Simple In Situ Passivation Method for High-Bandgap Hybrid Perovskites. *J. Phys. Chem. Lett.* **2017**, *8* (14), 3289–3298. https://doi.org/10.1021/acs.jpclett.7b01185.

(31) Braly, I. L.; Stoddard, R. J.; Rajagopal, A.; Jen, A. K.-Y.-; Hillhouse, H. W. Photoluminescence and Photoconductivity to Assess Maximum Open-Circuit Voltage and Carrier Transport in Hybrid Perovskites and Other Photovoltaic Materials. *J. Phys. Chem. Lett.* **2018**, *9* (13), 3779–3792. https://doi.org/10.1021/acs.jpclett.8b01152.

(32) Sunkari, P. P. Predicting Operational Lifetimes in Hybrid Perovskite Solar Cells: A Case Study of Machine Learning with Small Datasets, 2025. https://hdl.handle.net/1773/53447 (accessed 2025-12-12).
(33) Nelson, J. *The Physics of Solar Cells*; Imperial College Press ; Distributed by World Scientific Pub. Co: London : River Edge, NJ, 2003.
(34) Niemegeers, A.; Gillis, S.; Burgelman, M. A User Program for Realistic Simulation of Polycrystalline Heterojunction Solar Cells: SCAPS-1D. *Proc. 2nd World Conf. Photovolt. Energy Convers. JRC Eur. Comm. Juli* **1998**, 672–675.
(35) Burgelman, M.; Nollet, P.; Degrave, S. Modelling Polycrystalline Semiconductor Solar Cells. *Thin Solid Films* **2000**, *361–362*, 527–532. https://doi.org/10.1016/S0040-6090(99)00825-1.
(36) Burgelman, M.; Decock, K.; Khelifi, S.; Abass, A. Advanced Electrical Simulation of Thin Film Solar Cells. *Thin Solid Films* **2013**, *535*, 296–301. https://doi.org/10.1016/j.tsf.2012.10.032.
(37) Clugston, D. A.; Basore, P. A. PC1D Version 5: 32-Bit Solar Cell Modeling on Personal Computers. In *Conference Record of the Twenty Sixth IEEE Photovoltaic Specialists Conference - 1997*; 1997; pp 207–210. https://doi.org/10.1109/PVSC.1997.654065.
(38) Basore, P. A. Numerical Modeling of Textured Silicon Solar Cells Using PC-1D. *IEEE Trans. Electron Devices* **1990**, *37*, 337–343. https://doi.org/10.1109/16.46362.
(39) Froitzheim, A.; Stangl, R.; Elstner, L.; Kriegel, M.; Fuhs, W. AFORS-HET: A Computer-Program for the Simulation of Heterojunction Solar Cells to Be Distributed for Public Use. In *Proceedings of 3rd World Conference onPhotovoltaic Energy Conversion, 2003*; 2003; Vol. 1, pp 279-282 Vol.1.
(40) Koopmans, M.; Corre, V.; Koster, L. SIMsalabim: An Open-Source Drift-Diffusion Simulator for Semiconductor Devices. *J. Open Source Softw.* **2022**, *7* (70), 3727. https://doi.org/10.21105/joss.03727.
(41) Courtier, N. E.; Cave, J. M.; Walker, A. B.; Richardson, G.; Foster, J. M. IonMonger: A Free and Fast Planar Perovskite Solar Cell Simulator with Coupled Ion Vacancy and Charge Carrier Dynamics. *J. Comput. Electron.* **2019**, *18* (4), 1435–1449. https://doi.org/10.1007/s10825-019-01396-2.
(42) Clarke, W.; Bennett, L. J.; Grudeva, Y.; Foster, J. M.; Richardson, G.; Courtier, N. E. IonMonger 2.0: Software for Free, Fast and Versatile Simulation of Current, Voltage and Impedance Response of Planar Perovskite Solar Cells. *J. Comput. Electron.* **2022**. https://doi.org/10.1007/s10825-022-01988-5.
(43) Gummel, H. K. A Self-Consistent Iterative Scheme for One-Dimensional Steady State Transistor Calculations. *IEEE Trans. Electron Devices* **1964**, *11* (10), 455–465. https://doi.org/10.1109/T-ED.1964.15364.
(44) Scharfetter, D. L.; Gummel, H. K. Large-Signal Analysis of a Silicon Read Diode Oscillator. *IEEE Trans. Electron Devices* **1969**, *16* (1), 64–77. https://doi.org/10.1109/T-ED.1969.16566.
(45) Singh, A.; Gagliardi, A. Drift-Diffusion Modeling of Perovskite Solar Cells: Past and Future Possibilities. *EES Sol.* **2025**, *1* (5), 694–711. https://doi.org/10.1039/D5EL00040H.
(46) Sherkar, T. S.; Momblona, C.; Gil-Escrig, L.; Ávila, J.; Sessolo, M.; Bolink, H. J.; Koster, L. J. A. Recombination in Perovskite Solar Cells: Significance of Grain Boundaries, Interface Traps, and Defect Ions. *ACS Energy Lett.* **2017**, *2* (5), 1214–1222. https://doi.org/10.1021/acsenergylett.7b00236.

(47) Snaith, H. J.; Abate, A.; Ball, J. M.; Eperon, G. E.; Leijtens, T.; Noel, N. K.; Stranks, S. D.; Wang, J. T.-W.; Wojciechowski, K.; Zhang, W. Anomalous Hysteresis in Perovskite Solar Cells. *J. Phys. Chem. Lett.* **2014**, *5* (9), 1511–1515. https://doi.org/10.1021/jz500113x.

(48) Zhang, J.; Le Corre, V. M.; Wu, J.; Du, T.; Osterrieder, T.; Zhang, K.; Zhang, H.; Lüer, L.; Hauch, J.; Brabec, C. J. Autonomous Optimization of Air-Processed Perovskite Solar Cell in a Multidimensional Parameter Space. *Adv. Energy Mater.* **2025**, *15* (19), 2404957. https://doi.org/10.1002/aenm.202404957.

(49) Koster, L. J. A.; Smits, E. C. P.; Mihailetchi, V. D.; Blom, P. W. M. Device Model for the Operation of Polymer/Fullerene Bulk Heterojunction Solar Cells. *Phys. Rev. B* **2005**, *72* (8), 085205. https://doi.org/10.1103/PhysRevB.72.085205.

(50) Sherkar, T. S.; Momblona, C.; Gil-Escrig, L.; Bolink, H. J.; Koster, L. J. A. Improving Perovskite Solar Cells: Insights From a Validated Device Model. *Adv. Energy Mater.* **2017**, *7* (13), 1602432. https://doi.org/10.1002/aenm.201602432.

(51) These, A.; Koster, L. J. A.; Brabec, C. J.; Le Corre, V. M. Beginner's Guide to Visual Analysis of Perovskite and Organic Solar Cell Current Density–Voltage Characteristics. *Adv. Energy Mater.* **2024**, 2400055. https://doi.org/10.1002/aenm.202400055.

(52) Le Corre, V. M.; Sherkar, T. S.; Koopmans, M.; Koster, L. J. A. Identification of the Dominant Recombination Process for Perovskite Solar Cells Based on Machine Learning. *Cell Rep. Phys. Sci.* **2021**, *2* (2), 100346. https://doi.org/10.1016/j.xcrp.2021.100346.

(53) Clarke, W.; Cameron, P.; Richardson, G. Predicting Long-Term Stability from Short-Term Measurement: Insights from Modeling Degradation in Perovskite Solar Cells during Voltage Scans and Impedance Spectroscopy. *J. Phys. Chem. Lett.* **2024**, *15* (47), 11730–11736. https://doi.org/10.1021/acs.jpclett.4c02343.

(54) Clarke, W. Drift-Diffusion Modelling of Perovskite Solar Cells: Pushing the Boundaries of the Charge Transport Model. PhD Thesis, University of Southampton, United Kingdom, 2024.

(55) Sun, X.; Ji, L. Y.; Chen, W. W.; Guo, X.; Wang, H. H.; Lei, M.; Wang, Q.; Li, Y. F. Halide Anion–Fullerene π Noncovalent Interactions: N-Doping and a Halide Anion Migration Mechanism in p–i–n Perovskite Solar Cells. *J. Mater. Chem. A* **2017**, *5* (39), 20720–20728. https://doi.org/10.1039/C7TA06335K.

(56) Zai, H.; Ma, Y.; Chen, Q.; Zhou, H. Ion Migration in Halide Perovskite Solar Cells: Mechanism, Characterization, Impact and Suppression. *J. Energy Chem.* **2021**, *63*, 528–549. https://doi.org/10.1016/j.jechem.2021.08.006.

(57) Vasilopoulou, M.; Fakharuddin, A.; Coutsolelos, A. G.; Falaras, P.; Argitis, P.; Yusoff, A. R. bin M.; Nazeeruddin, M. K. Molecular Materials as Interfacial Layers and Additives in Perovskite Solar Cells. *Chem. Soc. Rev.* **2020**, *49* (13), 4496–4526. https://doi.org/10.1039/C9CS00733D.

(58) Saltelli, A.; Ratto, M.; Andres, T.; Campolongo, F.; Cariboni, J.; Gatelli, D.; Saisana, M.; Tarantola, S. *Global Sensitivity Analysis: The Primer*; John Wiley & Sons: Chichester, UK, 2008.

(59) Saltelli, A.; Chan, K.; Scott, E. M. *Sensitivity Analysis in Practice: A Guide to Assessing Scientific Models*; John Wiley & Sons: New York, 2000.

(60) Ingalls, B. P. A Sensitivity Analysis of a Generalized Mass-Action Model of Signaling Pathway Dynamics. *J. Theor. Biol.* **2003**, *222* (2), 211–228. https://doi.org/10.1016/S0022-5193(03)00008-7.

(61) Iooss, B.; Lemaître, P. A Review on Global Sensitivity Analysis Methods, 2014.

(62) Alexanderian, A.; Gremaud, P. A.; Smith, R. C. Variance-Based Sensitivity Analysis for Time-Dependent Processes, 2017.
(63) Heins, W. Mechanistic Modeling of Degrading Perovskite Solar Cells – Investigating Device-Level Degradation Phenomena and Informing Predictive Machine Learning (ML) Models of Operational Lifetime, 2025. https://github.com/wvheins/<repository-name>.
(64) Dai, T.; Cao, Q.; Yang, L.; Aldamasy, M. H.; Li, M.; Liang, Q.; Lu, H.; Dong, Y.; Yang, Y. Strategies for High-Performance Large-Area Perovskite Solar Cells toward Commercialization. *Crystals* **2021**, *11* (3), 295. https://doi.org/10.3390/cryst11030295.
(65) Jena, A. K.; Kulkarni, A.; Miyasaka, T. Halide Perovskite Photovoltaics: Background, Status, and Future Prospects. *Chem. Rev.* **2019**, *119* (5), 3036–3103. https://doi.org/10.1021/acs.chemrev.8b00539.
(66) Lee, J.-H.; Jung, K.; Lee, M.-J. Influence of Spin-Coating Methods on the Properties of Planar Solar Cells Based on Ambient-Air-Processed Triple-Cation Mixed-Halide Perovskites. *J. Alloys Compd.* **2021**, *879*, 160373. https://doi.org/10.1016/j.jallcom.2021.160373.
(67) Eguchi, N.; Fukazawa, T.; Kanda, H.; Yamamoto, K.; Miyake, T.; Murakami, T. N. Performance Optimization of Perovskite Solar Cells with an Automated Spin Coating System and Artificial Intelligence Technologies. *EES Sol.* **2025**, *1* (3), 320–330. https://doi.org/10.1039/D5EL00007F.
(68) Luo, C.; Gao, F.; Wang, X.; Zhan, C.; Zhang, X.; Zheng, G.; Zhang, X.; Gao, X.; He, Z.; Zhao, Q. Eliminating Performance Loss from Perovskite Films to Solar Cells. *Sci. Adv. 10* (39), eadp0790. https://doi.org/10.1126/sciadv.adp0790.
(69) Baltakesmez, A.; Biber, M.; Tüzemen, S. Improved Perovskite Film Quality and Solar Cell Performances Using Dual Single Solution Coating. *J. Appl. Phys.* **2017**, *122* (8), 085502. https://doi.org/10.1063/1.4985826.
(70) Iglewicz, B.; Hoaglin, D. C. *How to Detect and Handle Outliers*; The ASQC basic references in quality control: statistical techniques; ASQC Quality Press: Milwaukee, Wis, 1993.
(71) NIST/SEMATECH. *NIST/SEMATECH e-Handbook of Statistical Methods*; National Institute of Standards and Technology: Gaithersburg, MD, 2013.
(72) Piessens, R.; de Doncker-Kapenga, E.; Überhuber, C. W.; Kahaner, D. *QUADPACK: A Subroutine Package for Automatic Integration*; Springer Series in Computational Mathematics; Springer-Verlag, 1983.
(73) Gonnet, P. A Review of Error Estimation in Adaptive Quadrature. *ArXiv Prepr. ArXiv10034629* **2010**.
(74) Gander, W.; Gautschi, W. Adaptive Quadrature — Revisited. *BIT Numer. Math.* **2000**, *40* (1), 84–101. https://doi.org/10.1023/A:1009694520430.
(75) Press, W. H.; Teukolsky, S. A.; Vetterling, W. T.; Flannery, B. P. *Numerical Recipes: The Art of Scientific Computing*, 1st ed.; Cambridge University Press, 1992.
(76) Atkinson, K. E. *An Introduction to Numerical Analysis*, 2nd ed.; John Wiley & Sons, 1989.
(77) Van Heerden, R.; Procel, P.; Mazzarella, L.; Santbergen, R.; Isabella, O. Slow Shallow Energy States as the Origin of Hysteresis in Perovskite Solar Cells. *Front. Photonics* **2022**, *3*, 889837. https://doi.org/10.3389/fphot.2022.889837.

(78) Ortiz-Conde, A.; García Sánchez, F. J.; Muci, J. Exact Analytical Solutions of the Forward Non-Ideal Diode Equation with Series and Shunt Parasitic Resistances. *Solid-State Electron.* **2000**, *44* (10), 1861–1864. https://doi.org/10.1016/S0038-1101(00)00132-5.
(79) Sze, S. M.; Ng, K. K. *Physics of Semiconductor Devices*, 3rd ed.; Wiley: Hoboken, NJ, 2007.
(80) Oviedo-Casado, S.; Urbina, A.; Prior, J. Magnetic Field Enhancement of Organic Photovoltaic Cells Performance. *Sci. Rep.* **2017**, *7*, 4297. https://doi.org/10.1038/s41598-017-04621-9.
(81) Cong, T.; Wang, J.-M.; Niu, M.-L.; Zhu, L.; Peng, Q.-M.; Wang, J.-P. Magnetic Field Effects in Non-Magnetic Luminescent Materials: From Organic Semiconductors to Halide Perovskites. *Chin. Phys. B* **2021**, *71*, 20211872. https://doi.org/10.7498/aps.71.20211872.
(82) Zang, H.; Ivanov, I. N.; Hu, B. Magnetic Studies of Photovoltaic Processes in Organic Solar Cells. *IEEE J. Sel. Top. Quantum Electron.* **2010**, *16* (6), 1801–1806.
(83) Zhang, C.; Sun, D.-L.; Sheng, C.-X.; others. Magnetic Field Effects in Hybrid Perovskite Devices. *Nat. Phys.* **2015**. https://doi.org/10.1038/nphys3277.
(84) Herz, L. M. Charge-Carrier Mobilities in Metal Halide Perovskites: Fundamental Mechanisms and Limits. *ACS Energy Lett.* **2017**, *1* (6), 1289–1295. https://doi.org/10.1021/acsenergylett.7b00276.
(85) Chen, Y.; Yi, H. T.; Wu, X.; Haroldson, R.; Gartstein, Y. N.; Rodionov, Y. I.; Tikhonov, K. S.; Zakhidov, A.; Zhu, X.-Y.; Podzorov, V. Extended Carrier Lifetimes and Diffusion in Hybrid Perovskites Revealed by Hall Effect and Photoconductivity Measurements. *Nat. Commun.* **2016**, *7* (1), 12253. https://doi.org/10.1038/ncomms12253.
(86) Caselli, V. M.; Savenije, T. J. Quantifying Charge Carrier Recombination Losses in $MAPbI_3$ /C60 and $MAPbI_3$ /Spiro-OMeTAD with and without Bias Illumination. *J. Phys. Chem. Lett.* **2022**, *13* (32), 7523–7531. https://doi.org/10.1021/acs.jpclett.2c01728.
(87) Rivkin, B.; Fassl, P.; Sun, Q.; others. Effect of Ion Migration Induced Electrode Degradation on the Operational Stability of Perovskite Solar Cells. *Energy Environ. Sci.* **2018**. https://doi.org/10.1039/C8EE01437C.
(88) Chen, H.; Liu, C.; Xu, J.; Maxwell, A.; Zhou, W.; Yang, Y.; Zhou, Q.; Bati, A. S. R.; Wan, H.; Wang, Z.; Zeng, L.; Wang, J.; Serles, P.; Liu, Y.; Teale, S.; Liu, Y.; Saidaminov, M. I.; Li, M.; Rolston, N.; Hoogland, S.; Filleter, T.; Kanatzidis, M. G.; Chen, B.; Ning, Z.; Sargent, E. H. Improved Charge Extraction in Inverted Perovskite Solar Cells with Dual-Site-Binding Ligands. *Science* **2024**, *384* (6692), 189–193. https://doi.org/10.1126/science.adm9474.
(89) Richter, J. M.; Abdi-Jalebi, M.; Sadhanala, A.; Tabachnyk, M.; Rivett, J. P. H.; Pazos-Outón, L. M.; Gödel, K. C.; Price, M.; Deschler, F.; Friend, R. H. Enhancing Photoluminescence Yields in Lead Halide Perovskites by Photon Recycling and Light Out-Coupling. *Nat. Commun.* **2016**, *7* (1), 13941. https://doi.org/10.1038/ncomms13941.
(90) Staub, F.; Kirchartz, T.; Bittkau, K.; Rau, U. Manipulating the Net Radiative Recombination Rate in Lead Halide Perovskite Films by Modification of Light Outcoupling. *J. Phys. Chem. Lett.* **2017**, *8* (20), 5084–5090. https://doi.org/10.1021/acs.jpclett.7b02224.
(91) Crothers, T. W.; Milot, R. L.; Patel, J. B.; Parrott, E. S.; Schlipf, J.; Müller-Buschbaum, P.; Johnston, M. B.; Herz, L. M. Photon Reabsorption Masks Intrinsic Bimolecular Charge-Carrier Recombination in $CH_3 NH_3 PbI_3$ Perovskite. *Nano Lett.* **2017**, *17* (9), 5782–5789. https://doi.org/10.1021/acs.nanolett.7b02834.
(92) Yang, Y.; Yang, M.; Li, Z.; Crisp, R.; Zhu, K.; Beard, M. C. Comparison of Recombination Dynamics in $CH_3 NH_3 PbBr_3$ and $CH_3 NH_3 PbI_3$ Perovskite Films: Influence

of Exciton Binding Energy. *J. Phys. Chem. Lett.* **2015**, *6* (23), 4688–4692. https://doi.org/10.1021/acs.jpclett.5b02290.

(93) Filippetti, A.; Delugas, P.; Mattoni, A. Radiative Recombination and Photoconversion of Methylammonium Lead Iodide Perovskite by First Principles: Properties of an Inorganic Semiconductor within a Hybrid Body. *J. Phys. Chem. C* **2014**, *118* (43), 24843–24853. https://doi.org/10.1021/jp507430x.

(94) Brauer, J. C.; Tsokkou, D.; Sanchez, S.; Droseros, N.; Roose, B.; Mosconi, E.; Hua, X.; Stolterfoht, M.; Neher, D.; Steiner, U.; De Angelis, F.; Abate, A.; Banerji, N. Comparing the Excited-State Properties of a Mixed-Cation–Mixed-Halide Perovskite to Methylammonium Lead Iodide. *J. Chem. Phys.* **2020**, *152* (10), 104703. https://doi.org/10.1063/1.5133021.

(95) Ulatowski, A. M.; Elmestekawy, K. A.; Patel, J. B.; Noel, N. K.; Yan, S.; Kraus, H.; Huggard, P. G.; Johnston, M. B.; Herz, L. M. Contrasting Charge-Carrier Dynamics across Key Metal-Halide Perovskite Compositions through In Situ Simultaneous Probes. *Adv. Funct. Mater.* **2023**, *33* (51), 2305283. https://doi.org/10.1002/adfm.202305283.

(96) Klein, J. R.; Flender, O.; Scholz, M.; Oum, K.; Lenzer, T. Charge Carrier Dynamics of Methylammonium Lead Iodide: From PbI_2 -Rich to Low-Dimensional Broadly Emitting Perovskites. *Phys. Chem. Chem. Phys.* **2016**, *18* (16), 10800–10808. https://doi.org/10.1039/C5CP07167D.

(97) Manser, J. S.; Kamat, P. V. Band Filling with Free Charge Carriers in Organometal Halide Perovskites. *Nat. Photonics* **2014**, *8* (9), 737–743. https://doi.org/10.1038/nphoton.2014.171.

(98) Milot, R. L.; Eperon, G. E.; Snaith, H. J.; Johnston, M. B.; Herz, L. M. Temperature-Dependent Charge-Carrier Dynamics in $CH_3 NH_3 PbI_3$ Perovskite Thin Films. *Adv. Funct. Mater.* **2015**, *25* (39), 6218–6227. https://doi.org/10.1002/adfm.201502340.

(99) Wehrenfennig, C.; Eperon, G. E.; Johnston, M. B.; Snaith, H. J.; Herz, L. M. High Charge Carrier Mobilities and Lifetimes in Organolead Trihalide Perovskites. *Adv. Mater.* **2014**, *26* (10), 1584–1589. https://doi.org/10.1002/adma.201305172.

(100) Davies, C. L.; Filip, M. R.; Patel, J. B.; Crothers, T. W.; Verdi, C.; Wright, A. D.; Milot, R. L.; Giustino, F.; Johnston, M. B.; Herz, L. M. Bimolecular Recombination in Methylammonium Lead Triiodide Perovskite Is an Inverse Absorption Process. *Nat. Commun.* **2018**, *9* (1), 293. https://doi.org/10.1038/s41467-017-02670-2.

(101) Brenes, R.; Guo, D.; Osherov, A.; Noel, N. K.; Eames, C.; Hutter, E. M.; Pathak, S. K.; Niroui, F.; Friend, R. H.; Islam, M. S.; Snaith, H. J.; Bulović, V.; Savenije, T. J.; Stranks, S. D. Metal Halide Perovskite Polycrystalline Films Exhibiting Properties of Single Crystals. *Joule* **2017**, *1* (1), 155–167. https://doi.org/10.1016/j.joule.2017.08.006.

(102) Staub, F.; Hempel, H.; Hebig, J.-C.; Mock, J.; Paetzold, U. W.; Rau, U.; Unold, T.; Kirchartz, T. Beyond Bulk Lifetimes: Insights into Lead Halide Perovskite Films from Time-Resolved Photoluminescence. *Phys. Rev. Appl.* **2016**, *6* (4), 044017. https://doi.org/10.1103/PhysRevApplied.6.044017.

(103) Miyata, A.; Mitioglu, A.; Plochocka, P.; Portugall, O.; Wang, J. T.-W.; Stranks, S. D.; Snaith, H. J.; Nicholas, R. J. Direct Measurement of the Exciton Binding Energy and Effective Masses for Charge Carriers in an Organic-Inorganic Tri-Halide Perovskite. **2015**. https://doi.org/10.48550/ARXIV.1504.07025.

(104) Thiesbrummel, J.; Shah, S.; Gutierrez-Partida, E.; Zu, F.; Peña-Camargo, F.; Zeiske, S.; Diekmann, J.; Ye, F.; Peters, K. P.; Brinkmann, K. O.; Caprioglio, P.; Dasgupta, A.; Seo, S.; Adeleye, F. A.; Warby, J.; Jeangros, Q.; Lang, F.; Zhang, S.; Albrecht, S.; Riedl, T.; Armin, A.; Neher, D.; Koch, N.; Wu, Y.; Le Corre, V. M.; Snaith, H.; Stolterfoht, M. Ion-Induced

Field Screening as a Dominant Factor in Perovskite Solar Cell Operational Stability. *Nat. Energy* **2024**, *9* (6), 664–676. https://doi.org/10.1038/s41560-024-01487-w.
(105) Walsh, A.; Scanlon, D. O.; Chen, S.; Gong, X. G.; Wei, S. Self-Regulation Mechanism for Charged Point Defects in Hybrid Halide Perovskites. *Angew. Chem.* **2015**, *127* (6), 1811–1814. https://doi.org/10.1002/ange.201409740.
(106) Eames, C.; Frost, J. M.; Barnes, P. R. F.; O'Regan, B. C.; Walsh, A.; Islam, M. S. Ionic Transport in Hybrid Lead Iodide Perovskite Solar Cells. *Nat. Commun.* **2015**, *6* (1), 7497. https://doi.org/10.1038/ncomms8497.
(107) Selberherr, S. Analysis and Simulation of Semiconductor Devices. *Analysis and simulation of semiconductor devices*, 1984.
(108) Draper, N. R.; Smith, H. *Applied Regression Analysis*, 3rd ed.; Wiley: Hoboken, NJ, 1998.
(109) Bevington, P. R.; Robinson, D. K. *Data Reduction and Error Analysis for the Physical Sciences*, 3rd ed.; McGraw-Hill: New York, NY, 2003.
(110) Greene, W. H. *Econometric Analysis*, 7th ed.; Pearson: Upper Saddle River, NJ, 2011.
(111) Montgomery, D. C.; Peck, E. A.; Vining, G. G. *Introduction to Linear Regression Analysis*, 5th ed.; Wiley: Hoboken, NJ, 2012.
(112) Fisher, R. A. *Statistical Methods for Research Workers*; Oliver & Boyd: Edinburgh, UK, 1925.
(113) Volterra, V.; Hostinský, B. *Opérations Infinitésimales Linéaires*; Gauthier-Villars: Paris, France, 1938.
(114) Slavík, A. *Product Integration, Its History and Applications*; Springer Monographs in Mathematics; Matfyzpress: Prague, Czech Republic, 2007.
(115) Gill, R. D. *Product Integration*; Mathematical Institute, University of Utrecht, 2001.
(116) Stolterfoht, M.; Le Corre, V. M.; Feuerstein, M.; Caprioglio, P.; Koster, L. J. A.; Neher, D. Voltage-Dependent Photoluminescence and How It Correlates with the Fill Factor and Open-Circuit Voltage in Perovskite Solar Cells. *ACS Energy Lett.* **2019**, *4* (12), 2887–2892. https://doi.org/10.1021/acsenergylett.9b02262.
(117) Jiang, Q.; Tirawat, R.; Kerner, R. A.; Gaulding, E. A.; Xian, Y.; Wang, X.; Newkirk, J. M.; Yan, Y.; Berry, J. J.; Zhu, K. Towards Linking Lab and Field Lifetimes of Perovskite Solar Cells. *Nature* **2023**, *623* (7986), 313–318. https://doi.org/10.1038/s41586-023-06610-7.
(118) Escobar, L. A.; Meeker, W. Q. A Review of Accelerated Test Models. *Stat. Sci.* **2007**, *21* (4), 552–577. https://doi.org/10.1214/088342306000000691.
(119) Diao, W.; Xing, Y.; Saxena, S.; Pecht, M. Evaluation of Present Accelerated Temperature Testing and Modeling of Batteries. *Appl. Sci.* **2018**, *8* (10), 1786. https://doi.org/10.3390/app8101786.
(120) Lambert, B. J. Rationale for Practical Medical Device Accelerated Aging Methods. *Int. J. Pharm.* **2000**, *203* (1–2), 79–93. https://doi.org/10.1016/S0378-5173(00)00402-7.
(121) Cho, E.-C.; others. A Review of the Degradation of Photovoltaic Modules for Life Expectancy. *Energies* **2021**, *14* (14), 4278. https://doi.org/10.3390/en14144278.
(122) Authors, M. Review of Degradation and Failure Phenomena in Photovoltaic Modules. *Renew. Sustain. Energy Rev.* **2022**, *159*, 112160. https://doi.org/10.1016/j.rser.2022.112160.
(123) Alimi, O. A.; Meyer, E. L.; Olayiwola, O. I. Solar Photovoltaic Modules' Performance Reliability and Degradation Analysis–A Review. *Energies* **2022**, *15* (16), 5964. https://doi.org/10.3390/en15165964.

(124) Sunkari, P. Small-Data-Ml. *GitHub repository*, 2023. https://github.com/hillhouse-group/small-data-ml.
(125) Hastie, T.; Tibshirani, R.; Wainwright, M. *Statistical Learning with Sparsity: The Lasso and Generalizations*, 0 ed.; Chapman and Hall/CRC, 2015. https://doi.org/10.1201/b18401.
(126) Siekmann, J.; others. Apparent Defect Densities in Halide Perovskite Thin Films and Single Crystals. *ACS Energy Lett.* **2021**, *6*, 3244–3251. https://doi.org/10.1021/acsenergylett.1c01449.
(127) Ni, Z.; Bao, C.; Liu, Y.; others. Resolving Spatial and Energetic Distributions of Trap States in Metal Halide Perovskite Solar Cells. *Science* **2020**, *367* (6484), 1352–1358. https://doi.org/10.1126/science.aba0893.
(128) Jin, H.; Debroye, E.; others. It's a Trap! On the Nature of Localised States and Charge Trapping in Lead Halide Perovskites. *Mater. Horiz.* **2020**, *7*, 397–410. https://doi.org/10.1039/C9MH00500E.
(129) Wang, F.; Bai, S.; others. Defects Engineering for High-performance Perovskite Solar Cells. *Npj Flex. Electron.* **2018**, *2*, 22. https://doi.org/10.1038/s41528-018-0035-z.
(130) Caputo, M.; Cefarin, N.; Radivo, A.; Demitri, N.; Gigli, L.; Plaisier, J. R.; Panighel, M.; Di Santo, G.; Moretti, S.; Giglia, A.; Polentarutti, M.; De Angelis, F.; Mosconi, E.; Umari, P.; Tormen, M.; Goldoni, A. Electronic Structure of MAPbI3 and MAPbCl3: Importance of Band Alignment. *Sci. Rep.* **2019**, *9* (1), 15159. https://doi.org/10.1038/s41598-019-50108-0.
(131) Kato, Y.; Ono, L. K.; Lee, M. V.; Wang, S.; Raga, S. R.; Qi, Y. Silver Iodide Formation in Methyl Ammonium Lead Iodide Perovskite Solar Cells with Silver Top Electrodes. *Adv. Mater. Interfaces* **2015**, *2* (13), 1500195. https://doi.org/10.1002/admi.201500195.
(132) Besleaga, C.; others. Iodine Migration and Degradation of Perovskite Solar Cells Enhanced by Metallic Electrodes. *ACS Appl. Mater. Interfaces* **2016**. https://doi.org/10.1021/acsami.6b10250.
(133) Svanström, S.; others. Degradation Mechanism of Silver Metal Deposited on Lead Halide Perovskites. *ACS Appl. Mater. Interfaces* **2020**. https://doi.org/10.1021/acsami.9b20315.
(134) Rivkin, B.; Fassl, P.; Sun, Q.; others. Effect of Ion Migration-Induced Electrode Degradation on the Operational Stability of Perovskite Solar Cells. *Energy Environ. Sci.* **2018**. https://doi.org/10.1039/C8EE01437C.
(135) Aghaei, M.; others. Review of Degradation and Failure Phenomena in Photovoltaic Modules. *Renew. Sustain. Energy Rev.* **2022**. https://doi.org/10.1016/j.rser.2022.112160.
(136) Authors. Investigation into Fill Factor and Open-Circuit Voltage Degradations in Silicon Heterojunction Solar Cells under Accelerated Life Testing at Elevated Temperatures. *Sol. Energy Mater. Sol. Cells* **2023**. https://doi.org/10.1016/j.solmat.2023.112586.
(137) Atia, D. M.; others. Degradation and Energy Performance Evaluation of Mono-Crystalline Silicon PV Modules. *Sci. Rep.* **2023**. https://doi.org/10.1038/s41598-023-40168-8.
(138) Buin, A.; others. Taking Control of Ion Transport in Halide Perovskite Solar Cells. *ACS Energy Lett.* **2018**. https://doi.org/10.1021/acsenergylett.8b00764.
(139) Phung, N.; others. Photoprotection in Metal Halide Perovskites by Ionic Defect Formation. *Joule* **2022**, *6*, 2152–2174. https://doi.org/10.1016/j.joule.2022.06.029.
(140) Eames, C.; others. Ionic Transport in Hybrid Lead Iodide Perovskite Solar Cells. *Energy Environ. Sci.* **2015**. https://doi.org/10.1039/C5EE02498E.
(141) Yoon, S. J.; others. Shift Happens. How Halide Ion Defects Influence Mixed Halide Perovskites. *ACS Energy Lett.* **2017**. https://doi.org/10.1021/acsenergylett.7b00357.

(142) Reichert, S.; others. Probing the Ionic Defect Landscape in Halide Perovskite Solar Cells. *Nat. Commun.* **2020**. https://doi.org/10.1038/s41467-020-19769-8.
(143) Clarke, W. Charge Transport Modelling of Perovskite Solar Cells Accounting for Non-Boltzmann Statistics in Organic and Highly-Doped Transport Layers. *J Phys Energy* **2023**. https://doi.org/10.XXX/XXXXX.
(144) Mujahid, M. Recent Advancements in Understanding Hot Carrier Dynamics in Halide Perovskites. *Energies* **2025**.
(145) Fu, J.; others. Hot Carrier Cooling Mechanisms in Halide Perovskites. *Nat. Commun.* **2017**. https://doi.org/10.1038/s41467-017-01360-3.
(146) Roichman, Y.; Tessler, N. Generalized Einstein Relation for Disordered Semiconductors—Implications for Device Performance. *Appl. Phys. Lett.* **2002**, *80* (11), 1948–1950. https://doi.org/10.1063/1.1461419.
(147) Katsidis, C. C.; Siapkas, D. I. General Transfer-Matrix Method for Optical Multilayer Systems with Coherent, Partially Coherent, and Incoherent Interference. *Appl. Opt.* **2002**, *41* (13), 3978–3987. https://doi.org/10.1364/AO.41.003978.
(148) Tikhonravov, A. V.; Trubetskov, M. K.; Tikhonravov, A. A.; Duparré, A. Effects of Interface Roughness on the Spectral Properties of Thin Films and Multilayers. *Appl. Opt.* **2003**, *42* (25), 5144–5155. https://doi.org/10.1364/AO.42.005144.
(149) Yeh, P. *Optical Waves in Layered Media*; Wiley, 1988.
(150) Lin, Q.; Armin, A.; Nagiri, R. C. R.; Burn, P. L.; Meredith, P. Electro-Optics of Perovskite Solar Cells. *Nat. Photonics* **2015**, *9* (2), 106–112. https://doi.org/10.1038/nphoton.2014.284.
(151) Stranks, S. D.; Burlakov, V. M.; Leijtens, T.; Ball, J. M.; Goriely, A.; Snaith, H. J. Recombination Kinetics in Organic-Inorganic Perovskites: Excitons, Free Charge, and Subgap States. *Phys. Rev. Appl.* **2014**, *2* (3), 034007. https://doi.org/10.1103/PhysRevApplied.2.034007.
(152) Streetman, B. G.; Banerjee, S. *Solid State Electronic Devices*, 7th ed.; Pearson, 2015.
(153) Schroder, D. K. *Semiconductor Material and Device Characterization*, 3rd ed.; Wiley, 2006.
(154) Ono, L. K.; others. Reducing Detrimental Defects for High-Performance Metal Halide Perovskites. *Angew. Chem. Int. Ed.* **2020**, *59*, 8956–8974. https://doi.org/10.1002/anie.201905521.
(155) Sherkar, T. S.; others. Recombination in Perovskite Solar Cells: Significance of Grain Boundaries and Interfaces. *ACS Energy Lett.* **2017**, *2*, 1214–1222. https://doi.org/10.1021/acsenergylett.7b00236.
(156) Yin, W.-J.; Shi, T.; Yan, Y. Unusual Defect Physics in CH3NH3PbI3 Perovskite Solar Cell Absorber. *Appl. Phys. Lett.* **2014**, *104* (6), 063903. https://doi.org/10.1063/1.4864778.
(157) Yin, W.-J.; Shi, T.; Yan, Y. Superior Photovoltaic Properties of Lead Halide Perovskites: Insights from First-Principles Theory. *J. Phys. Chem. C* **2015**, *119* (10), 5253–5264. https://doi.org/10.1021/jp512077m.
(158) Yin, W.; Shi, T.; Yan, Y. Unique Properties of Halide Perovskites as Possible Origins of the Superior Solar Cell Performance. *Adv. Mater.* **2014**, *26* (27), 4653–4658. https://doi.org/10.1002/adma.201306281.
(159) Uratani, H.; Yamashita, K. Charge Carrier Trapping at Surface Defects of Perovskite Solar Cell Absorbers: A First-Principles Study. *J. Phys. Chem. Lett.* **2017**, *8* (4), 742–746. https://doi.org/10.1021/acs.jpclett.7b00055.

(160) Kim, J.; Lee, S.-H.; Lee, J. H.; Hong, K.-H. The Role of Intrinsic Defects in Methylammonium Lead Iodide Perovskite. *J. Phys. Chem. Lett.* **2014**, *5* (8), 1312–1317. https://doi.org/10.1021/jz500370k.
(161) Shi, T.; Yin, W.-J.; Yan, Y. Predictions for P-Type CH_3 NH_3 PbI_3 Perovskites. *J. Phys. Chem. C* **2014**, *118* (44), 25350–25354. https://doi.org/10.1021/jp508328u.
(162) Kim, N.-K.; Min, Y. H.; Noh, S.; Cho, E.; Jeong, G.; Joo, M.; Ahn, S.-W.; Lee, J. S.; Kim, S.; Ihm, K.; Ahn, H.; Kang, Y.; Lee, H.-S.; Kim, D. Investigation of Thermally Induced Degradation in CH3NH3PbI3 Perovskite Solar Cells Using In-Situ Synchrotron Radiation Analysis. *Sci. Rep.* **2017**, *7* (1), 4645. https://doi.org/10.1038/s41598-017-04690-w.
(163) Juarez-Perez, E. J.; Ono, L. K.; Maeda, M.; Jiang, Y.; Hawash, Z.; Qi, Y. Photodecomposition and Thermal Decomposition in Methylammonium Halide Lead Perovskites and Inferred Design Principles to Increase Photovoltaic Device Stability. *J. Mater. Chem. A* **2018**, *6* (20), 9604–9612. https://doi.org/10.1039/C8TA03501F.
(164) Yang, W.; Shi, R.; Lu, H.; Liu, K.; Yan, Q.; Bai, Y.; Ding, X.; Li, H.; Gao, Z. Revisiting the Thermal Decomposition Mechanism of MAPbI3. *Phys. Chem. Chem. Phys.* **2024**, *26* (26), 17999–18005. https://doi.org/10.1039/D4CP01318B.
(165) Juarez-Perez, E. J.; Ono, L. K.; Uriarte, I.; Cocinero, E. J.; Qi, Y. Degradation Mechanism and Relative Stability of Methylammonium Halide Based Perovskites Analyzed on the Basis of Acid–Base Theory. *ACS Appl. Mater. Interfaces* **2019**, *11* (13), 12586–12593. https://doi.org/10.1021/acsami.9b02374.
(166) Li, C.; Song, Z.; Chen, C.; Xiao, C.; Subedi, B.; Harvey, S. P.; Shrestha, N.; Subedi, K. K.; Chen, L.; Liu, D.; Li, Y.; Kim, Y.-W.; Jiang, C.; Heben, M. J.; Zhao, D.; Ellingson, R. J.; Podraza, N. J.; Al-Jassim, M.; Yan, Y. Low-Bandgap Mixed Tin-Lead Iodide Perovskites with Reduced Methylammonium for Simultaneous Enhancement of Solar Cell Efficiency and Stability. *Nat. Energy* **2020**, *5*, 768–776. https://doi.org/10.1038/s41560-020-00692-7.
(167) Yadegarifard, A.; Lee, H.; Seok, H.-J.; Kim, I.; Ju, B.-K.; Kim, H.-K.; Lee, D.-K. FA/Cs-Based Mixed Pb–Sn Perovskite Solar Cells: A Review of Recent Advances in Stability and Efficiency. *Nano Energy* **2023**, *112*, 108481. https://doi.org/10.1016/j.nanoen.2023.108481.
(168) Kong, T.; Liu, Y.; Zhao, Z.; Chen, W.; Bi, D. Vacuum-Assisted Crystallization for Highly Efficient and Thermally Stable FA-Based Sn-Pb Perovskite Solar Cells. *J. Phys. Chem. Lett.* **2025**, *16* (41), 10778–10784. https://doi.org/10.1021/acs.jpclett.5c02623.
(169) Tan, W.; Bowring, A. R.; Meng, A. C.; McGehee, M. D.; McIntyre, P. C. Thermal Stability of Mixed Cation Metal Halide Perovskites in Air. *ACS Appl. Mater. Interfaces* **2018**, *10* (6), 5485–5491. https://doi.org/10.1021/acsami.7b15263.
(170) Wang, P.; Chai, N.; Wang, C.; Hua, J.; Huang, F.; Peng, Y.; Zhong, J.; Ku, Z.; Cheng, Y. Enhancing the Thermal Stability of the Carbon-Based Perovskite Solar Cells by Using a CsxFA1−xPbBrxI3−x Light Absorber. *RSC Adv.* **2019**, *9* (21), 11877–11881. https://doi.org/10.1039/C9RA00043G.
(171) Haeger, T.; Heiderhoff, R.; Riedl, T. Thermal Properties of Metal-Halide Perovskites. *J. Mater. Chem. C* **2020**, *8* (41), 14289–14311. https://doi.org/10.1039/D0TC03754K.
(172) Zhang, H.; Mao, Z.; Ma, Y.; Zhang, Y.; Wang, J.; Huang, Z.; Shi, X.; Xue, X.; Zhao, B.; Jung, Y. M. Deciphering Thermal Degradation Pathways of Metal Halide Perovskite Thin Films under Ambient Conditions. *J. Colloid Interface Sci.* **2025**, *700* (Pt 1), 138341. https://doi.org/10.1016/j.jcis.2025.138341.

(173) Helander, M. G.; Greiner, M. T.; Wang, Z. B.; Lu, Z. H. Pitfalls in Measuring Work Function Using Photoelectron Spectroscopy. *Appl. Surf. Sci.* **2010**, *256*, 2602–2605. https://doi.org/10.1016/j.apsusc.2009.11.002.
(174) Baddorf, A. P. Identifying the Secondary Electron Cutoff in Ultraviolet Photoemission Spectra for Work Function Measurements of Non-Ideal Surfaces. *Sci. Rep.* **2023**, *13*, 13452. https://doi.org/10.1038/s41598-023-40187-5.
(175) Whitten, J. E. Ultraviolet Photoelectron Spectroscopy: Practical Aspects and Best Practices. *Appl. Surf. Sci. Adv.* **2023**, *13*, 100384. https://doi.org/10.1016/j.apsadv.2023.100384.
(176) Kim, J. W.; Kim, A.; Hwang, H. U.; others. Work Function Measurement by Ultraviolet Photoelectron Spectroscopy: Versailles Project Interlaboratory Study. *J. Vac. Sci. Technol. A* **2023**. https://doi.org/10.1116/6.0002852.
(177) Unknown, A. Challenges and Opportunities for the Characterization of Electronic Properties in Halide Perovskite Solar Cells. *Chem. Sci.* **2025**. https://doi.org/10.1039/D5SC00504C.
(178) Jacobsson, T. J.; Hultqvist, A.; García-Fernández, A.; Anand, A.; Al-Ashouri, A.; Hagfeldt, A.; Crovetto, A.; Abate, A.; Ricciardulli, A. G.; Vijayan, A.; Kulkarni, A.; Anderson, A. Y.; Darwich, B. P.; Yang, B.; Coles, B. L.; Perini, C. A. R.; Rehermann, C.; Ramirez, D.; Fairen-Jimenez, D.; Di Girolamo, D.; Jia, D.; Avila, E.; Juarez-Perez, E. J.; Baumann, F.; Mathies, F.; González, G. S. A.; Boschloo, G.; Nasti, G.; Paramasivam, G.; Martínez-Denegri, G.; Näsström, H.; Michaels, H.; Köbler, H.; Wu, H.; Benesperi, I.; Dar, M. I.; Bayrak Pehlivan, I.; Gould, I. E.; Vagott, J. N.; Dagar, J.; Kettle, J.; Yang, J.; Li, J.; Smith, J. A.; Pascual, J.; Jerónimo-Rendón, J. J.; Montoya, J. F.; Correa-Baena, J.-P.; Qiu, J.; Wang, J.; Sveinbjörnsson, K.; Hirselandt, K.; Dey, K.; Frohna, K.; Mathies, L.; Castriotta, L. A.; Aldamasy, M. H.; Vasquez-Montoya, M.; Ruiz-Preciado, M. A.; Flatken, M. A.; Khenkin, M. V.; Grischek, M.; Kedia, M.; Saliba, M.; Anaya, M.; Veldhoen, M.; Arora, N.; Shargaieva, O.; Maus, O.; Game, O. S.; Yudilevich, O.; Fassl, P.; Zhou, Q.; Betancur, R.; Munir, R.; Patidar, R.; Stranks, S. D.; Alam, S.; Kar, S.; Unold, T.; Abzieher, T.; Edvinsson, T.; David, T. W.; Paetzold, U. W.; Zia, W.; Fu, W.; Zuo, W.; Schröder, V. R. F.; Tress, W.; Zhang, X.; Chiang, Y.-H.; Iqbal, Z.; Xie, Z.; Unger, E. An Open-Access Database and Analysis Tool for Perovskite Solar Cells Based on the FAIR Data Principles. *Nat. Energy* **2022**, *7* (1), 107–115. https://doi.org/10.1038/s41560-021-00941-3.
(179) Hillhouse, H. W. Hillhouse Group UW GitHub Repository, 2025. https://github.com/hillhouse-group.

8 APPENDICES

8.1 Appendix A. Derivations and Justifications of Modeling Assumptions

8.1.1 Appendix A.1. Derivation of Volumetric Electron-Hole Pair Generation Rate Profile.

Although SIMsalabim enables calculation of the electron-hole pair generation rate profile over the active layer's active thickness with the transfer matrix method (TMM), wavelength-dependent index of refraction data were not obtained for all device layers. Thus, a profile normalized to the active layer's light-incident interface is specified. Assuming a uniform fractional conversion of photons to electron-hole pairs $x_{ph\rightarrow ehp}$, the volumetric electron-hole pair generation rate profile $G_{ehp}(x)$ in an infinitesimal volume element dV located at a position x from the active layer's light-incident side is

$$G_{ehp}(x)dV = x_{ph\rightarrow ehp}d\dot{n}_{ph,abs}$$

where $d\dot{n}_{ph,abs}$ is the element's total photon absorption rate. Assuming the active layer is a rectangular prism, the volume element is

$$dV = Adx$$

where A is the device area and dx is the element's infinitesimal thickness. The Bouguer-Lambert law equates the differential absorption intensity to the product of the material's absorption coefficient, light intensity, and optical path length element. Assuming normally incident illumination, the optical path length element is the active layer's active thickness element. Thus, the element's photon absorption rate is approximately

$$d\dot{n}_{ph,abs} = (\hat{n}_{ph,E>E_g,\tau}(x)A)\alpha dx = \hat{n}_{ph,E>E_g,\tau}(x)\alpha dV$$

where $\hat{n}_{ph,E>E_g,\tau}(x)$ is the transmitted above-bandgap photon flux as a function of position and α is the active layer's absorption coefficient. The volumetric electron-hole pair generation rate profile is thus

$$G_{ehp}(x) = \hat{n}_{ph,E>E_g,\tau}(x)\alpha$$

The exponential attenuation law equates one minus the negative exponent of absorption coefficient and light path length to the absorptivity a, or the fraction of light intensity which penetrates the material (i.e. is not reflected) that is absorbed.

$$a = 1 - e^{-\alpha x}$$

Assuming a thick, highly absorbing film with insignificant optical interference effects and reflectance dominated by surface reflectivity on the active layer's light-incident side, the transmittance τ is

$$\tau = (1 - a)(1 - R)$$

where R is the reflectance. By the definition of transmittance, the volumetric electron-hole pair generation rate profile is thus

$$G_{ehp}(x) = \hat{n}_{ph,E>E_g}\alpha e^{-\alpha x}(1 - R), 0 \leq x \leq L$$

where $\hat{n}_{ph,E>E_g}$ is the incident above-bandgap photon flux and L is the active layer's active thickness. The normalized profile $\tilde{G}_{ehp}$ is thus

$$\tilde{G}_{ehp} = e^{-\alpha x}, 0 \leq x \leq L$$

and the average volumetric electron-hole pair generation rate G_{ehp} is

$$G_{ehp} = \frac{1}{L}\int_0^L G_{ehp}(x)dx$$

$$G_{ehp} = \frac{1}{L}\int_0^L \hat{n}_{ph,E>E_g}\alpha e^{-\alpha x}(1-R)dx$$

Since the transmitted above-bandgap photon flux, surface reflectance, and absorption coefficient are spatially uniform, the integral simplifies to

$$G_{ehp} = \frac{\hat{n}_{ph,E>E_g}\alpha(1-R)}{L}\int_0^L e^{-\alpha x}dx$$

$$G_{ehp} = \frac{\hat{n}_{ph,E>E_g}\alpha(1-R)}{L}\left(-\frac{1}{\alpha}e^{-\alpha x}\Big|_0^L\right)$$

$$G_{ehp} = -\frac{\hat{n}_{ph,E>E_g}(1-R)}{L}(e^{-\alpha x}|_0^L)$$

$$G_{ehp} = -\frac{\hat{n}_{ph,E>E_g}(1-R)}{L}(e^{-\alpha L}-1)$$

$$G_{ehp} = \frac{\hat{n}_{ph,E>E_g}(1-R)}{L}(1-e^{-\alpha L})$$

Although, this device architecture's $MAPbI_3$ thickness is thin (≈300 nm) relative to high-performance devices, meaning optical interference effects in all device layers and multiple resultant reflectivity sources exist and weaken this transmittance expression. The transfer matrix model may thus result in different fitted parameter evolutions with degradation time due to the differing electron-hole pair generation profile.

8.1.2 Appendix A.2. Derivation of Degraded Thickness from Thickness-Related Generation Rate Loss

From the derivation in Section 8.1.1 (Appendix A.1), the average volumetric electron-hole pair generation rate G_{ehp} is given by

$$G_{ehp} = \frac{\hat{n}_{ph,E>E_g}(1-R)}{L}(1-e^{-\alpha L})$$

where $\hat{n}_{ph,E>E_g}$ is the incident above-bandgap photon flux, R is the reflectance, L is the active layer's active thickness, and α is the active layer's absorption coefficient. Although, the average volumetric electron-hole pair generation rate determined from drift-diffusion fitting ($G_{ehp,DD}$) does not account for active area extinction, meaning the true average volumetric electron-hole pair generation rate (G_{ehp}) is that obtained from drift-diffusion fitting multiplied by the ratio of initial ($A_{active,t=0}$) and current (A_{active}) active areas:

$$G_{ehp} = \frac{(A_{active})_i}{(A_{active})_f}\left(G_{ehp}\right)_{DD}$$

$$\frac{(A_{active})_i}{(A_{active})_f}\left(G_{ehp}\right)_{DD} = \frac{\hat{n}_{ph,E>E_g}(1-R)}{L_i}(1-e^{-\alpha L})$$

Moreover, we attribute the decrease in the true average volumetric electron-hole pair generation rate (G_{ehp}) unaccounted for by the dark-field (DF) image analysis to degradation of the absorber layer thickness, enabling calculation of effective active and degraded HP film thicknesses. Unfortunately, the equation cannot be rearranged explicitly for the absorber layer's active thickness, so we numerically solve the equation.

8.1.3 Appendix A.3. Justification for the Single Mid-Gap Trap Model for Nonradiative, Monomolecular, Shockley-Read-Hall (SRH) Recombination

Regarding trap energy levels, HPs possess many shallow and deep defect states according to density functional theory (DFT) simulations.[156–161] Although, shallow defects promote thermal excitation of trapped carriers back to their respective bands before trap-assisted recombination can occur while deep defect states promote the opposite. Deep defect states are thus the primary contributors to SRH recombination. Additionally, since SRH recombination rates change negligibly among deep defect states, a single mid-bandgap trap state accurately models SRH recombination in moderate- to high-bandgap semiconductors.[33] Mathematically, the probability of trapped carriers being thermally excited back to their respective bands prior to recombination exponentially decays with the energy difference between the band edges and the defect state. For a trapped carrier, these probabilities for electrons and holes, respectively, are

$$P_{esc,n_t} = \frac{R_{detrap,n}}{R_{trap,n}} = \frac{C_n n_1 N_t f_t}{C_n n N_t (1-f_t)} = \frac{n_1 f_t}{n(1-f_t)}$$

$$P_{esc,p_t} = \frac{R_{detrap,p}}{R_{trap,p}} = \frac{C_p p_1 N_t (1-f_t)}{C_p p N_t f_t} = \frac{p_1 (1-f_t)}{p f_t}$$

where P_{esc,n_t} and P_{esc,p_t} are the probabilities of trapped electrons and holes, respectively, detrapping before undergoing SRH recombination. The corresponding probabilities (P_{SRH,n_t} and P_{SRH,p_t}) of trapped carriers undergoing SRH recombination are

$$P_{SRH,n_t} = 1 - P_{esc,n_t} = \frac{R_{SRH,n}}{R_{trap,n}} = \frac{C_n n N_t (1-f_t) - C_n n_1 N_t f_t}{C_n n N_t (1-f_t)} = 1 - \frac{n_1 f_t}{n(1-f_t)}$$

$$P_{SRH,p_t} = 1 - P_{esc,p_t} = \frac{R_{SRH,p}}{R_{trap,p}} = \frac{C_p p N_t f_t - C_p p_1 N_t (1-f_t)}{C_p p N_t f_t} = 1 - \frac{p_1 (1-f_t)}{p f_t}$$

Although, these probabilities depend on the trap occupation probability (f_t), and this is generally time-dependent. Nevertheless, at steady state, the net SRH recombination rates for electrons and hole must be equivalent to ensure no charge buildup ($R_{SRH,n} = R_{SRH,p}$), fixing the trap occupation probability (f_t) to

$$f_t = \frac{C_n n - C_p p_1}{C_n (n + n_1) + C_p (p + p_1)}$$

and the bulk SRH recombination rate to

$$R_{SRH} = \frac{C_n C_p N_t (np - n_i^2)}{C_n (n + n_1) + C_p (p + p_1)}$$

Additionally, the rational function of trap occupation probability (f_t) above is

$$\frac{f_t}{1-f_t} = \frac{\dfrac{C_n n - C_p p_1}{C_n (n + n_1) + C_p (p + p_1)}}{1 - \dfrac{C_n n - C_p p_1}{C_n (n + n_1) + C_p (p + p_1)}}$$

$$\frac{f_t}{1-f_t} = \frac{C_n n - C_p p_1}{C_n(n+n_1) + C_p(p+p_1) - C_n n + C_p p_1}$$

$$\frac{f_t}{1-f_t} = \frac{C_n n - C_p p_1}{C_n n_1 + C_p p + 2C_p p_1}$$

To simplify this expression, we assume equal capture coefficients ($C_n \approx C_p \approx C_{np}$) as done by many studies including Sherkar *et al.*,[155] yielding

$$\frac{f_t}{1-f_t} \approx \frac{n - p_1}{n_1 + p + 2p_1}$$

The probabilities then become

$$P_{esc,n_t} = \frac{n_1 f_t}{n(1-f_t)} \approx \frac{1 - \frac{p_1}{n}}{1 + \frac{p}{n_1} + \frac{2p_1}{n_1}} = \frac{1 - \frac{N_v}{n}\exp\left[-\frac{\frac{E_g}{2} + \Delta E_{t,mg}}{k_B T}\right]}{1 + \frac{p}{N_c}\exp\left[\frac{\frac{E_g}{2} - \Delta E_{t,mg}}{k_B T}\right] + \frac{2N_v}{N_c}\exp\left[-\frac{2\Delta E_{t,mg}}{k_B T}\right]}$$

$$P_{esc,p_t} = \frac{p_1(1-f_t)}{p f_t} \approx \frac{\frac{n_1}{p} + 1 + \frac{2p_1}{p}}{\frac{n}{p_1} - 1}$$

$$= \frac{\frac{1}{p}N_c \exp\left[-\frac{\frac{E_g}{2} - \Delta E_{t,mg}}{k_B T}\right] + 1 + \frac{2N_v}{p}\exp\left[-\frac{\frac{E_g}{2} + \Delta E_{t,mg}}{k_B T}\right]}{\frac{n}{N_v}\exp\left[\frac{\frac{E_g}{2} + \Delta E_{t,mg}}{k_B T}\right] - 1}$$

Assuming the conduction and valence band effective densities of states (DOS) are equivalent ($N_c \approx N_v \approx N_{cv}$ as is commonly assumed)[33] and equal to the considered HP composition's literature value at 25°C ($3.34 * 10^{24}\ m^{-3}$ for $MAPbI_3$) and assuming the average simulated carrier concentration in the middle of the absorber layer at 25°C at 1 sun illumination ($n \approx p$) ($10^{21}\ m^{-3}$ for $MAPbI_3$ based on simulation output variables for typical $MAPbI_3$ device fits), the probabilities as a function of the difference in trap energy relative to mid-gap ($\Delta E_{t,mg}$) for all three HP compositions are given by the set of corresponding curves (see Section 6). For $MAPbI_3$ in this standard case, the SRH probability is higher than 99% for defect states farther than 0.33 eV from band edges, and the thermal excitation probability is higher than 99% only for defect states less than 0.09 eV from the band edges. Additionally, probability distributions for electrons (left) and holes (right) with varying electron concentration, hole concentration, carrier concentration (assuming $n \approx p$), bandgap, and temperature. For the range of tested temperatures (25°C to 85°C) and corresponding effective densities of states (DOS), the SRH probability is higher than 99% for defect states in the middle of the bandgap, and the thermal excitation probability is higher than 99% for defect states in the outer regions of the bandgap near the band edges. The trap occupation probability and SRH recombination rate exhibit the same behavior.

Thus, if the primary defect states exist in these ranges, SRH recombination is well-modeled by a single mid-gap trap. Although, if a high-concentration defect state exists in the energy range exhibiting the transition from SRH recombination to thermal excitation, this model would be inaccurate. Thus, we assume a single mid-bandgap trap state with energy $E_{trap} = E_v + \frac{E_g}{2} = E_c - \frac{E_g}{2}$.

8.1.4 Appendix A.4. Derivation of Expressions for the Influences of Lower-Level Parameters on Higher-Level Parameters in Our Unique Cumulative Sensitivity Analysis (CSA)

Photovoltaic cells may be described with various sets of experimental or model parameters. The power conversion efficiency (PCE) is the highest-level metric for photovoltaic performance and is described by remaining experimental solar cell parameters: short-circuit current J_{sc}, open-circuit voltage V_{oc}, fill factor FF, and maximum power point (MPP) current J_{MPP} and voltage V_{MPP}. In this study, the non-ideal diode model and Koster *et al.*'s drift-diffusion model are employed. Koster *et al.*'s model utilizes fewer assumptions and more parameters, providing a more detailed description. Thus, these experimental and model parameters may be classified into four levels from higher-to-lower levels: PCE, solar cell parameters, non-ideal diode model parameters, and drift-diffusion model parameters.

8.1.4.1 Appendix A.4.1. General Derivation

The infinitesimal change $(dY)_{X_i}$ in a higher-level parameter Y caused by a change dX_i in a lower-level parameter X_i is the product of dX_i with the partial derivative of Y with respect to X_i.

$$(dY)_{X_i} = \frac{\partial Y}{\partial X_i} dX_i$$

If the partial derivative is a function, the corresponding cumulative change ΔY_{X_i} in Y is thus the partial derivative's integral with respect to X_i.

$$\Delta Y_{X_i} = \int_{(X_i)_i}^{(X_i)_f} \frac{\partial Y}{\partial X_i} dX_i$$

where $(X_i)_i$ and $(X_i)_f$ are X_i's initial and final values, respectively. Although, many parameters evolve non-monotonically during device degradation, meaning $\{X_i\}$ and $\{\partial Y/\partial X_i\}$ possess relations to, but are not necessarily functions of, of $\{X_i\}$. Thus, we parameterize X_i with the degradation time and apply the chain rule to obtain

$$\left(\frac{\partial Y}{\partial t}\right)_{\{X_i\}\neq X_i} = \frac{\partial Y}{\partial X_i}\frac{dX_i}{dt}$$

$$(dY)_{X_i} = \frac{\partial Y}{\partial X_i}\frac{dX_i}{dt} dt$$

Indeed, $\{X_i\}$ and $\{\partial Y/\partial X_i\}$ are functions of degradation time, and $(dY)_{X_i}$ may be integrated to determine the cumulative change $(\Delta Y)_{X_i}$ due to the cumulative change ΔX_i during the elapsed degradation time Δt

$$\Delta Y_{X_i} = \int_{t_i}^{t_f} \frac{\partial Y}{\partial X_i}\frac{dX_i}{dt} dt$$

where t_i and t_f are the initial and final degradation times. Furthermore, if Y may be described by a complete basis set of lower-level parameters $\{X_i\}$, its infinitesimal change dY caused by changes in $\{X_i\}$ is its total derivative with respect to $\{X_i\}$.

$$dY = \sum_i (dY)_{X_i} = \sum_i \frac{\partial Y}{\partial X_i}\frac{dX_i}{dt}dt$$

The corresponding cumulative change ΔY in Y caused by changes in $\{X_i\}$ is the total derivative's integral with respect to each lower-level parameter

$$\Delta Y = \sum_i \int_{t_i}^{t_f} \frac{\partial Y}{\partial X_i}\frac{dX_i}{dt}dt$$

The fractional change in Y caused by changes in X_i is thus

$$\frac{\Delta Y_{X_i}}{Y_i} = \frac{1}{Y_i}\int_{t_i}^{t_f} \frac{\partial Y}{\partial X_i}\frac{dX_i}{dt}dt$$

Although, other metrics are useful for quantifying $\{X_i\}$'s influence on Y. The set of the absolute values of the fractional changes $\{\Delta Y_{X_i}\}$ may be normalized to yield the set of fractional contributions each element of $\{X_i\}$ makes to the changes which occur in Y during degradation.

$$\left\{\frac{\Delta Y_{X_i}}{\sum_i |\Delta Y_{X_i}|}\right\}$$

Moreover, the set of multiplicative changes in Y caused by changes in $\{X_i\}$ may also be quantified. The total multiplicative factor is Y_f/Y_i where Y_i and Y_f are Y's initial and final values. Although, the multiplicative factor may also be expressed as

$$\frac{Y_f}{Y_i} = e^{\int_{t_i}^{t_f}\frac{dY}{Y}}$$

$$\frac{Y_f}{Y_i} = e^{\int_{t_i}^{t_f}\sum_i \frac{1}{Y}\frac{\partial Y}{\partial X_i}\frac{dX_i}{dt}dt}$$

$$\frac{Y_f}{Y_i} = \prod_i e^{\int_{t_i}^{t_f}\frac{1}{Y}\frac{\partial Y}{\partial X_i}\frac{dX_i}{dt}dt}$$

Since each term of the continued product contains a single, unique element of $\{X_i\}$, the terms are independent and represent the multiplicative effects $\left(Y_f/Y_i\right)_{X_i}$ of their respective element of $\{X_i\}$.

$$\left(\frac{Y_f}{Y_i}\right)_{X_i} = e^{\int_{t_i}^{t_f}\frac{1}{Y}\frac{\partial Y}{\partial X_i}\frac{dX_i}{dt}dt}$$

These multiplicative factors' expressions may seem complex, but they provide an alternative method for quantifying fractional changes since

$$\frac{Y_f}{Y_i} = \frac{Y_i + \Delta Y}{Y_i}$$

$$\frac{Y_f}{Y_i} = 1 + \frac{\Delta Y}{Y_i}$$

Furthermore, if Y possesses an analytical expression as a function of $\{X_i\}$, these multiplicative factors may possess an exact solution which is a simpler function of $\{X_i\}$. Indeed, these multiplicative factors simplify to simple proportionalities $Y = PCE$ and $\{X_i\} = \{J_{sc}, V_{oc}, FF\}$. However, although all parameters' values are known and their changes easily calculated, all integrals must be determined by numerical evaluation, and we utilize the trapezoid method. Additionally, all derivatives which require numerical evaluation are calculated with the first-order central finite difference method.

8.1.4.2 Appendix A.4.2. Example – Power Conversion Efficiency (PCE) versus Solar Cell Parameters

The power conversion efficiency (PCE) of a photovoltaic cell is

$$PCE = J_{sc} V_{oc} FF$$

where J_{sc} is the short-circuit current, V_{oc} is the open-circuit voltage, and FF is the fill factor. The PCE's partial derivatives with respect to these parameters are

$$\frac{\partial(PCE)}{\partial J_{sc}} = V_{oc} FF$$
$$\frac{\partial(PCE)}{\partial V_{oc}} = J_{sc} FF$$
$$\frac{\partial(PCE)}{\partial FF} = J_{sc} V_{oc}$$

since these lower-level parameters are independent. The PCE's infinitesimal change is thus

$$d(PCE) = d(PCE)_{J_{sc}} + d(PCE)_{V_{oc}} + d(PCE)_{FF}$$
$$d(PCE)_{J_{sc}} = \frac{\partial(PCE)}{\partial J_{sc}} \frac{dJ_{sc}}{dt} dt = V_{oc} FF \frac{dJ_{sc}}{dt} dt$$
$$d(PCE)_{V_{oc}} = \frac{\partial(PCE)}{\partial V_{oc}} \frac{dV_{oc}}{dt} dt = J_{sc} FF \frac{dV_{oc}}{dt} dt$$
$$d(PCE)_{FF} = \frac{\partial(PCE)}{\partial FF} \frac{dFF}{dt} dt = J_{sc} V_{oc} \frac{dFF}{dt} dt$$
$$d(PCE) = \left(V_{oc} FF \frac{dJ_{sc}}{dt} + J_{sc} FF \frac{dV_{oc}}{dt} + J_{sc} V_{oc} \frac{dFF}{dt} \right) dt$$

The corresponding cumulative changes are

$$\Delta(PCE) = \Delta(PCE)_{J_{sc}} + \Delta(PCE)_{V_{oc}} + \Delta(PCE)_{FF}$$
$$\Delta(PCE)_{J_{sc}} = \int_{t_i}^{t_f} V_{oc} FF \frac{dJ_{sc}}{dt} dt$$
$$\Delta(PCE)_{V_{oc}} = \int_{t_i}^{t_f} J_{sc} FF \frac{dV_{oc}}{dt} dt$$

$$\Delta(PCE)_{FF} = \int_{t_i}^{t_f} J_{sc} V_{oc} \frac{dFF}{dt} dt$$

$$\Delta(PCE) = \int_{t_i}^{t_f} \left(V_{oc} FF \frac{dJ_{sc}}{dt} + J_{sc} FF \frac{dV_{oc}}{dt} + J_{sc} V_{oc} \frac{dFF}{dt} \right) dt$$

Although these cumulative changes are equally sound to the multiplicative factors, the multiplicative factors are much simpler to evaluate. The multiplicative factors are

$$\left(\frac{Y_f}{Y_i}\right)_{J_{sc}} = e^{\int_{t_i}^{t_f} \frac{1}{PCE} V_{oc} FF \frac{dJ_{sc}}{dt} dt} = e^{\int_{t_i}^{t_f} \frac{dJ_{sc}}{J_{sc}}} = e^{\ln\left(\frac{(J_{sc})_f}{(J_{sc})_i}\right)} = \frac{(J_{sc})_f}{(J_{sc})_i}$$

$$\left(\frac{Y_f}{Y_i}\right)_{J_{sc}} = e^{\int_{t_i}^{t_f} \frac{1}{PCE} J_{sc} FF \frac{dV_{oc}}{dt} dt} = e^{\int_{t_i}^{t_f} \frac{dV_{oc}}{V_{oc}}} = e^{\ln\left(\frac{(V_{oc})_f}{(V_{oc})_i}\right)} = \frac{(V_{oc})_f}{(V_{oc})_i}$$

$$\left(\frac{Y_f}{Y_i}\right)_{J_{sc}} = e^{\int_{t_i}^{t_f} \frac{1}{PCE} J_{sc} V_{oc} \frac{dFF}{dt} dt} = e^{\int_{t_i}^{t_f} \frac{dFF}{FF}} = e^{\ln\left(\frac{(FF)_f}{(FF)_i}\right)} = \frac{(FF)_f}{(FF)_i}$$

As expected, the PCE is independently proportional to J_{sc}, V_{oc}, and FF during degradation.

8.2 Appendix B. Supplementary Results

8.2.1 Appendix B.1. Linear Regression of The Initial Decline in Effective Active Area

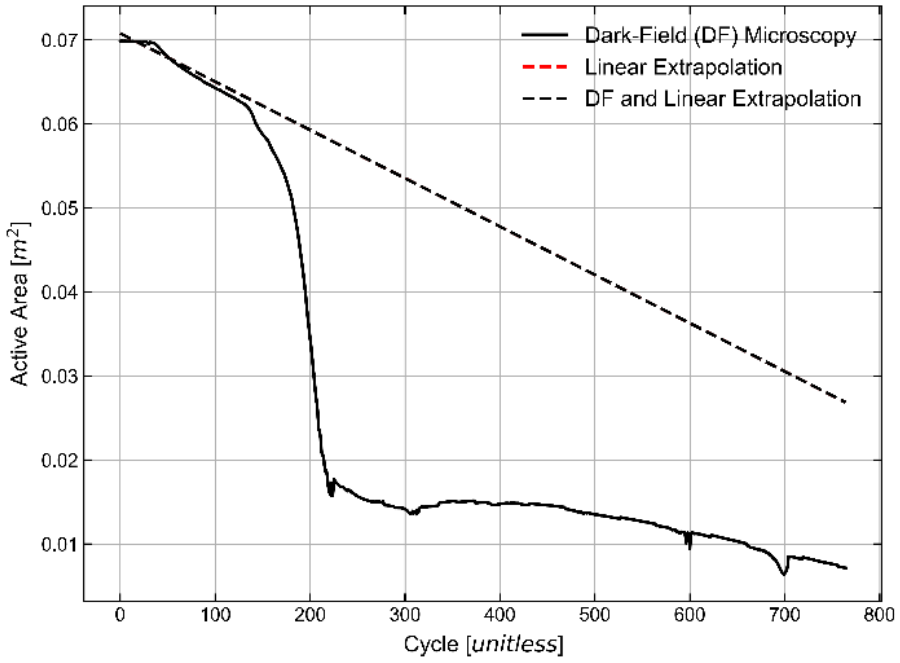

Figure 48. Scatterplot of the Effective Active Area of a $MAPbI_3$ Film Determined from Dark-Field (DF) Microscopy for the Degrading MAPbI3 Device in Figure 12. As for all devices, linear extrapolation of the initial decline in effective active area is performed to determine accurate extrapolations of the effective HP film area and thickness following the arrival of gaseous reactants to the HP-HTL interface.

8.2.2 *Appendix B.2. Profiles of Drift-Diffusion Simulation Output Variables Along the Simulation Thickness over Time for a $MAPbI_3$ Device Degradation Run*

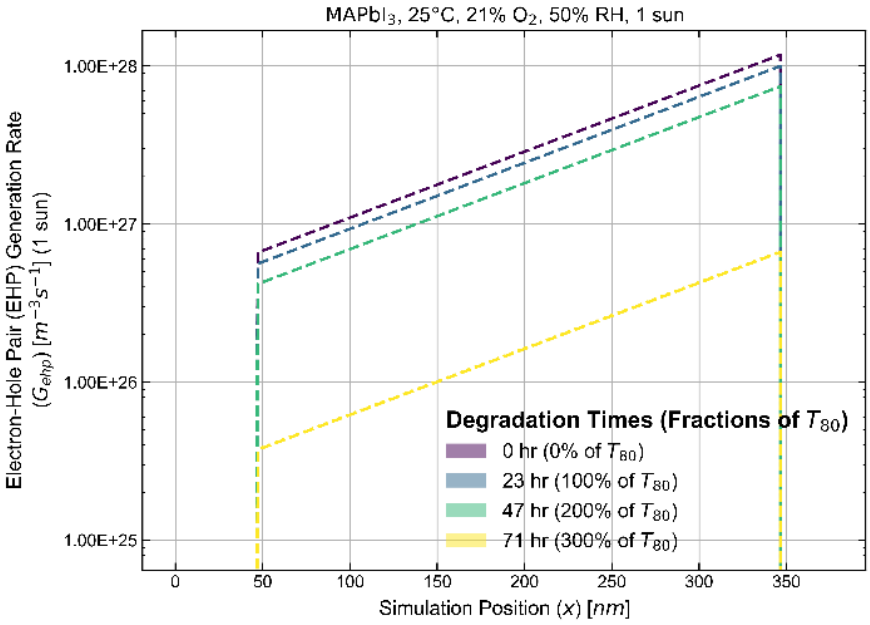

Figure 49. Line Plots of the Spatial Profiles of Electron-Hole Pair (EHP) Volumetric Generation Rate (G_{ehp}) Along the Simulation Thickness for the Degrading MAPbI3 Device in Figure 12. Note that G_{ehp} is plotted on a logarithmic scale, meaning the exponential attenuation law (i.e., Beer-Lambert law) manifests as a linear generation profile. See Table 9 for a complete list of the drift-diffusion simulation output variables.